

1

AGARD-R-767

AGARD-R-767

AD-A227 422

AGARD

ADVISORY GROUP FOR AEROSPACE RESEARCH & DEVELOPMENT

7 RUE ANCELLE 92200 NEUILLY SUR SEINE FRANCE

AGARD REPORT No. 767

Short-Crack Growth Behaviour in Various Aircraft Materials

(Le Développement des Petites Fissures dans Divers Matériaux Aéronautiques)

DLIC
ELECTE
OCT 15 1990
S B D

NORTH ATLANTIC TREATY ORGANIZATION



DISTRIBUTION AND AVAILABILITY ON BACK COVER

DISTRIBUTION STATEMENT A

Approved for public release; Distribution Unlimited

AGARD-R-767

NORTH ATLANTIC TREATY ORGANIZATION
ADVISORY GROUP FOR AEROSPACE RESEARCH AND DEVELOPMENT
(ORGANISATION DU TRAITE DE L'ATLANTIQUE NORD)

AGARD Report No.767

Short-Crack Growth Behaviour in Various Aircraft Materials

(Le Développement des Petites Fissures dans Divers
Matériaux Aéronautiques)

compiled by

P.R.Edwards
P P Data, Ltd
Fleet, Hampshire
United Kingdom

and

J.C.Newman, Jr
Materials Division
NASA Langley Research Center
Hampton, Virginia
United States

This publication was sponsored by the Structures and Materials Panel of AGARD.

The Mission of AGARD

According to its Charter, the mission of AGARD is to bring together the leading personalities of the NATO nations in the fields of science and technology relating to aerospace for the following purposes:

- Recommending effective ways for the member nations to use their research and development capabilities for the common benefit of the NATO community;
- Providing scientific and technical advice and assistance to the Military Committee in the field of aerospace research and development (with particular regard to its military application);
- Continuously stimulating advances in the aerospace sciences relevant to strengthening the common defence posture;
- Improving the co-operation among member nations in aerospace research and development;
- Exchange of scientific and technical information;
- Providing assistance to member nations for the purpose of increasing their scientific and technical potential;
- Rendering scientific and technical assistance, as requested, to other NATO bodies and to member nations in connection with research and development problems in the aerospace field

The highest authority within AGARD is the National Delegates Board consisting of officially appointed senior representatives from each member nation. The mission of AGARD is carried out through the Panels which are composed of experts appointed by the National Delegates, the Consultant and Exchange Programme and the Aerospace Applications Studies Programme. The results of AGARD work are reported to the member nations and the NATO Authorities through the AGARD series of publications of which this is one.

Participation in AGARD activities is by invitation only and is normally limited to citizens of the NATO nations



The content of this publication has been reproduced directly from material supplied by AGARD or the authors.

Accession For	
NTIS GRA&I	<input checked="" type="checkbox"/>
DTIC TAB	<input type="checkbox"/>
Unannounced	<input type="checkbox"/>
Justification	
By	
Distribution/	
Availability Codes	
Dist	Avail and/or Special
A-1	

Published August 1990
 Copyright © AGARD 1990
 All Rights Reserved

ISBN 92-835-0577-8



Printed by Specialised Printing Services Limited
 40 Chigwell Lane, Loughton, Essex IG10 3TZ

Preface

In 1982 the Structures and Materials Panel organized a Specialists' Meeting on the "Behaviour of Short Cracks in Aircraft Structures". The Meeting revealed the complexity of the short-crack growth behaviour and that a short-crack effect does exist, at least under certain test conditions. It also indicated that differences in test technique existed that made it very difficult to compare the data obtained by individual researchers and to assess the significance of the short-crack effect.

In 1984 the Panel organized a Cooperative Test Programme with as objectives: the development of a standard test method for the measurement of short-crack growth, the establishment of relevant short-crack growth data, to improve existing analytical crack growth models and to define the significance of the short-crack effects.

The programme was devised in two parts; a "core" and a "supplemental" portion. The "core" programme set out to establish a common test procedure and methods for data analysis. Test data were gathered on the same aircraft alloy — AA 2024-T3. The "supplemental" programme focused on the short-crack phenomenon in other aircraft alloys and on crack modelling.

The results of the "core" programme are described in AGARD report R 732 while this report describes the results obtained as part of the "supplemental" programme.

The cooperative programme was guided by a Panel sub-committee with the valuable assistance of two coordinators. Over the years the following Panel members participated in the sub-committee.

P.Bascary (FR)	W.G.Heath (UK)
H.J.G.Carvalhinhos (PO)	R.Labourdette (FR)
K.I. Collier (UK)	H.P.van Leeuwen (NL)
A.Deruyttere (BE)	R.D.J.Maxwell (UK)
M.Doruk (TU)	C.W.Skingie (UK)
J.L.Engerand (FR)	A.Salvetti (IT)
J.M.Fehrenbach (FR)	R.Schmidt (US)
G.Z.Harris (UK)	W.Wallace (CA)
L.A.Harris (US)	

The tests in the "supplemental" programme were performed by ten laboratories in eight nations represented by:

A.Ankara, METU, (TU)	C.J.Mazur, AFWAL, (US)
A.F.Blom, FFA, (SW)	H.Nowack, DLR, (GE)
A.W.Bowen, RAE, (UK)	J.C.Newman Jr, NASA, (US)
M.H.Carvalho, LNETI, (PO)	E.P.Phillips, NASA, (US)
R.Cook, RAE, (UK)	J.L.Rudd, AFWAL, (US)
M.de Freitas, CEMUL, (PO)	L.Schra, NLR, (NL)
P.R.Edwards, PP Data, (UK)	J.Strunk, DLR, (GE)
R.A.Everett, NASA, (US)	M.H.Swain, NASA, (US)
R.Galatolo, Univ. of Pisa, (IT)	K.H.Trautmann, DLR, (GE)
C.Kaynak, METU, (TU)	R.J.H.Wanhill, NLR, (NL)
A.Lanciotti, Univ. of Pisa, (IT)	

The coordinators for the programme were:

for Europe — P.R.Edwards
for North America — J.C.Newman, Jr

Many thanks are extended to all who participated in the programme, especially to the two coordinators for their considerable efforts in bringing to a successful completion this very valuable piece of research.

H.Zocher
Chairman, Sub-Committee on
Research for Short Crack Effects

Structures and Materials Panel

Chairman: Prof. Dr-Ing. Hans Försching
Direktor der DFVLR Institut für Aeroelastik
Bunsenstrasse 10
D-3400 Göttingen
Germany

Deputy Chairman: Mr Samuel L. Venneri
Director, Materials & Structures
Division (Code RM)
Office of Aeronautics & Space Technology
NASA Hq
Washington DC 20546
United States

SUB-COMMITTEE ON RESEARCH FOR SHORT CRACK EFFECTS

Chairman: Dipl. Ing. Horst Zocher
IABG mbH, Abt TF
Einsteinstrasse, 20
D-8012 Ottobrunn
West Germany

SMP MEMBERS

H.J.G.Carvalhinhos	PO
A.Deruyttere	BE
M Doruk	TU
R.Labourdette	FR
H.P.van Leeuwen	NL
A.Salvetti	IT

TECHNICAL COORDINATORS

P.R.Edwards — UK (Europe)
J.C.Newman — US (North America)

PANEL EXECUTIVE

Mr Murray C.McConnell — UK

From Europe
AGARD-OTAN
7, rue Ancelle
92200 Neuilly sur Seine
France
Tel: 33(1) 4738 5790 & 5792
Telex: 610176F

From US and Canada
AGARD-NATO
Attn: SMP Executive
APO New York 09777

Abstract

AGARD Report R-732 reviews the results of the first phase of an AGARD Cooperative Test Programme on the behaviour and growth of "short" fatigue cracks. That report describes, the establishment of a common test method, means of data collection, analysis and crack growth modelling in an aircraft alloy AA 2024-T3. The second and concluding phase of this Programme allowed participants to test various materials and loading conditions. The results of this second phase are described in this report.

All materials exhibited a "short-crack" effect to some extent. The effect was much less evident in 4340 steel than in the other materials. For the aluminium, aluminium-lithium and titanium alloys, short cracks grew at stress-intensity factor ranges lower, in some cases much lower, than the thresholds obtained from long crack tests. Several laboratories used the same crack growth model to analyze the growth of short cracks. Reasonable agreement was found between measured and predicted short-crack growth rates and fatigue lives.

This publication was sponsored by the Structures and Materials Panel of AGARD.

Abrégé

Le rapport AGARD R-732 rend compte des résultats de la première phase du programme collaboratif d'essais AGARD sur le développement des petites fissures. Ce rapport décrit, l'élaboration d'une méthode d'essai commune, les moyens utilisés pour la collecte et l'analyse des données, et la modélisation du développement des fissures dans un alliage aéronautique AA 2024T3. La deuxième et dernière phase de ce programme a permis aux participants de tester divers matériaux dans différentes conditions de sollicitation. Les résultats obtenus lors de cette deuxième phase sont présentés dans ce rapport.

Tous les matériaux testés ont présenté le défaut "petites fissures" dans une certaine mesure. Le phénomène était beaucoup moins marqué dans le cas de l'acier 4340 que pour les autres matériaux. En ce qui concerne les alliages d'aluminium, d'aluminium-lithium et de titane, les petites fissures se sont propagées selon des facteurs d'intensité de contrainte moins élevés, et dans certains cas, beaucoup moins élevés que les seuils obtenus lors des essais sur le développement des grandes fissures.

Plusieurs laboratoires ont utilisé le même modèle du développement des fissures pour analyser le développement des petites fissures. Les prévisions concordent avec les résultats dans une large mesure en ce qui concerne les vitesses de propagation des fissures et l'endurance en fatigue.

Cette publication a été cautionnée par le Panel AGARD des Structures et Matériaux

Contents

	Page
Preface	iii
Structures and Materials Panel	iv
Abstract/Abrégé	v
	Reference
An AGARD Supplemental Test Programme on the Behaviour of Short Cracks under Constant Amplitude and Aircraft Spectrum Loading by P.R.Edwards and J.C.Newman, Jr	1
Determination of the Short Crack Effect in 2090-T8E41 Aluminium Lithium by C.J.Mazur and J.L.Rudd	2
Short Crack Behaviour in Al-Li Alloy 2090 by M.H.Carvalho and M.de Freitas	3
Crack Behaviour of 2024-T3, 2090-T8E41 and 7075-T6 under Constant Amplitude and Different Types of Variable Amplitude Loading, Especially Gaussian Loading by H.Nowack, K.H.Trautmann and J.Strunck	4
The Growth of Short Fatigue Cracks in 2024 and 2090 Aluminium Alloys under Variable Amplitude Loading R.Cook	5
Short Crack Growth under Realistic Flight Loading: Model Predictions and Experimental Results for Al 2024 and Al-Li 2090 by A.F.Blom	6
The Growth of Short Cracks in 4340 Steel and Aluminum-Lithium 2090 by M.H.Swain, R.A.Everett, J.C.Newman, Jr and E.P.Phillips	7
Short and Long Fatigue Crack Growth in 2024-T3 under Fokker 100 Spectrum Loading by R.J.H.Wanhill and L.Schra	8
Growth of Short Fatigue Cracks in 7075-T6 Aluminum Alloy by C.Kaynak and A.Ankara	9
Short Crack Observations in Ti-6Al-4V under Constant Amplitude Loading by A.Lanciotti and R.Galatolo	10
Annex: Texture Analysis of 2090-T8E41 Aluminum-Lithium Alloy Sheet by A.W.Bowen	11

AN AGARD SUPPLEMENTAL TEST PROGRAMME ON THE BEHAVIOUR OF SHORT CRACKS
UNDER CONSTANT AMPLITUDE AND AIRCRAFT SPECTRUM LOADING

by
P. R. Edwards
P P Data Ltd.
Fleet, Hampshire
UNITED KINGDOM

and

J. C. Newman, Jr
Materials Division
NASA Langley Research Center
Hampton, Virginia
USA

SUMMARY

An AGARD Supplemental Test Programme on the growth of "short" fatigue cracks was conducted to allow participants to test various materials and loading conditions that were of interest to their laboratories. Twenty-two participants from ten laboratories in eight countries contributed to the supplemental test programme. Each laboratory submitted a paper on their test and analysis results, and these papers are included in this AGARD publication. The objective of this paper is to review the supplemental test programme and to summarize the results obtained from all laboratories. The materials tested in the supplemental programme were, 2024-T3 and 7075-T6 aluminum alloys, 2090-T8E11 aluminum-lithium alloy, Ti-6Al-4V titanium alloy and 4340 steel. Tests on single-edge-notch-tension specimens were conducted under several constant-amplitude loading conditions (stress ratios of -2 , -1 , 0 , and 0.5) and spectrum loading conditions (FALSTAFF, Inverted FALSTAFF, GAUSSIAN, TWIST, Felix and the Fokker 100 spectra). The plastic-replica method was used to measure the growth of short cracks at the notch root.

The results from the supplemental test programme show good agreement among the several laboratories who measured short-crack growth rates on the aluminum-lithium alloy. In this alloy, short surface cracks at a notch grew under mixed-mode conditions (usually 30 to 35 degrees from the loading axis). All materials exhibited a "short-crack" effect to some extent. The effect was much less evident in the 4340 steel than in the other materials. For the aluminum, aluminum-lithium, and titanium alloys, short cracks grew at stress-intensity factor ranges lower, and in some cases much lower, than the thresholds obtained from long-crack tests under the same loading conditions. The short-crack effects were more pronounced as the stress ratio became more negative. This applied for both constant-amplitude and spectrum loading. For the 2024-T3 aluminum alloy and the 2090 aluminum-lithium alloy, the short surface cracks grew equal to or faster than long cracks when subjected to the same stress ratio (except $R = 0.5$) and to the same stress-intensity factor range above the long-crack threshold. The short-crack growth rates for the 7075-T6 aluminum alloy and the Ti-6Al-4V titanium alloy were equal to or slower than those for long cracks under the same stress ratio and the same stress-intensity factor range above the long-crack threshold. The short-crack growth rates for the 4340 steel usually agreed with the long-crack growth rates over a wide range in rates, except for results at low growth rates and at $R = -1$. All materials, except 4340 steel, tested at the high stress ratio ($R = 0.5$) generally showed that short cracks grew slower than long cracks above the long-crack threshold.

Three laboratories used the crack-growth model (FASTRAN) which incorporates crack-closure effects to analyze the growth of short cracks from small (inclusion) defects along the notch surface in the 2024-T3 aluminum alloy and 4340 steel. The assumed defect sizes were consistent with experimental observations of initiation sites at inclusion-particle clusters or voids left behind by the inclusions during the machining or polishing process. Analyses were conducted under constant-amplitude loading and spectrum loading (FALSTAFF, inverted FALSTAFF, GAUSSIAN, TWIST and Felix). Reasonable agreement was found between measured and predicted short-crack growth rates and fatigue lives for most loading conditions.

1. INTRODUCTION

Linear-elastic fracture mechanics methods are widely accepted for damage-tolerance analyses. Recently, there has also been a trend towards the use of the same methodology for fatigue durability analyses. To obtain acceptably long lives without a significant weight penalty, the analyses must assume a very small initial crack. Numerous investigators [1-18] have observed that the growth characteristics of short fatigue cracks in plates and at notches differ from those of long cracks in the same material. These studies have concentrated on the growth of short cracks ranging in length from 10 μm to 1 mm. On the basis of linear-elastic fracture mechanics (LEFM), the short cracks grew much faster than would be predicted from long crack data. This behaviour is illustrated in Figure 1, where the crack-growth rate is plotted against the linear-elastic stress-intensity factor range, ΔK . The solid (sigmoidal) curve shows typical results for a given material and environment under constant-amplitude loading. The solid curve is usually obtained from tests with long cracks. At low growth rates, the threshold stress-intensity factor range, ΔK_{th} , is usually obtained from load-reduction (K-decreasing) tests. Some typical experimental results for short cracks in plates and at notches are shown by the dashed curves. These results show that short cracks grow at ΔK levels below threshold and that they also can grow faster than long cracks at the same ΔK level above threshold.

A Specialists' Meeting organized by the AGARD Structures and Materials Panel (SMP) on "The Behaviour of Short Cracks in Aircraft Structures" [15] revealed the complexity of short-crack growth behaviour. Many views were expressed on the data obtained from experimental and analytical investigations, but there was no consensus of opinion. Some tests appeared to confirm the existence of the short-crack effect, whereas other experimenters did not confirm these findings. During the round table discussion [15], however, it became clear that tests which did not confirm the existence of the

short-crack effect had not included compressive loading cycles. The applicability of LEFM concepts to short-crack growth behaviour was also questioned. Some of the "classical" short-crack experiments [1-3] were conducted at high stress levels which would invalidate LEFM procedures. Nonlinear or elastic-plastic fracture mechanics concepts were also used to explain the observed short-crack effects. In addition, the metallurgical similitude [16] breaks down for short cracks (which means that the growth rate is no longer an average taken over many grains). Thus, the local growth behaviour is controlled by metallurgical features [6,12]. If the material is markedly anisotropic (differences in modulus and yield stress in different crystallographic directions), the local grain orientation will determine the rate of growth. Crack front irregularities and small particles or inclusions affect the local stresses and, therefore, the crack growth response. In the case of long cracks (which have long fronts), all of these metallurgical effects are averaged over many grains, except in very coarse-grained materials. LEFM and nonlinear fracture mechanics concepts are only beginning to explore the influence of metallurgical features on stress-intensity factors, strain-energy densities, J -integrals and other crack-driving parameters.

As the crack size approaches zero, a crack size must exist below which the assumptions of the ΔK concept are violated. However, the transition from valid to invalid conditions does not occur abruptly. For many engineering applications, a ΔK -based analysis that extends into the "gray area" of validity may still prove to be very useful. Certainly from a structural designer's viewpoint, a single analysis methodology that is applicable to all crack sizes is very desirable. If for no other reason than that ΔK analyses are already being used for long-crack problems, the application of a ΔK analysis to short-crack problems should be thoroughly explored.

The outcome of the AGARD SMP meeting [15] was to encourage further activity on the growth behaviour of short cracks. As a result, an AGARD Cooperative Test Programme was initiated in 1984 to investigate the short-crack growth behaviour under various loading conditions for a common airframe aluminum alloy (2024-T3) and to improve methodologies to predict the growth of short cracks. The results from the Cooperative Test Programme are reported in reference 19.

The objectives of the AGARD Cooperative Test Programme on the Behaviour of Short Cracks were to: (1) define the "short-crack" specimen, core-programme material, and loading conditions, (2) develop standard test methods to measure growth of short cracks, (3) calibrate test techniques used by the participating laboratories, (4) establish relevant short-crack data under specified test conditions, (5) define the regime where long-crack data are applicable to short cracks, (6) improve existing analytical crack-growth models, and (7) define the significance of the short-crack effect.

The "short-crack" specimen used in the cooperative test programme was selected to produce naturally-occurring cracks at material defects and to propagate cracks through a stress field similar to that encountered in aircraft structures. Herein, material "defects" refer to inclusion or constituent particles, voids or pits left by inclusion particles during machining and polishing, and other discontinuities. Single edge-notch tensile specimens made of 2024-T3 aluminum alloy sheet material, as shown in Figure 2, were used. The cracks generally initiated from inclusion-particle clusters or voids on the notch surface and grew as surface cracks. A wide range in loading conditions was applied in the test programme. Tests were conducted under several constant-amplitude and spectrum (FALSTAFF [20,21] and GAUSSIAN [22]) loading conditions. Thirteen laboratories participated in the Cooperative Test Programme, see Tables 1 and 2.

Several methods of measuring the growth of "short" cracks (lengths from about 10 μm) were considered. These methods were the electrical-potential method [23], ultrasonic surface wave [24], marker bands [25], and plastic replicas [25,26]. For the aluminum alloy, the plastic-replica method was found to be accurate for use down to the short-crack lengths required in the programme. This method is very simple to apply but the data collection is very labor intensive. Nevertheless, the growth of short cracks was recorded by all participants using the plastic-replica method.

To verify the existence and significance of the short-crack effects for other materials and under different loading conditions, an AGARD Supplemental Test Programme was initiated in 1986.

2. SUPPLEMENTAL TEST PROGRAMME

The AGARD Supplemental Test Programme on the growth of "short" fatigue cracks was conducted to allow participants to test various materials and loading conditions that were of interest to their laboratory. Twenty-two participants from ten laboratories in eight countries contributed to the supplemental test programme (see Table 3). Each laboratory submitted a paper on their test and analysis results, and these papers are included in this AGARD publication. The objective of this paper is to summarize the supplemental test programme and to review the results obtained from all participants.

The supplemental test programme consisted of testing single-edge-notch and center-crack tension specimens made of various sheet materials under constant- and variable-amplitude loading. The basic test procedures and short-crack specimen design that were used in the AGARD Cooperative Test Programme [19] (referred to as the Core Programme) were also used in the supplemental test programme. In the core test programme, all participants tested 2024-T3 aluminum alloy specimens. The materials tested in the supplemental programme were: 2024-T3 and 7075-T6 aluminum alloys, 2090-TSE-11 aluminum-lithium alloy, Ti-6Al-4V titanium alloy and 4340 steel. Six laboratories tested the aluminum-lithium alloy. Table 4 summarizes the laboratory test matrix in the supplemental test programme. Tables 5 and 6 summarize the nominal chemical compositions and mechanical properties for all materials tested. All tests were conducted at room temperature and under laboratory air conditions. The initiation and growth of short fatigue cracks (5 μm to about 2 mm) from the root of a semi-circular notch in the sheet materials were monitored under various loading histories. Growth of the short cracks was recorded using a plastic-replica technique [19]. Tests were conducted under several constant-amplitude loading conditions (stress ratios of -2, -1, 0, and 0.5) and spectrum loading conditions (FALSTAFF [20,21], Inverted FALSTAFF [28], GAUSSIAN [22], TWIST [29], Felix [30] and the Marker 100 [31] spectra). Long-crack growth rate data for cracks greater than 2 mm in length were obtained for each of the constant-amplitude and spectrum loading conditions tested by each participant. The long-crack results were used to define the regime where long-crack data are applicable to short cracks in the materials tested in the supplemental programme.

Three laboratories used the semi-empirical crack-growth model (FASTRAN [32,33]), which incorporates crack-closure effects, to analyze the growth of short cracks from small (inclusion) defects along the notch surface in the 2024-T3 aluminum alloy and 4340 steel. The model was used to correlate long crack-growth rate data over a wide range in rates for various constant-amplitude loading conditions. Using the long-crack data, the model was then used to predict crack growth and closure behaviour of short cracks emanating from semi-circular edge notches, to predict fatigue lives from an initial defect size, and to predict crack shapes. Analyses were conducted under both constant-amplitude loading and spectrum loading (FALSTAFF, Inverted FALSTAFF, GAUSSIAN, TWIST and Felix).

The following sections describe the short-crack specimens, materials, loading conditions, test procedures, and data analysis procedures used to obtain short-crack growth rate data. The procedures used to obtain long-crack growth rate data from center-crack tension specimens are discussed in reference 19.

2.1 Short-Crack Specimen

The short-crack specimen used in the core programme, a single-edge-notch tensile (SENT) specimen (shown in Figure 2), was used by all participating laboratories in the supplemental programme, except the laboratory that tested the 4340 steel. Because of test machine capabilities, a smaller width SENT specimen, shown in Figure 3, was used for the steel. The SENT specimen was selected because naturally-occurring cracks would be produced at material "defects" and they would propagate through a stress field similar to that encountered in aircraft structures. The notch was semi-circular with a radius of 3.18 mm. The stress concentration was 3.17 for the 50-mm wide specimen and 3.30 for the 25-mm wide specimen, based on gross-section stress [31]. Figure 4 shows the normal stress distribution near the notch root for the 50-mm wide SENT specimen (solid curve). For comparison, the normal stress distribution for a circular hole in an infinite plate is shown as the dashed curve. The normal stress distribution for the SENT specimen is similar to that for an open hole in an infinite plate, but the stresses are slightly higher because of the finite width. Therefore, the SENT specimen simulates a hole in an aircraft structure, but the side notch allows the notch root to be observed with a microscope and allows plastic replicas to be taken with ease during testing.

The specimen blanks for the SENT specimens were machined from sheets of the various materials. The long dimension of all specimens was parallel to the rolling direction of the sheet. The semi-circular edge notch was carefully milled and polished to minimize residual stresses at the notch root.

Specimens were tested in either wedge grips, hydraulic grips, or flat plate friction grips. The grip lines are shown in Figures 2 and 3. In some laboratories, bolt holes were also used in the gripping area to apply pressure in gripping the specimen. The specimens were not gripped directly. Either aluminum or plastic spacers were used between the specimen and the grip jaws. These spacers were used so that the specimen would not crack in the gripping area.

2.2 Materials

The supplemental short-crack test programme involved five materials, two conventional aluminum alloys (2024-T3 and 7075-T6), a new aluminum-lithium alloy (2090-T8E41), a titanium alloy (Ti-6Al-4V), and a high-strength steel (4340). The two aluminum alloys and the steel specimens were provided by the NASA Langley Research Center. The aluminum-lithium alloy was provided by Alcoa and the specimens were machined by the Air Force Wright Aeronautical Laboratory (AFWAL). The titanium alloy was provided by Aeritalia GVC and the specimens were machined by the University of Pisa. Tables 5 and 6 give the nominal chemical compositions and average tensile properties for the supplemental programme materials.

The notch-root region of the SENT specimens were either chemically polished (2024-T3, 7075-T6 and 2090-T8E41), electro-polished (4340) or mechanically polished (Ti-6Al-4V) to smooth machining marks on the notch surface and to deburr the edges of the notch. This also provided further assurance that there were no significant residual stresses present at the notch root. The edges of the notches were mildly rounded during the polishing process, thus preventing premature initiation of cracks at the edges.

2.2.1 Aluminum Alloy 2024-T3

The core-programme material was 2024-T3 aluminum alloy sheet (2.3 mm thick). This material was taken from a special stock of aluminum-alloy sheets retained at NASA Langley Research Center for fatigue testing. Fatigue-crack-growth properties of this material are discussed in references 35 and 36.

Typical grain dimensions in the crack-growth direction, $2a$ (along the notch root) and in the crack-growth direction, c (away from the notch root) were 25 μm and 55 μm , respectively. The grain dimension in the rolling direction was typically 95 μm . Clusters of inclusion particles were quite evident throughout the material. References 19 and 36 give a more complete description of a microstructural examination of the core-programme material.

Specimens from the same lot used for the core-programme were provided to various participants. Nowack, Trautmann, and Strunck [37] conducted additional tests at a high-R ratio condition, while Cook [28], Blom [38], and Wanhil and Schra [31] conducted tests under various aircraft load spectra.

2.2.2 Aluminum Alloy 7075-T6

The 7075-T6 aluminum alloy sheet (2.3 mm thick) was also taken from a special stock of material retained at NASA Langley Research Center for fatigue testing. The fatigue-crack-growth properties of this material are also discussed in

reference 35. Typical grain dimensions in the crack-growth directions, $2a$ and c , were $7 \mu\text{m}$ and $25 \mu\text{m}$, respectively. The dimension of the grains in the rolling direction was typically $30 \mu\text{m}$.

Specimens from the same lot of material were used by Ankara and Kaynak [39] and Swain [40] for short-crack tests, and Phillips [41] for long-crack tests, under a wide range in constant-amplitude loading conditions.

2.2.3 Aluminum-Lithium Alloy 2090-T8E41

The aluminum-lithium 2090-T8E41 material was furnished by Alcoa as a single sheet, 2.15 mm thick, with composition as specified in Table 5. The material exhibited a pancake microstructure, typical of a rolled aluminum sheet, with an average grain dimension along the short transverse direction (thickness of the sheet) of about $5 \mu\text{m}$. The microstructure is believed to be predominantly recrystallized with the "pancake grain" appearance resulting from a small difference in orientation between the fine grains formed within each one of the previous solidification cells of the Al-Li ingot that have become elongated in the rolling direction. The Al-Li sheet was also highly textured. A texture analysis of the Al-Li sheet used in the supplemental test programme was conducted by A. W. Bowen (Royal Aerospace Establishment) and is reported in the Annex. The yield stress and ultimate tensile strength were 525 and 580 MPa, respectively (see Table 6).

Because this was a new material, very little baseline crack growth rate data were available. Thus, long crack growth rate tests were conducted by Mazur and Rudd [42] on center-crack tension (CCT) specimens as a parallel effort for comparison with the short crack results. The CCT specimens were produced from the same sheet as the SENT specimens.

Mazur and Rudd [42], Carvalho and de Freitas [43], Blom [38] and Swain et al. [44] conducted short-crack tests on the SENT specimens under various constant amplitude loading conditions ($R = -2, -1, 0$ and 0.5). Short-crack tests were conducted under various aircraft spectra by Mazur and Rudd [42], Blom [38], Nowack et al. [37] and Cook [28].

2.2.4 Titanium Alloy Ti-6Al-4V

Annealed Ti-6Al-4V titanium alloy sheet, 1.5 mm thick, was supplied by Aeritalia GVC. Optical microscope observations revealed that the grain size in the rolling direction was about $8 \mu\text{m}$ and the typical dimension in the crack growth direction, $2a$, was $5 \mu\text{m}$.

Long-crack and short-crack tests were conducted by Lanciotti and Galatolo [45] under constant-amplitude loading conditions ($R = 0$ and -1). Specimens were machined from a single sheet by the University of Pisa.

2.2.5 Steel 4340

The steel specimens were manufactured from a single AISI 4340 steel plate, 9.5 mm in thickness, supplied in the annealed condition. The chemical composition of the steel is given in Table 5. All specimens were machined with the loading axis parallel to the rolling direction of the plate and were ground to a thickness of 5.1 mm. Specimens were heat treated to a hardness level of 45 on the Rockwell C scale. The yield stress and ultimate tensile strength were 1400 and 1500 MPa respectively. The tempered martensite microstructure had prior austenite grain sizes of about $10 \mu\text{m}$. Two types of inclusion particles, spherical calcium-aluminate particles and manganese-sulfide stringers elongated in the rolling direction of the plate were identified by X-ray analyses of broken specimens. These particles and stringers were shown to serve as crack initiation sites in the SENT specimens.

Swain et al. [44] conducted short- and long-crack tests over a wide range of constant-amplitude load conditions ($R = -1, 0$ and 0.5) and under the standard helicopter spectrum, Felix/28, a shortened version of Felix [30]. Additional long-crack data ($R = -1, 0.1$ and 0.5) were supplied by Wanhill and Schra (NLR).

2.3 Loading

A wide range of loading conditions was applied in the supplemental test programme. Fatigue tests were conducted under several constant-amplitude loading conditions and under six spectrum load sequences. The spectra were: FALSTAFF [20,21], Inverted FALSTAFF [28], a Gaussian spectrum [22], TWIST [29], Felix (or Felix/28) [30] and the Fokker 100 spectrum [31]. In all tests, the frequencies ranged from 5 to 20 Hz.

Each laboratory was required to align their test machines and gripping fixtures to produce a nearly uniform tensile stress field on an un-notched sheet specimen with strain gauges. Specimens (identical to the short-crack specimen without a notch) were supplied to each laboratory for alignment verification. The alignment procedures are presented in Annex C of reference 19.

Anti-buckling guides lined with teflon sheets, shown schematically in Figure 5, were used in all tests where compressive loads were applied. They were loosely bolted together on both sides of the specimen. Guide plates were not used when the minimum applied load was zero or positive. If a test was interrupted, the steady-state minimum load was not lower than the required minimum load in the test. The following sections briefly describe the various load histories.

2.3.1 Constant-amplitude loading

Four stress ratios, $R = -2, -1, 0$ and 0.5 , were used in the programme. The large negative stress ratios were selected because, as previously mentioned, the short-crack effect is more pronounced under compressive loading conditions. In

contrast, the short-crack effect is less evident at high positive stress ratios. At each R -ratio, several stress levels were selected by the participating laboratory. Table 4 gives a summary of the stress ratios tested by each laboratory.

2.3.2 Standard manoeuvre load sequence FALSTAFF

A large number of participants in the core programme carried out fatigue tests under the FALSTAFF (Fighter Aircraft Loading STANDARD For Fatigue) loading sequence, see Table 2. Those laboratories conducting FALSTAFF spectrum load tests in the core programme were independently checked by a programme coordinator to verify the accuracy of their spectrum loading. The results of the on-line spectrum loading accuracy verification are discussed in Annex D of reference 19. This exercise was quite beneficial and resulted in several modifications and improvements made at several laboratories on spectrum load testing. In the supplemental test programme, two laboratories [38,42] carried out tests on the aluminum-lithium (2090-T8E11) alloy using the FALSTAFF load sequence.

FALSTAFF [20,21] is based on a large number of actual flight load-time histories pertaining to five different fighter aircraft types operated by three different air forces. The load sequence represents the load-time history in the lower wing skin near the wing root of a fighter aircraft. The essential properties are summarized as follows. FALSTAFF represents a load sequence, defined by successive peaks and troughs, covering a "block" of 200 flights. The block size conforms to average European annual fighter utilization. Flights in FALSTAFF belong to three different groups of mission types, flights with repetitive patterns of severe manoeuvring (air-to-ground missions), flights with severe manoeuvring (air combat) and flights with only light to moderate manoeuvring (navigation missions). FALSTAFF contains taxi-load cycles and the majority of these are associated with a crossing of the zero-stress level. The complete FALSTAFF sequence consists of 35966 numbers, ranging in magnitude from 1 to 32. The "FALSTAFF load levels" ranging from 1 to 32 are arbitrary units. The "zero"-stress level corresponds to FALSTAFF level 7.5269. The smallest load variation ("omission level") considered is two FALSTAFF levels or about 8 percent of the highest stress contained in FALSTAFF. The highest stress ("truncation level") considered is the one exceeded once in one-hundred flights. References 20 and 21 give a complete FALSTAFF sequence in tabular form and give a FORTRAN listing of the program to generate the sequence.

2.3.3 Fighter manoeuvre load sequence Inverted FALSTAFF

Inverted FALSTAFF [28] is a simple inversion of the FALSTAFF sequence. Part of the air-ground-air cycle and the taxi loads are applied in tension while the gust and manoeuvre loads are applied in compression, such as might be experienced by an upper wing surface. This load sequence was applied to SENT specimens from the same lot of material (2024-T3) as the core programme specimens [28]. (Note that the use of 2024-T3 was for the purpose of comparing test results. This alloy would not, of course, be used in practice as an upper wing-skin material.)

2.3.4 Standard random load sequence GAUSSIAN

In the core programme, four laboratories carried out fatigue tests using a Gaussian type random load sequence. Only one laboratory in the supplemental programme conducted tests under the Gaussian load sequence. Nowack et al. [37] carried out tests on the aluminum-lithium alloy.

The Gaussian load sequence [22] is used for general application in fatigue testing. The sequence was originally defined in three forms, each one having a different irregularity factor (ratio of number of zero crossings to number of peaks). The version specified for the core and supplemental test programmes is that with the narrowest bandwidth. The narrow bandwidth sequence has an irregularity factor (I) of 0.99. Herein, this particular sequence is referred to as GAUSSIAN.

The characteristic properties of the GAUSSIAN random load sequence are as follows. The sequence has a frequency distribution of level crossings equal to that of a stationary Gaussian process. Sequence length is defined by about 10^6 mean level crossings (N_0) with positive slope. The number of peaks N_1 (equal to the number of troughs) depends upon the irregularity factor $I = N_0/N_1 = 0.99$. The total range of possible peaks and troughs is divided into 32 intervals. For $I = 0.99$, the spectrum shows very little variation in the mean value (nearly zero) and the spectrum is very close to an $R = -1$ variable-amplitude loading.

2.3.5 Standard transport gust load sequence TWIST

In the supplemental test programme, one laboratory carried out short- and long-crack tests under the TWIST load sequence on two materials. Blom [38] conducted these tests on both 2024-T3 and 2090-T8E11 alloys.

TWIST [29] is a European standard gust load sequence for flight simulation tests on transport aircraft wing structures. Load spectra pertaining to the wing root stresses were obtained from a number of transport aircraft types. The standardized flight load sequence was taken as the average of the different load spectra. TWIST represents a load sequence that covers a block of 4000 flights. The 4000 flights are composed of ten different flight types. Stress levels in each flight have been normalized by the one-g stress level S_{mf} (mean stress in flight) under cruise conditions. The severest flight has one occurrence of the highest peak level ($S_{max} = 2.6S_{mf}$). The lowest trough (or minimum stress) in the total sequence is $S_{min} = -0.6S_{mf}$. The cumulative number of load cycles per block of 4000 flights is 398.665 cycles. Reference 29 gives a complete TWIST sequence in flight types and gives a FORTRAN listing of a program to generate the sequence.

2.3.6 Standard helicopter load sequence Felix and Felix/28

Two laboratories, in the supplemental test programme, carried out short- and long-crack tests under the Felix or Felix/28 load sequences. Cook [28] conducted tests on both 2024-T3 and 2090-T8E41 alloys under Felix, while Swain et al. [44] used the shortened version (Felix/28) to test 4340 steel.

Felix [30] is a standard load sequence for helicopters with 'fixed' or semi-rigid rotors. The load sequence is composed of 140 sorties or flights. These sorties are constructed of 33 different load levels and the maximum load level was scaled to 100. The minimum trough was level -23. In Felix, the number of full load cycles was over 2 million cycles. In order to reduce the time required to complete fatigue tests, a shortened version, Felix/28, was developed. This version contains only about 160,000 cycles with the majority of alternating cycles at level 28 and below omitted.

2.3.7 Gust load sequence for Fokker 100

Wanhill and Schra [31] used the Fokker 100 gust load spectrum to evaluate short- and long-crack behaviour on the core programme material (2024-T3). Besides center-crack tension panels and SENT specimens, they also used an unusual specimen to obtain some long-crack data. This specimen, a bonded patch three hole crack tension (BPHTT) specimen, was selected for two reasons. First, in the BPHTT specimen, the stress-intensity factor naturally decreases with increasing crack length, thereby enabling spectrum fatigue tests to go down to low intensities without imposing load shedding. And second, unlike pin-loaded (compact) specimens, the BPHTT specimen is suitable for load histories containing compressive loads. However, the BPHTT specimen turned out to be very sensitive to crack initiation on the side of the hole opposite the primary crack (see [31]). Thus, the use of this specimen is not practical.

The Fokker 100 test load sequence consists of blocks of 5000 different flights. There are eight different flight types ranging from storm to calm conditions. There are eight gust load levels and three taxi load levels. The flight stresses have been expressed in non-dimensional form by dividing them by the stress pertaining to the undisturbed cruising flight or mean stress in flight (S_{mf}).

2.4 Short-Crack Test Conditions and Procedures

The test matrix for the supplemental programme is summarized in Table 4. For each material group, each participant was assigned or selected either constant-amplitude or spectrum-load conditions. All test conditions were to be carried out at stress levels selected by the participant on the basis of fatigue tests conducted on a preliminary series of specimens. For each test condition, there were two objectives: (1) obtain surface-crack-length-against-cycles data, and (2) obtain surface-crack-depth information. To achieve these objectives, two types of tests were required.

Some specimens were to be tested to obtain surface-crack-length-against-cycles data (using the plastic-replica method) until one continuous crack was all the way across the notch root. The specimen was then pulled to failure.

Some specimens were to be tested until the total surface-crack length along the bore of the notch was much less than the sheet thickness. The specimen was then monotonically pulled to failure. An examination of the fracture surface would reveal the surface crack (or cracks) so that information on the surface-crack shape could be obtained.

2.4.1 Short-crack measurement method

Several methods of measuring the growth of "short" cracks from lengths of 10 μm to 2 mm were considered in the core programme. These methods were electrical potential [23], ultrasonic surface waves [24], marker bands [25], and plastic replicas [26].

The electrical-potential method is widely used in monitoring the growth of "long" cracks. This method has been successfully used to monitor the growth of short cracks in steels and superalloys [23] but the sensitivity of this method for aluminum alloys had not been established at the time of the present programme. Several factors must be considered for accurate and reproducible electrical potential monitoring of short cracks. First, a calibration between measured voltage and crack size must be established. Also, the electrical probe must be accurately located with respect to the crack location. The cooperative programme objective of monitoring the growth of naturally-initiated cracks and the possibility of multiple crack initiation sites would make the application of this method very difficult, if not impossible.

The ultrasonic surface wave method [24] was shown to be effective in detecting a surface crack (or multiple surface cracks) at the root of a notch in an aluminum alloy material. This method was capable of detecting surface cracks down to about 300 μm . However, reference 24 also demonstrated that the plastic-replica method could detect a surface crack or multiple surface cracks, as small as about 10 μm .

The marker-band method, using either a high R -ratio or a small spike overload marker, could not be used to detect small surface cracks [25]. Reference 25 also showed that the plastic-replica method could be used to monitor the growth of "short" cracks.

Because the replica method was found to be accurate down to the short crack lengths required in the programme, this method was selected as the primary method. Each participant could select any other short method to monitor short cracks provided that they calibrate their method against the replica method. All participants, however, chose the replica method. This method is very simple to apply, but the method is very labor intensive. Many replicas have to be taken to determine crack length against cycles. The suggested plastic-replica procedures are presented in Annex E of reference 19.

Figure 6 shows the area over which cracks were to be monitored. The crack length or lengths (L_i) were measured along the bore of the notch. The crack lengths were determined from observations made on plastic replicas and were defined as the horizontal projection, as shown in Figure 7. This figure is a montage of photographs of replicas showing a crack and the initiation site. The values of L_i and their location were recorded on a "Data Chart" as a function of cycles. The Data Chart, shown in Figure 8, includes the specimen number, loading type, peak stress, and a grid upon which the information obtained from a replica was recorded. Each record of crack length, location, and cycles were taken at specified cycle intervals. Replicas were taken at a cycle interval chosen so that at least 25 to 30 replicas were taken during one test. A test was terminated when a crack had grown across the total specimen thickness, B . The estimated number of cycles to breakthrough ($L = B$) was obtained from fatigue tests conducted by each participant. Replicas were also taken while the specimen was under tensile load. (The loading procedures for taking replicas under constant-amplitude and spectrum loading are presented in the next section.) When a test was terminated the specimen was monotonically pulled to failure. Some test specimens, however, were monotonically pulled to failure early in life to determine the shape of the cracks. The data charts provided approximate locations for determining crack initiation sites, for calculating stress-intensity factors, and for applying the crack non-interaction criteria (see reference 19). The methods of calculating stress-intensity factors and crack-growth rates are presented in Section 2.5.

2.4.2 Constant-amplitude and spectrum loading

Replicas were taken while the specimen were under tensile load so that any cracks that were present would be open and allow the replica material to infiltrate the cracks. The loading procedures are as follows.

Constant-amplitude loading - The test was stopped at mean (or minimum) load. The applied load was then manually increased to 80 percent of the maximum test load. This load was held while a replica was taken of the bore of the notch. After the replica was removed from the notch, the load was reduced to mean (or minimum) load and the test was restarted.

Spectrum loading - To take replicas under spectrum-load conditions, the test machine was programmed (or manually set) to stop and hold at a specified peak level after the desired number of cycles had been completed. The replica was taken of the bore of the notch. The specified level for the various spectra was between 60 and 80 percent of the peak level in the spectra. After the replica was removed from the notch, the test machine was restarted and continued from the specified peak level.

2.4.3 Crack shape

The replica method provides information only on surface- or corner-crack length (L) along the notch root. The surface- or corner-crack depth, c , as shown in Figure 9, had to be determined by either an experimental or analytical calibration. (Note that the surface-crack length is defined as "2a" and the corner-crack length is defined as "a". Similarly, the thickness "t" is one-half sheet thickness for surface cracks and is full sheet thickness for corner cracks. These definitions are convenient for developing stress-intensity factor equations, see Section 2.5. B is always the full sheet thickness.) Results from the core programme [19] indicated that the crack shape for the 2024-T3 aluminum alloy could be approximated by

$$c/a = 0.9 - 0.25(a/t)^2 \quad (1)$$

for a/t ratios greater than about 0.05. No information was obtained in the core programme on the shape of cracks with an a/t ratio less than 0.04. Most participants used equation (1) to estimate crack depths in the supplemental test programme.

Wanhill and Schra [31] determined crack shapes down to extremely small a/t values (0.007), about 20 μm , on the 2024-T3 aluminum alloy SENT specimens using the Fokker 100 load spectrum. This particular spectrum marked the crack-front profile. Comparisons are made herein between their results and equation (1).

Calvalho and de Freitas [43] determined crack shapes on the 2090-T8E41 aluminum-lithium alloy specimens. They also found that the Al-Li alloy fatigue surfaces were marked quite well even under constant-amplitude loading. The Al-Li alloy, however, exhibited an unusual crack-surface orientation (normally 30 to 35 degrees to the loading axis). This orientation made it difficult to interpret the crack aspect ratio (a/c). They arrived at a crack-shape equation in the form of

$$c/a = 1.18 + 0.51(a/t) \quad (2)$$

Comparisons are made between stress-intensity factors and short-crack growth rates calculated using either equation (1) or (2) for the Al-Li alloy. Also, a different interpretation of the aspect ratio (a/c) for the Al-Li alloy is made herein.

Swain et al. [44] determined the crack shapes on the AISI 4340 steel SENT specimens. They developed an equation in the form of

$$c/a = 1 - 0.25(a/t) \quad (3)$$

for a limited range of data. Equation (3) shows the same trends in crack shapes as observed in the core programme for the aluminum alloy.

2.5 Short-Crack Data Analysis Procedures

In the following, approximate stress-intensity factor equations for a surface crack or a corner crack emanating from a semi-circular edge notch are discussed [19]. These equations were used by all participants in the supplemental test programme. These equations are used later to compare crack-growth rates measured for short cracks with those measured for long cracks as a function of the stress-intensity factor range. A modification to these equations as made by Swain et al. [44] to account

for the different stress concentration factor of the steel specimens (Fig. 3). The method of calculating the crack-growth rates for short cracks is also presented.

2.5.1 Calculation of stress-intensity factors

The calculation of stress-intensity factor assumes that either a semi-elliptical surface crack is located at the center of the edge notch, as shown in Figure 9(a), or a quarter-elliptical corner crack is located at an edge, as shown in Figure 9(b). (Note definition of a and t in Figure 9.) For a surface crack located at other locations along the bore of the notch, the calculation is adequate if the crack is small compared to thickness. However, if several cracks are close to one another then the calculation is in error. No provisions have been made to account for multiple crack interaction in the calculation of the stress-intensity factors. Crack-growth-rate data for cracks that may be interacting with each other have been eliminated from the data sets by using a "non-interaction" criterion (see Section 4.2 in reference 19 on Short-Crack Growth Rate Data and Non-Interaction Criteria). These criteria are also discussed in the present document, see Wanhill and Schra [31].

To calculate the stress-intensity factor at the point where the crack intersects the notch surface ($\phi = \pi/2$), the crack length, a , and the crack depth, c , must be known. For a surface crack, " $2a$ " (or L) is the projection of the crack on a horizontal plane, as shown in Figure 7. For a corner crack, " a " is equal to L . The crack depth, c , was calculated from equation (1) for either a surface crack or corner crack at the notch in all materials except the aluminum-lithium alloy and the steel. Equation (1) is in good agreement with experimental measurements and analytical calculations made on surface cracks growing from an edge notch in an aluminum alloy in references 19 and 25. Comparisons are made herein between the crack shapes predicted from equation (1) and those obtained from the results of tests on 2024-T3 aluminum alloy under the Fokker 100 load sequence and the 2090-T8E41 aluminum-lithium alloy under constant-amplitude loading. Equation (3) was used to calculate the crack depth, c , for the 4340 steel specimens.

The stress-intensity factor range equation for a surface crack located at the center of the edge notch, Figure 9(a), subjected to remote uniform stress [25], is

$$\Delta K = \Delta S \sqrt{\pi a/Q} F_{sn} \quad (4a)$$

for $0.2 \leq a/c \leq 2$ and $a/t < 1$. Equations for Q , the shape factor, and F_{sn} , the boundary-correction factor, are given in Annex F of reference 19.

For a corner crack, the stress-intensity factor is

$$\Delta K = \Delta S \sqrt{\pi a/Q} F_{cn} \quad (4b)$$

for $0.2 \leq a/c \leq 2$ and $a/t < 1$, where

$$\begin{aligned} F_{cn} &= F_{sn}(1.13 - 0.09 a/c) \quad \text{for } a/c \leq 1 \\ F_{cn} &= F_{sn}(1 + 0.01 c/a) \quad \text{for } a/c > 1 \end{aligned}$$

The stress range (ΔS) is full range ($S_{\max} - S_{\min}$) for constant-amplitude and spectrum loading. For example, $\Delta S = 2S_{\max}$ for $R = -1$ loading. For spectrum loading, the highest peak stress is S_{\max} and the lowest trough is S_{\min} .

2.5.2 Calculation of crack-growth rates

The calculation of crack-growth rates for constant-amplitude and spectrum loading is a simple point-to-point calculation:

$$da/dN = \Delta a/\Delta N = (a_2 - a_1)/(N_2 - N_1) \quad (5)$$

where a_i is the crack length at N_i cycles. The cycle interval, $N_2 - N_1$, is the interval between replicas. The cycle interval was chosen so that at least 25 to 30 replicas were taken during a test.

The corresponding stress-intensity factor range (ΔK) is calculated at an average crack length, a , (see Fig. 9) as

$$a = (a_1 + a_2)/2 \quad (6)$$

using equations (1) to (3), for crack shape, and equation (4) for the stress-intensity factor.

2.6 Long Crack-Growth Rate Tests

Fatigue crack-growth rate tests were conducted on long cracks (lengths greater than about 2 mm) under the various constant-amplitude stress ratios and various spectrum load sequences used in the supplemental test programme. The objective was to generate near-threshold fatigue crack-growth rate data for the various materials using a load-shedding procedure. This load-shedding procedure is consistent with the guidelines of the ASTM Standard Test Method for Measurement of Fatigue Crack Growth Rates (E647-87). Tests were conducted on center-crack tension specimens made from the same sheet of material that was used to make the SENT specimens. These data were used to define the regime where long-crack data are applicable to short cracks. The results from the long-crack tests are given in references 28, 31 and 37 to 45. Best-fit lines or test data on long cracks are compared herein with short-crack data for all materials and loading conditions used in the supplemental test programme.

3. SHORT-CRACK EXPERIMENTAL DATA

Some of the experimental data generated in the Supplemental Test Programme on short-crack growth behaviour in the various materials are summarized here. Data generated under various loading conditions are compared with long-crack data generated under the same load history. These data will establish the regions where short-crack behaviour is significantly different from long-crack behaviour. The crack-growth rate data are presented as a function of the stress-intensity factor range (ΔK). Note that short-crack data is presented as da/dN (crack-growth rates along the notch root) while long-crack data is dc/dN . Herein, the equivalence between da/dN and dc/dN as a function of ΔK is assumed. For some materials, however, the growth rates in these two directions may be significantly different.

As previously mentioned, several cracks may initiate along the notch root in each specimen and it was appreciated that as the cracks approached each other they could affect each other's crack-growth rates. Accordingly, a simple system for rejecting crack-growth rate data, where such interaction could occur, was devised (J. Foth, IABG, West Germany). This non-interaction criterion is described in Section 4.2 of reference 19, and it will not be repeated here. The non-interaction criterion was used by each participant to screen their data and only valid data were presented.

3.1 Aluminum Alloy 2024-T3

For completeness, some typical short-crack growth data generated in the AGARD Cooperative Test Programme on the core-programme material are presented here. Figures 10 to 12 show in detail the crack-growth rate data obtained by the various participants under each load history, respectively. Each figure refers to one stress level and one particular load history (constant-amplitude or spectrum loading). The individual participants are identified by a letter. The long-crack data (solid curve) are also shown for comparison. For all stress levels and load histories, the results from the various participants agreed well. The scatter in the data is attributed to experimental error and to cracks growing through different microstructure that is not accounted for in the analysis. For almost all of the load histories, crack-growth rates for short cracks were found to be significantly higher than those for long cracks at the same stress-intensity factor range.

Under constant-amplitude loading, the higher crack-growth rates for short cracks were most significant for tests conducted at negative stress ratios ($R = -2$ and -1). The results for $R = -2$ are shown in Figure 10. Short-crack results at the $R = 0$ test condition showed about the same rates as long cracks for the same ΔK for ΔK -ranges above the long-crack threshold (ΔK_{th}). The $R = 0.5$ short-crack tests, on the other hand, showed slower growth rates than long cracks for the same ΔK for ΔK -ranges above the long-crack threshold. For constant-amplitude loading, the most significant event was the growth of short cracks below the long-crack thresholds for all stress ratios considered. Growth of short cracks were recorded at ΔK values as low as $0.6 \text{ MPa}\cdot\text{m}^{1/2}$. These low values of ΔK for short cracks were from 15 to 30 percent of the respective long-crack thresholds.

The short-crack growth rates obtained under FALSTAFF loading (fig. 11) were found to be about a factor-of-4 times faster than those for long cracks for ΔK values around $10 \text{ MPa}\cdot\text{m}^{1/2}$. The crack-growth rate data for long cracks under the GAUSSIAN loading (Fig. 12) did not cover the same stress-intensity factor range as short cracks but an extrapolation of the long-crack data would be expected to show significant differences in rates for the same ΔK .

In the supplemental programme, Cook [28] conducted short-crack tests on the 2024-T3 material under the Inverted FALSTAFF load sequence. The Inverted FALSTAFF sequence is typical of the load sequence that the upper wing surface of a tactical aircraft experiences during flight, that is, the loading is primarily compression-compression with tensile ground loading, as shown in Figure 13. A comparison of short-crack growth rates measured under the two spectra is shown in Figure 14. The "x" symbols show the data generated by the Royal Aerospace Establishment in the core programme. The open symbols, Inverted FALSTAFF data, compare well with the FALSTAFF data for a given value of ΔK . These results suggest that the crack-driving forces on the short cracks are nearly identical for both spectra. Cook concluded that the explanation for this behaviour was due to crack closure differences between the two spectra. A discussion on the crack-opening stresses (or effective stress ranges) for the two spectra is presented in Section 4.2.2. The results may also be explained by considering the local stress-strain behaviour for the normal and inverted FALSTAFF spectra.

The solid curve in figure 14 shows the results of long-crack (load-shedding) tests conducted under the FALSTAFF spectrum [19]. These results show that short cracks under both normal and inverted FALSTAFF grow much faster than the long cracks for ΔK values below about $20 \text{ MPa}\cdot\text{m}^{1/2}$. The long-crack data is expected to reach a threshold at about $4 \text{ MPa}\cdot\text{m}^{1/2}$, based on constant-amplitude data for an R ratio of -0.27 (overall spectrum stress ratio based on the lowest and highest stress level in FALSTAFF), see Annex G in reference 19.

Blom [38] carried out tests on the core-programme material under the TWIST spectrum. Figure 15 shows the short-crack growth rates measured on tests conducted at two different stress levels. The short-crack data extended down to ΔK values of about $7 \text{ MPa}\cdot\text{m}^{1/2}$. These data indicate that a stress level effect may exist. The high stress level tests caused higher growth rates at a given ΔK value. Long-crack tests conducted under a TWIST load-shedding procedure are shown as the solid curve. These results show a long-crack threshold at about $23 \text{ MPa}\cdot\text{m}^{1/2}$. The apparently high threshold under the TWIST spectrum may be an artifact of the load-shedding procedure (caused by a too rapid reduction in load with crack extension). The long-crack threshold for TWIST would, again, be expected to be about $4 \text{ MPa}\cdot\text{m}^{1/2}$ based on the overall spectrum stress ratio ($R = -0.23$). However, the TWIST spectrum may produce a lot of fretting debris which may induce higher closure loads and, consequently, a higher threshold. A more detailed examination of this behaviour may be justified.

Wanhill and Schra [31] studied the short- and long-crack growth rate behaviour under the Fokker 100 load spectrum. Figure 16 shows K_{mf} , stress-intensity factor calculated using the mean stress in flight and the current crack length, against the crack-growth increment per flight, da/dF . The short- and long-crack data did not overlap but an extrapolation of the

long-crack data would be expected to show significant differences in rates for the same ΔK and short-crack growth below the long-crack threshold.

The long-crack results under the Fokker 100 spectrum in Figure 16 also show some large differences. Wanhill and Schra [31] used three different specimen types to obtain their data (center-crack, SENT and BPTHT specimens). They concluded that the primary difference between long cracks for center-crack and SENT specimens was due to different constraint being developed during the peak load application because of different specimen configurations. Also, there may be differing start-up effects during which crack-closure levels gradually rise and stabilize [19]. The reason for the large difference between the results from the BPTHT specimen and the other two specimens is not known.

The Fokker 100 load sequence was also found to mark the crack surfaces while the crack sizes were extremely small [31]. A comparison of crack shapes measured during spectrum loading and those determined from constant-amplitude tests in the core programme [19] are shown in Figure 17. (Note that Wanhill and Schra used the reverse definition for crack length and crack depth in their paper [31] but their data have been replotted in Figure 17 using the same nomenclature that was used in this report.) Figure 17 shows c/a plotted against a/t (a is measured along the notch root and c is crack depth). An a/t value of unity is the breakthrough conditions where a surface crack has become a through crack. The x-symbols show Wanhill's and Schra's results which show that a crack has initiated with a c/a ratio of about 0.4. The inclusion-particle clusters, that are elongated in the c -direction, would suggest that an initial c/a value should be much greater than unity. The data obtained from the core programme (open symbols) provided no information on c/a values below an a/t ratio of about 0.04. The dashed curve shows the predictions from a crack-growth analysis using equation (4(a)) where the initial (c/a), ratio was assumed to be 4. The solid curve is the crack-shape equation (eqn. (1)) used in the core and supplemental programmes. The large differences between the measured and expected crack shapes suggest that further studies need to be conducted to determine whether these differences are due to loading effects.

Nowack, Trautmann and Strunck [37] also conducted some additional short-crack tests on the core-programme material under the high- R ratio test condition.

3.2 Aluminum Alloy 7075-T6

Ankara and Kaynak [39] conducted short-crack tests on 7075-T6 aluminum alloy over a wide range in stress ratios ($R = -1, 0$ and 0.5). Figure 18 shows some typical data at a stress ratio of zero. Additional short-crack data have been provided by Swain [40]. Long-crack tests on this material were also performed by Phillips [41]. Above the long-crack threshold, the short-crack data agreed quite well with the long-crack data (solid curve). But the short cracks did grow below the long-crack threshold, as was observed in the core-programme material, 2024-T3.

Nowack, Trautmann and Strunck [37] also conducted some long-crack tests on a 7075-T6 aluminum alloy sheet material under the GAUSSIAN load sequence to compare with their test results on the aluminum-lithium alloy, 2090-T3E41.

3.3 Aluminum-Lithium Alloy 2090-T8E41

The primary material of interest in the supplemental test programme was the 2090-T8E41 aluminum-lithium alloy. The use of aluminum-lithium alloys in the aerospace industry would save substantial weight (8 to 12 percent). Six laboratories agreed to test this alloy under a wide variety of loading conditions (see Table 4). The long-crack data on center-crack tension specimens were determined by Mazur and Rudd [42]. These results were supplied to all participants so that they could compare long-crack data with their short-crack results.

Very early in the test programme, the unusual crack-surface orientation at the notch root, as shown in Figure 19, became evident. Cracks tended to grow at 30 to 35 degrees to the loading axis. The surface and corner cracks that initiated along the bore of the notch would be subjected to mixed-mode loading conditions (K_I , K_{II} and K_{III}) around the crack front. This crack orientation behaviour is a consequence of the propensity towards planar slip characteristic of some aluminum-lithium alloys [46], in combination with the detected preferred crystallographic orientation (see the Annex). A minimum yield stress and tensile strength has been frequently found at 50 to 60 degrees to the working direction in aluminum-lithium mill products and attributed to the presence of a $\{110\}\{112\}$ texture [47,48]. This texture is present in the supplemental programme aluminum-lithium sheet as the main component at mid-thickness of the sheet and one of the three components at 1/4 thickness [28].

As previously mentioned, a systematic slant (about 30 to 35 degrees from the loading axis) of the cracks was found in all short-crack tests on the aluminum-lithium alloy except, surprisingly, the TWIST spectrum [38]. Later, tests using Mini-TWIST [40] also showed that the cracks do not grow on a slant for this spectrum either. For all constant-amplitude loading conditions and all other spectra tested (FALSTAFF, GAUSSIAN and Felix) the cracks tended to grow on a slant. For a slant crack, the remote stress causes a resultant shear-stress and normal-stress component on the crack plane. Mixed mode conditions exist along the crack front. Simplified models for these conditions were attempted by Mazur and Rudd [42] and Carvalho and de Freitas [43]. The model presented in reference 43 will be briefly reviewed here. At the point where the surface or corner crack intersects the notch-root surface, the crack tip is subjected to Mode I and II conditions. The maximum depth location is subjected to Mode I and III conditions.

For an embedded elliptical crack of length $2a$ and depth $2c$ subjected to uniform uniaxial tensile stress σ and uniform shear stress τ , the stress-intensity factors are given in reference 49. When the ellipse becomes a circle ($a = c$), then the stress-intensity factors are given by

$$K_I = \sigma \sqrt{\pi a/Q} \quad (7)$$

$$K_{II} = \tau[2/(2-\nu)](\cos \theta)\sqrt{\pi a/Q} \quad (8)$$

$$K_{III} = \tau[(2-2\nu)/(2-\nu)](\sin \theta)\sqrt{\pi a/Q} \quad (9)$$

where $Q = \pi^2/4$ and θ is the angle measured on the crack plane between the shear-stress direction and the point of interest on the crack front.

On the basis of equations (7)-(9), approximate equations for mixed-mode stress-intensity factors were obtained for a slant surface crack at the edge of the notch. It was assumed that the boundary-correction factors F_{sn} (or F_{cn} for a corner crack) are the same for all three modes. The equations for the three modes, in terms of the remote applied stress S , are.

$$K_I = S(\sin^2 \beta)\sqrt{\pi a/Q} F_{sn} \quad (10)$$

$$K_{II} = S[2/(2-\nu)](\cos \theta)(\sin \beta \cos \beta)\sqrt{\pi a/Q} F_{sn} \quad (11)$$

$$K_{III} = S[(2-2\nu)/(2-\nu)](\sin \theta)(\sin \beta \cos \beta)\sqrt{\pi a/Q} F_{sn} \quad (12)$$

where β is the angle measured between the loading axis and the plane of the crack. From the mixed-mode equations, an equivalent stress-intensity factor, K_{eq} , was calculated from the strain-energy release rate G . For plane stress conditions,

$$G = [K_I^2 + K_{II}^2 + (1-\nu)K_{III}^2] / E \quad (13)$$

and

$$K_{eq} = \sqrt{EG} \quad (14)$$

The equivalent stress-intensity factor range, ΔK_{eq} , was calculated from equation (14) by replacing S with ΔS .

For the point where the crack front intersects the notch surface, θ is equal to $\pi/2$ and the equivalent stress-intensity factor range is

$$\Delta K_{eq} = \sqrt{\Delta K_I^2 + \Delta K_{II}^2} \quad (15)$$

Carvalho and de Freitas [43] carried out short-crack tests for a wide range of constant-amplitude conditions (see Table 1). Some typical results for $R = 0$ loading are shown in figure 20. A comparison between using the mixed-mode equation (eqn. (15)) and the horizontal projection of the crack (eqn. (4)), Mode I only, shows that data using equation (1a) agree better with the long-crack data (solid curve) [42] above the long-crack threshold. The data using the mixed-mode equation fall well to the left of the long-crack data. Whether the mixed-mode equation is more accurate than using the horizontal projection must await further study, but the simplicity and good correlation with equation (1a) does allow the use of current life-prediction methodologies.

As previously discussed, Carvalho and de Freitas [43] determined crack shapes on the aluminum-lithium alloy. They developed a crack-shape equation (eqn. (2)) from their experimental data. Figure 21 shows a comparison between short-crack data reduced using equation (2) or equation (1) (core-programme equation). The data reduced with the core-programme equation agreed better with the long-crack data [42] for stress-intensity factors above the long-crack threshold.

The unusual orientation of the crack surfaces made the interpretation of the crack aspect ratio (c/a) difficult. Figure 22 shows a schematic of the fracture surface on the aluminum-lithium alloy with a corner crack. The crack length, a , is measured as the horizontal projection and a' is the length measured on the crack surface. Because of the acute angle with the horizontal plane, there is a large difference between the ratio c/a and c/a' . Note that the a/t ratio is identical to the a'/t' ratio. If the c/a' ratio is plotted against the a'/t' ratio for the aluminum-lithium alloy, then better correlation with the core-programme is obtained, as shown in Figure 23. Again, the solid curve is equation (1) (core-programme results are open symbols) and the dashed curve is the prediction from a crack growth analysis using equation (1a). This may explain why equation (1) correlated short-crack data better than equation (2).

Several laboratories tested the aluminum-lithium alloy under the same loading conditions. A typical comparison between short-crack growth rates determined by Carvalho and de Freitas [43], Mazur and Rudd [12] and Swain et al. [14] are shown in Figure 24. Results from the three laboratories agreed quite well. Part of the scatter in the data sets is due to plotting results from all stress levels tested ($S_{max} = 80$ to 105 MPa). These results show that using the horizontal projection (Mode I only) stress-intensity factor ranges against crack-growth rates, a short-crack effect does exist. These results are quite similar to those for the 2024-T3 aluminum alloy in the core programme [19].

Figures 25-27 show short- and long-crack tests results on the aluminum-lithium alloy tested under the GAUSSIAN [37], TWIST [38] and Felix [28] load sequences, respectively. Again, these results clearly show that a short crack effect exists under all spectra tested. Short-crack growth rates were either faster than long-crack growth rates or the short cracks grew at stress-intensity factor levels below the long-crack threshold.

3.4 Titanium Alloy Ti-6Al-4V

Lancioti and Galatolo [45] conducted short-crack tests on Ti-6Al-4V titanium alloy for two stress ratios ($R = -1$ and 0). Figure 28 shows some typical data at a stress ratio of -1 . Part of the scatter in the data sets is due to plotting results from all stress levels. Long-crack tests on this material were also performed [45]. Again, above the long-crack threshold, the short-crack data agreed reasonably well with the long-crack data (solid curve). But the short cracks grew faster than long cracks at the same stress-intensity factor range and also grew below the long-crack threshold.

3.5 Steel 4340

Swain, Everett, Newman and Phillips [44] studied the crack initiation and short-crack growth characteristics of a high-strength steel (AISI 4340). Unlike the core-programme material, where multiple cracks initiated at the notch root, the single-edge-notched steel specimens (Fig. 3) usually initiated only a single crack at the notch root and the crack-surface profile was extremely flat. Some typical initiation sites are shown in Figure 29. Two particles were identified at the initiation sites: (1) a spherical calcium-aluminate inclusion particle, 10 to 40 μm in diameter (Fig. (29a)) and (2) an elongated manganese-sulfide particle, 2 to 5 μm wide along the notch root (Fig. (29b)).

They carried out short- and long-crack tests on the 4340 steel over a wide range in constant-amplitude loading conditions ($R = -1, 0$ and 0.5) and under the Felix/28 helicopter spectrum. Unlike the other materials, the short-crack data and long-crack data agreed quite well, even down to and including the long-crack threshold, for the positive R -ratio and Felix/28 tests. The only difference observed between short and long cracks on the steel was under the negative stress ratio condition. Figure 30 shows the short-crack data at $R = -1$ (symbols). Long-crack tests were also performed on the same material [44] and the scatterband on these data is shown by the solid lines. Above the long-crack threshold, the short-crack data agreed reasonably well with the long-crack data. But, again, the short cracks did grow below the long-crack threshold. The results reinforce the previous conclusion from the core programme that short-crack effects are more pronounced under compressive loading.

4. MODELS OF SHORT-CRACK GROWTH BEHAVIOUR

Many investigators have shown that LEFM concepts are inadequate to explain short-crack growth behaviour [1-18]. Using nonlinear fracture mechanics, some investigators have tried to explain the growth of short cracks in plates and at notches. In particular, the J -integral concept and an empirical length parameter [3,4] have been used to correlate short-crack and long-crack growth rate data. The physical interpretation of the length parameter, however, is unclear. Several other researchers [12,17] have also introduced "length" parameters into crack-growth models. These length parameters have been associated with microstructural features (or barriers to crack growth) such as grain size. Short cracks have been observed to slow down or stop at grain-boundary locations. Many other investigators [5-11,33] have suggested that crack closure [50] (or lack of crack closure in the early stages of crack initiation) may be a major factor in causing some of the differences between the growth of short and long cracks. Reference 51 has shown, on the basis of crack closure, that a large part of the short-crack effect in an aluminum alloy was caused by a short crack emanating from a defect "void" of incoherent inclusion particles and a breakdown of LEFM concepts.

In the supplemental test programme, several participants used the crack-closure model, FASTRAN [52], to calculate crack-opening stresses, short-crack growth rates and fatigue lives. In the following sections, the model will be briefly reviewed. Some examples of how crack-opening stresses vary as a function of load history for short cracks are shown. Comparisons of experimental and predicted short-crack growth rates on two of the materials used in the test programme are presented. Similar comparisons are made between experimental and predicted fatigue lives.

4.1 Analytical Crack-Closure Model

The crack-closure model developed in reference 32, and applied to short cracks in references 33 and 51, was used by several participants in the supplemental programme to analyze crack growth and closure under constant- and variable-amplitude loading. The following includes a description of the closure model and of the assumptions made in the application of the model to the growth of short and long cracks.

The closure model [32] was developed for a central crack in a finite-width specimen subjected to uniform applied stress. This model was later extended to through cracks emanating from a circular hole in a finite-width specimen also subjected to uniform applied stress [33]. The model is based on the Dugdale model [53], but modified to leave plastically deformed material in the wake of the crack. The primary advantage in using this model is that the plastic-zone size and crack-surface displacements are obtained by superposition of two elastic problems: a crack in a plate subjected to a remote uniform stress and a uniform stress applied over a segment of the crack surface.

Figure 31 shows a schematic of the model at maximum and minimum applied stress. The model is composed of three regions: (1) a linear-elastic region containing a circular hole with a fictitious crack of half-length $c' + \rho$, (2) a plastic region of length ρ , and (3) a residual plastic deformation region along the crack surface. The physical crack is of length $c' - r$, where r is the radius of the hole. (The model was also assumed herein to apply for a crack emanating from a semi-circular notch.) The compressive plastic zone is ω . Region 1 is treated as an elastic continuum. Regions 2 and 3 are composed of rigid-perfectly plastic (constant-stress) bar elements with a flow stress, σ_0 . The flow stress (σ_0) is the average between the yield stress and the ultimate strength. The shaded regions in Figures 31(a) and 31(b) indicate material that is in a plastic state. At any applied stress level, the bar elements are either intact (in the plastic zone) or broken (residual plastic deformation). The broken elements carry compressive loads only, and then only if they are in contact. The elements yield in compression when the contact stress reaches $-\sigma_0$. To account for the effects of state of stress on plastic-zone size, a constraint factor α was used to elevate the tensile flow stress for the intact elements in the plastic zone. The effective flow stress $\alpha\sigma_0$ under simulated plane-stress conditions is σ_0 and under simulated plane-strain conditions is $3\sigma_0$. For thin sheet material, fully plane-strain conditions may not be possible. Irwin [54] suggested accounting for through-the-thickness variation in stress state by introducing a constraint factor ($\alpha = 1.73$) to represent nominal plane-strain conditions. For the core-programme material (2024-T3), a constraint factor of 1.73 was found to correlate crack-growth rate data for various stress ratios ($-2 \leq R \leq 0.7$) in the near threshold region [19] and to give crack-opening stresses in reasonable agreement with experimental measurements [55] made on the core-programme material.

The closure model is used to calculate crack-opening stress as a function of crack length and load history. The applied stress level at which the crack surfaces are fully open is denoted as S_o , the crack-opening stress. The crack-opening stress calculated for a through crack was also assumed to apply at each location along a surface- or corner-crack front. The crack-opening stress is then used to calculate the effective stress-intensity factor range, ΔK_{eff} [50]. In turn, the crack growth rate is calculated using a ΔK_{eff} -against-crack-growth-rate relationship determined from long-crack data. Generally, long-crack thresholds are ignored because reliable methods to measure or calculate crack-opening stresses during load shedding are not available.

4.2 Crack-Opening Stresses

The influence of the initial defect "void" size on the crack-closure behaviour of short cracks under constant-amplitude and spectrum loading is presented here. For all loading conditions, Irwin's plane-strain constraint factor of 1.73 was assumed to apply for the growth of "short" cracks in the 2024-T3 aluminum alloy. A constraint factor of 2.5 was assumed to apply for "short" crack growth in the 4340 steel specimens. These results are used later to predict short-crack growth rates and fatigue lives.

4.2.1 Constant-amplitude loading

The closure model was used to study the influence of defect void size on the closure behaviour of short cracks growing from a notch [19], as shown in Figure 9(a). Some typical results of calculated crack-opening stresses normalized by the maximum applied stress as a function of half-crack length, a , are shown in Figure 32. The crack-growth simulation was performed under the four stress ratios used in the core and supplemental test programmes with an initial defect (void or crack) size a_i of 3 μm , c_i of 12 μm , and a defect-void height, $h \geq 0.4 \mu\text{m}$. The particular values of S_{max}/σ_o used in the simulation are as shown. Experimental and numerical results from the core programme suggest that part of the short-crack effect may be due to an initial defect void height that is sufficient to prevent closure over the initial defect surfaces. In the core programme, cracks were found to initiate at inclusion-particle clusters or voids left by the removal of these particles from the machining or polishing process. For defect-void heights, h , greater than about 0.4 μm , the initial defect surfaces do not close, even under the $R = -2$ compressive loading. The newly created crack surfaces, however, do close as the crack grows and the crack-opening stresses are shown by the solid curves. The crack-opening stresses start initially at the minimum applied stress, but rapidly rise and tend to level off as the crack grows. The high R -ratio ($R = 0.5$) results show that the crack is always fully open, that is, $S_o = S_{min}$. Results at $R = 0$ stabilized very quickly after about 20 μm of crack growth. Negative R -ratio results showed the largest transient behaviour on crack-opening stresses. Results at $R = -2$ had not stabilized after about 100 μm of crack growth. The results at the negative stress ratios are also strongly influenced by the maximum applied stress level [33,51].

4.2.2 FALSTAFF and Inverted FALSTAFF load sequence

The closure model, FASTRAN, was also used by Cook [28] to calculate the crack-opening stresses under the two variable-amplitude load spectra. The initial defect-void size (a_i, c_i, h) was the same as that used for the constant-amplitude loading, previously discussed. Figures 33 and 34 show crack-opening stresses plotted against crack length, a , for the FALSTAFF and Inverted FALSTAFF load sequences, respectively. Only a small part of the opening values calculated from the model is shown in the figures. The dashed lines indicate the peak stress (S_{max}) and the lowest stress (S_{min}) in the stress spectra. As pointed out by Cook [28], the effective stress range for "short" cracks was nearly the same for both spectra (crack lengths less than about 0.025 mm). And crack-growth rates for short cracks should be about the same under either spectrum. However, the crack-opening stresses in the Inverted FALSTAFF load sequence rise more rapidly than in the FALSTAFF sequence. In both sequences, the opening stresses tend to level off after about 0.25 mm of crack growth. For long-crack lengths, the effective stress range for FALSTAFF is about 40 percent larger than the Inverted FALSTAFF sequence, and consequently, the crack-growth rates should be about 2 times faster under FALSTAFF.

4.3 Short-Crack Growth Rates

In this section, comparisons of experimental and predicted short-crack growth rates are made only on two materials: 2024-T3 aluminum alloy and 4340 steel. Similar procedures would be required for the other materials. The 2090-T8E41 aluminum-lithium material, however, may require some major modifications in the analysis because of the mixed-mode nature observed in short-crack growth. To apply the closure model, an effective stress-intensity factor against crack-growth rate relation must be obtained. The crack-growth rates measured on long cracks were correlated against ΔK_{eff} using the closure model for a wide range of constant-amplitude stress ratios. Center-crack tension specimens were used to obtain crack-growth rate data on long cracks ($c > 2 \text{ mm}$), in the 2024-T3 aluminum alloy [19] and in the 4340 steel [44]. The effective stress-intensity factor [50] is given by

$$\Delta K_{eff} = [(S_{max} - S_o)/(S_{max} - S_{min})]\Delta K \quad (16)$$

where S_o was calculated from equations given in reference 56.

4.3.1 Aluminum alloy 2024-T3

To establish the ΔK_{eff} -rate relation for the aluminum alloy, a constraint factor (α) of 1.1 was used for rates greater than 7.5E-07 m/cycle (end of transition from flat-to-slant crack growth) and $\alpha = 1.73$ (equivalent to Irwin's plane-strain condition) was used for rates lower than 9.0E-08 m/cycle (beginning of transition from flat-to-slant crack growth). A constraint factor of

1.73 was also found to give calculated crack-opening stress levels in quantitative agreement with experimental measurements of crack-opening stresses made near the beginning of the load-reduction threshold test [54]. For intermediate rates, α was varied linearly with the logarithm of crack-growth rate.

Instead of using an equation to relate crack-growth rate to ΔK_{eff} , a table-lookup procedure was chosen. The primary advantage in using a table is that the baseline data can be described more accurately than with a multiple parameter equation, especially in the transitional region (flat-to-slant crack growth). The effective stress-intensity factor range against crack-growth rate relation is listed in the following table:

ΔK_{eff} , MPa-m ^{1/2}	dc/dN , m/cycle
1.43	3.56E-10
2.42	3.05E-09
3.30	6.10E-09
4.40	1.52E-08
5.50	4.06E-08
11.0	4.32E-07
27.5	1.78E-05
49.5	2.54E-04

In the low-growth rate regime near and at threshold, some tests [57] have indicated that the threshold develops because of a rise in crack opening stress. This rise has not been accounted for in the analysis of the threshold test data. Therefore, an extrapolation of the long-crack data into the region below the long-crack threshold was used because the data did not extend to low ΔK_{eff} values where short cracks were expected to grow. The crack-growth model required a baseline ΔK_{eff} -rate relation in the low ΔK_{eff} region in order to predict the growth of short cracks. For ΔK_{eff} values below or above the extreme values listed in the table, a power law using the first-two or last-two points, respectively, was used to obtain rates. The upper limit for the power-law relation is, of course, defined by fracture toughness. A lower limit or short-crack threshold, $(\Delta K_{\text{eff}})_{\text{th}}$, was established in Annex B of reference 19 and is 1.05 MPa-m^{1/2}. (See reference 19 for more details on the development of the ΔK_{eff} -rate relation.)

In the following, comparisons are made between the measured and predicted crack-growth rates against stress-intensity factor range (ΔK) for short cracks under constant-amplitude and spectrum loading. The experimental data analyzed with the non-interaction criteria [19] were used. Results for the long-crack data on the same material and loading are also shown for comparison. To compare the short- and long-crack growth rate data, the rate da/dN is assumed to be equivalent to dc/dN for the same ΔK value. The short cracks are growing in the a -direction while the long cracks are growing in the c -direction. This assumption also applies in predicting short-crack growth behaviour from long-crack results.

Constant-amplitude loading. Figure 35 shows a comparison for the $R = -2$ loading from the core programme [19]. Experimental data for each stress level are denoted by a particular symbol. The solid curves show predictions from the closure model for various maximum applied stress levels. The dashed line shows long-crack data generated under the same conditions. These results show a strong influence of stress level (S_{max}) on the growth rates for short cracks. The short cracks grow faster at higher stress levels for the same value of ΔK . To make predictions, the initial crack size was selected as 3 by 12 by 0.4 μm and an effective stress-intensity factor threshold, $(\Delta K_{\text{eff}})_{\text{th}}$, was chosen as 1.05 MPa-m^{1/2}. This initial defect size was selected because "short" cracks tended to initiate at inclusion-particle clusters or voids on or near the notch-root surface. These material defects were of about the same size as assumed in the analysis. The reasons for selecting this particular defect size and effective threshold value are discussed in Annex B of reference 19. The predictions from the model show a similar stress-level effect on the growth of short cracks. Although the initial crack-growth rates from the model were in qualitative agreement with the measured rates, the model predicted slower rates in the mid-range than those measured. The predicted rates approached the long-crack rates more rapidly than in the test. As previously mentioned, Irwin's plane-strain condition ($\alpha = 1.73$) was assumed for the growth of short cracks. The actual behaviour, however, may be closer to plane stress for short cracks.

At 50 MPa, the predictions show that the crack nearly arrested. The minimum rate occurred at a ΔK_{eff} of 1.08 MPa-m^{1/2}. Another prediction was made at an applied stress level of 49 MPa. The prediction demonstrates that a short crack can initiate and grow from a defect, but as the crack-opening stresses rise (decreasing the value of ΔK_{eff}), the crack can be arrested. Here the crack was arrested at a ΔK value of about 3 MPa-m^{1/2}.

TWIST load sequence - Blom [38] used FASTRAN to predict short-crack growth rates for 2024-T3 specimens subjected to the TWIST load sequence, see Figure 36. Here the "average" crack-growth rate is plotted against the "maximum range" stress-intensity factor (see Section 2.5.1 and 2.5.2). The predicted crack length against cycles curve was treated similar to the experimental data. Crack length ($2a$) and cycles were taken from the analysis at equal cycle intervals between the initial crack length (6 μm) and breakthrough ($2a = t$). The predicted results for the TWIST spectrum showed a very small stress-level effect. The analyses, however, tended to predict rates along the upper scatter band of the measured rates for ΔK values below the long-crack threshold. The predicted rates approached the long-crack data (dashed curve) at a ΔK value of about 25 MPa-m^{1/2}. These results suggest that the closure model, with the current assumptions, would underpredict fatigue lives on notched 2024-T3 aluminum alloy specimens subjected to the TWIST spectrum.

4.3.2 Steel 4340

To establish the ΔK_{eff} -rate relation for the 4340 steel, a constraint factor (α) of 2.5, reflecting plane-strain conditions, was used over the entire range of crack-growth rates from the center-crack tension specimens [44]. Again, a wide range in stress ratios ($R = 0.5, 0$ and -1) was used to obtain long-crack data. The closure model correlated the long-crack-growth rate data quite well over a wide range in rates. The effective stress-intensity factor range against crack-growth rate relation is listed in the following table:

ΔK_{eff} , MPa-m ^{1/2}	dc/dN , 1a/cycle
3.75	3.0E-10
5.30	2.0E-09
7.30	7.0E-09
15.0	4.5E-08
50.0	5.5E-07
120.0	3.0E-05

A long-crack ΔK_{eff} threshold value of 3.75 MPa-m^{1/2} was selected to fall within the range of "effective" thresholds for crack-growth rate data from the three stress ratios.

Figure 37 shows the predictions of short-crack growth rates from Swam et al. [44] using FASTRAN for 4340 steel specimens subjected to the Felix/28 load sequence. Again, the "average" crack-growth rate is plotted against the "maximum range" stress-intensity factor. The predicted crack length against cycles curve was treated in a similar way to the experimental data. Crack length ($2a$) and cycles were taken from the analysis at equal cycle intervals between the initial crack length ($a_0 = 8 \mu\text{m}$) and breakthrough ($2a = t$). The predicted rates from the Felix/28 spectrum fell along the upper scatter band of the measured rates for short cracks. These predicted rates were also slightly higher than the experimental rates for long cracks (dashed curve).

4.4 Fatigue Life

Figure 38 shows a comparison between the experimental and predicted fatigue lives for SENT specimens made of 4340 steel subjected to the Felix/28 spectrum. The test data, from reference 44, are shown as symbols (symbols with an arrow indicate that the test was terminated). The large amount of scatter in fatigue lives was attributed to different size defects at the crack initiation site (larger defects caused shorter lives). The calculated fatigue lives (solid curve) were made using FASTRAN with a ΔK_{eff} -rate relationship that was obtained from long-crack data (see Section 4.3.2) and an initial mean defect size. The initial defect "void" size was $a_0 = 8 \mu\text{m}$ and $c_0 = 13 \mu\text{m}$. This flaw size was determined from a statistical analysis of a large number of crack initiation sites. The void height (h) was assumed to be about $4 \mu\text{m}$. The ΔK_{eff} threshold for short cracks was assumed to be 3.75 MPa-m^{1/2} (same value as for long cracks). The predicted lives for the Felix/28 spectrum were somewhat shorter than the test lives. This behavior is consistent with the fact that the model tended to predict slightly higher crack-growth rates for short cracks (see Fig. 37).

5.0 SIGNIFICANCE OF THE SHORT-CRACK EFFECT

Because the use of fracture mechanics (ΔK -based) methodologies to characterize the growth of fatigue cracks in metals is well established in the design of aerospace structures, the significance of the short-crack effects is expressed here in the same terminology. The experimental data generated in the AGARD Cooperative and Supplemental Test Programmes and the analytical crack-closure model have identified several significant features of short-crack growth behaviour in various aerospace materials under a wide range of load histories. These features are briefly discussed in the following sections.

At stress concentrations typical of aircraft structures, short cracks initiate very early in the fatigue life, if the applied stress levels are above the fatigue limit. As non-destructive inspection (NDI) techniques improve, which is inevitable, smaller crack sizes will be detected in aircraft structures. In particular, Wainhill [58] points out that as the design philosophy changes from a fail-safe approach to a damage-tolerance or durability evaluation, a better understanding of the behaviour of short cracks is required, especially in aircraft engines. The growth of these short cracks is strongly influenced by load history and stress level. The growth differences between short and long cracks, at the same stress-intensity factor range, were more pronounced for load histories which included compressive loading. Short-crack growth behaviour in tests with only positive loading was nearly the same as the behaviour of long cracks for growth above the long-crack threshold. Short cracks tended to grow well below the long-crack threshold even for positive loading in aluminum, aluminum-lithium, and titanium alloys. For the 4340 steel, however, short-crack and long-crack behaviour were nearly identical, except for load histories which included compressive loading. But why do short cracks grow faster than long cracks? The answer to this question lies in several reasons. (1) the loss of similitude [16] which occurs when stress levels are too high and small-scale yielding conditions are exceeded, (2) local microstructural features are favorable for rapid crack growth or severe retardation [6,12], and (3) the lack of crack closure in the early stages of crack growth [5-11,33]. Perhaps, the most significant feature of short-crack growth behavior, observed in the test programmes, was the growth of short cracks well below the long-crack thresholds. This observation should have the largest impact on design-life calculations. Long-crack data that include a threshold clearly cannot be used in analyses that treat the early stages of crack growth in aluminum, aluminum-lithium and titanium alloys because it leads to prediction of infinite life for crack sizes as much as an order-of-magnitude larger than the crack sizes actually monitored in the test programmes. Thus, the use of long-crack thresholds in damage-tolerance and durability analyses is likely to be non-conservative. This topic should be thoroughly investigated.

In the future, the short-crack effect may have a large impact on design-life calculations if procedures are adopted that treat the fatigue process as entirely crack growth [59]. Basing all life calculations on crack-growth analyses seems reasonable in view of test results in this study and others [60,61] in which crack growth was actually monitored over more than 90 percent of the total fatigue life. A crack-growth-based approach to design life may be a viable alternative to traditional "crack initiation" safe-life analyses currently used for such structures as landing gear, helicopter rotor systems, and turbine engines. One advantage of a crack-growth-based procedure is that the measure of damage "crack size" is a physically measurable quantity that can be used to gain a better understanding and evaluation of life-prediction analyses. Another advantage would be the use of a single analysis procedure for all life calculations, rather than one procedure for initiation and another for crack growth. Disadvantages of the crack-growth-based procedure are that generation of short-crack data is more difficult than classical fatigue testing and more complex stress analyses would be required. However, with continually improving computerized stress analyses and encouraging results from models to predict short-crack effects, a continued exploration of crack-growth-based life design is warranted.

6. CONCLUSIONS

An AGARD Supplemental Test Programme on the growth of "short" fatigue cracks was conducted to allow participants to test various materials and loading conditions that were of interest to their laboratory. Twenty-two participants from ten laboratories in eight countries contributed to the programme. The materials tested in the supplemental programme were: 2024-T3 and 7075-T6 aluminum alloys, 2090-T8E41 aluminum-lithium alloy, Ti-6Al-4V titanium alloy and 4340 steel. Six laboratories conducted tests on the aluminum-lithium alloy. Tests on single-edge-notch tension specimens were conducted under several constant-amplitude loading conditions (stress ratios of -2, -1, 0, and 0.5) and spectrum loading conditions (FALSTAFF, Inverted FALSTAFF, GAUSSIAN, TWIST, Felix and the Fokker 100 spectra). The plastic-replica method was used to measure the growth of short cracks at the notch root.

Three laboratories used the crack-growth model (FASTRAN), which incorporates crack-closure effects, to analyze the growth of short cracks from small (inclusion) defects along the notch surface in 2024-T3 aluminum alloy and 4340 steel. Analyses were conducted under constant-amplitude loading and spectrum loading (FALSTAFF, Inverted FALSTAFF, GAUSSIAN, TWIST and Felix).

Short-crack tests and analyses conducted on single-edge-notched tension fatigue specimens made of various aircraft materials support the following conclusions:

Supplemental Test Programme

- 1 Short-crack growth rate data from several participants agreed well for constant-amplitude tests conducted on the 2090-T8E41 aluminum-lithium alloy. All participants showed about the same amount of scatter in growth rate data.
- 2 The short-crack specimen and plastic-replica monitoring technique, developed in the AGARD Cooperative Test Programme, allowed the various participants to obtain short-crack data on other materials and under different load histories.
- 3 Several participants successfully used the crack-growth analysis program, FASTRAN, to predict short-crack growth rate behaviour in aluminum alloy and steel specimens.

Experimental Results

- 1 Materials: 2024-T3 and 7075-T6 aluminum alloy, 2090-T8E41 aluminum-lithium, and Ti-6Al-4V titanium alloy exhibited a strong short-crack effect under both constant-amplitude and spectrum loading. Short cracks grew at stress-intensity factors well below the long-crack thresholds. In many cases, short cracks grew faster than long cracks at the same stress-intensity factor range.
- 2 The 4340 steel did not exhibit a significant short-crack effect. Short-crack and long-crack growth rates agreed well for most test conditions. A slight short-crack effect was observed under constant-amplitude loading with a stress ratio of -1.
- 3 The 2090-T8E41 aluminum-lithium alloy material exhibited an extremely oblique crack surface profile in the short-crack specimens. This unusual behaviour is attributed to the highly textured microstructure.
- 4 Short-crack growth rate data for the 2090-T8E41 aluminum alloy correlated well with long-crack data using the horizontal projections of crack lengths and Mode I stress-intensity factor analysis.
- 5 For all materials, further study is needed on the particular crack shapes that develop at the crack-initiation sites under both constant- and variable-amplitude loading.
- 6 Short-crack tests on the Inverted FALSTAFF spectrum, primarily a compression-compression load sequence, exhibited similar growth rates as FALSTAFF, primarily a tension-tension load sequence.

Analytical Results

The analytical crack-closure model, FASTRAN, was applied only to the 2024-T3 aluminum alloy and the 4340 steel specimens.

1. For most constant-amplitude loading ($R = -2, -1$ and 0), the "analytical crack-closure" model predicted growth rates and stress-level effects like those observed in tests. For $R = 0.5$, the model generally predicted higher rates than those observed in tests.
2. For FALSTAFF and Inverted FALSTAFF loading, the "analytical crack-closure" model predicted effective stress ranges consistent with experimentally measured growth rates on the 2024-T3 aluminum alloy short-crack specimens.
3. For the Felix/28 spectrum, the "analytical crack-closure" model predicted slightly higher growth rates and slightly lower fatigue lives than tests on 4340 steel short-crack specimens.

7. NOMENCLATURE

a	one-half surface-crack (or total corner-crack) length, m
a_i	initial one-half surface-defect (or crack) length, m
B	full sheet thickness, m
c	surface-crack depth or through-crack length, m
c_i	initial surface-defect (or crack) depth, m
c'	crack length plus hole radius, m
E	modulus of elasticity, MPa
F	boundary-correction stress-intensity factor
G	strain-energy release rate, N/m
h	one-half surface-defect (or crack) height, m
I	irregularity factor for Gaussian sequence
K, K_I	Mode I stress-intensity factor, $\text{MPa}\cdot\text{m}^{1/2}$
K_{II}, K_{III}	Mode II and III stress-intensity factor, $\text{MPa}\cdot\text{m}^{1/2}$
K_{mf}	mean stress-intensity factor in flight, $\text{MPa}\cdot\text{m}^{1/2}$
K_T	stress concentration factor
L	total length of surface or corner crack along bore of notch, m
N	cycles
Q	shape factor for surface or corner crack
R	stress ratio (S_{\min}/S_{\max})
r	semi-circular notch radius, m
S	applied gross stress, MPa
S_{\max}	maximum applied gross stress, MPa
S_{mf}	mean stress in flight, MPa
S_{\min}	minimum applied gross stress, MPa
S_o	crack-opening stress, MPa
t	one-half (full) specimen thickness for surface crack (corner crack), m
w	specimen width, m
x, y	Cartesian coordinates
α	constraint factor
β	angle between load axis and crack plane
ΔK	stress-intensity factor range, $\text{MPa}\cdot\text{m}^{1/2}$
ΔK_{eff}	effective stress-intensity factor, $\text{MPa}\cdot\text{m}^{1/2}$
$(\Delta K_{\text{eff}})_{th}$	effective threshold stress-intensity factor range, $\text{MPa}\cdot\text{m}^{1/2}$
ΔK_{th}	long-crack threshold stress-intensity factor range, $\text{MPa}\cdot\text{m}^{1/2}$
ν	Poisson's ratio
ρ	length of tensile plastic zone, m
σ_o	flow stress (average between σ_{ys} and σ_u), MPa
σ_u	ultimate tensile strength, MPa
σ_{ys}	yield stress (0.2 percent offset), MPa
σ_{yy}	normal stress acting in y -direction, MPa
ϕ	parametric angle of ellipse
ω	length of cyclic plastic zone, m

8. REFERENCES

1. Pearson, S. Initiation of Fatigue Cracks in Commercial Aluminum Alloys and the Subsequent Propagation of Very Short Cracks. *Engineering Fracture Mechanics*, Vol. 7, No. 2, 1975, pp. 235-247.
2. Kitagawa, H., and Takahashi, S.: Applicability of Fracture Mechanics to Very Small Cracks or the Cracks in the Early Stage, *Proceedings of the 2nd International Conference on Mechanical Behavior of Materials*, Boston, MA, 1976, pp. 627-631.
3. El Haddad, M. H.. A Study of the Growth of Short Fatigue Cracks Based on Fracture Mechanics, Ph.D. Thesis, University of Waterloo, Waterloo, Ontario, Canada, 1978.
4. El Haddad, M. H., Dowling, N. E., Topper, T. H.; and Smith, K. N.. J-Integral Application for Short Fatigue Cracks at Notches, *International Journal of Fracture*, Vol. 16, No. 1, 1980, pp. 15-30.
5. Broek, D.. The Propagation of Fatigue Cracks Emanating from Holes. National Aerospace Laboratory, NLR Technical Report 72134U, 1972.
6. Morris, W. L., James, M. R., and Buck, O. Growth Rate Models for Short Surface Cracks in Al 2219-T851, *Metallurgical Transactions A*, Vol. 12A, January 1981, pp. 57-64.
7. Hudak, S. J., Jr.. Small Crack Behavior and the Prediction of Fatigue Life. *Journal of Engineering Materials and Technology*, Vol. 103, 1981, pp. 26-35.
8. Nisitani, H., and Takao, K. I.. Significance of Initiation, Propagation, and Closure of Microcracks in High Cycle Fatigue of Ductile Materials, *Engineering Fracture Mechanics*, Vol. 15, No. 3-4, 1981, pp. 445-456.
9. Schijve, J.. Difference Between the Growth of Small and Large Fatigue Cracks--The Relation to Threshold K -Values, *Fatigue Thresholds*, Vol. II, 1982, pp. 881-908. (Also. Delft University of Technology Report LR-327, 1981)
10. Taylor, D.; and Knott, J. F.: Fatigue Crack Propagation Behavior of Short Cracks--The Effects of Microstructure, *Fatigue of Engineering Materials and Structures*, Vol. 4, No. 2, 1981, pp. 147-155.
11. Leis, B. N.; and Forte, T. P.. Fatigue Growth of Initially Physically Short Cracks in Notched Aluminum and Steel Plates *Fracture Mechanics Thirteenth Conference*, Richard Roberts, ed., American Society for Testing and Materials, ASTM STP 743, 1981, pp. 100-124.
12. Lankford, J.. The Growth of Small Fatigue Cracks in 7075-T6 Aluminum, *Fatigue of Engineering Materials and Structures*, Vol. 5, No. 3, 1982, pp. 233-248.
13. Wood, H. A.; and Rudd, J. L.. Evaluation of Small Cracks in Airframe Structures, AGARD Report No. 696, 1983, pp. 1.1-1.12.
14. Anstee, R. F. W., and Edwards, P. R.. A Review of Crack Growth Threshold and Crack Propagation Rates at Short Crack Lengths, AGARD Report No. 696, 1983, pp. 2.1-2.12.
15. *Behaviour of Short Cracks in Airframe Components*, AGARD Conference Proceedings, AGARD-CP-328, H. Zocher, ed., 1983.
16. Leis, B. N., Kanninen, M. F., Hopper, A. T.; Ahmad, J.; and Broek, D.: A Critical Review of the Short Crack Problem in Fatigue, AFWAL-TR-83-4019, 1983.
17. Miller, K. J., and de los Rios, E. R. (eds). *The Behaviour of Short Fatigue Cracks*, European Group on Fracture, Publication No. 1, 1986.
18. Ritchie, R. O.; and Lankford, J.: *Small Fatigue Cracks*, The Metallurgical Society, 1986.
19. Newman, J. C., Jr., and Edwards, P. R. (coordinators), Zocher, H. (chairman). *Short-Crack Growth Behaviour in an Aluminum Alloy—An AGARD Cooperative Test Programme*, AGARD R-732, 1988.
20. Description of a Fighter Aircraft Loading Standard for Fatigue Evaluation, FALSTAFF, F+W (Switzerland), LBF (Germany), NLR (Netherlands), and IABG (Germany), March 1976.
21. van Dijk, G. M.; and de Jonge, J. B.. Introduction to a Fighter Aircraft Loading Standard for Fatigue Evaluation FALSTAFF, NLR MP 75017U, May 1975.
22. Huck, M.; Schutz, W., Fischer, R.; and Kobler, H. G.. A Standard Random Load Sequence of Gaussian Type Recommended for General Application in Fatigue Testing LBF Report No. 2909 IABG Report No. TF-570, April 1976.
23. Gangloff, R. P.. Electrical Potential Monitoring of Crack Formation and Subcritical Growth from Small Defects, *Fatigue of Engineering Materials and Structures*, Vol. 4, No. 1, 1981, pp. 15-33.

24. Walker, A. C.: Continuous Fatigue Crack Inspection of Aluminum Alloy Plate Specimens Undergoing Spectrum Loading Using Ultrasonic Surface Waves, National Research Council Canada, National Aeronautical Establishment, LTR-ST-1465, July 1983.
25. Swain, M. H.; and Newman, J. C., Jr.: On the Use of Marker Loads and Replicas for Measuring Growth Rates for Small Cracks, Fatigue Crack Topography, AGARD Conference Proceedings No. 376, 1984, pp. 12.1-12.17.
26. Brown, C. W.; and Smith, G. C.: A Two Stage Plastic Replication Technique for Monitoring Fatigue Crack Initiation and Early Fatigue Crack Growth, Advances in Crack Length Measurement, C. J. Beevers, ed., Engineering Materials Advisory Services LTD, 1982, pp. 41-51.
27. Lee, J. J.; and Sharpe, W. N., Jr.: Short Fatigue Cracks in Notched Aluminum Specimens, Small Fatigue Cracks, R. O. Ritchie and J. Lankford, eds., The Metallurgical Society, 1986.
28. Cook, R.: The Growth of Short Fatigue Cracks in 2024 and 2090 Aluminum Alloys under Variable Amplitude Loading, Short-Crack Growth Behaviour in Various Aircraft Materials, AGARD R-767 (this report).
29. de Jonge, J. B.; Schutz, D.; Lowak, H.; and Schijve, J.: A Standardized Load Sequence for Flight Simulation Tests on Transport Aircraft Wing Structures, National Lucht- en Ruimtevaartlaboratorium, NLR TR 73029U, 1973.
30. Edwards, P. R.; and Darts, J.: Standardised Fatigue Loading Sequences for Helicopter Rotors (Helix and Felix). Part 2: Final Definition of Helix and Felix, Royal Aircraft Establishment TR-84085, August 1984.
31. Wanhill, R. J. H.; and Schra, L.: Short and Long Fatigue Crack Growth in 2024-T3 under Fokker 100 Spectrum Loading, Short-Crack Growth Behaviour in Various Aircraft Materials, AGARD R-767 (this report).
32. Newman, J. C. Jr.: A Crack-Closure Model for Predicting Fatigue Crack Growth Under Aircraft Spectrum Loading, Methods and Models for Predicting Fatigue Crack Growth Under Random Loading, J. B. Chang and C. M. Hudson, eds., American Society for Testing and Materials, ASTM-STP 748, 1981, pp. 53-84.
33. Newman, J. C., Jr.: A Nonlinear Fracture Mechanics Approach to the Growth of Small Cracks, Behaviour of Short Cracks in Airframe Components, AGARD Conference Proceedings No. 328, 1982, pp. 6.1-6.26.
34. Tan, P. W.: The Boundary Force Method for Stress Analysis of Arbitrarily Shaped Plates with Notches and Cracks. Ph.D. Thesis, George Washington University, 1986.
35. Hudson, C. Michael: Effect of Stress Ratio on Fatigue-Crack Growth in 7075-T6 and 2024-T3 Aluminum Alloy Specimens. NASA TND-5390, 1969.
36. Wanhill, R. J. H.: Low Stress Intensity Fatigue Crack Growth in 2024-T3 and T351, Engineering Fracture Mechanics, Vol. 30, pp. 233-260, 1988.
37. Nowack, H.; Trautmann, K. H.; and Strunck, J.: Crack Behaviour of 2024-T3, 2090-T8E41 and 7075-T6 Under Constant Amplitude and Different Types of Variable Amplitude Loading, Especially Gaussian Loading, Short-Crack Growth Behaviour in Various Aircraft Materials, AGARD R-767 (this report).
38. Blom, A. F.: Short Crack Growth Under Realistic Flight Loading. Model Predictions and Experimental Results for AL 2024 and AL-LI 2090, Short-Crack Growth Behaviour in Various Aircraft Materials, AGARD R-767 (this report).
39. Ankara, O. A.; and Kaynak, C.: Growth of Short Fatigue Cracks in 7075-T6 Aluminum Alloy, Short-Crack Growth Behaviour in Various Aircraft Materials, AGARD R-767 (this report).
40. Swain, M. H.: Private communication with Lockheed Engineering & Sciences. Co., Hampton, Virginia, 1989.
41. Phillips, E. P.: Private communication with NASA Langley Research Center, Hampton, Virginia, 1989.
42. Mazur, C. J.; and Rudd, J. L.: Determination of the Short Crack Effect in 2090-T8E41 Aluminum Lithium, Short-Crack Growth Behaviour in Various Aircraft Materials, AGARD R-767 (this report).
43. Carvalho, M. H.; and de Freitas, M.: Short Crack Behaviour in Al-Li Alloy 2090, Short-Crack Growth Behaviour in Various Aircraft Materials, AGARD R-767 (this report).
44. Swain, M. H.; Everett, R. A.; Newman, J. C., Jr.; and Phillips, E. P.: The Growth of Short Cracks in 4340 Steel and Aluminum-Lithium 2090, Short-Crack Growth Behaviour in Various Aircraft Materials, AGARD R-767 (this report).
45. Lanciotti, A.; and Galatolo, R.: Short Crack Observations in Ti-6Al-4V under Constant Amplitude Loading, Short-Crack Growth Behaviour in Various Aircraft Materials, AGARD R-767 (this report).
46. Lavernia, E. J.; and Grant, N. J.: Review of Aluminum-Lithium Alloys, Journal of Materials Science, Vol. 22, 1987, pp. 1521-1529.
47. Smith, A. F.: Aluminum-Lithium Alloys for Helicopter Structures, Metals and Materials, August 1987, pp. 438-444.

48. Gregson, P. J., and Flower, H. M.: Microstructural Control of Toughness in Aluminum-Lithium Alloys, *Acta Metallurgica*, Vol. 33, 1985, pp. 527-537.
49. Rooke, D. P.; and Cartwright, D. J.: *Compendium of Stress Intensity Factors*, Her Majesty's Stationary Office, London, 1976.
50. Elber, W.: The Significance of Fatigue Crack Closure, American Society for Testing and Materials, ASTM STP 486, 1971, pp. 230-242.
51. Newman, J. C., Jr.; Swain, M. H.; and Phillips, E. P.: An Assessment of the Small-Crack Effect for 2024-T3 Aluminum Alloy, Small Fatigue Cracks, R. O. Ritchie and J. Lankford, eds., The Metallurgical Society, 1986.
52. FASTRAN—Fatigue Crack Growth Analysis of Structures—A Closure Model, Computer Software Management and Information Center, University of Georgia, Athens, Georgia, December 1984.
53. Dugdale, D. S.: Yielding of Steel Sheets Containing Slits, *Journal of Mechanics and Physics of Solids*, Vol. 8, No. 2, 1960, pp. 100-104.
54. Irwin, G. R.: Plastic Zone Near a Crack and Fracture Toughness, *Proceedings of the 7th Sagamore Conference*, 1960, p. IV-63.
55. Phillips, E. P.: The Influence of Crack Closure on Fatigue Crack Growth Thresholds in 2024-T3 Aluminum Alloy, Mechanics of Fatigue Crack Closure, J. C. Newman, Jr. and W. Elber, eds., American Society for Testing and Materials, ASTM STP 982, 1988.
56. Newman, J. C., Jr.: A Crack-Opening Stress Equation for Fatigue Crack Growth, *International Journal of Fracture*, Vol. 24, 1984, R131-R135.
57. Minikawa, K.; and McEvily, A. J.: On Near-Threshold Fatigue Crack Growth in Steels and Aluminum Alloys, Fatigue Thresholds, Vol. I, 1982, pp. 373-390.
58. Wanhill, R. J. H. Short Cracks in Aerospace Structures, The Behaviour of Short Fatigue Cracks, Mechanical Engineering Publications Ltd., London, 1986, pp. 27-36.
59. Phillips, E. P.; and Newman, J. C., Jr.: Impact of the Small-Crack Effect on Design-Life Calculations, *Experimental Mechanics*, Vol. 29, No. 2, 1989, pp. 221-225.
60. Potter, J. M.; and Yee, B. G. W.: Use of Small Crack Data to Bring About and Quantify Improvements to Aircraft Structural Integrity, *Proceedings of ACARD Specialists Meeting on Behaviour of Short Cracks in Airframe Components*, AGARD-CP-328, 1983.
61. Wang, D. Y.: A Study of Small Crack Growth Under Transport Spectrum Loading, *Proceedings of AGARD Specialists Meeting on Behaviour of Short Cracks in Airframe Components*, AGARD-CP-328, 1983.

TABLE 1
Participants in Short-Crack Cooperative Test (Core) Programme

Country	Laboratory	Participants
France	Centre d'Essais Aeronautique de Toulouse - CEAT	A. Labege
Germany (a)	Deutsche Forschungsanstalt für Luft- und Raumfahrt--DLR	H. Nowack
	Industrieanlagen Betriebsgesellschaft - IABG	J. Foth P. Heuler
Italy	University of Pisa	G. Cavallini R. Galatolo
Netherlands	Nationaal Lucht-en Ruimtevaartlaboratorium - NLR	R. J. H. Wenhull L. Schra
Portugal	Laboratorio Nacional de Engenharia e Tecnologia Industrial--LNETI	M. H. Carvalho
	Centro de Mecanica e Materiais da Universidade Tecnica de Lisboa -CEMUL	M. de Freitas
Sweden	Aeronautical Research Institute--FFA	A. F. Blom
Turkey	Middle East Technical University --METU	O. A. Ankara C. Kaymak
United Kingdom	Royal Aerospace Establishment - RAE	P. R. Edwards D. S. Lock R. Cook
		W. N. Sharpe J. J. Lee J. Cieslowski
United States of America (b,c,d)	The Johns Hopkins University JHU	M. H. Swain E. P. Phillips J. C. Newman, Jr
	National Aeronautics and Space Administration - NASA Langley Research Center	C. Mazur J. Rudd
	Air Force Wright Aeronautical Laboratory-- AFWAL--FIBEC	

- (a) P. Heuler, IABG, conducted long-crack tests on core-programme material under GAUSSIAN loading.
 (b) F. Adams and J. M. Potter, U.S. Air Force Wright Aeronautical Laboratory, machined core-programme specimens.
 (c) E. P. Phillips, NASA Langley Research Center, conducted long-crack tests on core-programme material under constant-amplitude and FALSTAFF loading.
 (d) W. N. Sharpe, The Johns Hopkins University, conducted crack-closure measurements on short cracks [27].

TABLE 2
Laboratory Test Matrix in Short-Crack Cooperative Test (Core) Program^a

Participant	Constant Amplitude Loading ^(a)									Spectrum Loading									
	R = -2			-1			0			0.5			FALSTAFF			GAUSSIAN			
	H	M	L	H	M	L	H	M	L	H	M	L	H	M	L	H	M	L	
France CEAT	X	X	X	X	X	X	X	X	X	X ^(b)				X	X				
Germany -DLR				X									X	X	X	X	X	X	
Germany -IABG				X	X	X	X	X	X				X	X	X	X	X	X	
Italy -Pisa				X	X	X	X	X	X	X	X	X	X	X					
Netherlands -NLR				X	X	X										X	X	X	
Portugal- LNETI/CEMUL	X	X	X	X	X	X	X	X	X	X	X	X							
Sweden -FFA	X	X	X	X	X	X	X	X	X				X	X	X				
Turkey METU	X	X	X	X	X	X	X	X	X	X	X	X							
United Kingdom -RAE	X	X	X	X	X	X	X	X	X	X	X	X	X	X	X	X	X	X	
USA-JHU	X	X	X	X	X	X	X	X	X	X	X	X							
USA-NASA	X	X	X	X	X	X	X	X	X	X	X	X	X	X	X				
USA-AFWAL	X	X	X	X	X	X	X	X	X	X	X	X	X	X	X				

(a) H, M and L represent high, medium and low stress levels, respectively

(b) Tests conducted at $R = 0.1$ for H, M and L stress levels.

TABLE 3
Participants in Supplemental Short-Crack Growth Programme

Country	Laboratory	Participants
Germany	Deutsche Forschungsanstalt für Luft- und Raumfahrt—DLR	H. Nowack K. H. Trautmann J. Strunck
Italy	University of Pisa	A. Lanciotti R. Galatolo
Netherlands	Nationaal Lucht-en Ruimtevaartlaboratorium - NLR	R. J. H. Wanhill L. Schra
Portugal	Laboratorio Nacional de Engenharia e Tecnologia Industrial—LNETI Centro de Mecânica e Materiais da Universidade Técnica de Lisboa—CEMUL	M. H. Carvalho M. de Freitas
Sweden	Aeronautical Research Institute—FFA	A. F. Blom
Turkey	Middle East Technical University—METU	O. A. Ankara C. Kaynak
United Kingdom (a)	Royal Aerospace Establishment—RAE	R. Cook D. S. Lock P. R. Edwards
United States of America	National Aeronautics and Space Administration - NASA Langley Research Center	M. H. Swain R. A. Everett J. C. Newman Jr E. P. Phillips
	Air Force Wright Aeronautical Laboratory—AFWAL—FIBEC	C. Mazur J. Rudd

(a) A. W. Bowen, Royal Aerospace Establishment, provided a texture analysis of the 2090-T8E41 aluminum-lithium alloy (see Annex).

TABLE 4
Laboratory Test Matrix in Supplemental Short-Crack Growth Program

Material	Laboratory	Constant Amplitude				Spectrum Loading					
		$R = -2$	-1	0	0.5	FALSTAFF	FALSTAFF (Inverted)	GAUSSIAN	TWIST	Felix	Fokker 100
2090-T8E41 (a)	USA-AFWAL	X	X	X		X					
	Portugal- LNETI/CEMUL	X	X	X							
	Sweden- FFA				X	X			X		
	USA-NASA		X								
	Germany- DLR England- RAE							X			X
2024-T3 (b)	Germany- DLR				X						
	England- RAE						X			X	
	Sweden- FFA								X		
	Netherlands- NLR										X
7075-T6 (c)	Turkey- METU		X	X	X						
	USA-NASA				X						
Ti-6Al-4V (d)	Italy- Pisa		X	X							
4340 Steel (e,f)	USA-NASA		X	X	X						X
											(g)

- (a) U.S. Air Force Wright Aeronautical Laboratory provided the 2090-T8E41 aluminum-lithium alloy material and specimens.
 (b) Core-programme material [19] provided by NASA Langley Research Center and specimens machined by U.S. Air Force Wright Aeronautical Laboratory.
 (c) NASA Langley Research Center provided the 7075-T6 aluminum alloy material and specimens
 (d) University of Pisa provided the Ti-6Al-4V titanium alloy material and specimens
 (e) NASA Langley Research Center provided the 4340 steel material and specimens
 (f) R. Wanhill, Nationaal Lucht-en Ruimtevaartlaboratorium, conducted long-crack tests on 4340 steel ($R = -1, 0.1$ and 0.5).
 (g) Felix/28, a shortened version of Felix [30], was used on the steel specimens.

TABLE 5
Nominal Chemical Composition of Materials in Supplemental Test Programme

Element	2024-T3 (a)	7075-T6	2090-T8E41	Ti-6Al-4V	4340 Steel
Silicon	.16	.07	.10	-	.27
Iron	.33	.22	.12	.3	Balance
Copper	4.61	1.53	3.00	-	.11
Manganese	.57	.16	.05	-	.69
Magnesium	1.51	2.56	.25	-	-
Chromium	.02	.24	.05	-	.79
Zinc	.06	5.68	.10	-	-
Aluminum	Balance	Balance	Balance	6	.007
Titanium	-	.07	.15	Balance	-
Lithium	-	-	2.60	-	-
Zirconium	-	-	.10	-	-
Carbon	-	-	-	.1	.39
Vanadium	-	-	-	4	.39
Nickel	-	-	-	-	1.75
Molybdenum	-	-	-	-	.25

(a) Core-programme material [19].

TABLE 6
A Mechanical Properties of Materials in Supplemental Test Programme

Material	Thickness B, mm	Ultimate tensile strength, MPa	Yield stress (0.2-percent offset), MPa	Modulus of elasticity, MPa	Elongation (51-mm gage length), percent
2024-T3 (a)	2.3	495	355	72,000	21
7075-T6	2.3	575	520	70,000	12
2090-T8E41	2.15	580	525	78,200	5
Ti-6Al-4V	1.5	970	920	115,000	8.5
4340 Steel	5.1	1500	1410	190,000	7.5

(a) Core-programme material [19].

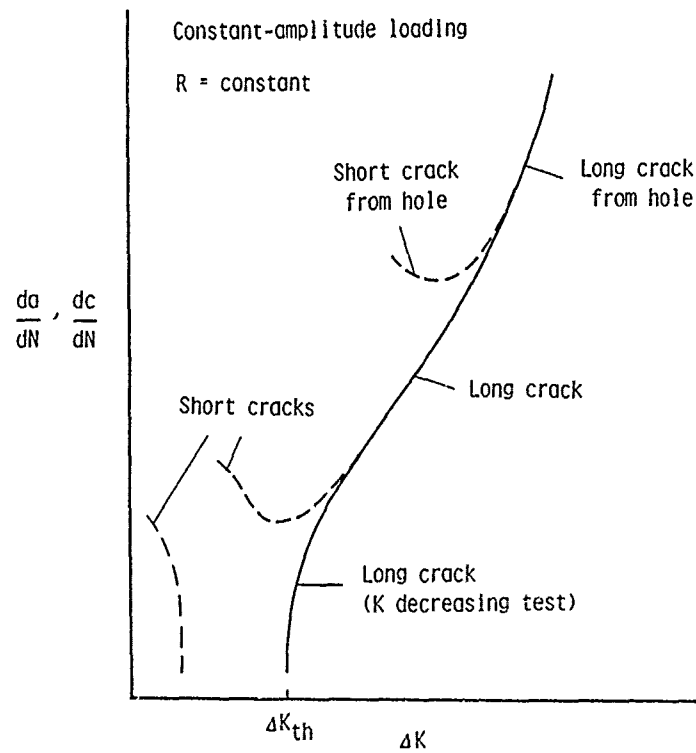


Figure 1.- Schematic fatigue-crack growth rate data for short and long cracks.

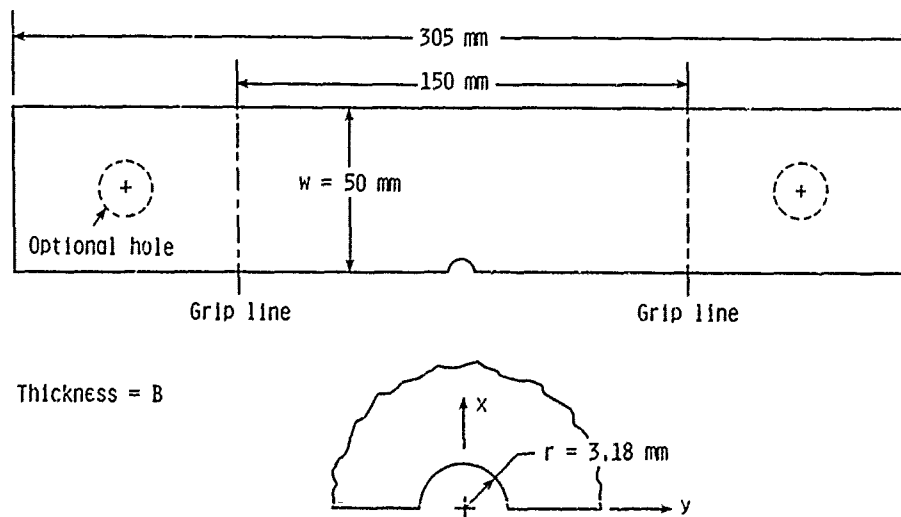


Figure 2.- Single-edge-notch-tension (SENT) fatigue specimen.

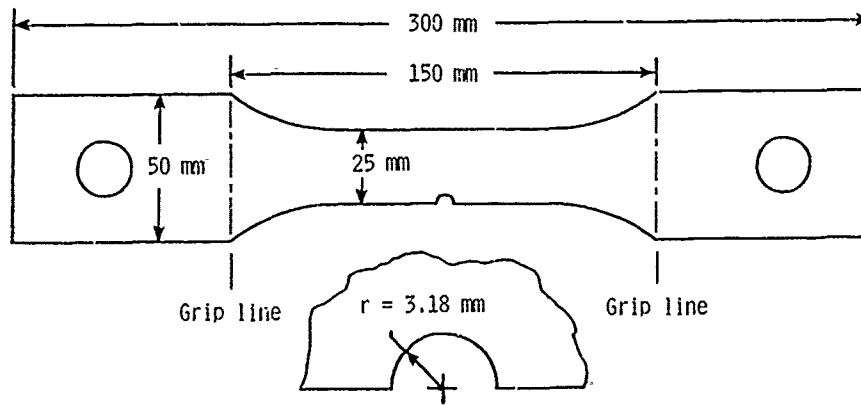


Figure 3.- Single-edge-notch-tension (SENT) fatigue specimen for 4340 steel.

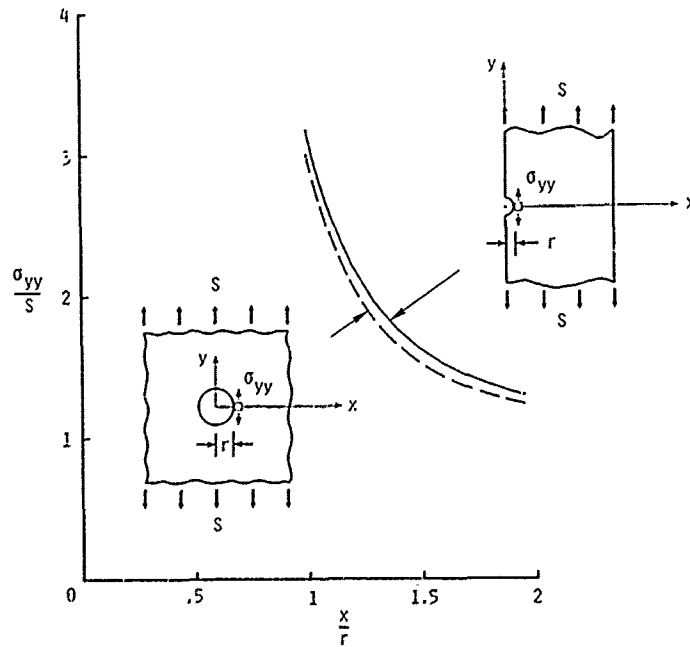


Figure 4.- Normal stress distribution for SENT specimen, and for open circular hole in an infinite plate.

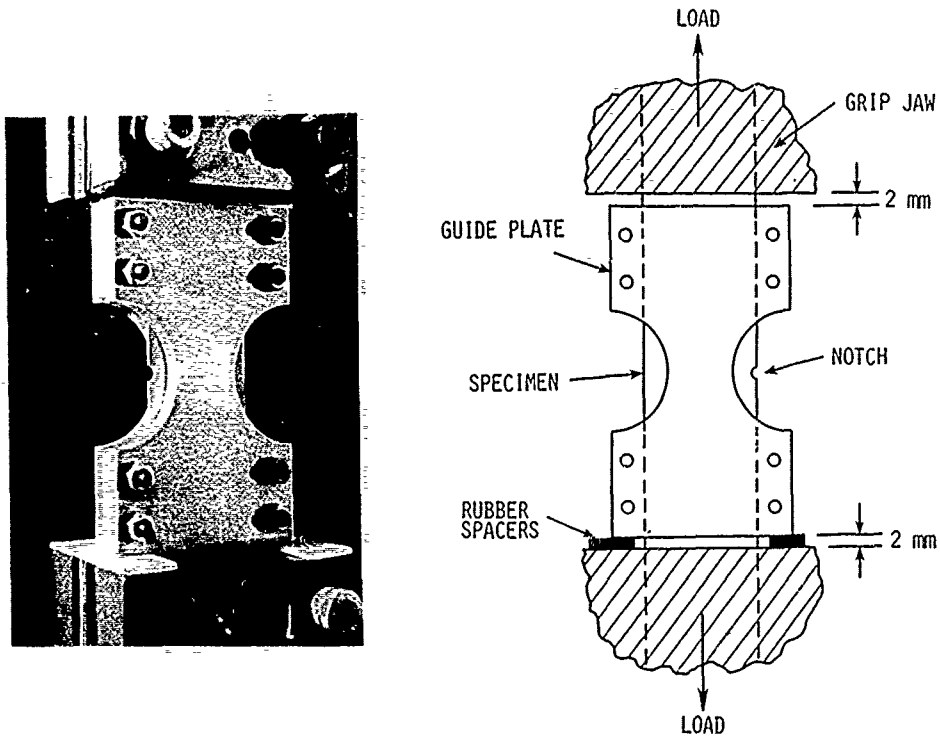


Figure 5.- A typical test stand showing guide plates for compressive load tests.

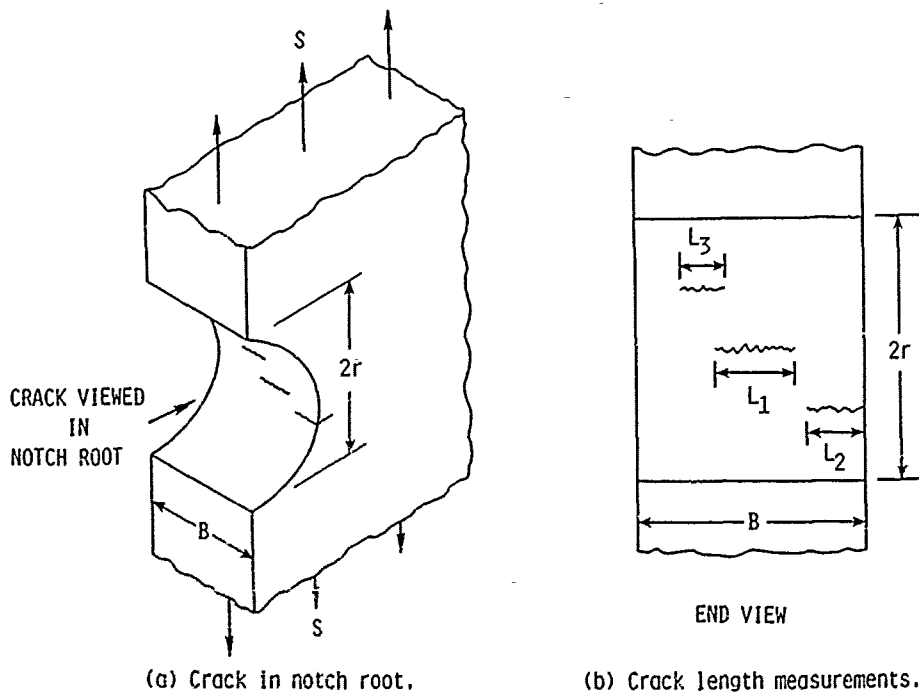


Figure 6.- Notch configuration and crack-length measurement in notch root.

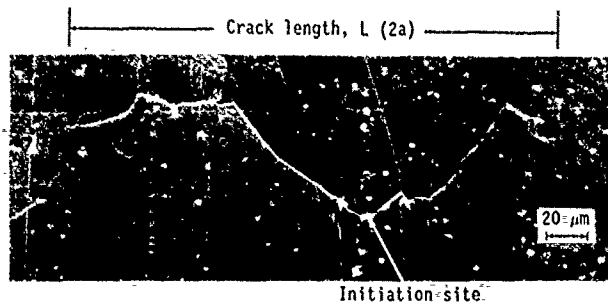


Figure 7.- Montage of photographs for surface replicas showing crack-length measurement.

AGARD Short Crack DATA CHART

Record of crack lengths and map

Page 2 of 2 Loading Type R = -1
 Specimen no A-15-05 Peak Stress 90.0 MPa

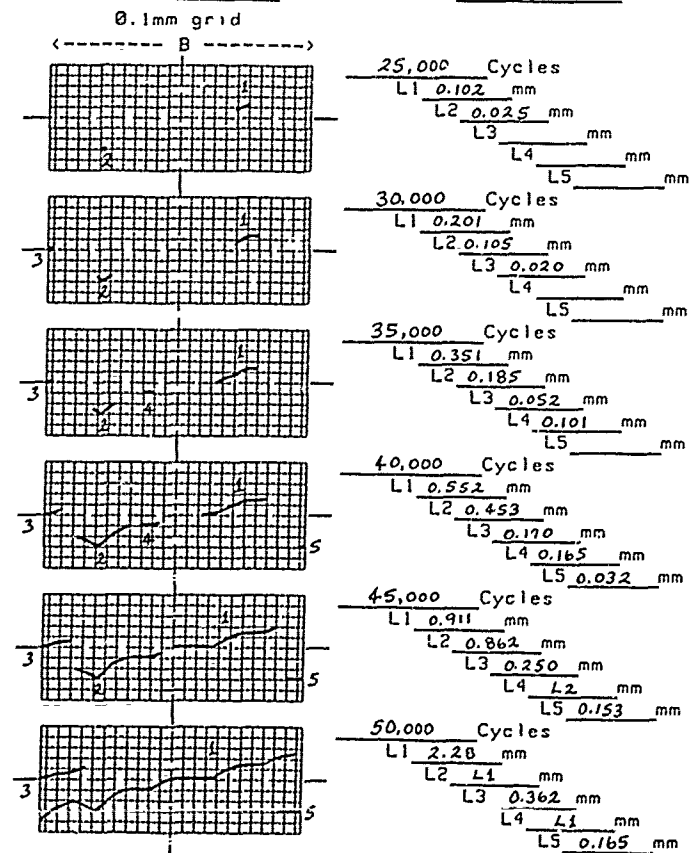


Figure 8.- Example of Data Chart for multiple cracks at notch root.

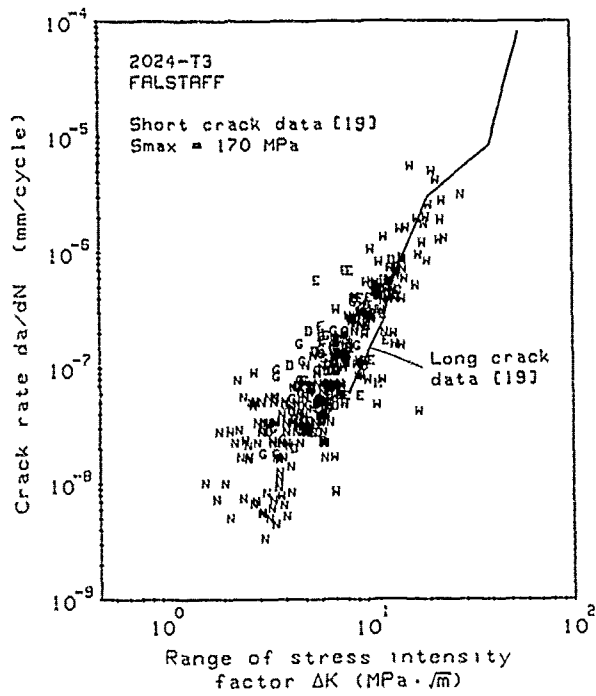


Figure 11.- Typical results from core-programme under FALSTAFF loading at S_{max} = 170 MPa after "non-interaction" analysis.

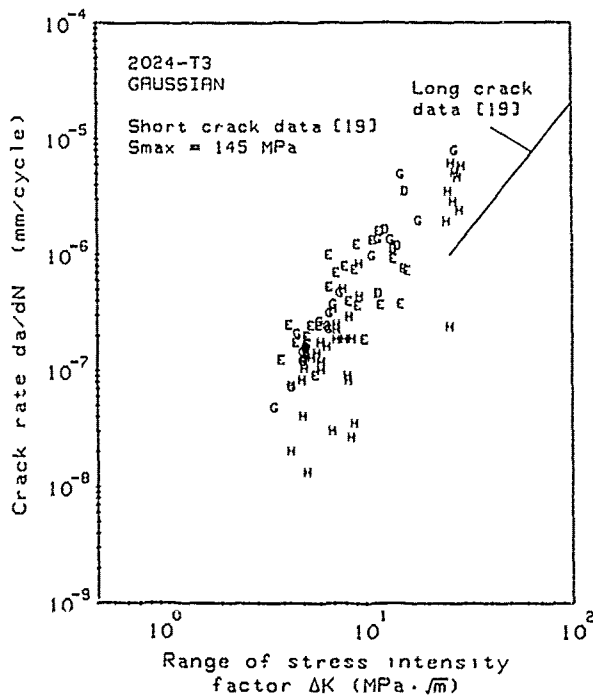


Figure 12.- Typical results from core-programme under GAUSSIAN loading at S_{max} = 145 MPa after "non-interaction" analysis.

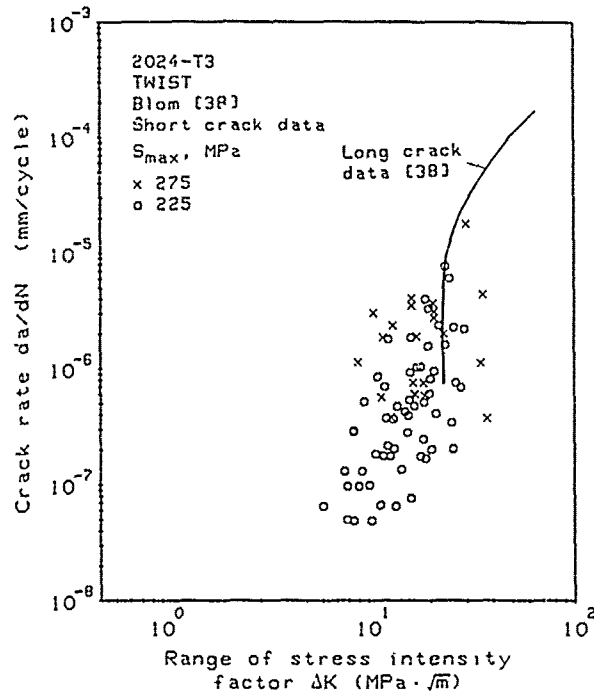


Figure 15.- Comparison of short- and long-crack growth rates under TWIST load sequence for 2024-T3 aluminum alloy.

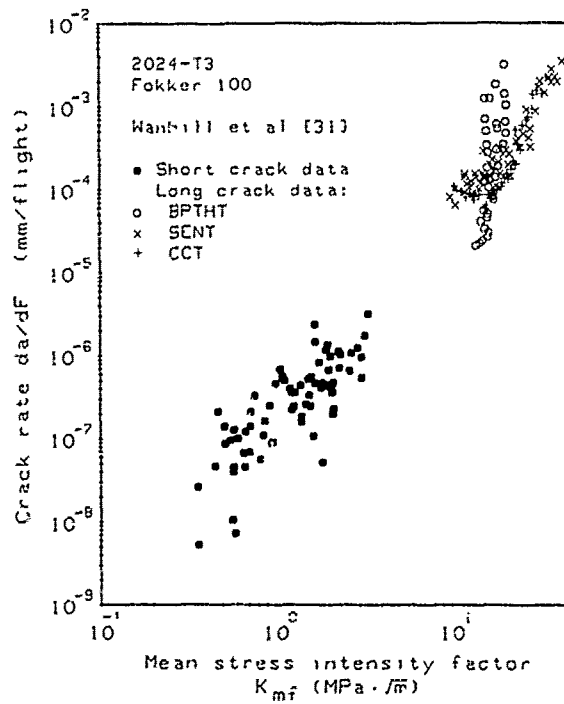


Figure 16.- Comparison of short- and long-crack growth rates under Fokker 100 load sequence for 2024-T3 aluminum alloy.

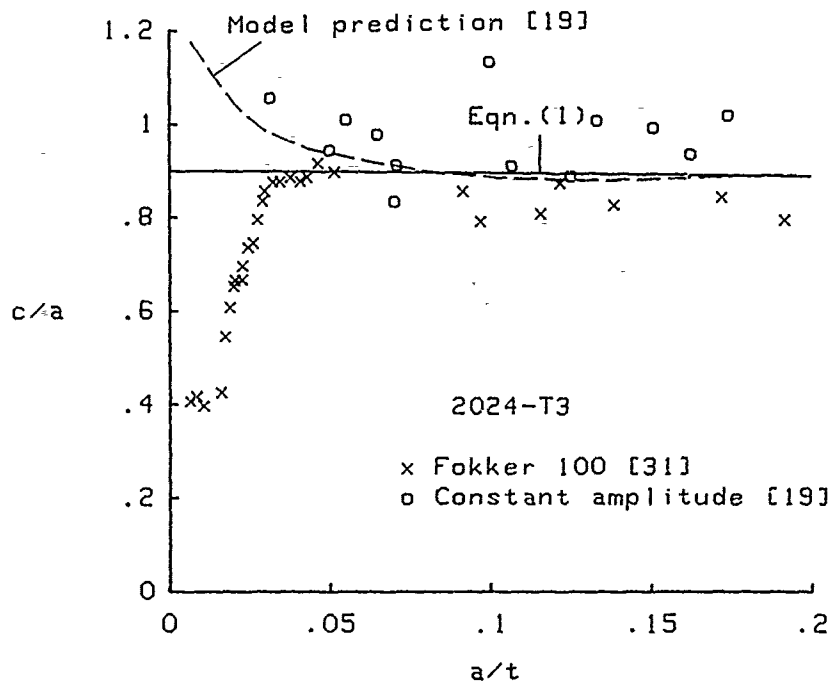


Figure 17.- Comparison of crack shape (c/a) against crack size (a/t) under constant-amplitude and Fokker 100 load sequence.

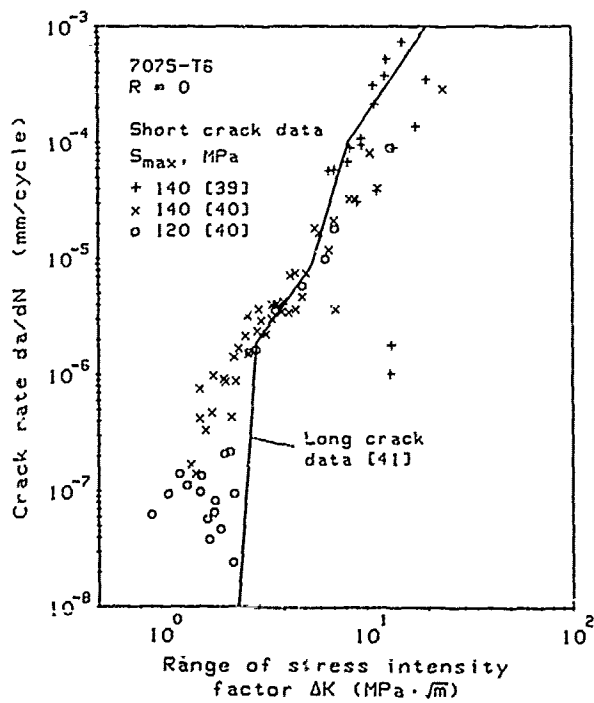


Figure 18.- Comparison of short- and long-crack growth rates under constant-amplitude loading (R = 0) for 7075-T6 aluminum alloy.

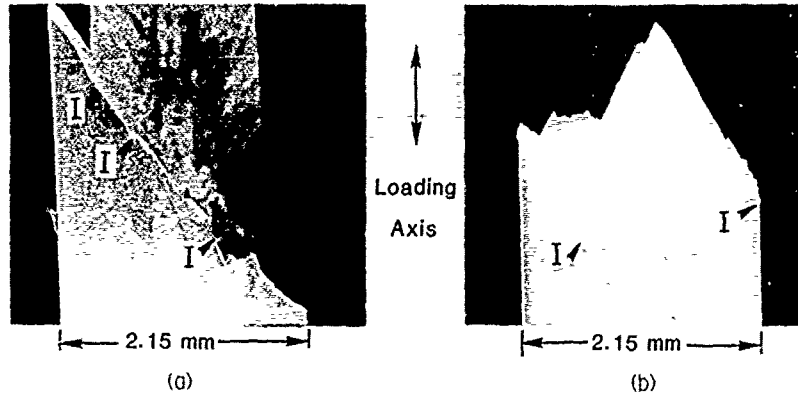


Figure 19.- Photos showing initiation sites (I) and fatigue failure profiles at notch root for 2090-T8E41 aluminum-lithium alloy with (a) overall slant fracture and (b) multi-slant fracture leading to "V"-shape crack-surface profile.

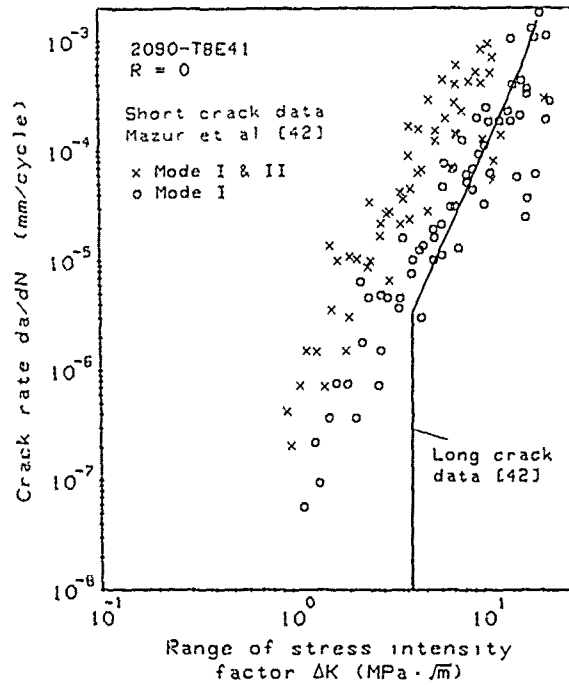


Figure 20.- Comparison of short-crack growth rates under constant-amplitude loading for 2090-T8E41 aluminum-lithium alloy using Mode I and mixed-mode (I and II) stress-intensity factor formulations.

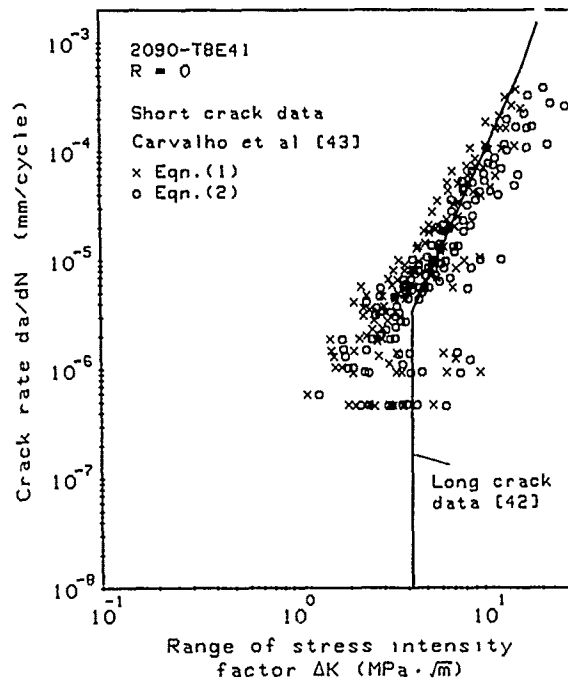


Figure 21.- Comparison of short-crack growth rates under constant-amplitude loading for 2090-T8E41 aluminum-lithium alloy using two different equations for predicting surface- or corner-crack depth, c .

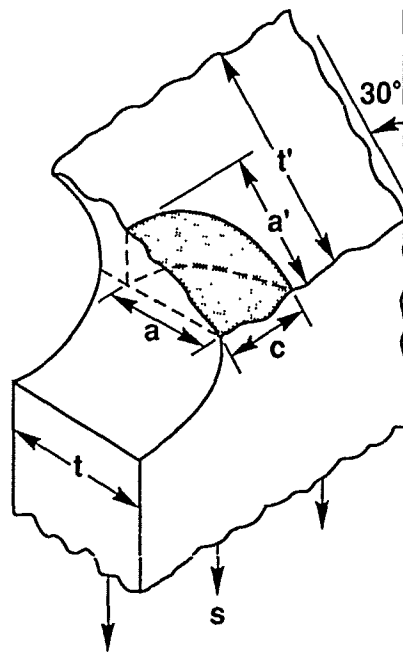


Figure 22.- Schematic of fatigue failure surface for 2090-T8E41 aluminum-lithium alloy showing various crack-length and thickness measurements.

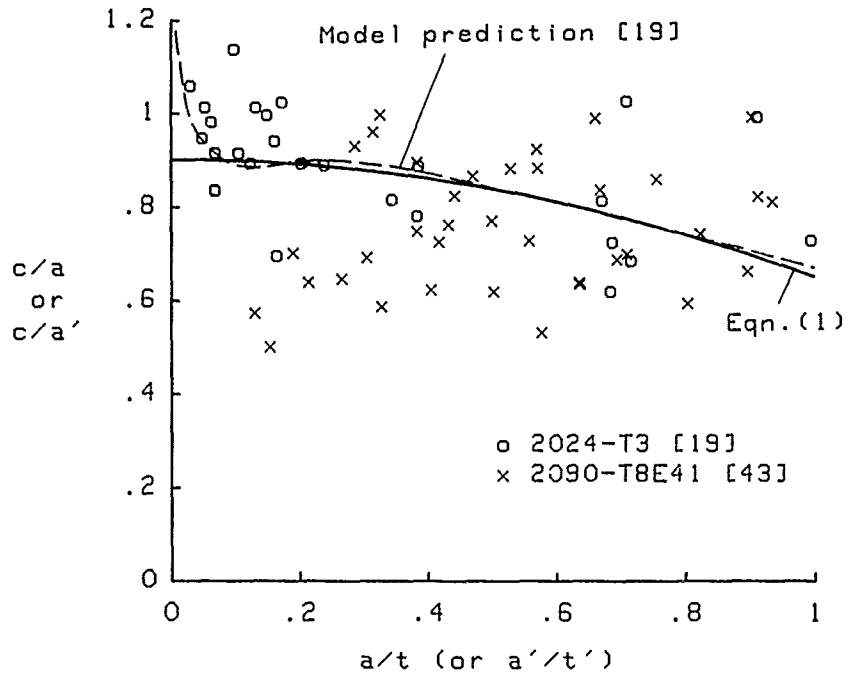


Figure 23.- Comparison of crack shape (c/a or c/a') against crack size (a/t or a'/t') for 2024-T3 aluminum and 2090-T8E41 aluminum-lithium alloys (a' and t' refer to Al-Li data only).

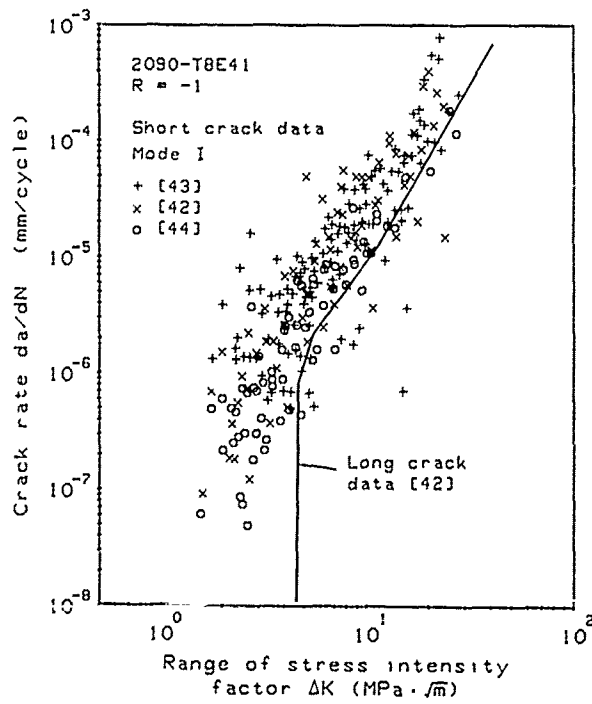


Figure 24.- Comparison of short- and long-crack growth rates under constant-amplitude loading ($R = -1$) for 2090-T8E41 aluminum-lithium alloy.

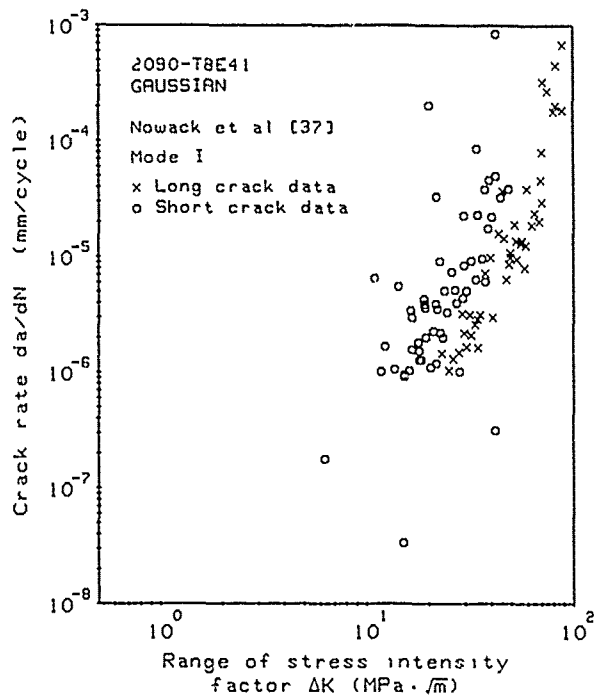


Figure 25.- Comparison of short- and long-crack growth rates under GAUSSIAN load sequence for 2090-T8E41 aluminum-lithium alloy.

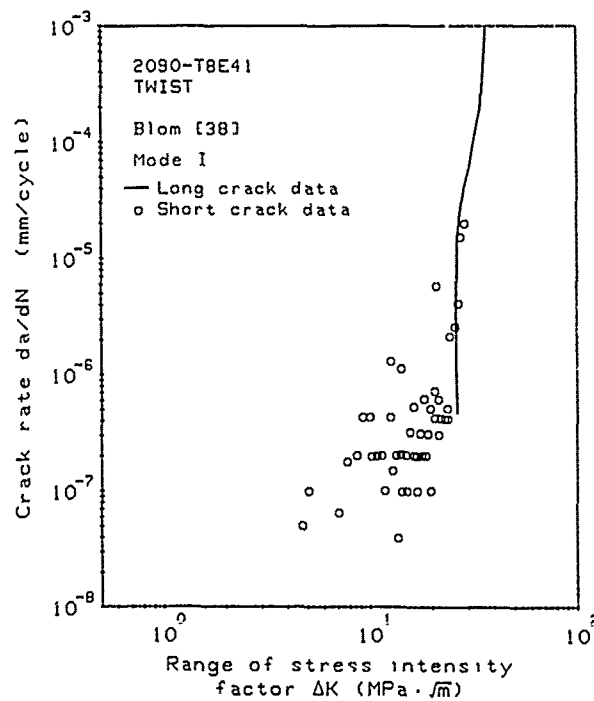


Figure 26.- Comparison of short- and long-crack growth rates under TWIST load sequence for 2090-T8E41 aluminum-lithium alloy.

NATIONAL BUREAU OF STANDARDS - Gaithersburg, Maryland 20899
 U.S. GOVERNMENT PRINTING OFFICE: 1975 O 271-101

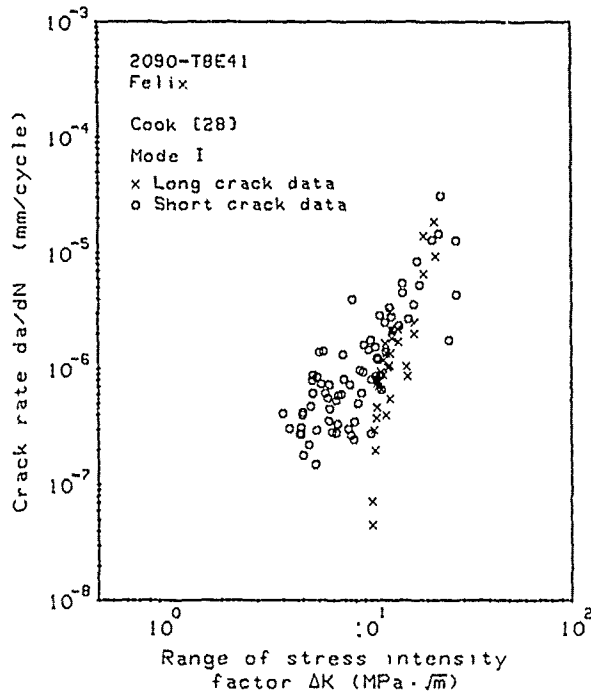


Figure 27.- Comparison of short- and long-crack growth rates under Felix load sequence for 2090-T8E41 aluminum-lithium alloy.

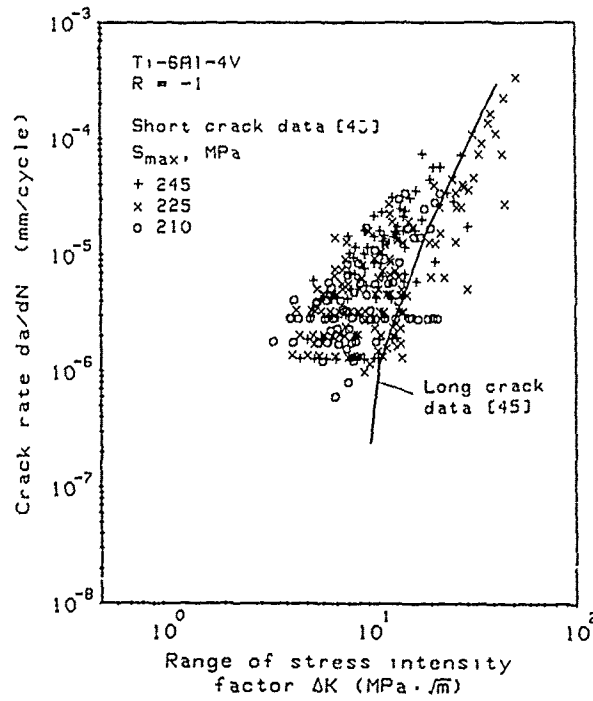


Figure 28.- Comparison of short- and long-crack growth rates under constant-amplitude loading (R = -1) for Ti-6Al-4V titanium alloy.

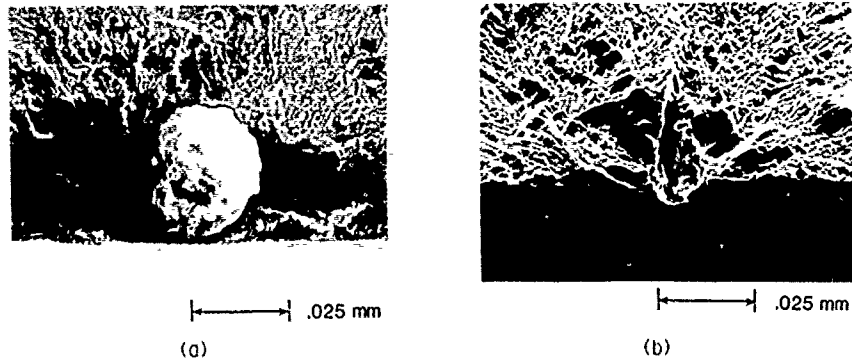


Figure 29.- Typical crack-initiation sites for 4340 steel SENT specimens showing (a) spherical calcium-aluminate inclusion particle and (b) manganese-sulfide stringer site.

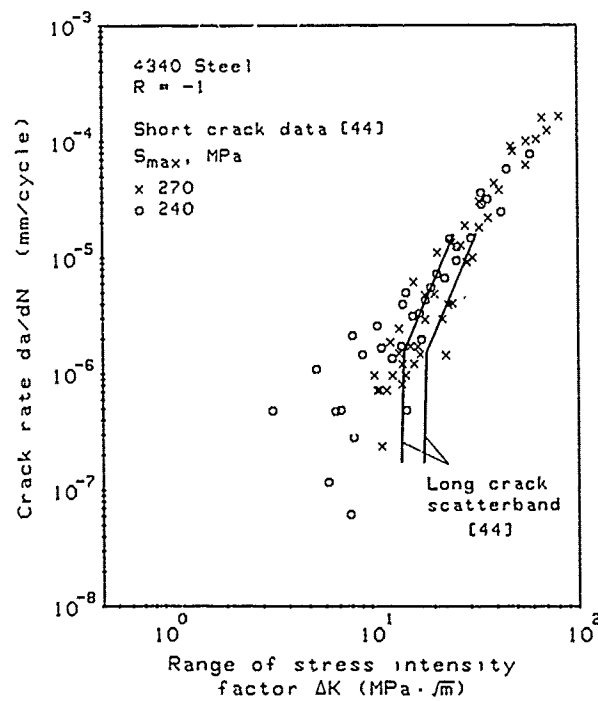


Figure 30.- Comparison of short- and long-crack growth rates under constant-amplitude loading ($R = -1$) for AISI 4340 steel.

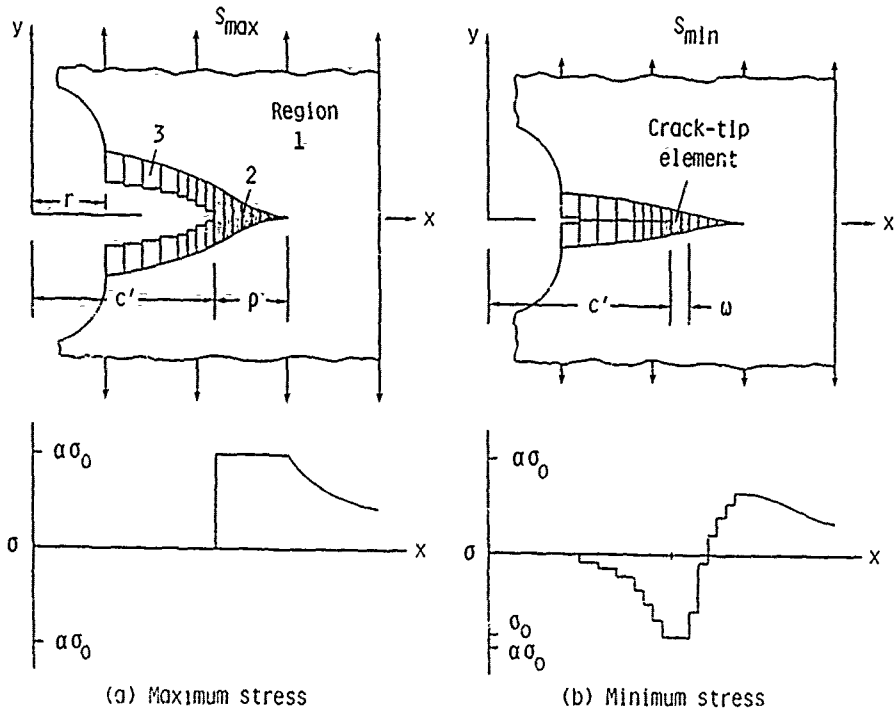


Figure 31.- Schematic of analytical crack-closure model showing crack-surface displacements and stress distributions along crack line.

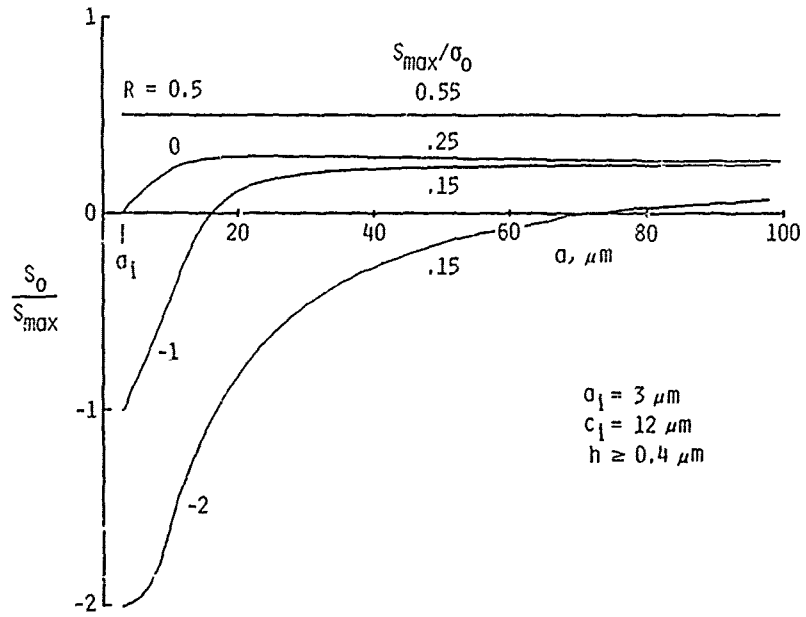


Figure 32.- Calculated crack-opening stresses for various constant-amplitude loadings as a function of crack length for a typical crack-initiation site "void" size.

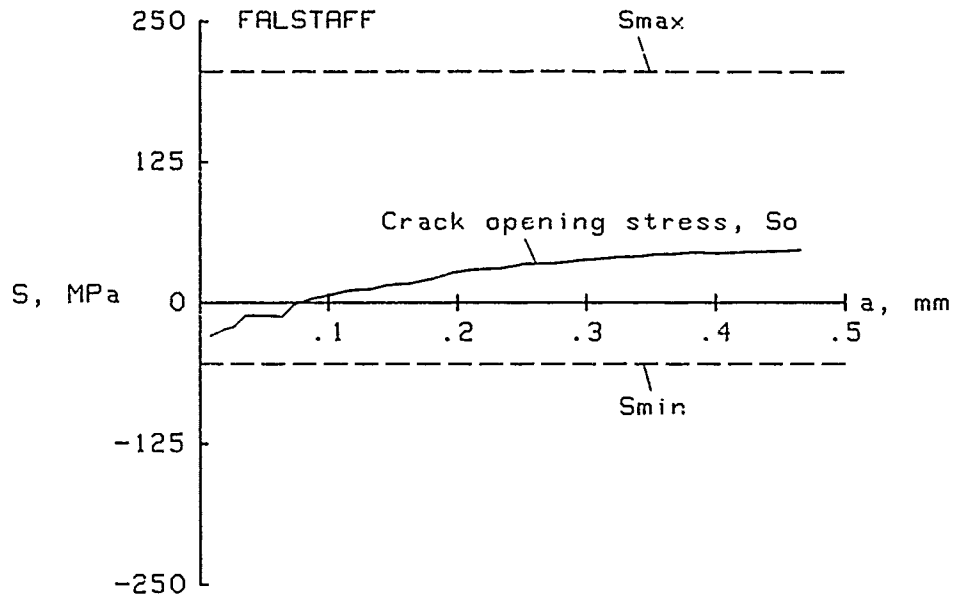


Figure 33.- Calculated crack-opening stresses for FALSTAFF load sequence showing maximum and minimum stresses applied in sequence.

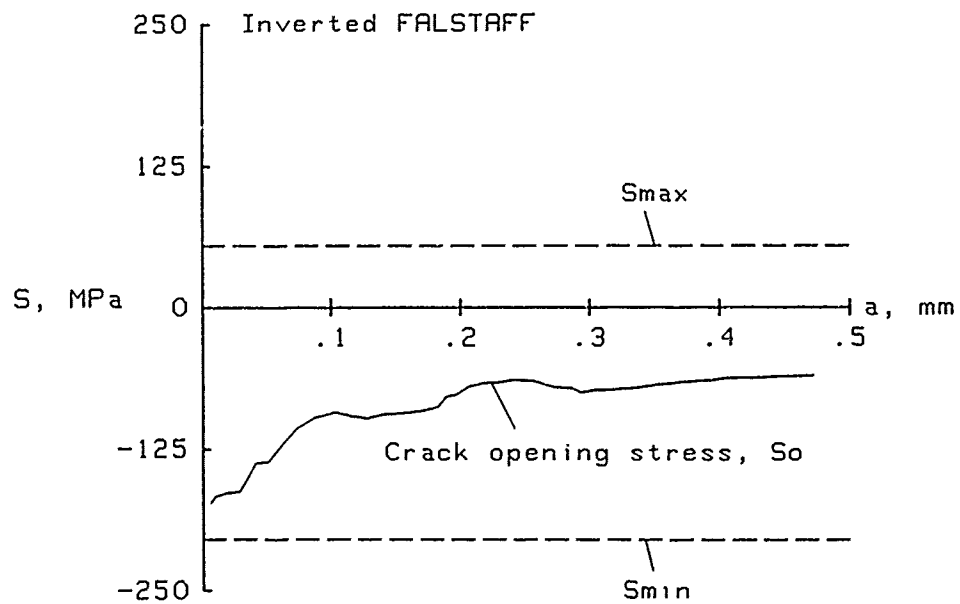


Figure 34.- Calculated crack-opening stresses for Inverted FALSTAFF load sequence showing maximum and minimum stresses in sequence.

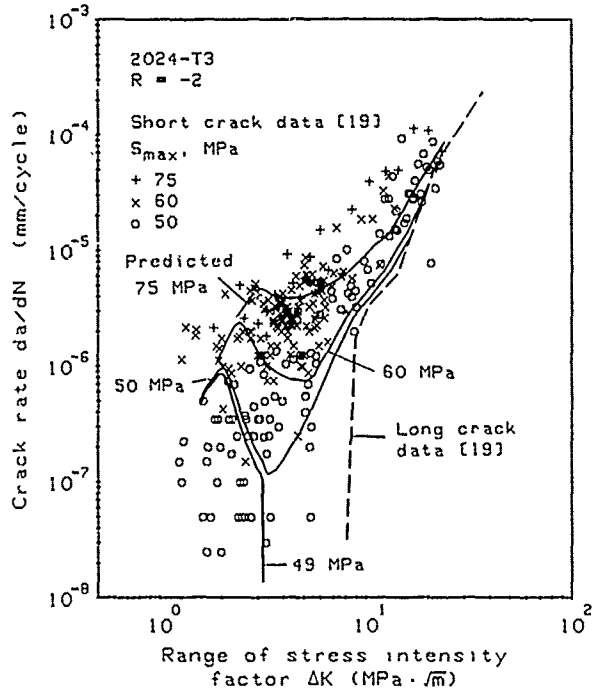


Figure 35.- Comparison of experimental and predicted short-crack growth rates for constant-amplitude loading (R = -2) for 2024-T3 aluminum alloy.

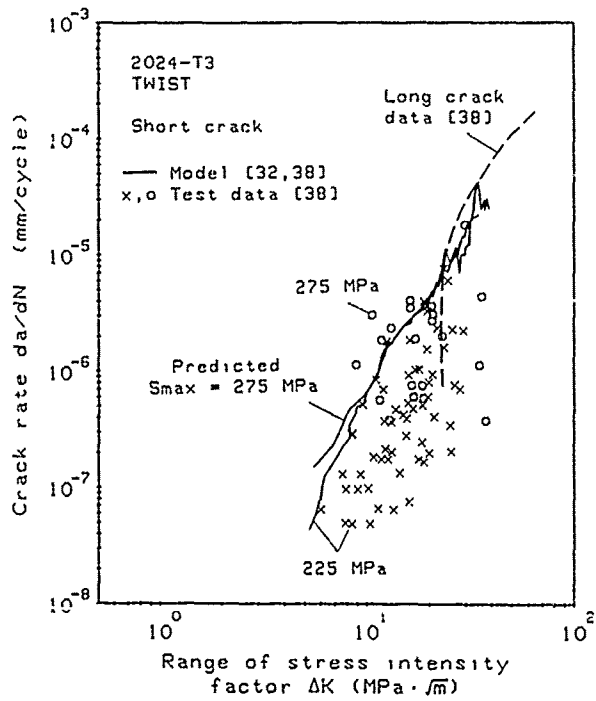


Figure 36.- Comparison of experimental and predicted short-crack growth rates under TWIST load sequence for 2024-T3 aluminum alloy.

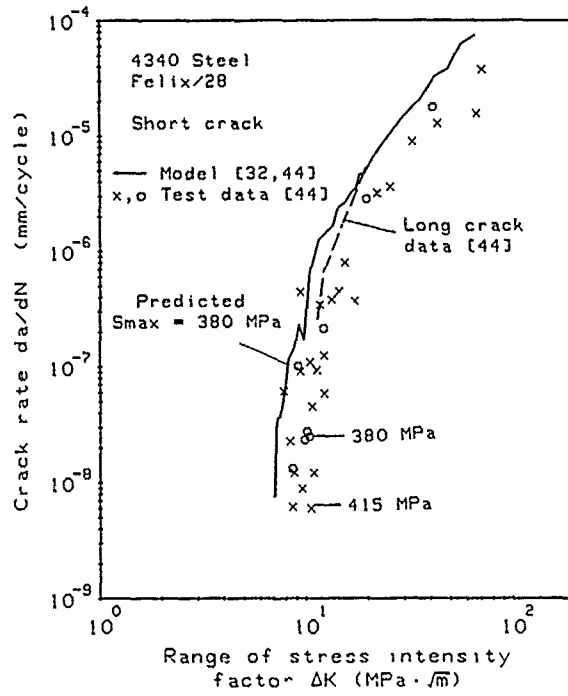


Figure 37.- Comparison of experimental and predicted short-crack growth rates under Felix/28 load sequence for AISI 4340 steel.

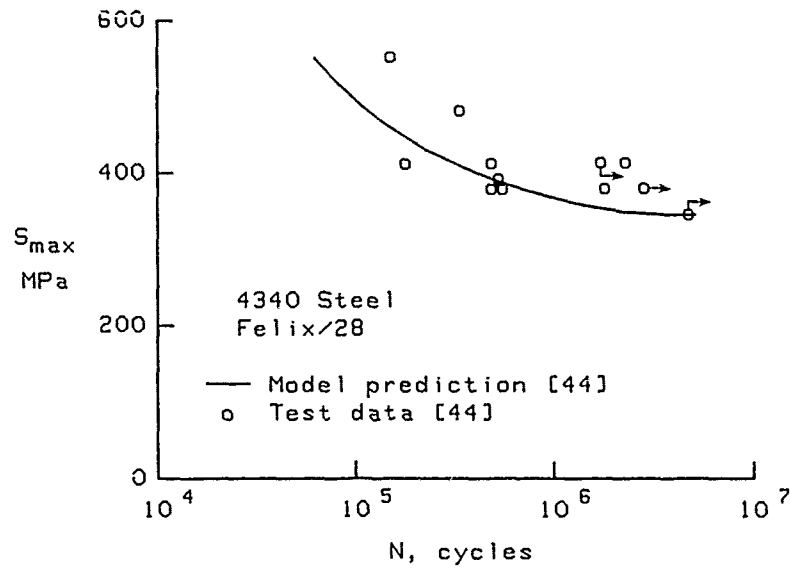


Figure 38.- Comparison of experimental and predicted fatigue lives under Felix/28 load sequence for AISI 4340 steel (arrow indicates that test was terminated).

Downloaded from ascelibrary.org by University of California, San Diego on 06/16/15. Copyright ASCE. For all rights reserved.

DETERMINATION OF THE SHORT CRACK EFFECT IN 2090-T8E41 ALUMINUM LITHIUM

by

Christopher J. Mazur, Capt. USAF
Structural Integrity Engineer

and

James L. Rudd, Tech. Manager
Fatigue Fracture & Reliability Grp.

Air Force Wright Aeronautical Laboratories (FIBEC)
Wright-Patterson AFB, Ohio 45433-6553
United States

ABSTRACT

The United States Air Force developed two primary sets of design requirements to ensure the structural integrity of aircraft: damage tolerance and durability. The purposes of these design requirements are to ensure structural safety and preclude the occurrence of expensive maintenance and repair costs, respectively. These requirements are generally satisfied through the use of linear elastic fracture mechanics and crack growth rate data experimentally generated for long cracks. Recently, various investigators have indicated that short cracks may grow significantly faster than long cracks for the same crack-driving force. The end result may be unconservative life predictions when situations arise where short crack lengths are included in the analysis. To accurately predict the growth of these short cracks, the short crack phenomenon must be understood.

The objective of this paper is to describe the work of the Flight Dynamics Laboratory as a participating agency in the AGARD Supplemental Test Program on Short Cracks. The manufacturing and testing of 2090-T8E41 aluminum-lithium short and long crack specimens were performed under this effort. Constant amplitude and spectrum fatigue tests were conducted at various stress ratios and stress levels. The short and long crack results were compared to verify the existence of any short crack effect. As a result of the unusual fracture patterns in the aluminum-lithium short crack tests, an analytical approach considering combined Mode I and Mode II type fracture was considered and compared to the standard Mode I analysis used in the previous AGARD Core Test Program.

1. INTRODUCTION

Recently, a number of investigators [1-8] have reported that small/short fatigue cracks propagate at rates significantly faster than long cracks subjected to an equivalent crack-driving force. In addition, these short cracks have been observed growing under conditions that are well below the threshold stress intensity factor estimated using current techniques (Fig. 1). This dissimilar behavior between long and short cracks has been attributed to a number of factors including crack closure [1,2], plasticity effects, microstructural interactions, violations of the continuum assumptions of solid mechanics, and violations of linear elastic fracture mechanics (LEFM) principals [3].

Investigators of these phenomena define short cracks in various ways. Three of the more common definitions are [3]:

- a. Cracks having lengths less than the dimension of the microstructure (grain size), typically on the order of .001 mm - 0.05mm (0.00004 inch - 0.002 inch).
- b. Cracks having lengths less than the plastic zone size, typically 0.01mm - 1mm (0.0004 inch - 0.04 inch).
- c. Cracks having lengths which are physically small, typically 0.5mm - 1mm (0.02 inch - 0.04 inch).

The first and second definitions result in a violation of the assumptions of continuum mechanics and LEFM, respectively. In the third definition, a physically short crack is long in terms of the continuum mechanics and LEFM definitions; however, it too behaves differently from long cracks for the same crack driving force. As one can imagine, the existence of the short crack effect is embroiled in controversy. However, one thing appears certain; the current analysis procedures for predicting the growth behavior of physically small cracks are inadequate.

The United States Air Force developed two primary sets of design requirements to ensure the integrity of aircraft structures: damage tolerance and durability [9]. The purposes of the damage tolerance and durability design requirements are to ensure structural safety and to preclude the occurrence of expensive maintenance and repair costs, respectively. The damage tolerance design requirements include the assumption of the existence of initial fatigue cracks in the most critical locations of the structure from day one. The sizes of these initial cracks are based on NDI capability. For close tolerance fasteners this initial primary damage size is assumed to be 1.27 mm (0.05 inch). However, if life enhancement fastener systems are present (e.g., interference-fit fasteners, cold-worked holes, etc.), a smaller initial primary damage size of 0.127 mm (0.005 inch) is assumed. Also, locations adjacent to the primary damage are assumed to have initial 0.127 mm (0.005 inch) cracks for both clearance-fit and life enhancement

fastener systems. Damage tolerance analyses are performed to predict when these initial flaws will reach a critical size. For the above mentioned sizes it can be seen that the "short crack effect" could significantly affect the damage tolerance lives predicted in aircraft design, schematically illustrated in Figure 2.

The most commonly used practice in Air Force durability design today is to assume the existence of an initial fatigue crack representative of the initial fatigue quality of the structure. The initial quality is a function of the material selected and the manufacturing and assembly techniques used. The initial flaw size normally assumed is 0.254 mm (0.01 inch). Durability analyses are performed to predict when this initial flaw will reach the functional impairment crack size, a_f . Commonly used definitions of functional impairment are fuel leakage and ligament breakage. Again, Figure 2 schematically illustrates that the "short crack effect" could significantly affect the durability lives predicted for aircraft structure. Recent work has been performed to improve durability design by more realistically representing the initial fatigue quality of the structure with a distribution of initial flaw sizes rather than a single flaw size [10]. The short crack effect should be accounted for in the determination of this distribution of initial flaw sizes. In addition to airframes, the short crack effect is also important in the design of aircraft engine components, where critical crack lengths may be similar to those of short cracks. Thus, researchers are devoting much time and resources to understand and predict the behavior of short cracks.

This paper describes short and long crack growth rate tests on 2090-T8E41 aluminum-lithium by the Flight Dynamics Laboratory in an attempt to validate the existence of the short crack effect and develop a short crack data base. Fatigue tests were conducted on single-edge-notch tension specimens under constant and variable amplitude load conditions. Long crack tests were conducted on center-crack-tension specimens under similar loading conditions for comparison with the short crack results. This program is the Flight Dynamics Laboratory's contribution to an AGARD (Advisory Group for Aerospace Research and Development) Cooperative Supplemental Test Program on Short Cracks.

2. TEST PROGRAM

The test program involved single-edge-notch tension (SENT) specimens made of 2090-T8E41 aluminum-lithium sheet. The SENT specimen geometry is depicted in Figure 3. This specimen geometry was chosen because it allows the generation and measurement of naturally occurring cracks similar to those that would occur in bolt holes of aircraft structures. The stress concentration factor for this specimen geometry is 3.17, based on gross section stress.

The 2090 specimens were produced from a single sheet of 2.3 mm thick ALCOA material. Since this is a new material, very little baseline crack growth rate data are available. Thus, long crack growth rate tests were conducted on center-crack-tension (CCT) specimens (Figure 4) as a parallel effort for comparison with the short crack results. These CCT specimens were produced from the same sheet of 2090 material as the SENT specimens. This should eliminate any manufacturing variability due to different batches of material. Baseline mechanical properties and the nominal chemical composition are presented in Tables 1 and 2, respectively. Note the low plane stress fracture toughness in Table 1 (brittle material). This is a result of the material heat treatment (T8E41) and is probably the cause of much of the difficulties in the short crack testing, as will be mentioned.

CCT and SENT specimen blanks were sheared from the sheets of material to a size larger than the final specimen dimensions. The long dimension of the specimens was parallel to the rolling direction of the material. Each specimen blank was milled to its final dimensions and engraved with a code number giving its location in the sheet (Fig. 5). The notch was then milled into the SENT specimen blanks with final milling cuts of 0.25, 0.1, and 0.05 mm using newly sharpened tools. The final radius of the notch was 3.18 mm (0.125 inch) (Fig. 3). A wire EDM (Electric Discharge Machine) was used on the CCT specimens to induce the flaws (Fig. 4). Great care was taken in the milling of the specimens to minimize residual stresses. Once machining operations were complete the specimen surfaces were deburred and polished. Chemical polishing of the SENT specimens was performed at NASA Langley Research Center. The chemical polishing was necessary to smooth machining marks and debur the edges of the notches to prevent premature crack initiation caused by defects in those locations. The polishing also provided additional assurance that no significant residual stresses remained in the notch vicinity. The specimens were chemically polished in a solution of 80% phosphoric acid, 5% nitric acid, 5% acetic acid, and 10% water by volume. The polishing cycle was five (5) minutes at 105°C. This resulted in the removal of about 0.02 mm (0.0008 inch) of material from the specimens. The specimens were then individually wrapped and distributed to various participants in the AGARD effort.

The SENT specimens were tested by the Flight Dynamics Laboratory using a servo-hydraulic MTS testing machine. The machine used MTS hydraulic grips lined with plastic spacers between the grip jaws and the specimen. These spacers were used to prevent fracture of the specimen in the grip area. An anti-buckling guide plates was used on all specimens to limit out-of-plane displacements of the specimen when compression loads were applied (Fig. 6). Load monitoring and load sequencing were accomplished using a computerized data acquisition system. The accuracy of the load system was $\pm 1\%$ of the intended load. All tests were conducted at a frequency of seven (7) Hertz under room

temperature laboratory air conditions.

Prior to any short crack testing, an alignment check was performed on the test machine and grips to ensure a uniform stress field throughout the cross-section of the SENT specimens. Both bending (lateral and torsional) and tensile misalignments were considered. The grips were shimmed to meet target tolerances. A description of the procedure and results of the alignment tests are documented in Reference 11.

Long crack tests were also conducted in a servo-hydraulic MTS test machine. These tests were conducted in accordance with ASTM Standard E647, "Test Method for Constant-Load Amplitude Fatigue Crack Growth Rates Above $10E-8$ m/cycle" [12]. Long crack growth measurements were visually monitored using a scale mounted on the test specimen. A sufficient number of readings were recorded to obtain a representation of the crack growth rate curve. The variable amplitude tests, although not covered by this ASTM Standard, were conducted in a similar manner. Load-shedding tests were also conducted to obtain threshold stress intensity values.

A wide range of loading conditions were applied in the short and long crack testing. Fatigue testing included three (3) constant amplitude loading conditions ($R = 0, -1, -2$) and one variable amplitude loading spectrum (FALSTAFF) [13]. The inclusion of compression loading in the constant amplitude test matrix was a result of expectations that the short crack effect would be more predominant under those conditions owing to crack closure effects. The FALSTAFF spectrum (Fighter Aircraft Loading STandard For Fatigue) is a general European test spectrum for fighter aircraft lower wing skins covering a host of mission scenarios including taxiing (compression loading): FALSTAFF is however tension-dominated.

The plastic replica method was used to document the short crack growth in the notch of the SENT specimen. A detailed description of the procedure used to take a replica is presented in Reference 11. Replicas were taken at selected intervals throughout the fatigue test so that sufficient readings could be obtained before the crack propagated through the thickness of the specimen. To obtain a replica at each interval the cycling was stopped at zero load. The specimen was then manually loaded to 80% of the maximum applied tensile load for constant amplitude tests and to 100% of the load level number 22 in the FALSTAFF spectrum. The replica was then made and cycling resumed for the next interval. All necessary data were recorded on the replicas for later analysis. Once the crack grew through the specimen thickness, the specimen was fractured to reveal the crack shape for comparison with the assumed shape. The replicas were then examined under a microscope with magnifications of 60-600X. A scale in the eyepiece of the microscope allowed crack measurements with a maximum resolution of 0.001 mm at the highest magnification. Each crack was first detected and measured at low magnifications and followed through consecutive replicas until it joined another crack and/or propagated through the thickness. Higher magnifications were subsequently used on earlier replicas to track the cracks back to their origins (usually inclusion particles) or as far as possible.

3. ANALYSIS

As a result of the unusual crack growth at acute angles with respect to the loading direction in the short crack tests, the data were analyzed using two approaches. The first approach was the standard Mode I type crack growth analysis where the horizontal projection of the cracks on to a plane normal to the specimen loading direction were measured for use in the crack growth rate and stress intensity factor calculations (Fig. 7a). The second approach was a combined Mode I/Mode II approach where the actual crack lengths are used in the analysis (Fig. 7b).

For the standard Mode I approach, two possible cases were considered for the calculation of the stress intensity factor [14]. The first was a semi-elliptical surface crack located in the center area of the notch. The second was a quarter-elliptical crack located at an edge of the notch. Figure 8 shows the pertinent dimensions for the two crack types. The crack depth was calculated from the following equation for both types of cracks,

$$a/c = 0.9 - 0.25(a/t)^2 \quad 1$$

where a , c and t are defined in Figure 8. This equation was verified by a comparison with the experimental data generated in the AGARD core test program (2024-T351 material) to ensure that it is a close representation of the actual crack shape. This was accomplished by fracturing the SENT specimens after each fatigue test and observing the shape of the crack.

The stress-intensity factor range equation for a surface crack located at the center of the notch is [14],

$$\Delta K = \Delta S(3.14a/Q)^{1/2} F_{SN} \quad 2$$

and for a corner crack,

$$\Delta K = \Delta S(3.14a/Q)^{1/2} F_{CN} \quad 3$$

for $0.2 \leq a/c \leq 2$ and $a/t < 1$, where

$$F_{CH} = F_{SN}(1.13 - 0.09a/c) \quad \text{for } a/c \leq 1 \quad 4$$

$$F_{CH} = F_{SN}(1.00 + 0.04c/a) \quad \text{for } a/c > 1 \quad 5$$

The stress range (ΔS) is the difference between the maximum and minimum stresses ($S_{max} - S_{min}$) applied for constant amplitude and spectrum loadings. Equations for the shape factor (Q) and the boundary correction factor (F_{SN}) may be obtained from Reference 14.

The crack growth rate (da/dN) was calculated for constant amplitude and spectrum loading using the secant method,

$$da/dN = \Delta a/\Delta N = \frac{a_2 - a_1}{N_2 - N_1} \quad 6$$

The corresponding stress-intensity factor range (ΔK) was calculated at an average crack length, a

$$a = (a_1 + a_2)/2 \quad 7$$

For the combined Mode I/Mode II approach, the calculation of the stress intensity factor was formulated for the problem of uniaxial extension of an inclined crack in an infinite plate (Fig. 7b) [15]. The equations describing the stress intensity factor for the Mode I and Mode II solutions are,

$$K_I = S \sin^2 \beta (\pi a)^{1/2} \quad 8$$

and,

$$K_{II} = S \sin \beta \cos \beta (\pi a)^{1/2} \quad 9$$

Using the Strain Energy Release Rate,

$$G = \frac{K_{I,II}^2}{E} = G_I + G_{II} = \frac{K_I^2}{E} + \frac{K_{II}^2}{E} \quad 10$$

one can obtain an equivalent stress intensity factor for the combined Mode I/Mode II case,

$$K_{I,II} = S \sin \beta (\pi a)^{1/2} \quad 11$$

Accounting for the various geometry differences between the solution for an infinite plate and the SENT type crack growth specimen, the following equivalent stress intensity factors are obtained for cracking at an angle in a SENT type specimen geometry:

$$\text{surface crack} \quad \Delta K_{I,II} = \Delta S \sin \beta (3.14a/Q)^{1/2} F_{SN} \quad 12$$

$$\text{corner crack} \quad \Delta K_{I,II} = \Delta S \sin \beta (3.14a/Q)^{1/2} F_{CH} \quad 13$$

Correction factors, shape factors and the stress range for the above equations are essentially the same as in the Mode I case except that the actual crack length should be used rather than the horizontal projection. It should be noted that to satisfy the equations for the edge effects and correction factors, the a/t ratio should be obtained using the horizontal projection of the crack so that the ratio does not exceed one. The crack extension (da/dN) is calculated using the actual crack length in the same manner as in Equation 6.

4. RESULTS AND DISCUSSION

Prior to conducting short crack tests, S-N curves were generated for the various constant amplitude test conditions proposed (Fig. 9) ($R = 0.5, 0, -1, \text{ and } -2$). The SENT type specimens were placed in the fatigue test machine and cycled to failure at various stress levels to generate this data base. This was accomplished to gain insight into what stress levels to use for the short crack tests so that they could be completed in a reasonable length of time. Because of a slight variability in these data and the high slopes, conservative stress levels and replica intervals were chosen for the initial short crack testing. As a result of this conservatism, it was not uncommon to take 150 replicas during a single short crack test. Of these replicas, most contained no cracks and thus were not used.

Long and short crack tests were conducted under constant amplitude ($R = 0, -1, -2$) and spectrum (FALSTAFF) loadings. Subject to specimen availability and test duration, multiple specimens at different stress levels were tested for each of the above conditions. Table 3 shows that this was not always possible. Cracks on the order of 0.01 mm (0.0004 inch) were detected and tracked in the test program using the replica method. Figure 10 (a through d), Figure 11 (a through d) and Figure 12 (a through d)

graphically present the resulting crack growth rate data for the long crack, short crack (Mode I analysis) and short crack (Mode I/Mode II analysis), respectively.

The various plots in Figure 10 (a thru d) represent all the long crack data generated to date for the 2090-T8E41 aluminum-lithium specimens. The solid lines on the plots represent visual fits to the data. These lines are used in Figures 11 and 12 for comparison with the short crack data. The long crack test results for the CGT specimens are typical of common aluminum materials. There was little observed out-of-plane crack growth and the material responded favorably to the various loading conditions. One observation worth noting was that at positive stress ratios it was very difficult to get a crack started. However, it appears that this material is very sensitive to compression loading which results in immediate crack initiation and growth.

The short crack test data for the 2090 aluminum-lithium specimens were very difficult to generate as compared to the previous 2024 aluminum AGARD Core Test Program. This aluminum-lithium material's resistance to crack initiation and subsequent fast crack growth resulted in great difficulty in obtaining an acceptable number of crack growth measurements during each test. More importantly, in the short crack test program, the cracks grew at an angle in the SENT specimens. Every crack observed during the constant amplitude short crack tests grew continuously or in a zig-zag pattern across the specimen at 60 ± 5 degrees with respect to a plane normal to the specimen loading direction (Fig. 13). This high angle indicates that the crack growth occurred mostly in shear. This high angle also made it difficult to determine the crack shape for comparison with the assumed shape and to detect any possible tunneling problems. Fig. 14 illustrates examples of the fracture surfaces for various specimens. As can be seen in Figure 14a, the crack shape is distinguishable; however, the more common occurrences are represented by Figures 14b and c, which do not reveal a crack shape. With a little imagination, one might argue that the cracks in Figures 14 b and c were actually tunneling. It was also noted that while testing at $R = -2$ the cracks were always corner cracks regardless of the stress level. This may be the result of buckling during the tests. The anti-buckling guide was designed to allow minimal specimen freedom (some buckling) so as to reduce anti-buckling guide interference with the specimen being tested.

Results of the short crack data analyzed using a Mode I approach are plotted in Figures 11 a thru d. Figures 11 a, b, & c represent the $R = 0$, -1 and -2 results, respectively. The solid lines on these plots are long crack data and the dashed lines represent a fit of the short crack data using a Paris type equation of the form,

$$da/dN = C(\Delta K)^n \quad 14$$

The empirical constants C and n were determined using a linear regression analysis. For Mode I short crack data, these constants are $C = 1.2588E-10$ and $n = 2.8169$ for $R = 0$, $C = 7.6116E-10$ and $n = 2.4916$ for $R = -1$, and $C = 3.8110E-10$ and $n = 2.6261$ for $R = -2$. The results of the FALSTAFF spectrum tests are presented in Figure 11d. The solid line represents long crack data and the dashed line is a visual fit to the short crack data.

The short crack data analyzed using a combined Mode I/Mode II approach are plotted in Figures 12 a thru d. Figures 12 a thru c represent the $R = 0$, -1 and -2 results, respectively. The solid lines represent the long crack data and dashed lines represent a fit to the short crack data using a Paris type equation as described above. The Paris constants are $C = 6.4203E-10$ and $n = 2.8751$ for $R = 0$, $C = 3.3846E-10$ and $n = 2.5540$ for $R = -1$, and $C = 2.0992E-10$ and $n = 2.6169$ for $R = -2$. The results for the FALSTAFF spectrum are presented in Figure 12(d), where the dashed line represents a visual fit to the short crack data.

As can easily be seen by comparing Figures 11 and 12, the combined Mode I/Mode II approach tends to increase the stress intensity factor for a given crack growth rate. The result is a more pronounced short crack effect. One problem with the combined Mode I/Mode II approach is that the data no longer tend to coalesce with the long crack data. This implies that the stress intensity solution used for the combined Mode I/Mode II approach may not be accurate or that the short crack data can no longer be compared to the long crack data (Mode I data). The inaccuracy in the combined Mode I/Mode II data may be in the crack shape or in accounting for the edge effects. Although the combined Mode I/Mode II approach appears to be more appropriate for these short crack data, additional analyses are needed to improve the fit for larger cracks. For simplicity, it would be best to use the Mode I short crack results.

In general, independent of the analysis chosen the test results indicate that the short crack effect does exist in 2090 aluminum-lithium when LEFH is used to analyze the crack growth rates, especially for the negative R-ratio tests. The effect also appears to be independent of the test conditions (i.e. constant amplitude or spectrum loading). As previously mentioned, there was difficulty obtaining short crack data for this material. This was a result of the aluminum-lithium's variability in crack initiation time (Fig 15) followed by poor crack growth properties, which in turn may be attributed to the material temper. An example of this variability was a crack which initiated and failed a specimen in 300,000 cycles, while the following test using the same test conditions resulted in a life to failure of 2,500,000 cycles. No defects were observed on either specimen prior to testing. Two explanations for this inconsistency are that a possible defect existed in the one specimen beneath the surface, where it was nonvisible, or there were residual stresses in the other specimen from improper

machining and polishing procedures. Most of the variability in the aluminum-lithium was observed for positive stress ratios at low stress levels. Any compression loading generally caused cracks to initiate quickly and consistently. One simplifying aspect of the aluminum-lithium short crack tests was that, independent of the stress level, it was unusual for multiple cracks to initiate and propagate in each specimen.

There was considerably less scatter observed in the 2090 aluminum-lithium short cracks data than expected. Much of the scatter that was present can be attributed to errors in the calculation of the stress intensity factor, ΔK . The shape of the cracks growing in the specimen is assumed to be elliptical, based on experimental data. However, a physically small newly initiated crack may not establish that assumed shape for a period of time.

5. CONCLUSIONS

Short crack tests were performed for constant amplitude and spectrum loading on 2090-T8E41 aluminum-lithium. The constant amplitude tests were conducted for stress ratios of 0, -1, and -2, while the spectrum tests involved FALSTAFF. The replicate technique used to monitor the growth of the short cracks proved to be adequate for the test conditions. Cracks on the order of 0.01 mm (0.0004 inch) were measured during this test program. One major problem encountered was too much variability in the initiation and growth time of the short cracks, resulting in many useless but necessary replicas taken to ensure that sufficiently small cracks would be measured. The short crack data were analysed using Mode I and combined Mode I/Mode II approaches. They were then correlated with long crack data generated using standard ASTM test procedures. This correlation indicates that the "short crack effect" does exist when the short crack data are analyzed using current LEFM methods, particularly for the negative R-ratios tested. The effect is also evident when the FALSTAFF spectrum is applied. Overall, the program successfully demonstrated the existence of the "short crack effect" and provides a necessary database to develop new analysis tools capable of accounting for this effect.

6. REFERENCES

1. Newman, J. C., Jr., "A Crack Closure Model for Predicting Fatigue-Crack Growth Under Aircraft Spectrum Loading," NASA TN 81914, National Aeronautics and Space Administration, 1981.
2. Elber, W., "The Significance of Fatigue Crack Closure," Damage Tolerance of Aircraft Structures, ASTM STP 486, American Society for Testing and Materials, pp 230-242, 1971.
3. Ritchie, R. O., and Suresh, S., "Mechanics and Physics of the Growth of Small Cracks," AGARD Conference Proceedings No. 328 on Behavior of Short Cracks in Airframe Components, pp 1-1 through 1-14, 1983.
4. Wood, H. A., Rudd, J. L. and Potter, J. M., "Evaluation of Small Cracks in Airframe Structures," AGARD Report No. 696 on Short Crack Growth Behavior in Aircraft Structures, pp 1-1 through 1-12, 1983.
5. Lankford, J., "The Growth of Small Fatigue Cracks in 7075-T6 Aluminum," Fat. of Eng. Matls. & Structures, Vol. 5, 1982.
6. Dowling, J. E., "Crack Growth During Low Cycle Fatigue of Smooth Axial Specimens," ASTM STP 637, American Society for Testing and Materials, pp 97-121, 1977.
7. Taylor, D. and Knott, J. F., "Fatigue Crack Propagation Behavior of Short Cracks -- The Effects of Microstructure," Fat. of Eng. Matls. & Structures, Vol 4, No. 2, pp 147-155, 1981.
8. Blom, A. F., "Relevance of Short Fatigue Crack Growth Data for Durability and Damage Tolerance Analyses of Aircraft," Aeronautical Research Institute of Sweden, FFA-TN-1986-23, Stockholm, 1986.
9. Anon., "Military Specification Aircraft Structures," MIL-A-87221, Air Force Aeronautical Systems Division, February, 1985.
10. Manning, S. D. and Yang, J. N., "Advanced Durability Analysis," AFWAL-TR-86-3017, Air Force Wright Aeronautical Laboratories, July 1987.
11. Mazur, C. J. and Rudd, J. L., "Short Crack Effect for Constant Amplitude and Spectrum Loadings, Technical Memorandum, AFWAL-TM-86-236-FIBE, Air Force Wright Aeronautical Laboratories, Dec 1986.
12. "1986 Annual Book of ASTM Standards, Section 3, Metals Test Methods and Analytical Procedures," American Society of Testing and Materials, 1986.
13. "Description of a Fighter Aircraft Loading Standard For Fatigue evaluation (FALSTAFF)," F + W (Switzerland), LEP (Germany), NLR (Netherlands), and IABG (Germany), March 1976.

14. Newman, J. C. and Edwards, P. R., "Short Crack Growth Behavior in an Aluminum Alloy - An AGARD Cooperative Test Programme," AGARD Report No. 732, In Printing, 1988.

15. Sih, G. C., "Handbook of Stress-Intensity Factors for Researchers and Engineers," Lehigh University, 1973.

7. ACKNOWLEDGEMENTS

This work was performed by the Structural Integrity Branch, Structures Division, Flight Dynamics Laboratory, Wright-Patterson AFB OH under work unit 2307N124 (funded by AFOSR) as part of an AGARD cooperative test program. The authors wish to thank the coordinators of the AGARD test program, P. R. Edwards and J. C. Newman. In addition, we would like to thank H. Stalnaker, L. Bates and D. Cook for performing the short crack tests from which this paper is derived.

Table 1 Baseline Mechanical Properties for 2090-T8E41.

Ultimate Tensile Strength	580 MPa
Yield Stress 0.2% Offset	525 MPa
Percent Elongation	5
Fracture Toughness **	22 MPa√m

** For 2.3 mm thick material.

Table 2 Chemical Composition of 2090-T8E41.

Element	Percent Volume
Silicon	0.10
Iron	0.12
Copper	3.00
Manganese	0.05
Magnesium	0.25
Chromium	0.05
Zinc	0.10
Titanium	0.15
Zirconium	0.15
Lithium	2.60
other	0.05
Aluminum	Balance

Table 3 Test Conditions for Short and Long Crack Tests.

TEST TYPE	LOADING CONDITION	MAX. STRESS	NUMBER OF SPECIMENS TESTED
LONG CRACK	R = 0.5	69 MPa	1
		34 MPa	1
	R = 0	34 MPa	1
		34 MPa	2
	R = -1	50 MPa	1
		34 MPa	1
	R = -2	50 MPa	1
		34 MPa	1
	FALSTAFF	137 MPa	1
		117 MPa	1
SHORT CRACK	R = 0	162 MPa	2
		151 MPa	2
	R = -1	96 MPa	2
		82 MPa	2
	R = -2	68 MPa	3
		54 MPa	1
FALSTAFF	204 MPa	2	

* Load-shedding type test.

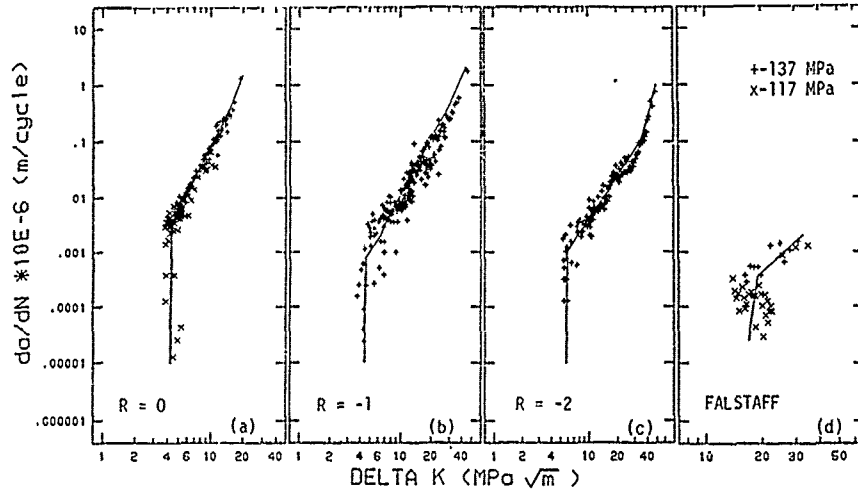


Figure 10 CCT Long Crack Test Results.

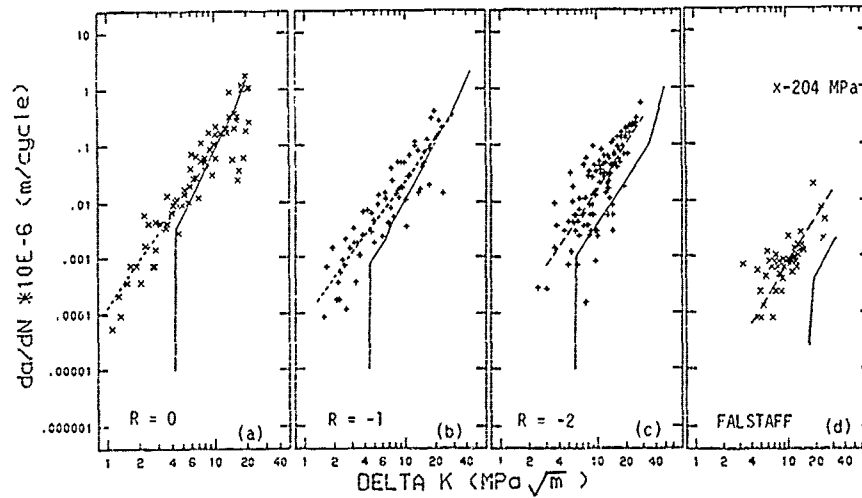


Figure 11 SENT Short Crack Test Results Using the Mode I Analysis.

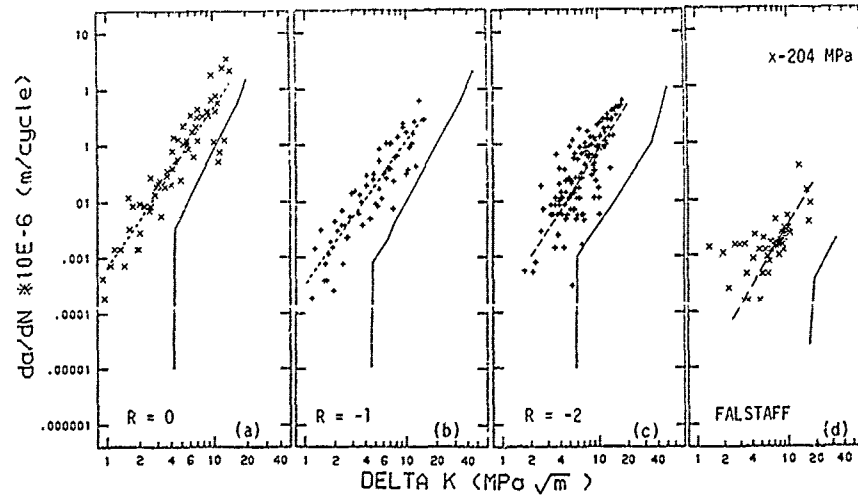


Figure 12 SENT Short Crack Test Results Using the Combined Mode I/Mode II Analysis.

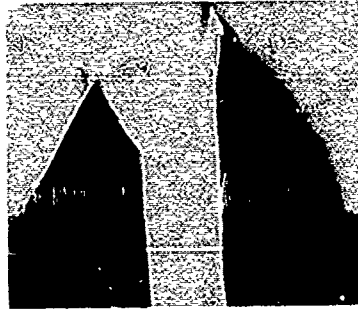


Figure 13 Typical Examples of Aluminum-Lithium Fracture Modes in SENT Specimens.

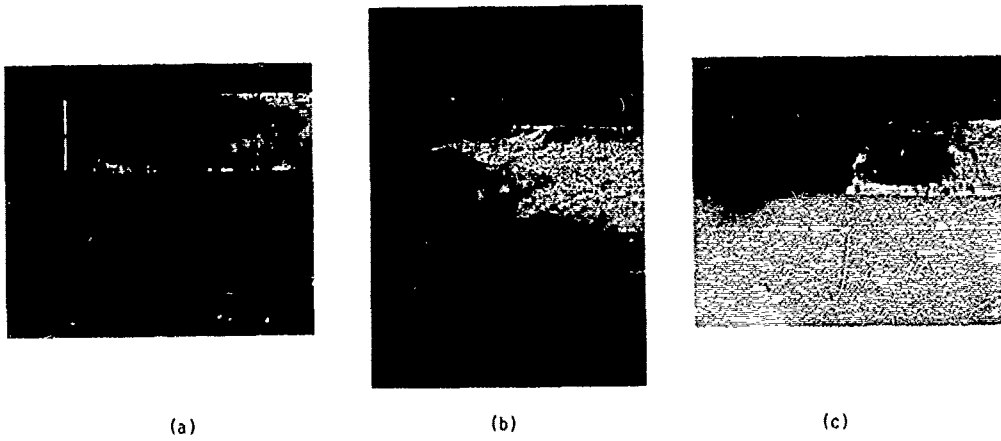


Figure 14 Examples of Typical Aluminum-Lithium Short Crack Fracture Surfaces in SENT Type Specimens.

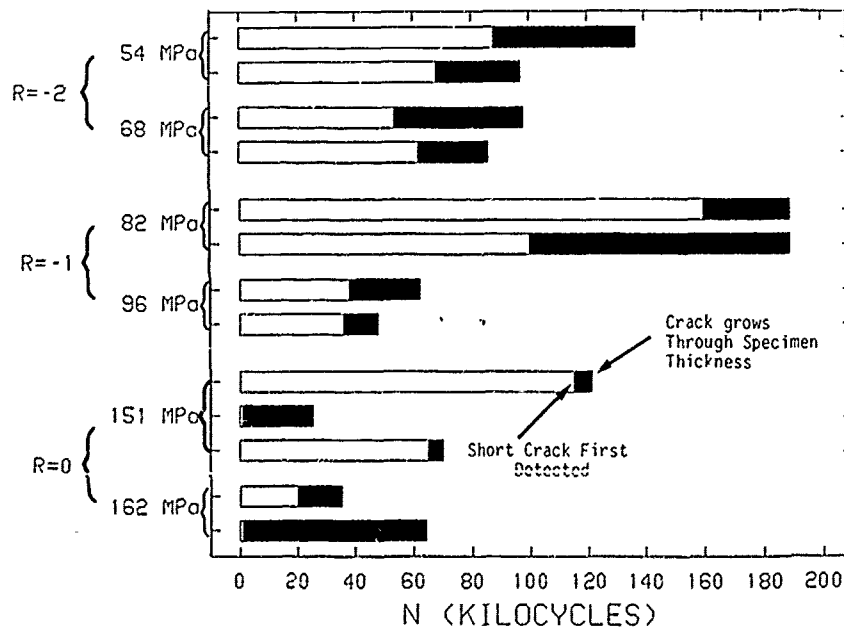


Figure 15 Examples of Typical SENT Specimen Fatigue Lives.

SHORT CRACK BEHAVIOUR IN Al-Li ALLOY 2090

M. Helena Carvalho
 LNETI - Laboratório Nacional de Engenharia e Tecnologia Industrial
 Lumiar
 1699 Lisboa Codex
 PORTUGAL

and

M. de Freitas
 CEMUL - Centro de Mecânica e Materiais da Universidade Técnica de Lisboa (INIC)
 Av. Rovisco Pais
 1096 Lisboa Codex
 PORTUGAL

SUMMARY

Within the AGARD Cooperative Test Programme on the behaviour of short cracks, a common airframe aluminium alloy (2024-T3) has been investigated and the significance of the short crack effect analysed from tests conducted on a single edge notched fatigue specimens of sheet material [1]. The follow up Supplemental Test Programme dealt with other alloys such as Ti6Al4V, steel 4340, Al 7075 and Al-Li 2090, all of them of interest to the aerospace industry. The present report describes the results obtained for the Al-Li alloy at LNETI/CEMUL.

NOMENCLATURE

a, c	crack dimensions
β	angle between a slant crack and the applied stress
da/dN	fatigue crack growth rate
E	Young's modulus
EDX	Energive Dispersive X-ray analysis
F_{sn}	boundary correction factor for a surface crack
F_{cn}	boundary correction factor for a corner crack
ϕ	parametric angle defining a point on crack boundary
G	strain energy release rate
K	stress intensity factor
K_I, K_{II}, K_{III}	stress intensity factors respectively for opening, sliding and tearing modes
ΔK	stress intensity factor range
ΔK_{eq}	equivalent stress intensity factor range ($=\sqrt{EG}$)
K_T	elastic stress concentration factor
L, T, S	longitudinal, long transverse and short transverse directions
N_i	number of cycles corresponding to the first detection of a crack
N_f	number of cycles corresponding to a through thickness crack
ν	Poisson's ratio
Q	shape factor
R	stress ratio ($= S_{min}/S_{max}$)
S	applied stress
S_{max}, S_{min}	maximum and minimum applied stress
ΔS	applied stress range
SEM	Scanning Electron Microscope
$\sigma_{0.2}$	yield stress (0.2 percent offset)
σ	uniform uniaxial tensile stress
t	one half (full) specimen thickness for surface (corner) crack
τ	uniform shear stress

MATERIAL AND SPECIMENS

The material was an Al-Li Alcoa alloy (2090) of nominal composition shown in Table 1, in the peak aged condition T8E41.

The yield stress (0.2% offset) and the ultimate tensile strength were given as 526 MPa and 568 MPa respectively. The constant amplitude fatigue limits were first estimated as 40% higher than those of 2024-T3, but following preliminary experiments were later estimated for ($K_T = 3$) as 160 - 100 - 60 - 50 MPa, respectively for R=0.5, 0, -1, -2 loadings.

The single edge notch tensile (SENT) specimens were of the same type and nominal dimensions as the ones used in the Core Programme (Fig. 2 of Ref. 1). They were prepared by the Air Force Wright Aeronautical Laboratory, USA, and received in the chemically polished condition. The notch was semicircular with a nominal radius of 3.18 mm. The stress concentration factor (K_T) was 3.17 based on gross section stress.

Typical photomicrographs of the 2090-T8E41 sheet are shown in Figs. 1 and 2. The scanning electron micrograph (Fig. 1) shows a slight etch given to the material by the mechanical polishing procedure. Most of the light intermetallic constituents are of the Al₃Cu₂Fe type and tend to be aligned in the rolling direction, some being also rich in Ti (EDX analysis).

The optical micrographs of an etched sample show a pancake type of structure (Fig. 2). The average grain dimension along the short transverse direction (thickness of the Al-Li sheet) is approximately 5 μm . Using only optical metallography it is not quite clear if part of the microstructure consists of grains or subgrains. However, on the basis of back reflection Lauegrams of the sheet that gave non-spotty, well-defined Debye-Scherrer rings, it is believed that the structure is predominantly recrystallized, the "pancake grain" appearance resulting from the small differences in orientation between the fine grains formed within each one of the previous solidification cells of the Al-Li ingot that have become elongated in the rolling direction during processing. The non-uniform intensity of the same Lauegram rings showed the Al-Li sheet to be textured.

EXPERIMENTAL PROCEDURE

Specimens were tested in a servo-hydraulic MTS fatigue machine with bolted "U" grips. Plastic spacers were used between the specimen and the grip jaws, so that the specimens would not crack in the gripping area.

Careful alignment of the testing rig was carried out according to the instructions of the Core Programme (Ref. 1, Annex C). Anti-buckling guides lined with teflon sheets were used for all tests where compressive loads were applied. If a test was interrupted the steady-state minimum load was not lower than the required minimum load in the test. A complete description of the fatigue testing procedure can be found in Ref. 1.

Fatigue tests were conducted under several constant amplitude loading conditions in laboratory air, (average temperature $23 \pm 4^\circ\text{C}$ and relative humidity $65 \pm 3\%$). In all tests the cycle frequencies ranged from 5 to 15 Hz. The real specimen thickness was less than the nominal thickness of 2.3 mm: the actual values (2.14 to 2.19 mm) were used when load conditions were calculated and crack length measurements corrected for replica shrinkage.

The stress ratios, $R = -2, -1$ and 0 were used. At each R ratio the stress levels were selected according to the ultimate strength, yield stress, and estimated fatigue limit. Table 2 shows the selected maximum gross stresses and the local notch root elastic stresses at maximum and minimum applied stress. The highest $R = -2$ and $R=0$ loading conditions cause the notch root to yield respectively under compression and tension. All conditions at $R = -1$ loading are elastic. These conditions were similar to those of the 2024 Core Programme.

A total number of 18 notched specimens was received, the main objective being to obtain surface crack length against cycles data. The specimens were fatigue tested until one continuous crack grew all the way across the notch root thickness and then the specimens were pulled to failure.

Each test was interrupted at regular intervals to allow obtaining the notch surface replica as described in Ref. 1, Annex A. The replica material used was 0.04 mm thick acetyl cellulose and the replicas were sputter coated with a thin layer of Au prior to observation in a SEM at 9 keV. Systematic analysis of several replicas starting from the last one allowed the location of crack initiation. Measurement of the crack length, projected in the horizontal/short transverse direction, was carried out for each replica and registered in the appropriate AGARD chart maps together with the corresponding number of cycles.

RESULTS AND DISCUSSION

From the 15 tests effectively run, only 11 provided meaningful data. For these the number of cycles corresponding to the first detection of a crack (N_i) and to the length of the main crack equalling the thickness of the specimen (N_f) have been represented as a function of the experimental conditions in Fig. 3. The percentage of life corresponding to crack initiation varied from 10 to 70%, with no systematic variation with either S_{max} or ΔS . The number of cracks detected in each test did not seem to vary systematically with either S_{max} or ΔS . The first crack initiated usually halfway between the centre and the edge of the notch. Characteristic length at first detection varied between 5 and 70 μm .

In all tests the last replica showed the through-thickness crack to appear with most of its length as a microscopically straight line at approximately 30° to the rolling/test direction or to have a V shape characterized by the same 30° angle. Fig. 4 shows the trace(s) of the fatigue surface(s) on the notch surface, illustrating a typical example of each case. When secondary cracks occurred, the same macroscopic preferential orientation is evident in them (Figs. 5 and 6). The V configuration can result either from the intersection of two cracks or from the deflection of one crack. Most of the cracks started with an initial horizontal length of 5 to 50 μm but assumed the typical 30° orientation shortly after (Figs. 7 and 8). The "serrations" that sometimes connect different parallel lengths of the cracks do not seem to be always related to short transverse grain size (Fig. 8).

This crack orientation behaviour is thought to be related to the propensity towards planar slip characteristic of some Al-Li alloys [2], in combination with the detected preferred crystallographic orientation. A minimum tensile/yield strength has been

frequently found at 50 to 60° to the working direction in Al-Li alloy mill products and attributed to the presence of a {110} [112] texture [3, 4]. This texture is in fact present in the investigated 2090 alloy sheet as the main component at mid thickness of the sheet and one of three components at 1/4 thickness [5]. If the replicated plane at the root of the notch is assumed to be (111), Fig. 12 shows there are four [110] directions contained in (111) planes which give traces on the replica at 30° to the rolling direction. The {110} [112] texture seems then consistent with crack propagation assisted by favourably oriented (111) [110] slip systems.

The fatigue and the tension fracture surfaces have respectively a transgranular and an intergranular/intersubgranular appearance, illustrated typically by Figs. 9 and 10. Delamination of the pancake structure is evident in Figs. 10 and 11.

For the $R = -2$ and $R = -1$ fatigue tests the fatigue fracture surfaces showed a black powdery deposit, assumed to be fretting debris, defining conchoidal marks. EDX analysis showed this fretting product to be rich in Al and Cu, probably Al Li H₄. These marks corresponded to successive positions of the crack front when the fatigue tests were interrupted to take replicas, and as such they give indications of the crack shape. For each mark the crack depth c and crack length a or $2a$ were measured according to Fig. 13 and a plot of c/a against a/t was obtained for several specimens, as shown in Fig. 14. Despite the poor correlation, an experimental equation of crack-shape c/a against specimen thickness can be obtained as:

$$c/a = 1.18 + 0.51 (a/t) \quad (1)$$

Crack growth data were obtained on length-cycles coordinates and analysed on crack growth rate - stress intensity factor range coordinates. Both projected crack length and actual crack length were considered.

Analysis based on projected crack length

The ΔK equation for a semi-elliptical surface crack located at the centre of the edge notch or for a quarter elliptical corner crack subjected to remote uniform stress can be obtained [1, 6] respectively as:

$$\Delta K = \Delta S \sqrt{\pi a/Q} \cdot F_{Sn} \quad (2)$$

$$\Delta K = \Delta S \sqrt{\pi a/Q} \cdot F_{Cn} \quad (3)$$

where ΔS is full stress range, Q is the shape factor and F_{Sn} and F_{Cn} are the boundary correction factors given in [6].

For both the shape and the boundary correction factors the crack length and crack depth must be known. In the Core Programme c/a was calculated as:

$$c/a = 0.9 - 0.25 (a/t)^2 \quad (4)$$

Figs. 15, 16 and 17 show, respectively for $R = -2$, -1 and 0 , the short crack growth rate against the stress intensity factor range assuming crack depth calculated by Eq.(4) and using the projected crack length, as per instructions. For each loading condition the short crack growth rate data is compared with the available long crack data generated under the same loading conditions on the same material, obtained by a different laboratory [7]. Fig. 18 shows for $R = 0$ the short crack growth rate against the stress intensity factor range assuming the experimentally determined crack depth Eq.(1). Comparison of Figs. 17 and 18 shows that for the same ΔK the crack growth rate is not significantly different and therefore only Eq.(4) was used henceforth.

Analysis based on actual crack length

As mentioned previously, a systematic 30° slant of the cracks was found in all the tests. The remote uniform stress has then a shear stress component in the crack plane and a normal stress component. Mixed mode conditions of crack propagation exist and a simplified model for these conditions was attempted in order to obtain more accurate analysis of the data.

At the points (A) where the crack intersects the notch surface a mixed mode composed of mode I plus mode II exists and at the maximum crack depth (B) a mixed mode composed of mode I plus mode III exists (Fig. 19).

For a slant crack of length $2a$ in a sheet, subjected to a uniform stress σ remote from the crack and making an angle β with the direction of σ (Fig. 20), the stress intensity factors K_I and K_{II} are given [8] by:

$$K_I = \text{sen}^2 \beta \sigma \sqrt{\pi a} \quad (5)$$

$$K_{II} = \text{sen} \beta \cos \beta \sigma \sqrt{\pi a} \quad (6)$$

For an elliptical crack of length $2a$ and depth $2c$ subjected to uniform uniaxial tensile stress σ (Fig. 21) or uniform shear stress τ (Fig. 22), the stress intensity factors are also found in Ref. 8. When the ellipse becomes a circle ($c = a$) they are given by:

$$K_I = 2\sigma \sqrt{a/\pi} \quad (7)$$

$$K_{II} = \frac{4}{\pi(2-\nu)} \cos \phi \cdot \tau \cdot \sqrt{\pi a} \quad (8)$$

$$K_{III} = \frac{4(1-\nu)}{\pi(2-\nu)} \text{sen} \phi \cdot \tau \cdot \sqrt{\pi a} \quad (9)$$

On the basis of Eqs. (2) and (3) an approximate stress intensity factor equation for modes I, II and III, can be calculated for a semi-elliptical surface slant crack at the edge of a notch. It assumes that the boundary correction factors F_{Sn} and F_{cn} are the same for the three modes, that the shape factor Q for modes II and III are the ones in Eqs. (8) and (9) and the applied stresses are taken from Eqs. (5) and (6).

For a surface crack, in the special case when the ellipse becomes a circle, the equations for the three modes are:

$$K_I = 2S \text{sen}^2 \beta \sqrt{a/\pi} \cdot F_{Sn} \quad (10)$$

$$K_{II} = \frac{4}{\pi(2-\nu)} \cdot S \cdot \text{sen} \beta \cos \beta \sqrt{\pi a} \cdot F_{Sn} \quad (11)$$

$$K_{III} = \frac{4(1-\nu)}{\pi(2-\nu)} \cdot S \cdot \text{sen} \beta \cdot \cos \beta \sqrt{\pi a} \cdot F_{Sn} \quad (12)$$

and the strain energy release rate G is, for plane stress conditions:

$$G = \frac{1}{E} [K_I^2 + K_{II}^2 + (1-\nu) K_{III}^2] \quad (13)$$

Fig. 23 compares crack growth rate against stress intensity factor range for modes I, II and III, for a slant surface crack growing under $R = -1$, $S_{max} = 80$ MPa conditions. The greatest contribution to the total ΔK can be seen as being given by mode II.

For the same surface crack, Fig. 24 compares crack growth rate against E.G. values calculated as $K_I^2 + K_{II}^2$ (at points A) and $K_I^2 + (1+\nu) K_{III}^2$ (at maximum crack depth, point B). As can be seen, for a given crack length the E.G. value at point B is smaller than at point A, so plots of ΔK against da/dN were obtained only for these points A and using a $\Delta K = \sqrt{E.G.}$ to compare with long crack data [7].

Such plots are shown in Figs. 25, 26 and 27 respectively for $R = -2$, $R = -1$ and $R = 0$ loading conditions. Direct comparison with Figs. 15, 16 and 17 shows that for a given ΔK a greater short crack growth rate is obtained with this mixed mode analysis, owing mainly to the 30° crack slant orientation.

The actual short crack effect will then be greater than any detected on the basis of the Eqs. (2) and (3) using the projected crack length.

CONCLUSIONS

The present study of the crack propagation behaviour of short naturally occurring cracks in an Al-Li alloy (2090 - T8E41) leads to the following conclusions:

1. A 30° slant cracking pattern was obtained in all tests. This behaviour is quite different from the one found for the 2024-T3 material tested in the AGARD Core Programme.
2. The systematic crack orientation is probably related to the texture of the Al-Li sheet.
3. Using the Core Programme type of analysis and the crack projected lengths:
 - 3.1. At equal nominal ΔK levels short crack growth rates were definitely faster

than long crack growth rates for constant amplitude loadings $R = -2$ and $R = -1$. For $R = -2$, short cracks grew faster at higher stress levels for the same ΔK .

- 3.2. For $R = 0$, short crack growth rate was only slightly faster than long crack growth rate for equivalent ΔK .
- 3.3. For $R = -2$, $R = -1$ and $R = 0$ short cracks grew below long crack threshold ΔK_{th} .
4. The attempted mixed mode analysis shows the enhancement of the short crack effect described in conclusion 3.

ACKNOWLEDGEMENTS

The X-ray diffraction experiments were conducted at the Centro de Cristalografia e Mineralogia (Instituto de Investigação Científica Tropical). Thanks are due to M. Ondina Figueiredo (IICT) and H. Carvalhinhos (LNETI) for helpful discussions.

REFERENCES

1. Newman, J. C. Jr. and Edwards, P. R.: Short Crack Growth Behaviour in an Aluminium Alloy - An AGARD Cooperative Test Programme, AGARD Report No. 732, 1988.
2. Lavernia, E. J. and Grant, N. J.: Journal of Materials Science, 22 (1987), 1521-1529.
3. Smith, A. F.: Metals and Materials, Aug. 1987, 438-444.
4. Gregson, P. J. and Flower, H. M.: Acta Metallurgica, 33 (1985), 527-537.
5. Cook, R.: this AGARD report.
6. Swain, H. H. and Newman, J. C. Jr.: AGARD Conference Proceedings No. 376, 1984, 12.1 - 12.17.
7. Mazur, C.: this AGARD report.
8. Rook, D. P. and Cartwright, D. J.: Compendium of Stress Intensity Factors, Her Majesty's Stationery Office, London, 1976.

Table 1 - Chemical composition of 2090-T8E41

Element	Percent
	Volume
Copper	2.4 - 3.0
Lithium	1.9 - 2.6
Magnesium	0.25
Zirconium	0.10
Iron	0.12
Manganese	0.05
Chromium	0.05
Titanium	0.15
Others	0.05 max. each 0.15 max. total
Aluminium	Balance

Table 2 - Local notch-root elastic stresses

Loading	Maximum	$\frac{K_T S_{max}}{\sigma_{0.2}}$	$\frac{K_T S_{min}}{\sigma_{0.2}}$
	Gross Stress S_{max} (MPa)		
R = -2	90	0.54	-1.08
	70	0.42	-0.84
	55	0.33	-0.66
R = -1	105	0.63	-0.63
	100	0.60	-0.60
	90	0.54	-0.54
	80	0.48	-0.48
R = 0	170	1.02	0
	155	0.93	0
	150	0.90	0
	140	0.84	0

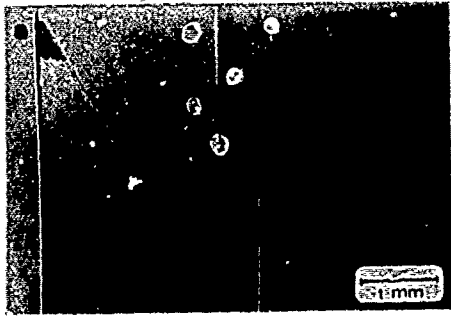


Figure 4 - SEM photographs of halves of fatigued specimens tested at: a) $R=-1$, $S_{max}=70$ MPa; b) $R=0$, $S_{max}=170$ MPa. Electron beam parallel to long transverse direction

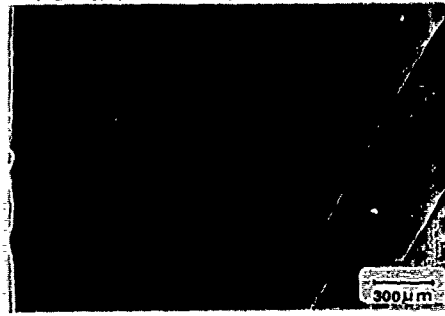


Figure 5 - Replica at 103,000 cycles for the specimen tested at $R=-2$, $S_{max}=55$ MPa



Figure 6 - Replica at 8,800 cycles for the specimen tested at $R=-2$, $S_{max}=90$ MPa



Figure 7 - Replica at 75,000 cycles for the specimen tested at $R=-2$, $S_{max}=110$ MPa. Arrow indicates crack initiation site

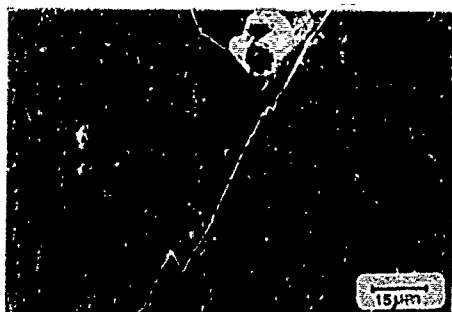


Figure 8 - Replica at 75,000 cycles for the specimen tested at $R=-1$, $S_{max}=80$ MPa. Arrow indicates crack initiation site

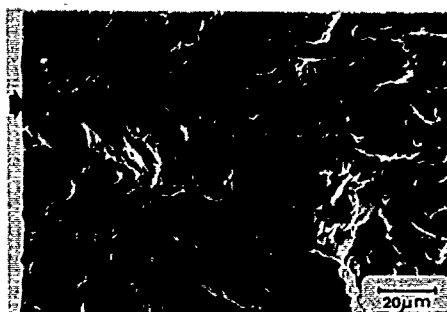


Figure 9 - Typical fatigue fracture surface ($R=0$, $S_{max}=170$ MPa). Arrow indicates crack initiation site. Electron beam parallel to tension axis

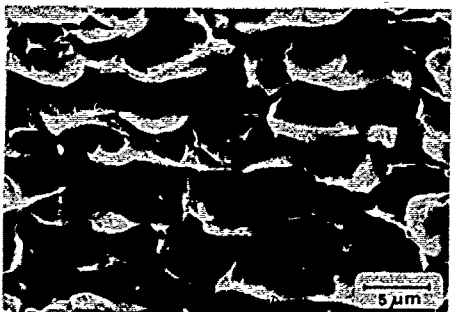


Figure 10 - Typical tension fracture surface ($R=-1$, $S_{max}=80$ MPa). Electron beam parallel to tension axis



Figure 11 - Typical tension fracture surface ($R=-1$, $S_{max}=80$ MPa). Electron beam normal to tension axis

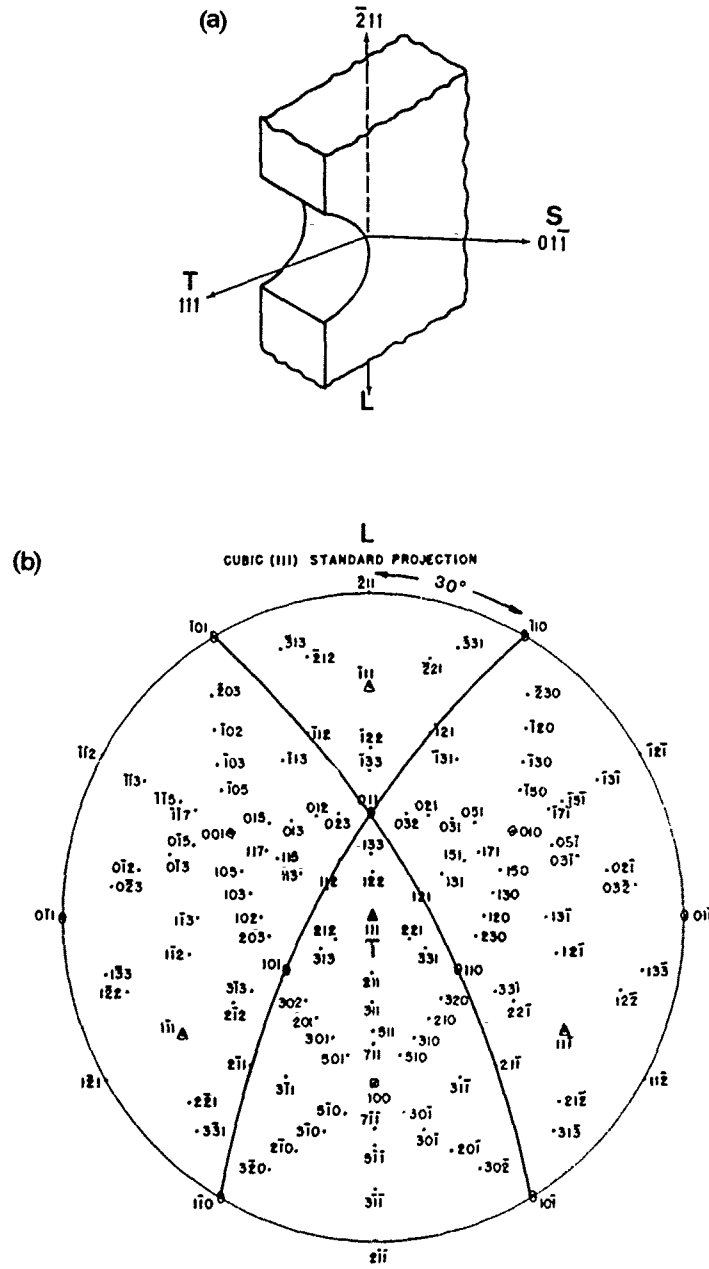


Figure 12 - a) Notch surface orientation assuming $\{011\} \langle 211 \rangle$ texture.
 b) (111) standard projection showing 30° angles between longitudinal direction and the traces of two (111) planes

10. 11. 12. 13. 14. 15. 16. 17. 18. 19. 20. 21. 22. 23. 24. 25. 26. 27. 28. 29. 30. 31. 32. 33. 34. 35. 36. 37. 38. 39. 40. 41. 42. 43. 44. 45. 46. 47. 48. 49. 50. 51. 52. 53. 54. 55. 56. 57. 58. 59. 60. 61. 62. 63. 64. 65. 66. 67. 68. 69. 70. 71. 72. 73. 74. 75. 76. 77. 78. 79. 80. 81. 82. 83. 84. 85. 86. 87. 88. 89. 90. 91. 92. 93. 94. 95. 96. 97. 98. 99. 100. 101. 102. 103. 104. 105. 106. 107. 108. 109. 110. 111. 112. 113. 114. 115. 116. 117. 118. 119. 120. 121. 122. 123. 124. 125. 126. 127. 128. 129. 130. 131. 132. 133. 134. 135. 136. 137. 138. 139. 140. 141. 142. 143. 144. 145. 146. 147. 148. 149. 150. 151. 152. 153. 154. 155. 156. 157. 158. 159. 160. 161. 162. 163. 164. 165. 166. 167. 168. 169. 170. 171. 172. 173. 174. 175. 176. 177. 178. 179. 180. 181. 182. 183. 184. 185. 186. 187. 188. 189. 190. 191. 192. 193. 194. 195. 196. 197. 198. 199. 200. 201. 202. 203. 204. 205. 206. 207. 208. 209. 210. 211. 212. 213. 214. 215. 216. 217. 218. 219. 220. 221. 222. 223. 224. 225. 226. 227. 228. 229. 230. 231. 232. 233. 234. 235. 236. 237. 238. 239. 240. 241. 242. 243. 244. 245. 246. 247. 248. 249. 250. 251. 252. 253. 254. 255. 256. 257. 258. 259. 260. 261. 262. 263. 264. 265. 266. 267. 268. 269. 270. 271. 272. 273. 274. 275. 276. 277. 278. 279. 280. 281. 282. 283. 284. 285. 286. 287. 288. 289. 290. 291. 292. 293. 294. 295. 296. 297. 298. 299. 300. 301. 302. 303. 304. 305. 306. 307. 308. 309. 310. 311. 312. 313. 314. 315. 316. 317. 318. 319. 320. 321. 322. 323. 324. 325. 326. 327. 328. 329. 330. 331. 332. 333. 334. 335. 336. 337. 338. 339. 340. 341. 342. 343. 344. 345. 346. 347. 348. 349. 350. 351. 352. 353. 354. 355. 356. 357. 358. 359. 360. 361. 362. 363. 364. 365. 366. 367. 368. 369. 370. 371. 372. 373. 374. 375. 376. 377. 378. 379. 380. 381. 382. 383. 384. 385. 386. 387. 388. 389. 390. 391. 392. 393. 394. 395. 396. 397. 398. 399. 400. 401. 402. 403. 404. 405. 406. 407. 408. 409. 410. 411. 412. 413. 414. 415. 416. 417. 418. 419. 420. 421. 422. 423. 424. 425. 426. 427. 428. 429. 430. 431. 432. 433. 434. 435. 436. 437. 438. 439. 440. 441. 442. 443. 444. 445. 446. 447. 448. 449. 450. 451. 452. 453. 454. 455. 456. 457. 458. 459. 460. 461. 462. 463. 464. 465. 466. 467. 468. 469. 470. 471. 472. 473. 474. 475. 476. 477. 478. 479. 480. 481. 482. 483. 484. 485. 486. 487. 488. 489. 490. 491. 492. 493. 494. 495. 496. 497. 498. 499. 500. 501. 502. 503. 504. 505. 506. 507. 508. 509. 510. 511. 512. 513. 514. 515. 516. 517. 518. 519. 520. 521. 522. 523. 524. 525. 526. 527. 528. 529. 530. 531. 532. 533. 534. 535. 536. 537. 538. 539. 540. 541. 542. 543. 544. 545. 546. 547. 548. 549. 550. 551. 552. 553. 554. 555. 556. 557. 558. 559. 560. 561. 562. 563. 564. 565. 566. 567. 568. 569. 570. 571. 572. 573. 574. 575. 576. 577. 578. 579. 580. 581. 582. 583. 584. 585. 586. 587. 588. 589. 590. 591. 592. 593. 594. 595. 596. 597. 598. 599. 600. 601. 602. 603. 604. 605. 606. 607. 608. 609. 610. 611. 612. 613. 614. 615. 616. 617. 618. 619. 620. 621. 622. 623. 624. 625. 626. 627. 628. 629. 630. 631. 632. 633. 634. 635. 636. 637. 638. 639. 640. 641. 642. 643. 644. 645. 646. 647. 648. 649. 650. 651. 652. 653. 654. 655. 656. 657. 658. 659. 660. 661. 662. 663. 664. 665. 666. 667. 668. 669. 670. 671. 672. 673. 674. 675. 676. 677. 678. 679. 680. 681. 682. 683. 684. 685. 686. 687. 688. 689. 690. 691. 692. 693. 694. 695. 696. 697. 698. 699. 700. 701. 702. 703. 704. 705. 706. 707. 708. 709. 710. 711. 712. 713. 714. 715. 716. 717. 718. 719. 720. 721. 722. 723. 724. 725. 726. 727. 728. 729. 730. 731. 732. 733. 734. 735. 736. 737. 738. 739. 740. 741. 742. 743. 744. 745. 746. 747. 748. 749. 750. 751. 752. 753. 754. 755. 756. 757. 758. 759. 760. 761. 762. 763. 764. 765. 766. 767. 768. 769. 770. 771. 772. 773. 774. 775. 776. 777. 778. 779. 780. 781. 782. 783. 784. 785. 786. 787. 788. 789. 790. 791. 792. 793. 794. 795. 796. 797. 798. 799. 800. 801. 802. 803. 804. 805. 806. 807. 808. 809. 810. 811. 812. 813. 814. 815. 816. 817. 818. 819. 820. 821. 822. 823. 824. 825. 826. 827. 828. 829. 830. 831. 832. 833. 834. 835. 836. 837. 838. 839. 840. 841. 842. 843. 844. 845. 846. 847. 848. 849. 850. 851. 852. 853. 854. 855. 856. 857. 858. 859. 860. 861. 862. 863. 864. 865. 866. 867. 868. 869. 870. 871. 872. 873. 874. 875. 876. 877. 878. 879. 880. 881. 882. 883. 884. 885. 886. 887. 888. 889. 890. 891. 892. 893. 894. 895. 896. 897. 898. 899. 900. 901. 902. 903. 904. 905. 906. 907. 908. 909. 910. 911. 912. 913. 914. 915. 916. 917. 918. 919. 920. 921. 922. 923. 924. 925. 926. 927. 928. 929. 930. 931. 932. 933. 934. 935. 936. 937. 938. 939. 940. 941. 942. 943. 944. 945. 946. 947. 948. 949. 950. 951. 952. 953. 954. 955. 956. 957. 958. 959. 960. 961. 962. 963. 964. 965. 966. 967. 968. 969. 970. 971. 972. 973. 974. 975. 976. 977. 978. 979. 980. 981. 982. 983. 984. 985. 986. 987. 988. 989. 990. 991. 992. 993. 994. 995. 996. 997. 998. 999. 1000.

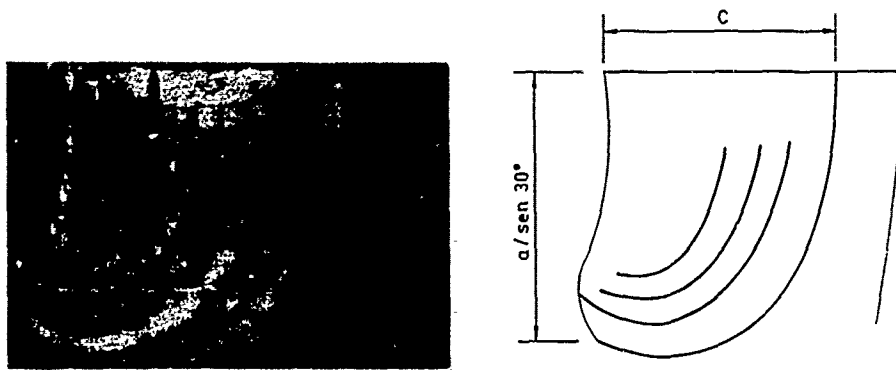


Figure 13 - Optical macrograph of fatigue fracture surface of specimen tested at $R = -1$, $S_{max} = 90$ MPa

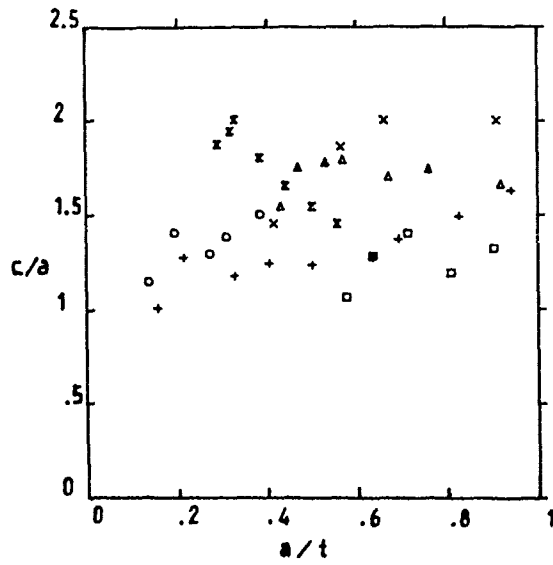


Figure 14 - Crack shape experimental measurements from specimens under $R = -1$ and $R = -2$ loading

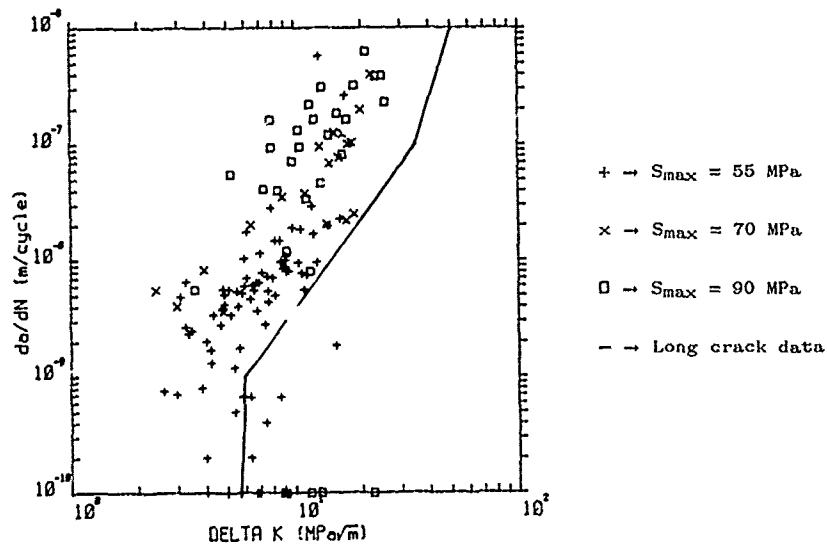


Figure 15 - Crack growth rate against stress intensity factor range, based on projected crack length for $R = -2$ loading, assuming $c/a = 0.9-0.25$ $(a/t)^2$

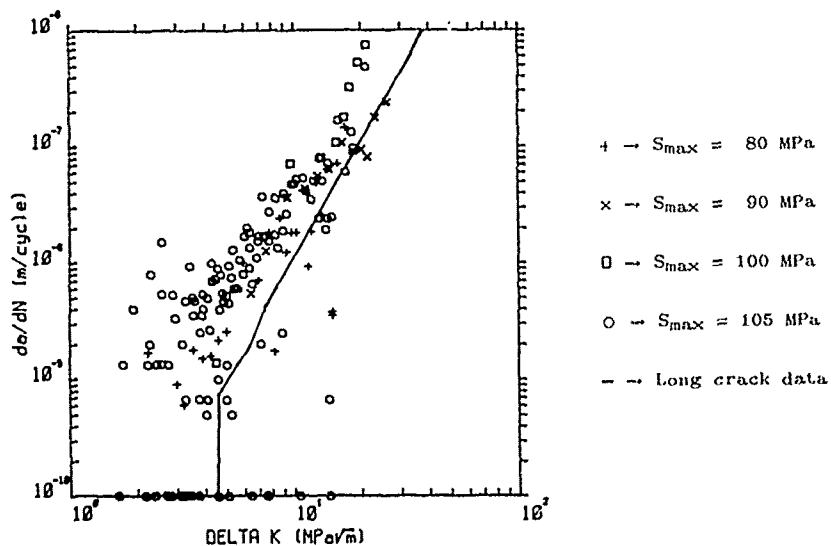


Figure 16 - Crack growth rate against stress intensity factor range, based on projected crack length for $R = -1$ loading, assuming $c/a = 0.9-0.25$ $(a/t)^2$

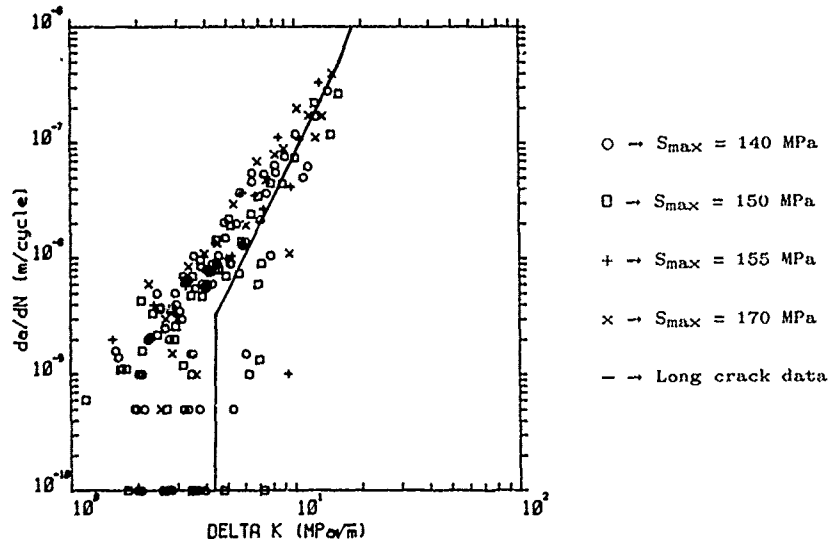


Figure 17 - Crack growth rate against stress intensity factor range, based on projected crack length for $R = 0$ loading, assuming $c/a = 0.9-0.25$ (a/t)

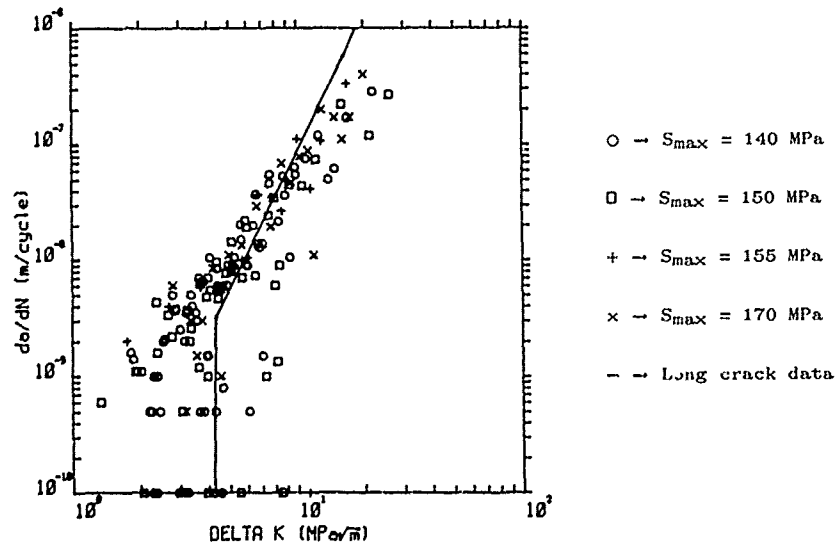


Figure 18 - Crack growth rate against stress intensity factor range, based on projected crack length for $R = 0$ loading, assuming $c/a = 1.18+0.51$ a/t

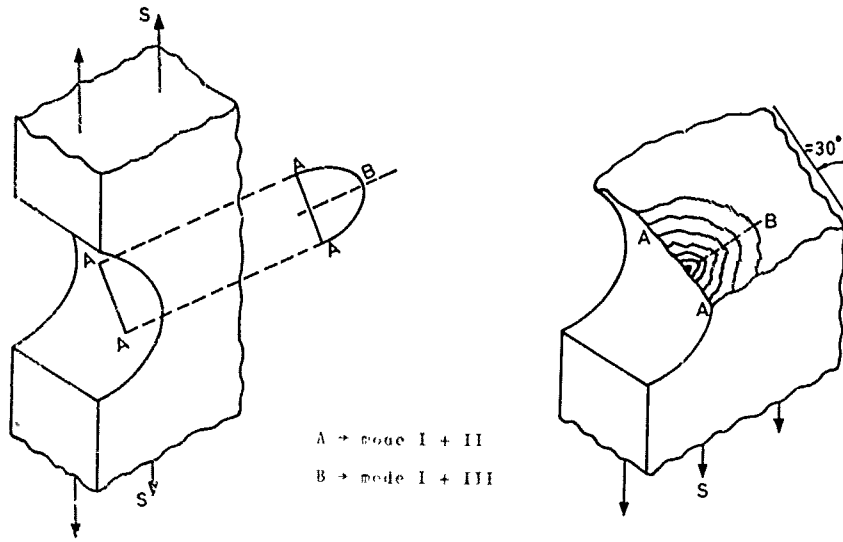


Figure 19 - Model for mixed mode crack growth

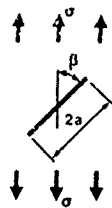


Figure 20
Slant crack subjected to a uniform uniaxial tensile stress

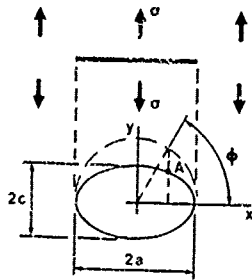


Figure 21
Plane elliptical crack subjected to a uniform uniaxial tensile stress

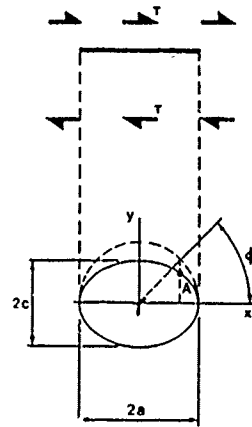


Figure 22
Plane elliptical crack subjected to a uniform shear stress

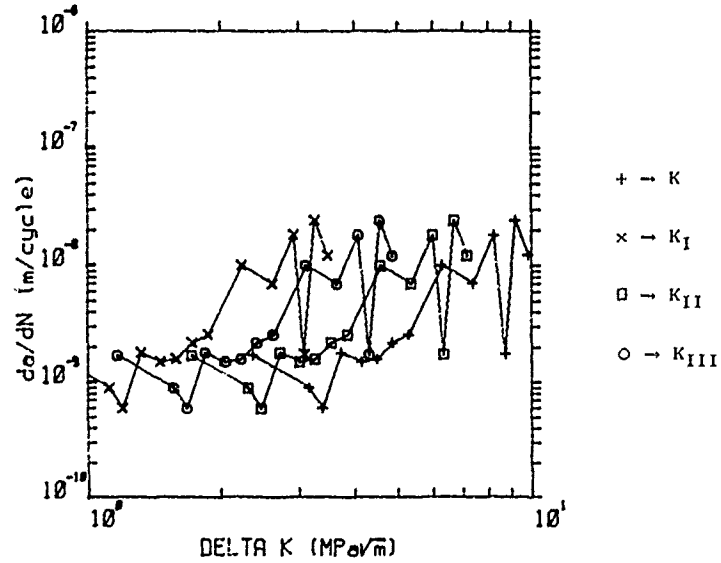


Figure 23 - Stress intensity factor contribution from modes I, II and III
 ($R = -1$, $S_{max} = 80$ MPa)

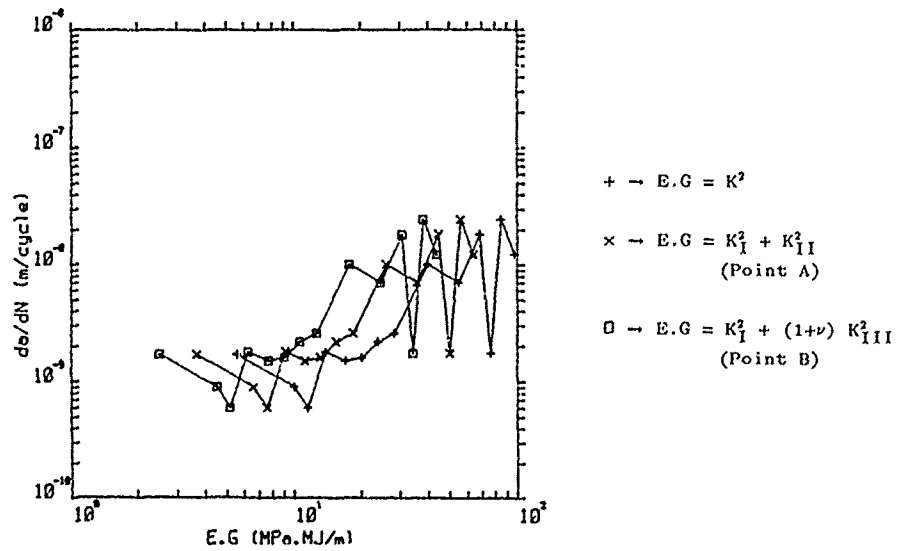


Figure 24 - Comparison of strain energy release rate G for points A and B
 (see Fig. 19)

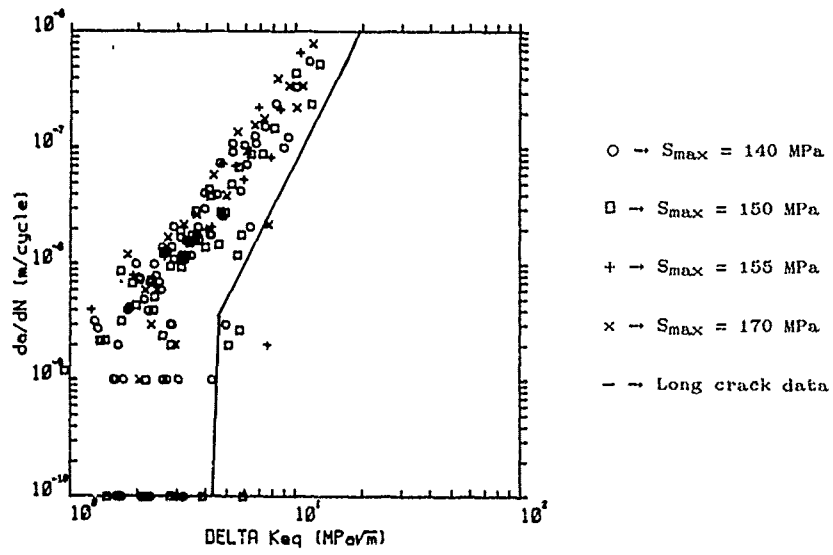


Figure 27 - Crack growth rate against equivalent stress intensity factor range, for $R = 0$ loading, assuming $c/a = 0.9 - 0.25 (a/t)^2$

CRACK BEHAVIOUR OF 2024-T3, 2090-T8E41 AND 7075-T6 UNDER CONSTANT AMPLITUDE AND
DIFFERENT TYPES OF VARIABLE AMPLITUDE LOADING, ESPECIALLY GAUSSIAN LOADING

H. Nowack, K.H. Trautmann, J. Strunck
Institute for Materials Research
Deutsche Forschungsanstalt für Luft- und Raumfahrt (DLR)
D-5000 Köln 90
FRG

SUMMARY

The present report describes the contribution of the DFVLR (DLR) to the AGARD cooperative test programme on short and long cracks. Within the core programme tests on 2024-T3 single edge notch (SENT) specimens were performed with constant amplitude, FALSTAFF, and Gaussian loading. Within the supplemental programme short and long crack tests on the aluminium-lithium alloy 2090-T8E41 were carried out with Gaussian loading and some further exploratory long crack tests with the conventional high strength aluminium alloy 7075-T6 were added. The long crack tests were performed on center crack (CCT-)specimens.

From the investigations it came out that 2024-T3 and 2090-T8E41 showed the so-called short crack effect. This effect is mainly attributed to the influence of crack closure.

The microscopical behaviour of 2024-T3 and 2090-T8E41 was different. At 2024-T3 several cracks initiated, normally as center cracks, whereas at 2090-T8E41 corner cracks were the predominant cracks.

In the long crack stage 2090-T8E41 turned out to be not such damage tolerant as expected.

1. INTRODUCTION

The economical life of airspace constructions can be extended if parts of the short crack stage are also included into the fatigue analysis. This requires a thorough knowledge of the short crack behaviour under service loading conditions. More specifically, two essential prerequisites have to be fulfilled: The length of the short cracks must be reliably detectable by NDI methods and the propagation behaviour of the cracks must be quantitatively known. The AGARD collaborative test programmes on short cracks had been initiated to investigate mainly the short crack stage but also the long crack stage for comparison by the combined effort of numerous fatigue laboratories which all used specimens with a same shape and manufactured from one batch, the same damage evaluation technique and the same selected constant amplitude and variable amplitude histories. An essential question was, if the so-called short crack effect (faster crack propagation than expected from long crack data and a different threshold value) could be observed on the materials investigated.

The short crack effect is not well understood until now from a physical viewpoint. Further on, analytical tools have to be available to predict the short crack behaviour adequately.

The core programme at DLR concentrated on the conventional 2024-T3 alloy. Within the supplemental programme the 2090-T8E41 was investigated in the short crack and in the long crack stage under a Gaussian loading history.

One essential aspect of the AGARD programme is that the advanced crack propagation prediction model by J. Newman [1] is available and used by the author to predict the short and long crack behaviour as observed in the experimental investigations of the participants of the programme.

2. EXPERIMENTS

2.1 Test Programme

Table 1 gives a survey of all tests which were performed by DLR in the core and in the supplemental programme. In the long crack stage some exploratory tests on the conventional high strength aluminium alloy 7075-T6 were also included. (The workloads of the participants of the AGARD programme are given in Tables 1a and 1b in the Appendix.)

2.2 Specimens and Material

All short crack tests were performed on SENT specimens and the long crack tests on CCT specimens. (The shape of the SENT and of the CCT specimens is shown in Figures 1a and 2b in the Appendix.)

The chemical composition and the mechanical properties of the alloys investigated are given in Tables 2a and 2b in the Appendix. (Because 2090-T8E41 is a high strength type of alloy, it was expected that this alloy compares more to 7075-T6 rather than to 2024-T3.)

2.3 Experimental Techniques

The initiation and propagation behaviour of short cracks appears complex, because multiple crack initiation often takes place. During their further growth the short cracks interact with each other. A special mapping procedure was used to document the short crack behaviour. On a (graphical) sketch of the notch surface of the SENT specimens the approximate locations, shapes and sizes of the short cracks were registered at certain cycle numbers during the tests. (An example of the mapping procedure is shown in Figure 2 in the

Appendix.) All data which were experimentally determined were collected by the coordinators of the AGARD programme, J. Newman, NASA, and P.R. Edwards, RAE, evaluated using a uniform analysis scheme, and distributed later on to all participants of the AGARD programme.

The measurements of the short cracks could be performed in a different manner, either by a foil replication technique or by direct optical observations. DLR applied both techniques.

2.4 Loading Histories

In the programme constant amplitude loading, FALSTAFF and a Gaussian loading history were applied. These histories are described in more detail in [1]. Because the Gaussian history was extensively used in the present investigation, some further information shall be given here.

Gaussian histories are the result of the combined action of a large number of sources/excitations, each of which are statistically normally distributed. If the cumulative frequency of the level crossings is considered, its envelope shows the typical bell shape. The ends of the bell shape curve are cut off at some certain value, very often at a value of 5.3 times the R.M.S.-value of the history. The distribution functions of the maxima and of the minima of a Gaussian history are Raleigh distributions.

Gaussian histories are completely described by two of the following parameters: Power spectral density function, irregularity factor, clipping ratio, level crossing spectrum, extreme value distributions, etc.

In practice, three typical Gaussian histories with irregularity factors around 0.9, 0.7, and 0.3 are of importance. In the present study a Gaussian history with an irregularity factor of 0.99 has been chosen. (The level crossing spectrum and a cut-out of the history are shown in Figure 3 in the Appendix.)

In contrast to the flight loading history FALSTAFF, the Gaussian history does not contain any induced loading events as air-to-ground cycles. In the course of the Gaussian history high peak loads occur at certain instants. These have a significant effect on the observed crack growth behaviour.

2.5 Testing Equipment

The tests at DLR were performed on a computer controlled servohydraulic testing machine together with the extreme value correction software ECOR[®] (Schenck AG), which guaranteed a sufficiently high accuracy, especially in the variable amplitude tests. This has also been confirmed by an AGARD inspection, which used an independent measuring and data acquisition device.

3. EXPERIMENTAL RESULTS

3.1 Short Crack Stage

The results of the tests with 2024-T3 with constant amplitude loading, FALSTAFF loading and Gaussian loading, which were run in the core programme, are presented together with the results of the other laboratories in [1]. (They are also reproduced for constant amplitude loading in Figure 4, for FALSTAFF loading in Figure 5, and for Gaussian loading in Figure 6 in the Appendix.)

Only those short crack data were considered, where no interactions of the short cracks did occur, following the non-interaction criteria as specified in [1]. In order to enable comparisons between the short crack and the long crack behaviour, the behaviour of long cracks is also included in the figures.

The short crack behaviour at the notch surface of 2090-T8E41 under Gaussian loading is presented in Figure 2. In the figure the surface crack length is plotted versus the cycle number. In contrast to 2024-T3, which was investigated within the core programme, the number of short cracks which were initiated was considerably lower, except in one case (specimen No. 1702), where four cracks started to grow. It is interesting to note that in this case those cracks which started early to grow did not form the final through crack at the end of the short crack stage. Since the number of short cracks at 2090-T8E41 was small, they grew independently of each other and there were only very few data points which had to be rejected, because they did not fulfil the non-interaction criterion.

Figure 3 gives a further overview of the short crack stage. In the figure the cycle numbers are given, where the first cracks were detected, the length of the cracks at this instant, and the cycle numbers, where the longest short crack penetrated the whole bore of the notch.

In Figures 4a and 4b the cycle numbers which were spent in the short crack stage between crack lengths of 0.25 mm and 0.5 mm, respectively, until the crack expanded across the bore of the notch are shown. From the figure it can be seen that there were no further significant variations in the behaviour after the short cracks had started to grow.

Figure 5 shows the propagation data of the short cracks under Gaussian loading in a da/dN versus ΔK format, whereby the ΔK values were determined after J. Newman's proposal in [1]. As the stresses for the calculation of the ΔK values the stress variations between the maximum and the minimum stress values within the Gaussian sequence were taken. Since the loading was symmetric around zero, the stress amplitudes are given in the figures.

3.2 Long Crack Behaviour

The long crack-behaviour of 2090-T8E41 under Gaussian loading with a maximum stress of 150 N/mm² is given in Figure 6. Since the number of specimens which were available for the long crack tests was rather limited, one other specimen was loaded at S_{max} values of 120 N/mm², 150 N/mm², and 180 N/mm² within one test in order to get some overview (compare Table 1). In Figure 6 that part of the sequence with S_{max} of

150 N/mm² is only shown. In the figure some regular variations of the da/dN versus N data can be observed. These are caused by the non-uniform distribution of the higher peak loads in the course of the Gaussian sequence. At moderate crack lengths high peak loads cause retardation in crack propagation. Later on, when the crack length has become large and the load carrying capacity of the specimen net section is significantly reduced, the peak loads cause unstable crack growth as soon as the critical stress intensity factor of the material is reached. Figure 7 shows the long crack behaviour of 2090-T8E41 in terms of da/dN versus ΔK . These data include those parts of the loading history as applied at specimen B1305 with S_{max} values of 120 N/mm² and 180 N/mm².

In order to get some insight, how the conventional high strength aluminium alloy 7075-T6 compares to 2090-T8E41, two exploratory tests on 7075-T6 were performed with a S_{max} value of the Gaussian sequence of 150 N/mm². The crack propagation direction was longitudinal (specimen H20) and transverse (specimen H21) to the loading direction. Although the test results were too few to draw any more general conclusions, there is some tendency that the cracks propagate a little slower at 2090-T8E41, but become critical at a smaller crack length than at 7075-T6.

Figure 7 shows the da/dN versus ΔK behaviour for 2090-T8E41 and for 7075-T6. It can be seen that both data fall within one scatter band in the range of medium da/dN versus ΔK values. At higher da/dN versus ΔK values 2090-T8E41 shows the tendency to develop higher da/dN rates as already mentioned before.

3.3 Comparison of the Short and Long Crack Data

In Figure 8 all short and long crack data of 2090-T8E41 are plotted into one da/dN versus ΔK diagramme.

4. EVALUATION AND DISCUSSION OF EXPERIMENTAL RESULTS

4.1 Short Crack Stage

2024-T3 showed the so-called short crack effect in the core programme and it was of interest if 2090-T8E41 behaved in a similar manner. Especially the following two phenomena had been observed at 2024-T3:

- the da/dN data of the short cracks followed under Gaussian loading roughly that slope as given by the long crack da/dN versus ΔK data at medium crack rates
- the absolute da/dN values were in their trends somewhat higher than the da/dN values from the long crack tests if plotted against the same ΔK values

Figure 8 shows that the trend for 2090-T8E41 was similar.

One reason for the existence of such a short crack effect which is quite often mentioned is a difference in the crack closure behaviour between short and long cracks. There exist indeed more recent investigation results which indicate that, if closure is avoided in the long crack tests by the choice of a suitable testing procedure (high constant K_{max} value in the tests and increasing the K_{min} value in the course of the tests [2,3] or two-step tests with a same high K_{max} value in both steps and a significantly lower ΔK value in the second step [4]), the corresponding long crack da/dN versus ΔK curves tend to fall considerably closer to the da/dN versus ΔK curves of the short cracks. Because the crack surfaces, where loads can be transferred, are much smaller for short cracks than for long cracks, it is reasonable to assume that crack closure plays a less significant part for short cracks. If, in addition, compression loads are included in a loading history (as it is the case under Gaussian loading), the crack surfaces which are formed during the early growth of short cracks and which are still very small may be easily reformed by the compression loads. That means that the crack closure effect is further reduced, especially at the beginning of the short crack stage. 2090-T8E41 also shows another microscopical phenomenon (which will be described in more detail later on): The short cracks actually start to grow at 45° to the loading direction. Under such circumstances crack closure is less important.

Summarizing, it is concluded that crack closure is seen as a most significant reason for the observed differences in the short and long crack behaviour.

Another important point is in how far ΔK values based on linear elastic fracture mechanics can be used to represent the short crack behaviour. Although tests with Gaussian loading are less suitable to answer this question than constant amplitude tests, the authors tend to follow the statement by J. Newman in [1] that the present knowledge is not sufficient to define fixed limits for the application of the tools of linear elastic fracture mechanics to represent short crack data. Numerous investigations with long cracks have shown that the range where the stress intensity factor could be used to represent crack data was much larger than previously expected.

The da/dN data under Gaussian loading were plotted against a ΔK value based on the variation between the maximum and the minimum stress in the Gaussian history. This way of representing the crack propagation cannot be satisfactory, if the following two aspects are considered: The first aspect is that the ΔK values of the majority of the cycles in the Gaussian history are much smaller. The second is that, even if the adequate individual cycle-by-cycle da/dN versus ΔK values could be determined, there are further load sequence effects on crack propagation, which lead to a deviation from a linear crack propagation. One possibility to explicitly work out such sequence effects is an indirect one: to apply an advanced crack propagation prediction model where the main causes of sequence effects as they are known today are considered, as for example, the FASTRAN model by J. Newman [1], and to evaluate how the predictions of this model compare to the actual experimental behaviour.

Besides phenomenological and fracture mechanics aspects as they were mentioned before, the microscopical crack propagation mechanism is of interest, as well. The following main differences between 2024-T3 and 2090-T8E41 were observed: At 2024-T3 usually more short cracks were initiated at the notch of the SENT specimen than at 2090-T8E41. At 2024-T3 most of the cracks started as center cracks. At 2090-T8E41 center cracks initiated less frequently. In that case where a center crack started first, also other center cracks

were initiated. The important cracks, however, were corner cracks. They predominantly controlled the short crack stage. Even in that case where the first crack was a center crack, the crack which became dominant later on was again one which interfered with the corner of the notch. Because at 2024-T3 a large number of short cracks were initiated, the non-interaction criterion had a higher significance for this alloy. Considerably more data points had to be rejected than for 2090-T8E41. Another difference between 2024-T3 and 2090-T8E41 which was observed was that at the later alloy a strong tendency to form cracks at an angle of 45° to the loading direction was present. This is shown in Figure 9. (Although one crack only is to be seen at 2024-T3, there were several more small cracks which did not become visible due to imperfections in the illumination and due to the unevenness of the specimen surface.) The tendency of 2090-T8E41 to form cracks at 45° may be seen as a consequence of the strong texture of the material due to the TMT applied.

4.2 Long Crack Stage

In the da/dN versus ΔK data in Figure 7 the typical bending down of the data towards a threshold value does not become visible. A reason is that the data were integrally determined over a large number of cycles which are quite different in their magnitude. Such a procedure is not suitable to reveal the crack extension also during small load variations. All details of the crack propagation process including the load sequence effects remain hidden. In order to get at least some information, comparisons with the predictions of advanced crack propagation prediction models can be performed. Because the assumptions about the mechanics environments and the other operating mechanisms in the model are known, the comparison gives valuable information about most significant influences and controlling parameters regarding long crack propagation.

In Figure 6 the phenomenological long crack data of 2090-T8E41 and 7075-T6 were compared. Although the number of tests was very small, there were indications that the crack propagation at 2090-T8E41 is somewhat slower at small crack lengths. At higher crack lengths, however, the transition to unstable crack growth occurred quite rapidly. This may indicate that the damage tolerance properties of 2090-T8E41 are a little worse than those of 7075-T6. (It has to be emphasized again that the data base is still too small to allow for more general conclusions.)

In Figure 10 photographic reproductions of the fracture surfaces of 2090-T8E41 and 7075-T6 are shown. There exist some essential differences between both alloys. At 7075-T6 the crack started at 90° to the loading direction and remained in this position for a long range in crack length until it gradually changed its position into 45° to the loading direction. At 2090-T8E41 the 45° transition was observed at short crack lengths. There were furthermore signs of a strong formation of deposits on the fracture surfaces at 2090-T8E41. In a recent investigation [5] a similar observation was made on an aluminium-lithium alloy. In this work the more intense production of deposits on the fracture surfaces was interpreted as an extensive closure of the cracks during the fatigue test. A more intensive crack closure can also give the reasoning for the somewhat slower crack propagation at 2090-T8E41 at smaller crack lengths under Gaussian loading. Figure 10 shows that the fracture surfaces of 2090-T8E41 appear more irregularly at the onset of crack growth than at 7075-T6.

5. CONCLUSIONS

In the present study short crack tests on 2024-T3 with constant amplitude, FALSTAFF and Gaussian loading (core programme) and short and long crack tests with Gaussian loading on 2090-T8E41 (supplemental programme) were performed. Some exploratory long crack tests on 7075-T6 with Gaussian loading were added. Although the number of specimens available for testing was limited, the following trends have been observed:

- 2024-T3 and 2090-T8E41 showed the so-called "short crack effect" in so far as the da/dN versus ΔK data followed roughly a straight line elongation of the medium range of the long crack da/dN versus ΔK data and that the da/dN versus ΔK data of the short cracks were somewhat higher than for long cracks. Crack closure seems to be the main reason for the observed short crack behaviour.
- At 2024-T3 usually more than one short crack nucleated, which were mainly center cracks. These cracks interacted later on intensively such that various data points had to be eliminated to fulfil the non-interaction criterion. Except in one case the number of cracks at 2090-T8E41 was smaller and the dominant cracks turned out to be corner cracks.
- At 2024-T3 and 7075-T6 the short cracks usually initiate at 90° to the loading direction and remain in this position for some range in crack length. At 2090-T8E41 the short cracks showed a strong tendency to take a position of 45° to the loading direction.
- In the long crack stage the data (which were unfortunately too few to allow for more general conclusions) showed some tendency that the cracks advanced somewhat slower at shorter crack lengths at 2090-T8E41 than at 7075-T6 but then propagated faster during the high loads of the Gaussian sequence.
- The determination of da/dN and the representation of the short and long crack data on the basis of ΔK as derived from the peak-to-peak stresses of the Gaussian sequence hides important details of the actual cycle-by-cycle crack propagation behaviour. More detailed interpretations of the physical crack propagation behaviour are expected by comparisons of the data with the predictions of advanced cycle-by-cycle propagation prediction models as the FASTRAN model by J. Newman where the basis is well understood.

6. REFERENCES

1. Newman, J.C., Jr., Edwards, P.R. (coordinators), Zocher, J.H. (chairman): Short-Crack Growth Behaviour in an Aluminum Alloy - an AGARD Cooperative Test Programme, AGARD Rep. No. AGARD-R-732, Neuilly sur Seine, France, 1988.

2. Döker, H., Bachmann, V.: Determination of Crack Opening Load by Use of Threshold Behaviour, ASTM-STP 982: Mechanics of Fatigue Crack Closure (J.C. Newman, Jr., W. Elber, eds.), American Society for Testing and Materials, Philadelphia, 1987, pp. 247-259.
3. Herman, W.A., Hertzberg, R.W., Jaccard, R.: A Simplified Laboratory Approach for the Prediction of Short Crack Behaviour in Engineering Structures, Fatigue and Fracture of Engineering, Materials and Structure, 1988 (11); pp. 303-320.
4. Marci, G., Castro, D.E., Bachmann, V.: Fatigue Crack Growth Rates as a Function of ΔK : Variability and Material Properties, Proc. Int. Conf. on "Spacecraft Structures and Mechanical Testing", Noordwijk, Netherlands, 19-21 Oct. 1988.
5. Peters, M., Welpmann, K., McDermid, D.S., 't Hart, W.G.J.: Fatigue Properties of Al-Li Alloys, AGARD Specialists' Meeting on New Light Alloys, Mierlo, Netherlands, 3-5 Oct. 1988, to be published.

7. ACKNOWLEDGEMENTS

The authors should like to thank Dr. M. Peters for fruitful discussions of the test results and Mrs. Ch. Kotsauschek for preparing the manuscript.

| Material | | Const. appl. load. | | | FALSTAFF | | GAUSSIAN Random | |
|------------|-------------|--------------------|------------|-----|----------|------------|-----------------|------------|
| | | Spec. No | S max, MPa | R | Spec. No | S max, MPa | Spec. No | S max, MPa |
| 2024-T3 | short crack | A55-06 | 205 | 0.5 | A56-12 | 275 | A52-19 | 145 |
| | short crack | A57-30 | 105 | -1 | A50-01 | 170 | A65-05 | 125 |
| | short crack | | | | | | A60-10 | 170 |
| 2090-T8E41 | short crack | | | | | | B1424 | 210 |
| | short crack | | | | | | B1762 | 190 |
| | short crack | | | | | | B1713 | 190 |
| | short crack | | | | | | B1703 | 170 |
| | long crack | | | | | | B1501 | 150 |
| 7075-T6 | long crack | | | | | | A20 | 150 |
| | long crack | | | | | | A21 | 150 |

Figure 1.- Survey of DFVLR (DLR) tests.

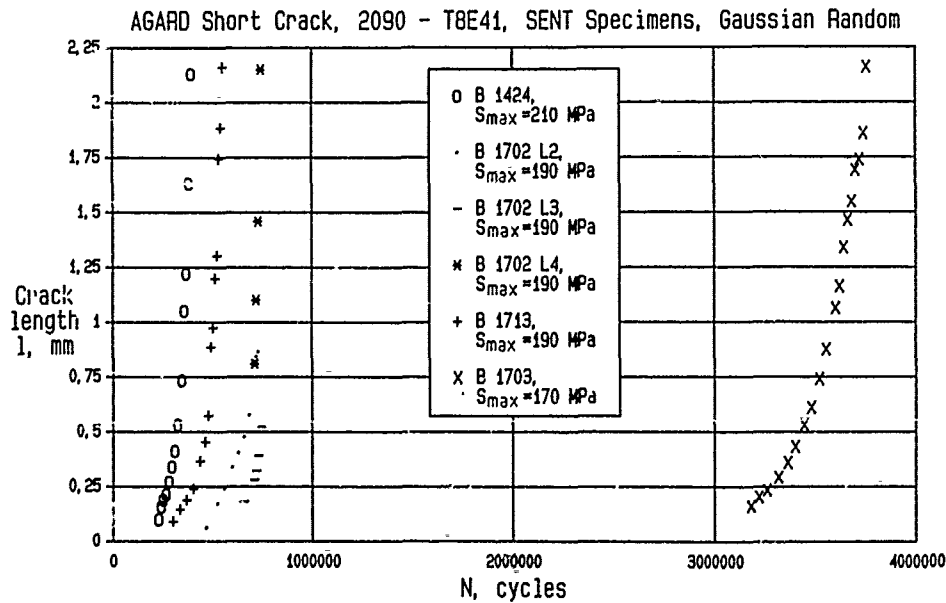


Figure 2.- Short crack behaviour of 2090-T8E41 (surface cracks).

AGARD-AR-144 (1988) 1-11

AGARD Short Crack, 2090 - T8E41, Gaussian Random

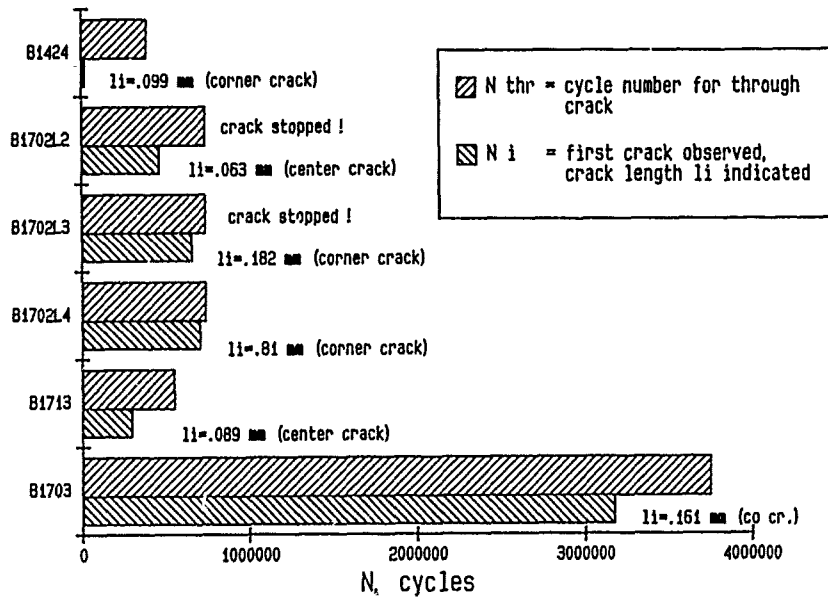


Figure 3.- Cycle number and crack lengths at first detection of the short cracks and cycle numbers as the short cracks penetrated the bore of the notch of the SENT specimens.

a) AGARD Short Crack, 2090 - T8E41, Gaussian Random

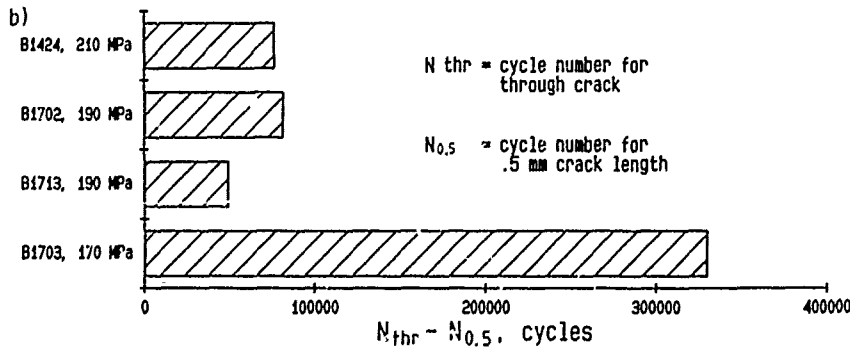
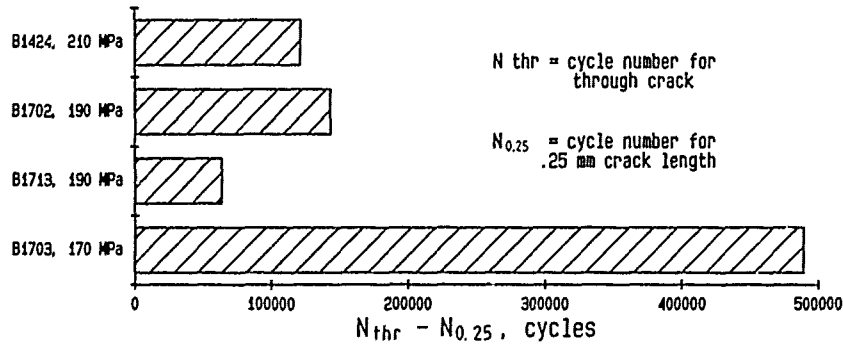


Figure 4.- Cycle number in the short crack stage; initial crack lengths 0.25 mm (a) and 0.5 mm (b).

AGARD Short Crack, 2090 - T8E41,
SENT Specimens, Gaussian Random

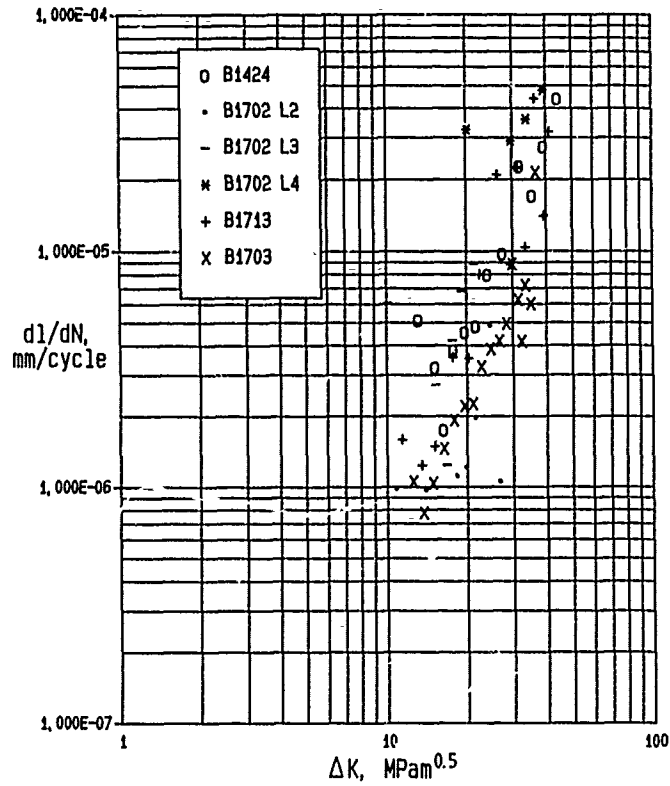


Figure 5.- Crack propagation in the short crack stage under Gaussian loading.

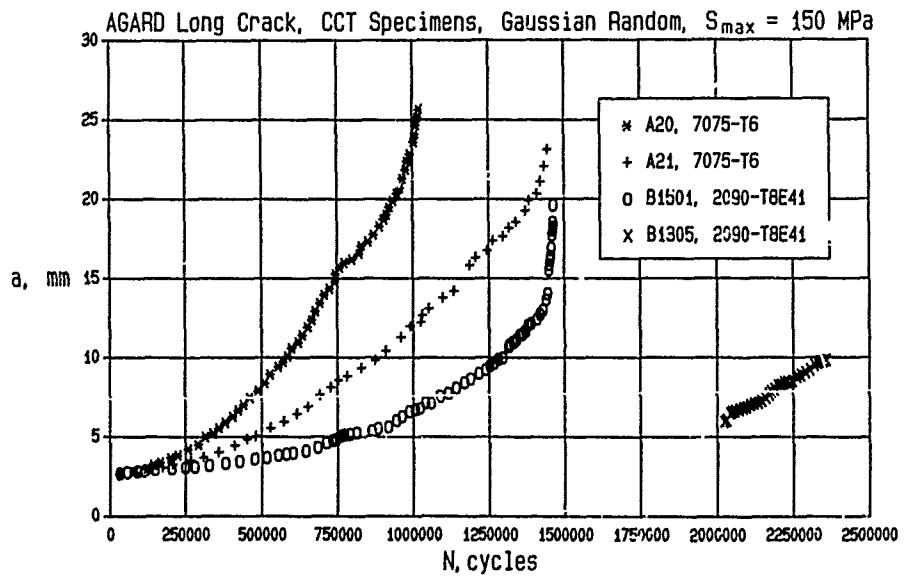


Figure 6.- Long crack behaviour of 2090-T8E41 and 7075-T6 under Gaussian loading.

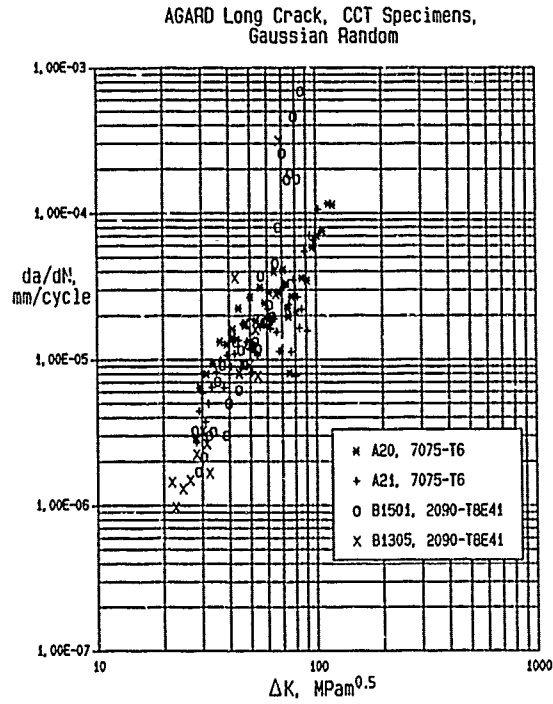


Figure 7.- da/dN vs. ΔK behaviour of 2090-T8E41 and of 7075-T6 under Gaussian loading in the long crack stage.

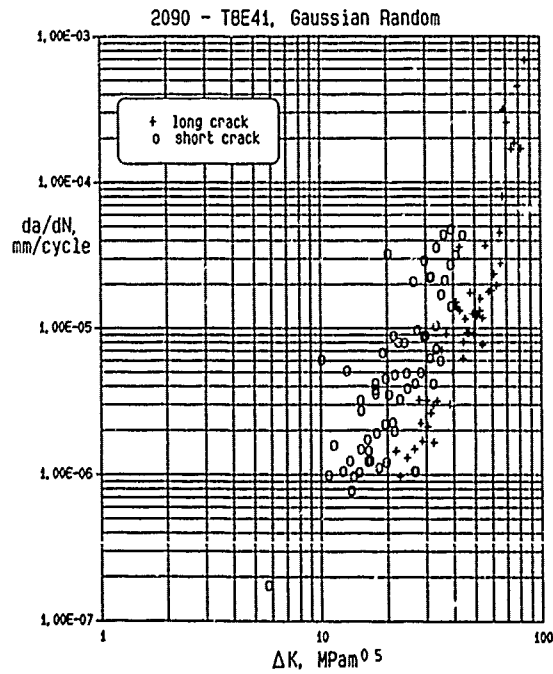


Figure 8.- Comparison of short and long crack behaviour of 2090-T8E41 under Gaussian loading.

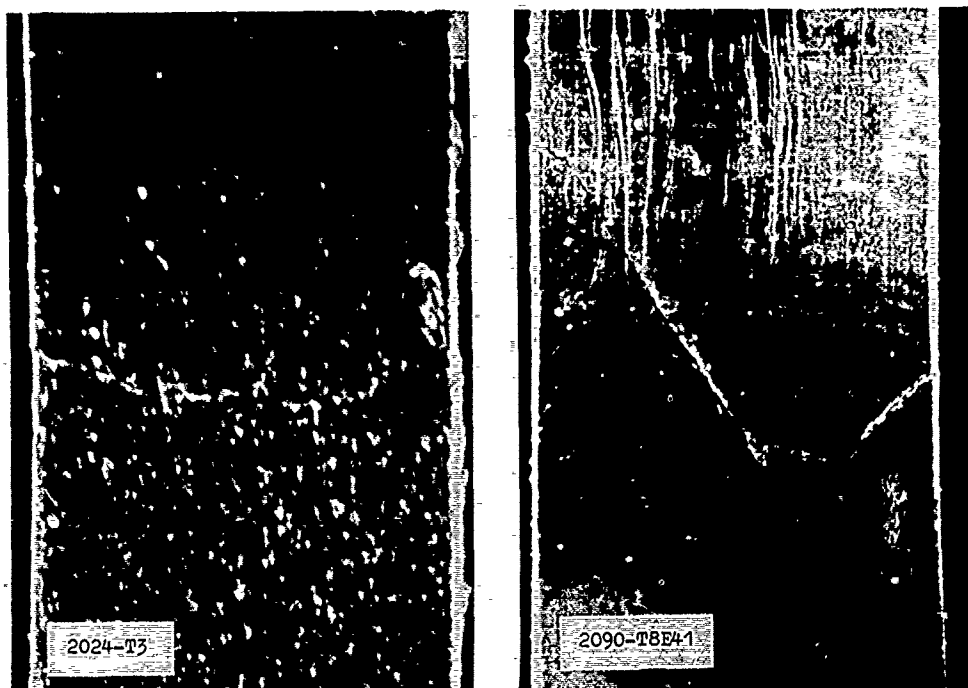


Figure 9.- Formation of short cracks at the notches of the 2024-T3 and of the 2090-T8E41 SENT specimens under Gaussian loading.

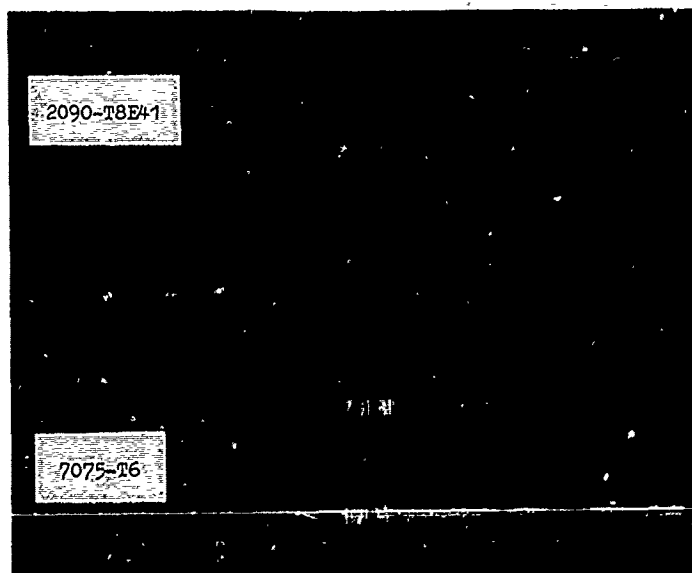


Figure 10.- Fracture surfaces of the long cracks of the 2090-T8E41 and the 7075-T6 CCT specimens under Gaussian loading.

APPENDIX

TABLE 1

Participant Test Matrix on Short Crack Growth - Core Programme - after [1] (a)
 Test Matrix of the Supplemental Programme (b)

a)

| Participant | Constant Amplitude Loading (a) | | | | Spectrum Loading | |
|---------------------------|--------------------------------|-------------|----------------------|--------------|-------------------|-------------------|
| | R = -2
H M L | -1
H M L | 0
H M L | 0.5
H M L | FALSTAFF
H M L | GAUSSIAN
H M L |
| France
-CEAT | X X X | X X X | X X X ^(b) | | X X | |
| Germany
-DFVLR | | X | | | X X X | X X X |
| Germany
-iABG | | X X X | X X X | | X X X | X X X |
| Italy
-Pisa | | X X X | X X X | X X X | X X | |
| Netherlands
-NLR | | X X X | | | | X X X |
| Portugal-
LNETI/CEMUL | X X X | X X X | X X X | X X X | | |
| Sweden
-FFA | X X X | X X X | X X X | | X X X | |
| Turkey
-METU | X X X | X X X | X X X | X X X | | |
| United
Kingdom
-RAE | X X X | X X X | X X X | X X X | X X X | X X X |
| USA-JHU | X X X | X X X | X X X | X X X | | |
| USA-NASA | X X X | X X X | X X X | X X X | X X X | |
| USA-AFWAL | X X X | X X X | X X X | | X X X | |

(a) H, M and L represent high, medium and low stress levels, respectively.

(b) Tests conducted at R = 0.1 for H, M and L stress levels.

b)

| Participant | Constant Amplitude Loading | | | | Spectrum Loading | | | |
|--------------------|----------------------------|----|----|----|------------------|----------|-------|-------|
| | R = -2 | -1 | 0 | .5 | FALSTAFF | GAUSSIAN | TWIST | FELIX |
| Germany
-DFVLR | | | | | | | | SL(a) |
| Portugal
-LNETI | S | S | S | | | | | |
| Sweden
-ARI | | | | S | | | | SL |
| England
-RAE | | | | | | | | SL |
| USA-AFWAL | L | SL | SL | SL | SL | | | |
| USA-NASA | S | S | | | | | | |

(a) S = Short-crack tests and L = Long-crack tests.

TABLE 2
Chemical and Mechanical Properties of 2024-T3, 2090-T8E41, and 7075-T6

| Alloy | Cu | Zn | Mg | Mn | Cr | Si | Fe | Ti | Zr | Li | Al |
|------------|---------|------|------|------|------|------|------|------|------|---------|---------|
| 2024-T3 | 4.61 | 0.06 | 1.51 | 0.57 | 0.02 | 0.16 | 0.33 | | | | Balance |
| 2090-T8E41 | 2.4-3.0 | 0.10 | 0.25 | 0.05 | 0.05 | 0.10 | 0.12 | 0.15 | 0.12 | 1.9-2.6 | Balance |
| 7075-T6 | 1.68 | 5.60 | 2.50 | 0.08 | 0.25 | 0.40 | 0.50 | 0.20 | | | Balance |

| Alloy | Ultimate tensile strength, MPa | Yield stress (0.2-percent offset), MPa | Modulus of elasticity, MPa | Elongation (51-mm gage length), percent |
|------------|--------------------------------|----------------------------------------|----------------------------|-----------------------------------------|
| 2024-T3 | 495 | 355 | 72,000 | 21 |
| 2090-T8E41 | 580 | 525 | 78,200 | 5 |
| 7075-T6 | 567 | 486 | 72,000 | (12) |

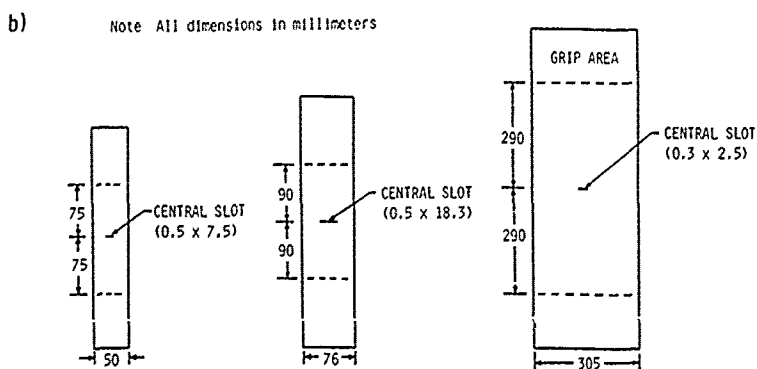
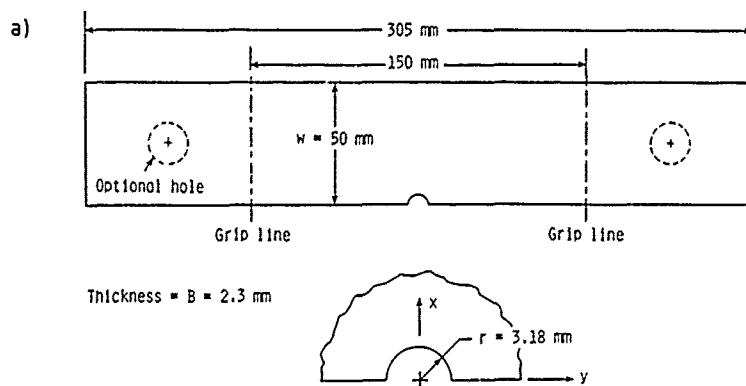


Figure 1.- Single Edge Notch Tension (SENT) fatigue specimens for short crack tests (a) and Center Crack Tension (CCT) fatigue specimens for long crack tests (b).

AGARD Short Crack DATA CHART
Record of crack lengths and map

Page 2 of 2 Loading Type R = -1
Specimen no. A-15-05 Peak Stress 90.0 MPa

0.1mm grid

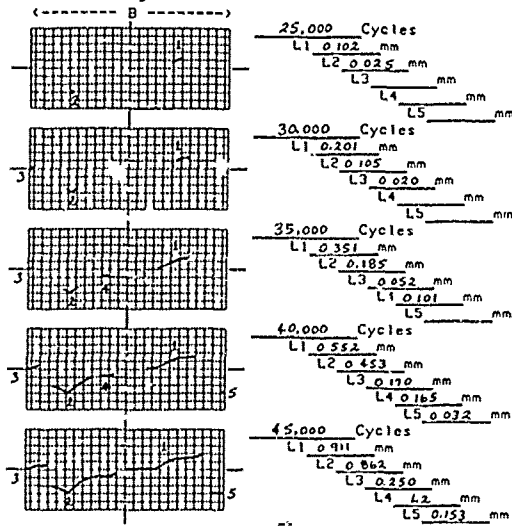


Figure 2.- Mapping procedure for the documentation of the short crack behaviour (example).

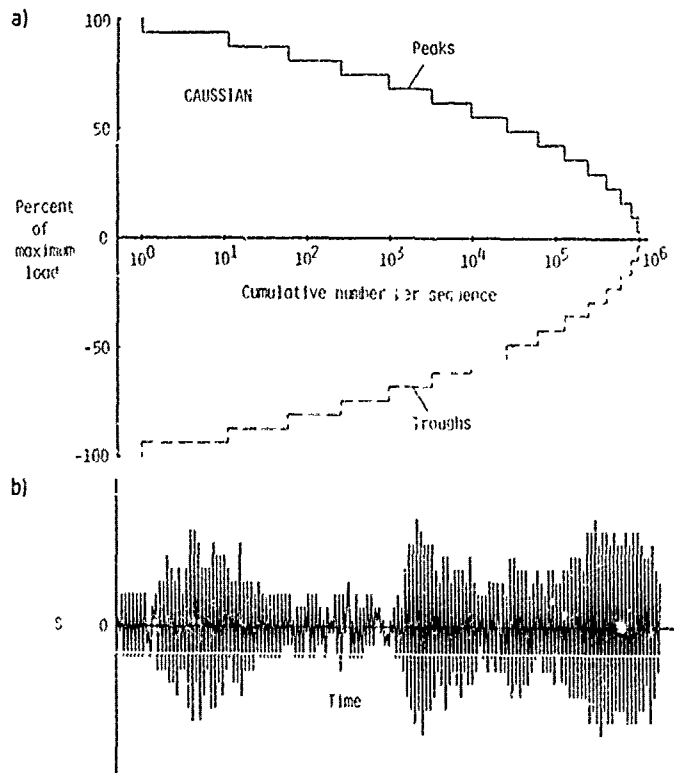


Figure 3.- Cumulative number of peaks and troughs in GAUSSIAN sequence ($I = 0.99$) (a) and cut-out of the GAUSSIAN sequence (b).

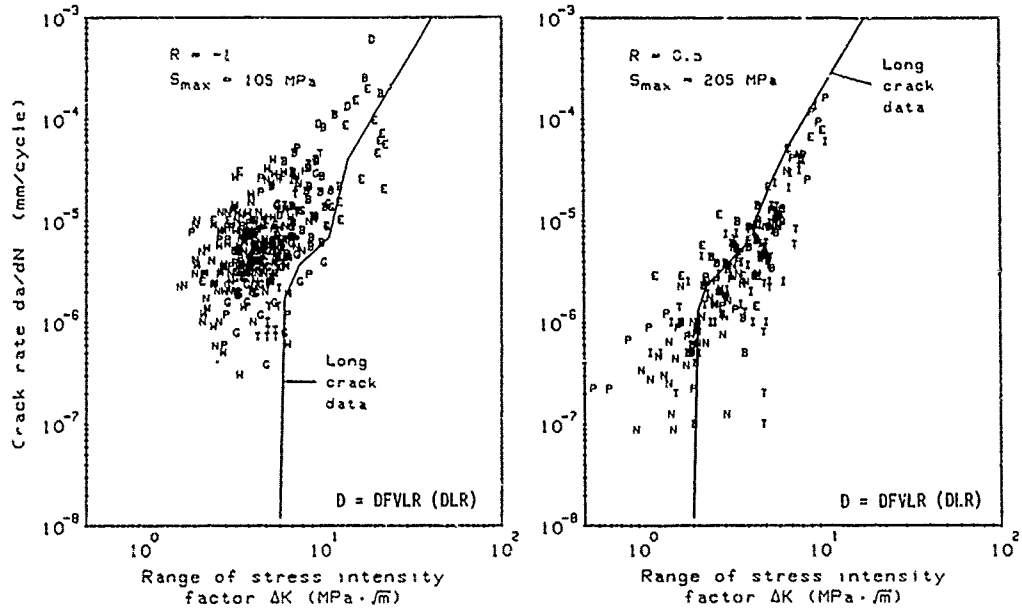


Figure 4.- Short crack behaviour under constant amplitude loading after [1].

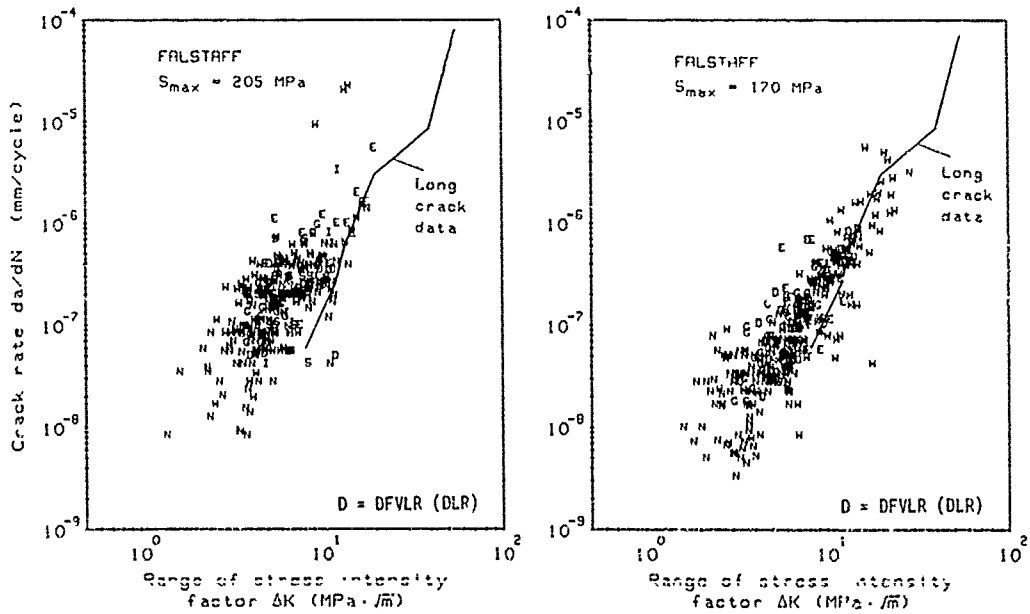


Figure 5.- Short crack behaviour under FALSTAFF loading after [1].

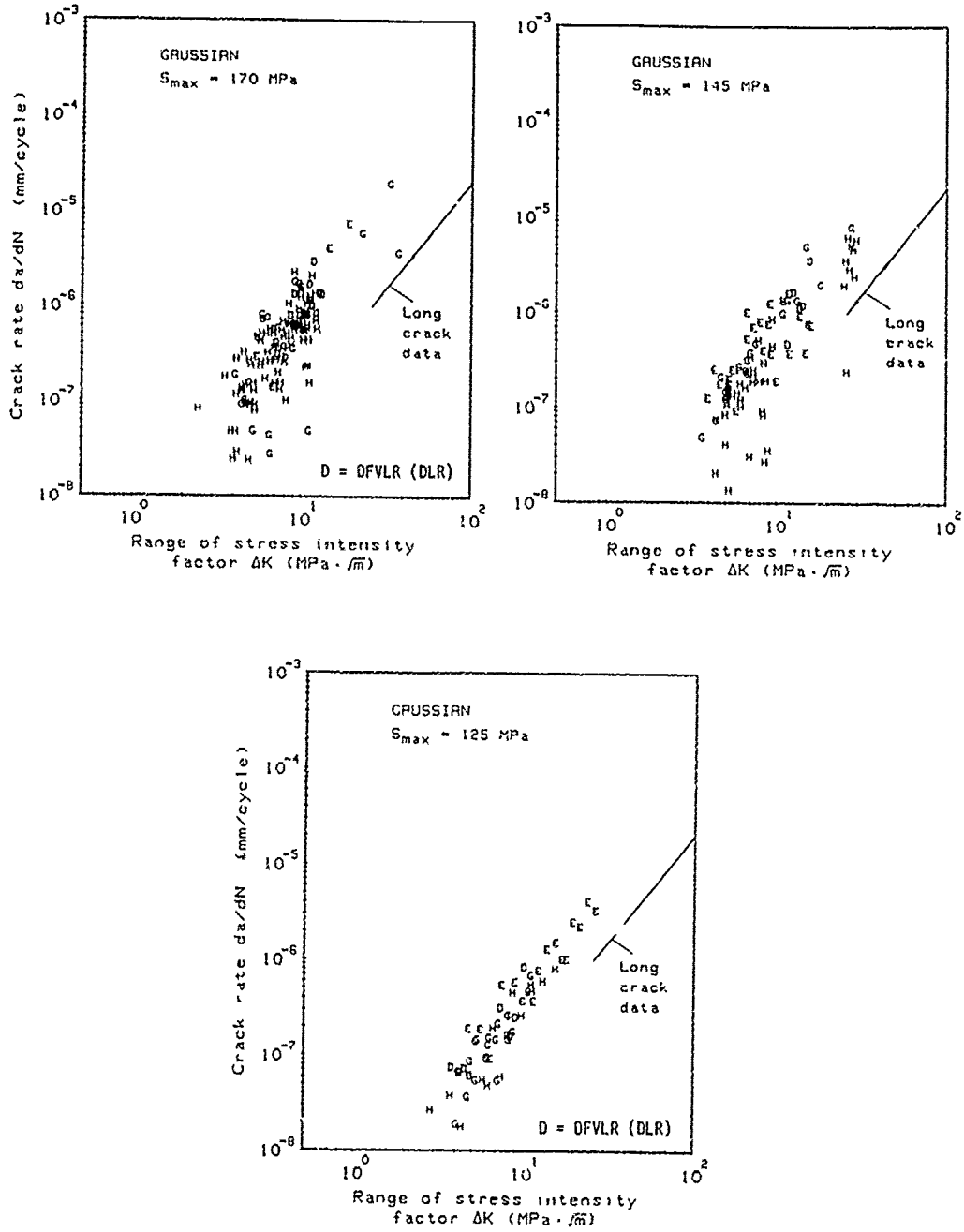


Figure 6.- Short crack behaviour under GAUSSIAN loading after (1).

THE GROWTH OF SHORT FATIGUE CRACKS IN 2024 AND 2090 ALUMINIUM ALLOYS
UNDER VARIABLE AMPLITUDE LOADING

by

R. Cook

Royal Aerospace Establishment
Farnborough
Hants
GU14 6TD
UK

SUMMARY

Fatigue crack growth measurements have been made on 2024-T3 and 2090-T8E41 aluminium alloys subjected to FALSTAFF, Inverted FALSTAFF and FELIX standard loading sequences. Crack growth rates at short crack lengths under FALSTAFF and Inverted FALSTAFF in 2024-T3 were found to be similar at each of three applied stress levels. This result is explained in terms of crack opening stress levels and is qualitatively predicted by a closure based crack growth model. Short fatigue cracks were shown to grow at stress intensity factors well below the long crack growth threshold in 2090-T8E41 alloy under FELIX loading. The short cracks, however grew initially perpendicular to the applied loading direction and then abruptly changed direction and grew at 60° to the initial crack direction. Short crack growth rates in 2024-T3 and 2090-T8E41 were compared and found to be similar if the length of the short cracks in the 2090 alloy were taken to be the length of the crack projected onto the axis perpendicular to the loading direction. This work represents the United Kingdom contribution to the supplemental programme of the AGARD coordinated short fatigue crack growth investigation.

1 INTRODUCTION

The growth of short fatigue cracks has been the subject of a number of recent investigations. Many investigators have observed a phase of rapid early crack growth when cracks are relatively small. It was shown that if conventional linear elastic fracture mechanics were applied to the observed crack growth rates then, for certain loading conditions, short cracks propagated faster than long cracks at the same calculated stress intensity factor. This is generally referred to as the short crack anomaly. In order to examine the conditions under which such an anomaly could exist, an AGARD coordinated international collaborative working group was formed. The working group was tasked with investigating under what testing conditions the anomaly was observed and what were the most likely causes of the effect.

A collaborative fatigue test programme was devised in order to study the behaviour of short fatigue cracks. The programme was split into two parts, a core programme and a supplemental programme. In the core programme the participants undertook fatigue testing under common conditions using specimens manufactured at a single site from a common batch of material. The main aims of the core programme were to check data variability between participants, to generate an extensive database of short fatigue crack growth and to compare these data with predictions made using an analytical crack-closure model. The core programme testing details and results have been published separately¹. The main aim of the supplemental programme was to generate crack growth data for a range of materials, specimen types and load spectra of interest to individual participants and to establish the range of conditions under which the short crack anomaly was observed. This Report summarizes the UK contribution to the supplemental programme. The UK work was conducted at the Royal Aerospace Establishment. The materials used were 2024-T3 aluminium alloy (core programme material) and 2090-T8E41 aluminium-lithium alloy. The load sequences used were Inverted FALSTAFF and FELIX. In addition to measuring crack growth rates at short crack lengths, comparable long crack data were generated under the FELIX loading sequence. Crack shapes and the number of applied load cycles to grow a crack across the thickness of the specimens were also investigated. Crack growth data were compared with predictions made using the FASTRAN closure-based crack growth programme of Newman⁴.

2 SPECIMENS AND MATERIALS

Two specimen types were used throughout the programme. Short crack measurements were made on single side notch specimens of the dimensions given in Fig 1a. Long crack growth measurements were made on centre cracked specimens of the dimensions given in Fig 1b. Specimens were supplied ready machined, and chemically polished at the notches, by USAF Wright Aeronautical Laboratory. Details of the manufacturing routes are described in Ref 1. Prior to fatigue testing, an area around the notch of the short crack specimens was lightly etched to reveal the microstructure. Both short and long crack type specimens were tested using antibuckling guides when compressive loading was applied. The antibuckling guides were lightly clamped to the specimens with teflon sheets inserted between the guides and the specimen.

The two materials used in the UK supplemental programme were 2024-T3 aluminium alloy and 2090-T8E41 aluminium-lithium alloy. The materials were both supplied by NASA-Langley Research Center and their average chemical and mechanical properties are given in Table 1.

3 FATIGUE TESTING PROGRAMME

All specimens were tested using an INSTRON 100kN electro-hydraulic fatigue testing machine. Alignment of the wedge grips was measured as part of the core programme requirements and found to be within the tolerances defined. The loading sequences were generated by a Hewlett-Packard 2836 computer. Achieved load levels were measured and where necessary errors corrected by an amplitude adaptive control loop within the generation programme. Errors in peak and trough values were generally better than 1% of the demanded load range. The loading frequency used throughout the programme was 15 Hz.

Tests were performed under Inverted FALSTAFF and FELIX loading sequences. FALSTAFF is a standard loading sequence which represents a typical load history at a lower surface wing root on a fighter aircraft. The sequence is defined as a series of 35966 load transitions which constitute 200 aircraft flights. Inverted FALSTAFF is a simple inversion of the FALSTAFF sequence. Part of the air-ground-air cycle and the taxiing loads are applied in tension and the gust and manoeuvre loads are applied in compression, such as might be experienced by an upper wing surface. FELIX is a standard loading sequence which represents a typical load history for the lower surface blade root on a fixed or semi-rigid rotor helicopter. It consists of some 4.5 million load transitions which constitute 140 aircraft flights^{2,3}.

Finite element tests were carried out to measure crack propagation at short and long crack length. The specimens described in section 2. Testing details for short and long cracks are described in sections 3.1 and 3.2 respectively.

3.1 Short crack test programme

Short fatigue crack growth measurements were made on specimens of 2024-T3 and 2090-T8E41 under the FELIX loading sequence. Measurements were also made on specimens of 2024-T3 under the Inverted FALSTAFF loading sequence. The matrix of test conditions is given in Table 2. Test cycling was stopped periodically for the crack length to be measured using acetate replicas. The intervals between measurements were designed to produce a minimum of 20 replicas per test. In order to improve the accuracy of surface crack length measurements, a tensile load was applied to each specimen before replicas were taken. For the FELIX sequence this tensile load was FELIX level 80 which represents about 80% of the maximum load in the sequence. For Inverted FALSTAFF this load was FALSTAFF level 2 again representing about 80% of the maximum load in the sequence.

The method of crack measurement was the acetate replica technique. Thin acetate strips were softened with acetone, bent to a tight radius and inserted into the notch of the specimen. The replica was pressed onto the notch surface using a rod and elastic bands. It was then removed after 3 minutes and examined under an optical microscope. If the quality of the replica was satisfactory, testing was resumed and the crack length measured using a graduated eyepiece.

3.2 Long crack test programme

Long fatigue crack growth data were obtained for the 2024-T3 material under the FELIX loading sequence. The method chosen to obtain long crack propagation data was that of load shedding. The specimen (see Fig 1b) was subjected to FELIX loading with a peak gross applied stress level of 110 MPa. Cracks were grown from both ends of the slot until they both reached a length of at least 2 mm. A surface replica technique was used for crack monitoring; this was similar to that described for the short crack programme. The applied load levels in the sequence were reduced by 6% and the test restarted at the beginning of the FELIX sequence. The cracks were grown this time by a minimum of 0.5 mm, when the load levels were again reduced by 6%. This procedure was repeated until a maximum load level was reached at which no crack propagation was observed (for a period of 2.5 million cycles). At this point the load was increased by 6% and the test continued for a further 2.5 million cycles. During this period no crack propagation was observed. The loads were increased by a further 6% and the cracks were observed to propagate. This propagation was allowed to continue until the cracks had grown by at least 0.5 mm at which point the load was increased by 6%. This process was continued until the specimen failed.

4 FATIGUE TEST RESULTS

4.1 Inverted FALSTAFF short crack test results

Crack length measurements were made on short crack type specimens of 2024-T3 material as described in section 3. A plot of the crack growth rate data obtained as a function of stress intensity factor range is presented in Fig 2 for each of the three stress levels used. Crack rates were calculated from consecutive replica crack length measurements. The stress intensity factor solution is described in Ref 1. It is based on the full applied stress range, ΔK from FALSTAFF level 1 to 32, and on the average crack length, \bar{a} the average of the crack lengths measured on consecutive replicas.

The fatigue endurance to initial crack and full specimen width crack are presented in Fig 3. The results of FALSTAFF tests obtained in the core programme are also presented in this Figure.

4.2 FELIX short crack test results

Fatigue tests using the FELIX sequence were carried out on both 2024-T3 and 2090-T8E41 materials. The crack propagation results on the 2024-T3 material are presented in Fig 4. The calculation of crack growth rate and stress intensity factor are as described in the previous section for Inverted FALSTAFF loading. The total stress range from FELIX level -28 to 100 was used in the calculation of stress intensity factor.

The fatigue tests using the 2090-T8E41 material exhibited unusual crack growth behaviour. With the 2024-T3 material cracks grew in an approximate straight line across the throat of the notch. With the 2090-T8E41 material, cracks grew for a period of time across the notch and then abruptly changed direction and grew at approximately 60° to the original crack. At high applied stress levels the length of crack prior to the change in direction was relatively small, whilst at low applied stress levels the crack length was somewhat longer before the abrupt change in direction occurred. Photographs showing the angular crack growth behaviour and points of crack initiation are presented in Fig 5. In order to calculate the crack growth rates and stress intensity factors from replicas, the length of crack was taken to be the length of the crack projected onto the axis perpendicular to the loading direction. Fig 6 shows crack growth rates as a function of stress intensity factor.

4.3 FELIX long crack test results

Cracks were grown in long crack type specimens (Fig 1b) as described in section 3.2. The stress intensity factor solution for the long crack geometry is described in Ref 1. The applied stress range once again was from the maximum to the minimum applied stress in the FELIX sequence, i.e. FELIX level 100 to FELIX level -28. A discontinuous crack path was observed on one side of the specimen as illustrated in Fig 7, conventional crack growth was observed on the opposite side. As the loads were progressively shed the crack growth became more conventional on both sides of the specimen, i.e. one discrete crack was observed which grew along a continuous path. As the load was increased following the threshold value being obtained, the discontinuous type of crack growth observed earlier (see Fig 7) was once again noted. In this regime a crack appeared slightly ahead of and above or below the main crack. This small crack then grew both towards and away from the continuous crack until it joined up to it. This discontinuous crack path was associated with the shear lip seen in Fig 8 where the point of breakthrough to the surface was highly dependent on the local microstructure. Crack lengths were measured from the initial slot to the tip of any observable crack on both sides of the specimen and the average value was recorded. The results of the long crack propagation test are shown in Fig 9 along with those of the short crack tests described in section 4.1.

5 DISCUSSION OF RESULTS

5.1 Inverted FALSTAFF loading

Crack propagation data obtained under Inverted FALSTAFF loading at three different applied stress levels are presented in Fig 2. As can be seen from this figure, for any value of stress intensity factor range, cracks propagated fastest at the highest applied stress level and slowest at the lowest applied stress level (eg $\Delta K = 8 \text{ MPa}\cdot\text{m}^{1/2}$ as shown by the dotted line). This means that for a given value of stress intensity factor short cracks propagated faster than long cracks. It is apparent therefore that the so-called short crack anomaly was observed under Inverted FALSTAFF loading. Similar observations were made in the core programme with the normal FALSTAFF loading sequence.

Crack propagation rates calculated from the Inverted FALSTAFF loading tests are compared with those from equivalent FALSTAFF core programme tests in Figs 10, 11 and 12, for the three peak stress levels of 275 MPa, 205 MPa and 170 MPa respectively. The peak stress levels refer to maximum compressive gross section stress for the Inverted FALSTAFF tests and maximum tensile gross section stress for the FALSTAFF loading tests. As can be seen from Figs 10 and 11, for peak stress levels of 275 and 205 MPa the crack propagation rates for FALSTAFF and Inverted FALSTAFF are very similar. For the lowest stress level of 170 MPa (Fig 12), the range of stress intensity factors for the normal and Inverted FALSTAFF sequence only just overlap and it is therefore not possible to say if the crack propagation rates are similar in both cases. For the limited data where the ΔK values do overlap, the crack propagation rates appear to be similar.

The number of cycles taken to initiate a crack (the first observed crack, 20-50 μm) and to propagate it across the width of the specimen are shown in Fig 3 for FALSTAFF and Inverted FALSTAFF sequences. The number of cycles to initiate and propagate cracks to full width under FALSTAFF and Inverted FALSTAFF loading are similar at the two higher stresses. At the lowest stress level, however, the number of cycles to initiate cracks are greater for Inverted FALSTAFF loading. It can be concluded that crack initiation and growth is similar under FALSTAFF and Inverted FALSTAFF loading at the higher applied stress levels but that the FALSTAFF sequence is more damaging than the Inverted FALSTAFF sequence at the lowest stress level.

When comparing normal FALSTAFF tests with Inverted FALSTAFF tests, it should be remembered that the stress intensity factor ranges (ΔK) applied in both test sequences are the same. However, the value of ΔK experienced at the crack tip will depend on crack opening stress levels. Fig 13 shows crack opening stress levels calculated for both

the Inverted and normal FALSTAFF sequences, using the FASTRAN programme based on the crack closure model described in Ref 4. The opening stress levels are shown up to a crack length of 0.5 mm which is of the order of the maximum crack length used to determine the crack growth data shown in Fig 2. Generally multiple cracks initiated in the notches and data for cracks of greater than 0.5 mm length were discarded due to crack interaction effects. The criteria for rejecting data due to crack interactions are described in Ref 1. As can be seen in Fig 13 for Inverted FALSTAFF loading the crack opening stress levels remain entirely in compression whilst cracks grow to 0.5 mm. In contrast, the opening stress levels for the FALSTAFF sequence start in compression but become tensile. The effective stress range experienced by the crack tip is from the solid line to the dotted line, as shown by the shaded areas in Fig 13. A comparison of the shaded areas and the peak-trough distributions for FALSTAFF and Inverted FALSTAFF load sequences indicates that the stress ranges experienced by the crack tip are similar for both sequences, particularly for cracks up to 250 μ m long and peak stresses of 205 MPa and 205 MPa. This accounts for the experimental observations described earlier whereby the damaging effect of the FALSTAFF and Inverted FALSTAFF sequences were similar at short crack lengths. The situation is less clear in the case of a peak stress of 170 MPa. Further work to assess the relative fatigue damage caused by these two sequences is planned.

5.2 FELIX loading

The results of the FELIX tests using the 2024-T3 core programme material are presented in Fig 4. The results are for three applied stress levels with only one specimen per stress level. There is no evidence of a stress level effect as was observed under FALSTAFF and Inverted FALSTAFF loading. The results of the FELIX tests using the 2090-T8E41 material are presented in Fig 6. In this case, however, a slight stress level effect is observable, where for a given ΔK , cracks tested at the higher stress levels (shorter cracks) propagate faster than those tested at the lower stress levels (longer cracks).

The crack propagation rates observed in the two alloys were similar (see Fig 14). This is perhaps surprising since cracks in the 2090-T8E41 alloy grew predominantly at approximately 60° to the normal crack growth axis. One might expect that the degree of crack closure would be different in the two materials and that cracks in the 2090-T8E41 alloy would not be propagating under purely mode I conditions. The cause of this angular crack growth is not fully understood, but appears to be related to the strong deformation textures observed (described in Ref 5). However, the situation is complicated by the presence of a steep texture gradient from surface to mid-plane of the 2090-T8E41 sheet. The length of initial crack perpendicular to the load axis was dependent on applied stress level; the longest initial crack was observed at the lowest stress level. As the stress level increased, the length of initial crack decreased. This suggests that there may be a threshold K level below which cracks will grow entirely perpendicular to the load axis.

The long crack FELIX data obtained for 2090-T8E41 material is presented in Fig 15. It is obvious that the decreasing load crack growth rate data is somewhat faster than the increasing load data at the same stress intensity factor range. There are a number of possible explanations for this observed trend. FELIX is an extremely long sequence (4.5×10^6 turning points) which is reasonably well mixed. However, the number of applied load cycles at a given stress level is considerably greater in the decreasing load phase than in the increasing load phase due to the change in crack length. In both cases the number of cycles is considerably less than one complete FELIX sequence. It is possible therefore, that the relatively small number of load cycles at the start of the FELIX sequence applied in the increasing load tests are less damaging per cycle than the somewhat longer FELIX sequence applied in the decreasing load phase. The fatigue test lasted for approximately six months and it is possible that changes in crack closure levels occurred due to corrosion products. Changes in the nature of the fracture surface with applied load during testing, the presence/absence of shear lip, may also have affected crack closure levels.

The long and short crack data under FELIX loading of the 2090-T8E41 alloy are compared in Fig 8. It is clear that short cracks propagate at stress intensity factors well below the long crack threshold. At stress intensity factors above the threshold value, however, the short and long crack growth data are similar. The short crack effect has, therefore, been demonstrated under these testing conditions and a similar effect is expected for 2024-T3 alloy under FELIX loading. Comparative long crack data on 2024-T3 alloy has not yet been generated but will be included in a subsequent report together with analysis of the FELIX test results using the FASTRAN programme of Newman.

6 CONCLUSIONS

- (a) FALSTAFF and Inverted FALSTAFF loading sequences can be equally damaging at short crack lengths. A crack closure model has been used to qualitatively explain this observation.
- (b) Crack growth data obtained with single-edge-notch tension short crack specimens showed that crack growth rates at a given stress intensity factor were faster for short cracks than for long cracks propagating under Inverted FALSTAFF loading in 2024-T3 alloy. In the case of 2090-T8E41 alloy under FELIX loading there was evidence of a similar effect but appeared to be much less marked.

- (c) Short cracks grew initially at 90° to the load axis and subsequently at 60° to the initial crack in 2090-T8E41 alloy under FELIX loading. As the peak applied stress level decreased, the extent of initial crack growth perpendicular to the load axis increased.
- (d) Crack growth rates in the two alloys 2024-T3 and 2090-T8E41 were similar under FELIX loading if the projection of the crack length onto an axis perpendicular to the loading axis in the 2090-T8E41 alloy was used.
- (e) Short cracks propagated at stress intensity factors well below the long crack threshold in tests under FELIX loading using 2090-T8E41 alloy.

REFERENCES

- 1 J.C. Newman, Jr, P.R. Edwards, "Short crack growth behaviour in an aluminium alloy" - An AGARD Cooperative Test Programme, AGARD Report No.732 (1988)
- 2 P.R. Edwards, J. Darts, "Standardised fatigue loading sequences for helicopter rotors (HELIX and FELIX), Part 1: Background and fatigue evaluation", RAE Technical Report 84084 (1984)
- 3 P.R. Edwards, J. Darts, "Standardised fatigue loading sequences for helicopter rotors (HELIX and FELIX), Part 2: Final definition of HELIX and FELIX", RAE Technical Report 84085 (1984)
- 4 J.C. Newman, Jr., "A crack-closure model for predicting fatigue crack growth under aircraft spectrum loading", ASTM STP 748 (1981)
- 5 A.W. Bowen, "Texture analysis of 2090 Aluminium-Lithium alloy sheet", AGARD Report No.757 (1983)

Table 1
 NOMINAL CHEMICAL COMPOSITION AND AVERAGE MECHANICAL PROPERTIES OF 2024-T3 AND
 2090-T8E41 ALUMINIUM ALLOY SHEET

NOMINAL CHEMICAL COMPOSITION OF 2024-T3 AND 2090-T8E41 ALUMINIUM ALLOY SHEET

| Element | Per cent | |
|-----------|----------|------------|
| | 2024-T3 | 2090-T8E41 |
| Lithium | | 1.9 to 2.6 |
| Silicon | 0.16 | |
| Iron | 0.33 | 0.12 |
| Copper | 4.61 | 2.4 to 3.0 |
| Manganese | 0.57 | 0.05 |
| Magnesium | 1.51 | 0.25 |
| Chromium | 0.02 | 0.05 |
| Zinc | 0.06 | |
| Titanium | | 0.15 |
| Zirconium | | 0.10 |
| Aluminium | Balance | Balance |

AVERAGE MECHANICAL PROPERTIES OF 2024-T3 AND 2090-T8E41
 ALUMINIUM ALLOY SHEET IN L-T DIRECTION

| Material | Ultimate tensile strength
MPa | Yield stress
(0.2 per cent offset)
MPa | Modulus of elasticity
MPa | Elongation
(51 mm gauge length)
per cent |
|------------|----------------------------------|----------------------------------------------|------------------------------|------------------------------------------------|
| 2024-T3 | 495 | 355 | 72000 | 21 |
| 2090-T8E41 | 580 | 525 | 78200 | 5 |

Table 2
 FATIGUE TEST MATRIX

| Short/Long | Alloy | Loading sequence | Peak stress
(gross)
MPa |
|------------|------------|----------------------|-------------------------------|
| Short | 2024-T3 | Inverted
FALSTAFF | -275
-205
-170 |
| Short | 2024-T3 | FELIX | 200
185
170
155 |
| Short | 2090-T8E41 | FELIX | 240
225
210
195 |
| Long | 2090-T8E41 | FELIX | Load shed |

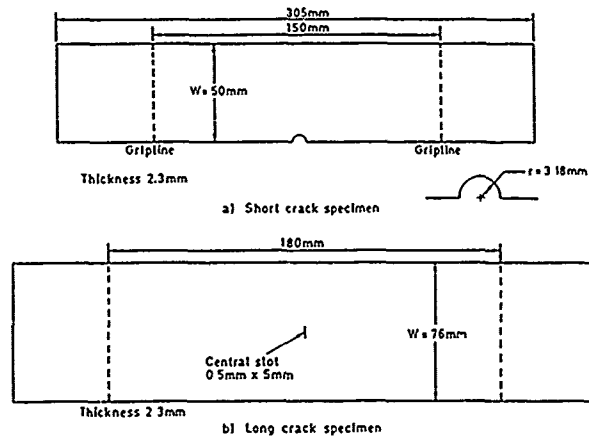


Fig 1 Fatigue test specimens

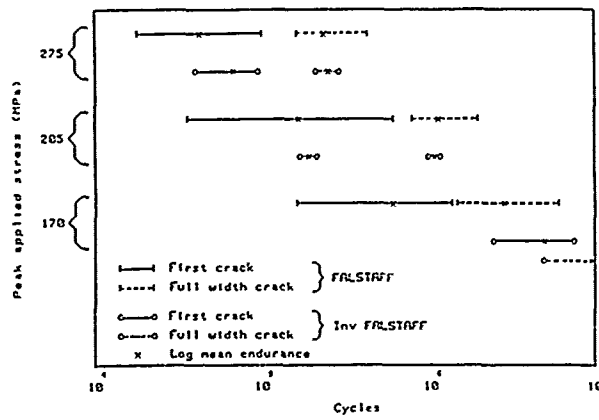


Fig 3 Life to first crack and fullwidth crack - FALSTAFF and inverted FALSTAFF loading

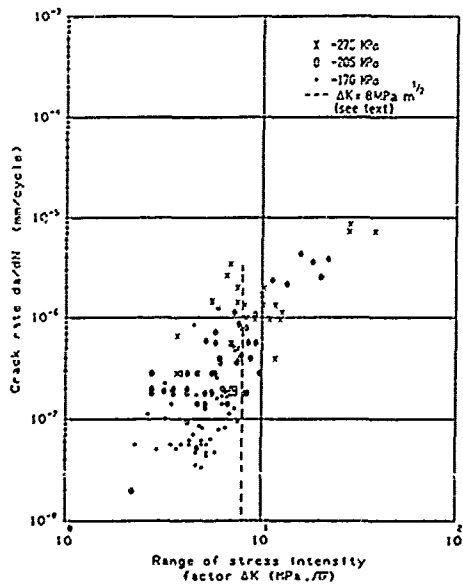


Fig 2 Short crack propagation rates inverted FALSTAFF loading - 2024-T3

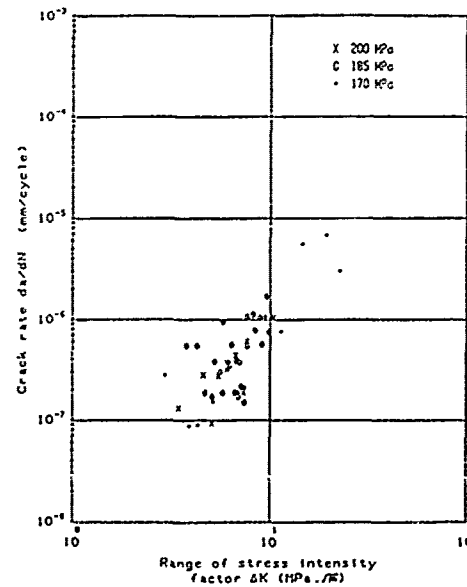


Fig 4 Short crack propagation rates Felix loading - 2024-T3

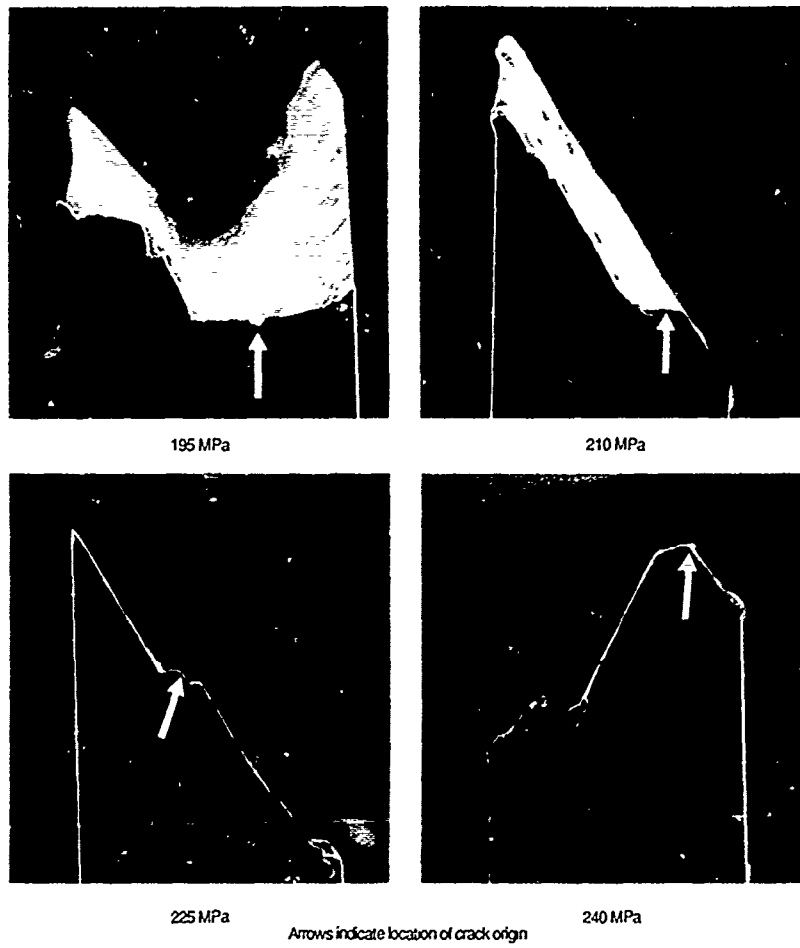


Fig 5 Crack paths in short crack 2090-T8E41 FeTiX loading

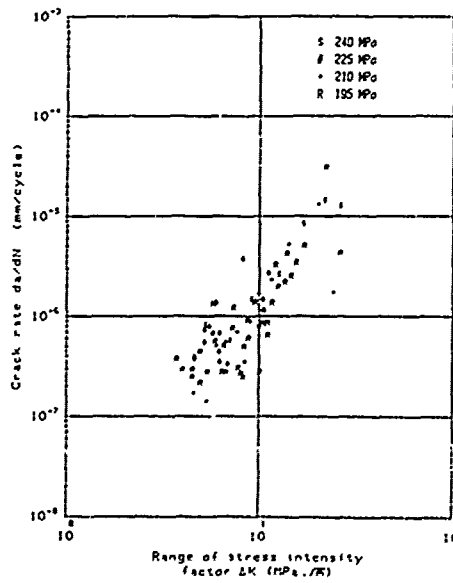


Fig 6 Short crack propagation rates FeTiX loading - 2090-T8E41

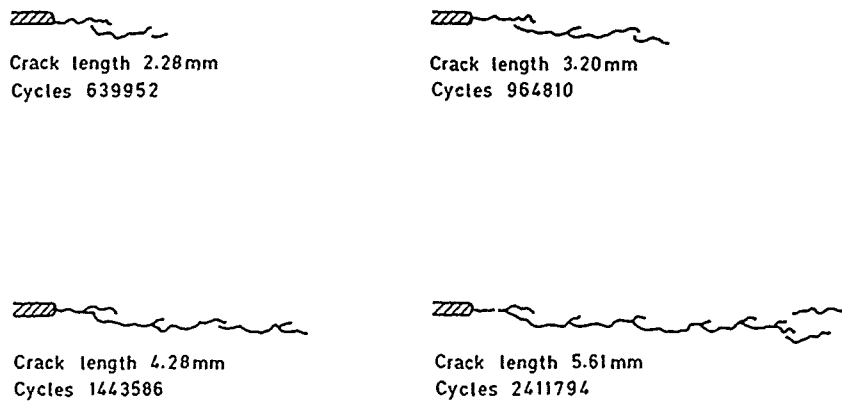


Fig 7 Crack path in long crack 2090-T8E41 FELIX specimen

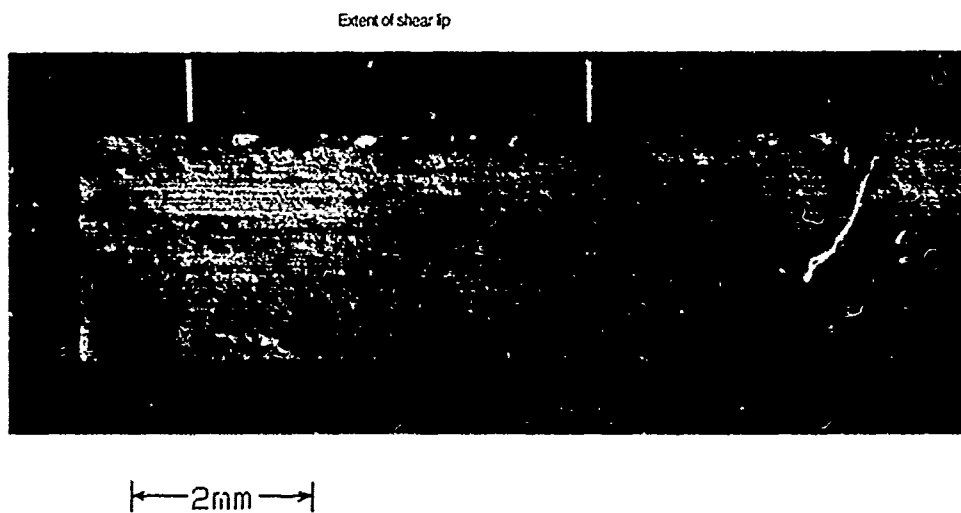


Fig 8 Fracture surface of long crack specimen - FELIX loading - 2090-T8E41

Vertical text on the right margin, possibly a page number or reference.

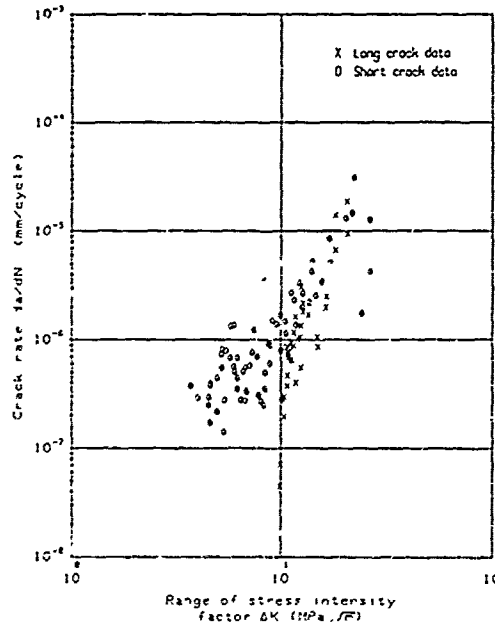


Fig 9 Short and long crack propagation rates Félix loading - 2090-T8E41

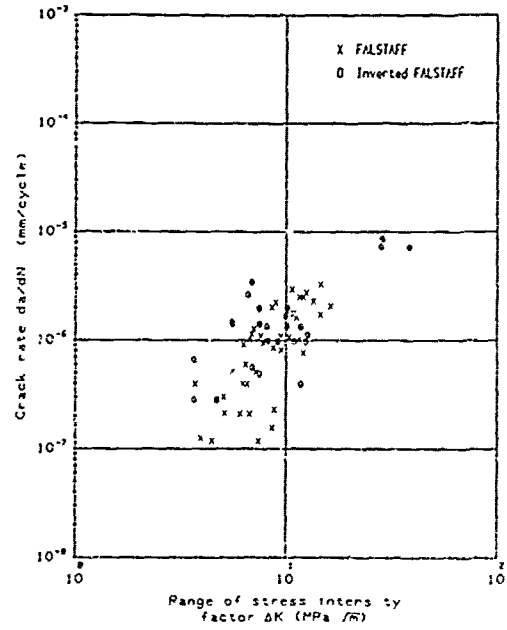


Fig 10 Short crack propagation rates FALSTAFF and inverted FALSTAFF loading 2024-T3, [275 MPa]

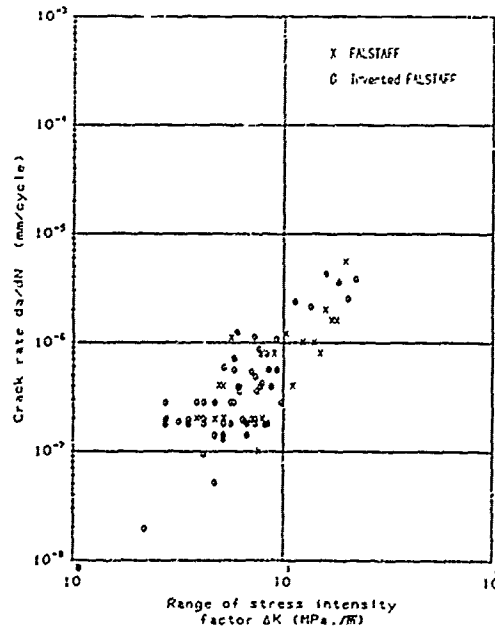


Fig 11 Short crack propagation rates FALSTAFF and inverted FALSTAFF loading 2024-T3, [205 MPa]

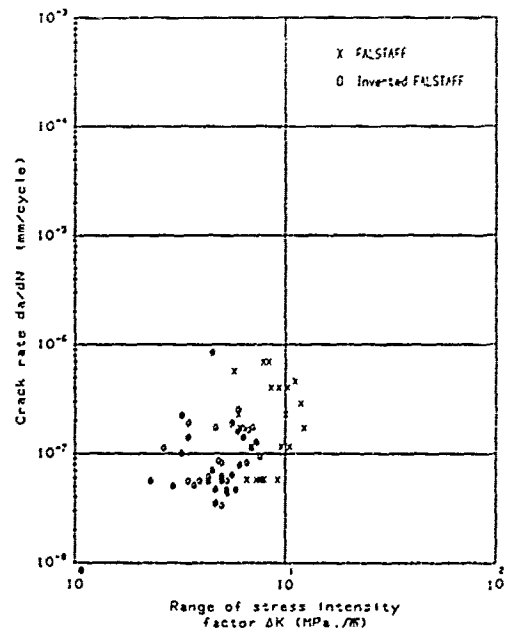


Fig 12 Short crack propagation rates FALSTAFF and inverted FALSTAFF loading 2024-T3, [170 MPa]

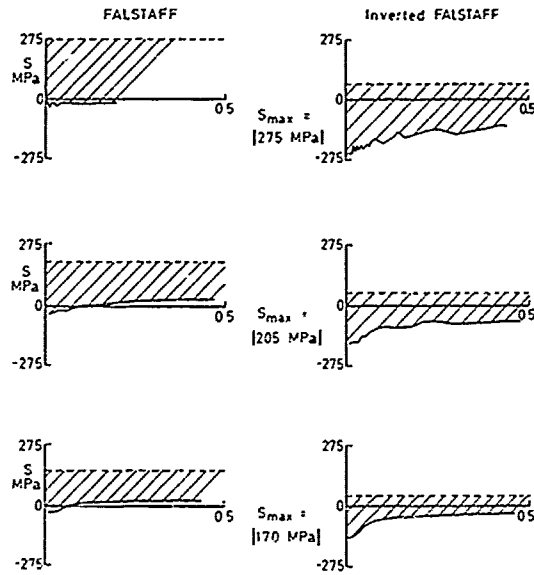


Fig 13 Crack opening stress level for FALSTAFF and inverted FALSTAFF loading

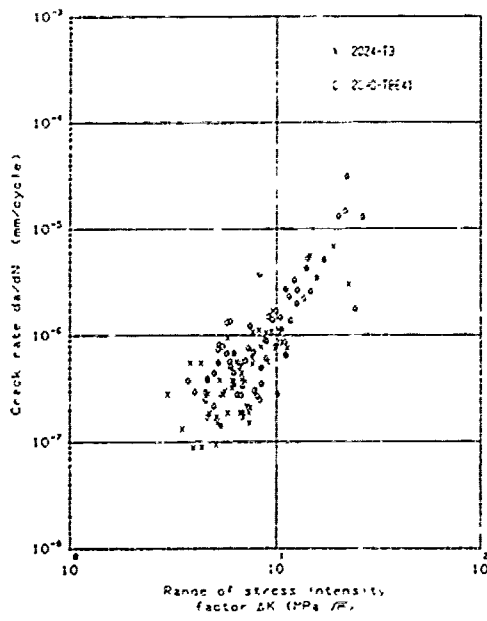


Fig 14 Short crack propagation rates FeTi loading

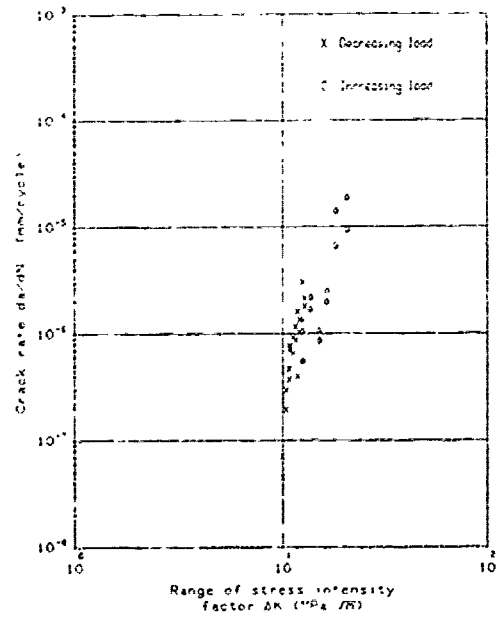


Fig 15 Long crack propagation rates FeTi loading - 2090-T8E41

SHORT CRACK GROWTH UNDER REALISTIC FLIGHT LOADING:
MODEL PREDICTIONS AND EXPERIMENTAL RESULTS FOR AL 2024 AND AL-LI 2090

by
A.F. Blom
Structures Department
The Aeronautical Research Institute of Sweden (FFA)
P.O. Box 11021, S-161 11 Bromma
Sweden

SUMMARY

The Swedish contribution to the AGARD effort on short fatigue crack growth includes various experimental investigations on the aluminium alloys Al 2024-T3 and Al-Li 2090-T8E41. These two materials were subjected both to constant amplitude loading, at stress ratios $R = -2, -1, 0$ and 0.5 and also to spectrum loading with the standardized load sequences FALSTAFF and TWIST, representative for the lower wing surface of fighter and civil aircraft, respectively. The TWIST sequence was also used to generate long crack growth data for the two alloys.

This paper summarizes the experimental results and also includes numerical predictions by means of a modified Dugdale-Barenblatt model originally proposed by Newman. Numerical results correspond well to the observed experimental behaviour for most of the performed tests.

1. INTRODUCTION

Short fatigue cracks have been a primary topic for fatigue related research during the past several years, as evidenced from two recent books on the subject area [1, 2]. It is now well documented that differences in behaviour between long and short cracks are due to a number of reasons, including both microstructural and mechanical aspects. The accumulated knowledge regarding short fatigue crack growth behaviour is still essentially restricted, however, to constant amplitude loading. Although clearly of large academic interest, such loading conditions are hardly representative for the vast majority of mechanical components which are invariably subjected to more or less complex load spectra. Some early investigations on short crack behaviour under spectrum conditions were presented at the AGARD Structures and Materials Panel (SMP) Specialists' Meeting [3]. However, some of those investigations were indeed rather contradictory as to whether there actually does exist a short crack effect under spectrum loading. Consequently, an AGARD Cooperative Test Programme was initiated with 12 laboratories from nine different countries participating.

The core programme, which encompassed testing on the aluminium alloy Al 2024-T3, is now evaluated and reported [4]. It was found that short cracks grew faster than long cracks at the same nominal stress intensity range for FALSTAFF and GAUSSIAN loading, i.e. the so-called short crack anomaly did occur for these load spectra.

Besides from the experimental results themselves, an important outcome of the core programme was that the short crack growth data from the various participants agreed well for both constant amplitude and spectrum load conditions. Also, all participants showed about the same amount of scatter in growth rate data. Several measures, however, were taken prior to testing in order to achieve uniformity in test conditions. These included distribution of machined specimens cut and manufactured from the same batch of material, certain alignment procedures of test machines and gripping fixtures, independent on-line spectrum loading accuracy verification etc., see Ref. [4] for details.

In the supplemental programme, the test matrix was expanded to include both other materials, e.g. Al 7075-T6, Al-Li 2090-T8E41, Ti-6Al-4V and 4340 Steel, and other load spectra, e.g. TWIST, HELIX and inverted FALSTAFF. The various participants have chosen different materials and test conditions depending on specific interest.

This paper summarizes the Swedish part of the supplemental programme. The experimental work involves the same Al 2024-T3 alloy as tested in the core programme, but subjected to TWIST loading. An aluminium-lithium alloy, 2090-T8E41, was also investigated under both constant amplitude loading, at $R = \sigma_{\min}/\sigma_{\max} = 0.5$, and under TWIST and FALSTAFF spectrum loading. Besides from the experimental data, numerical predictions by a modified Dugdale-Barenblatt model are included. Model predictions are performed both for all the various test conditions in the core programme and also for the supplemental testing of the Al 2024-T3 alloy.

2. EXPERIMENTAL PROCEDURES

As the experimental procedures used for the work in the supplemental programme are largely similar to those in the core programme, only the most basic information will be given below. For specific details, see Ref. [4].

2.1 Test Specimens

All short crack growth tests were carried out using single edge notch specimens. The semi-circular notch had a radius of 3.18 mm resulting in an elastic stress concentration $K_t = 3.17$, based on gross-section stress. The 305 mm long and 50 mm wide specimens were cut from sheets, of 2.3 mm (Al 2024-T3) and 2.15 mm (Al-Li 2090-T8E41) thickness, so that the loading direction was applied in the rolling direction of the materials, i.e. L-T orientation.

For the long crack growth data obtained under load shedding of the THIST spectrum, conventional centre-cracked specimens of 76.2 mm width, L-T orientation, were used.

2.2 Materials

A detailed microstructural description of the Al 2024-T3 alloy is given in Annex A of Ref. [4]. The ultimate tensile strength is 495 MPa, yield strength is 355 MPa and elongation is 21%. The grain size in the rolling direction is about 95 μm . Typical grain dimensions in the crack growth directions, 2a and c, are 25 μm and 55 μm , respectively.

The Al-Li 2090-T8E41 alloy was obtained from the United States Air Force Wright Aeronautical Laboratories. The ultimate tensile strength is 568 MPa, yield strength is 526 MPa and elongation is 5% [5]. Further details on the same aluminium-lithium alloy can be found in, for example, Ref. [6]. The sheet, which is in the un-recrystallized form, has a very strongly developed deformation texture that changes its type from the surface to the mid-plane [7]. This texture is related to the mechanical anisotropy in the material. It is reported that the yield strength is about 15% lower in the 50°-plane where the ductility is largest [5].

2.3 Test Equipment

All tests were performed in MTS servohydraulic testing machines in ambient laboratory air. Hydraulic grips were used throughout and anti-buckling guides, with teflon sheets, were used for all constant amplitude tests at negative stress ratios and for all spectrum tests. Constant amplitude tests were run at cyclic frequencies in between 5 to 20 Hz. Spectrum tests were performed with constant displacement rates resulting in frequencies around 10 Hz. Prior to testing the test machines and the gripping fixtures were aligned in accordance with the methodology described in Annex C in Ref. [4].

2.4 Loading Conditions

In the core programme the Al 2024-T3 alloy was tested at $R = 0, -1, -2$ and with FALSTAFF. Other participants also investigated $R = 0.5$ and GAUSSIAN loading. For each test condition three different load levels were used. These are given in Table 6 in Ref. [4].

In the supplemental programme the Al 2024-T3 alloy was also investigated under THIST spectrum loading with maximum gross stress levels of 225 and 275 MPa. The Al-Li 2090-T8E41 alloy was tested at $R = 0.5$, with maximum gross stress levels of 150, 180 and 200 MPa, with FALSTAFF, with maximum gross stress levels of 200 and 240 MPa, and with THIST at a maximum gross stress level of 240 MPa.

FALSTAFF [8, 9] is a standardized load spectrum, based on a large number of actual flight load-time histories pertaining to five different fighter aircraft types operated by three different air forces, representative of the load-time history in the lower wing skin near the wing root of a fighter aircraft. The total sequence, constituting 200 flights, consists of 35 996 half cycles distributed over 32 different load levels as indicated in the cumulative exceedance distribution shown in Figure 1(a). An example of typical flights is shown in Figure 1(b). The severity of the spectrum is here identified by the stress which the test specimen experiences at the highest load level in the total sequence. During the core programme, the ability to accurately apply the FALSTAFF loading sequence was independently checked, see Annex D in Ref. [4], with a good set of results as outcome.

THIST [10, 11] is also a standardized load spectrum. It is representative for the load history of the wing root of transport aircraft and is based on center of gravity measurements on DC-9, Boeing 737, BAC 1-11 and the military transport Transall, and on theoretical frequency distribution of DC-10, Fokker F-27 and F-28 aircraft. The total sequence, with a return period length of 4000 flights, consists of 398 665 load cycles distributed over ten different flights. The load spectrum, based on a level crossing count of gust load cycles and tie ground to air cycles, is shown as a cumulative exceedance distribution in Figure 2(a) and the first 150 cycles of flight type H are shown in Figure 2(b). Taxi loads are omitted in THIST. The severity of the spectrum is here identified in analogy to the FALSTAFF sequence above, i.e. by the stress level related to the highest load level in the total sequence.

2.5 Short Crack Measurements

All measurements of short crack growth data were performed with a plastic replica method as outlined in Annex E of Ref. [4]. It was found that best results were obtained when the specimens were not etched prior to testing.

For each test condition, i.e. combination of loading and applied stress, two different sorts of tests were performed. Firstly, in order to obtain surface crack length versus no. of load cycles data, one specimen was tested until one continuous crack was all the way across the notch root. The specimen was then statically pulled to failure. Secondly, in order to obtain information on surface crack length to crack depth shape, one specimen was tested until the total surface crack length along the bore of the notch was between 0.5 and 1.0 mm. Then, the specimen was broken statically.

Measurement results were recorded on data charts, as shown in Figures 12 and 14 of Ref. [4], giving a means to illustrate both the exact shape of the cracks and the growth behaviour in the case of several cracks. Crack lengths used for data evaluation are the projected crack lengths normal to the loading axis. Crack growth rates and stress intensity factors were calculated according to section 3.5 and Annex F of Ref. [4]. The non-interaction criteria given in section 4.2 of that reference were applied to the raw data, which significantly reduced the total amount of scatter in the data.

2.6 Long Crack Measurements

The TWIST load sequence was applied to centre cracked specimens in order to obtain long crack growth data over a wide range of crack growth rates. This was done by firstly load shedding the total sequence down to the threshold regime and then increasing the reference load by a certain fraction to obtain crack growth data under R -increasing conditions until fracture occurred. The load shedding was performed by reducing the reference load with 5% of the immediately prior load level after a crack growth increment of 0.5 mm. The test procedure is extremely tedious with some tests running up to six months. The same sort of experiments were performed on FALSTAFF, but with larger load reduction in each step, Annex G of Ref. [4], and on the GAUSSIAN load sequence with a fixed load decrement, Annex H of Ref. [4].

3. NUMERICAL MODELLING

Although both microstructural and statistical models have been proposed to account for short crack effects, e.g. [1, 2], these have in common that they rely on extensive experimental data to fit various constants in the derived crack growth equations. From a mechanistical point of view, the very origin of the small crack effect arises primarily from the lack of an appropriate crack driving force for short cracks. This problem is both related to the inability of the elastic stress intensity factor to describe the crack tip fields when the crack is small compared to microstructural features or the crack tip plastic zone size, and that crack tip shielding mechanisms are not fully developed for short cracks [12]. These latter mechanisms, principally involving crack closure in its various forms, were recently found to be the primary cause for differences in the behaviour between long and short cracks [12]. However, as cracks of small size were found to propagate below the effective threshold stress intensity range, such other factors as mentioned above are clearly relevant.

In the following, only plasticity-induced crack closure will be used as a basis for modelling of short crack effects. This is because this form of crack closure is the only one that can be used to predict the development of closure with increasing crack length in a quantitative way, as evidenced from recent finite element modelling [12-14]. However, it should be pointed out that measured closure levels (in plane strain) were found to be significantly higher than numerical plane strain predictions [12, 14]. Such discrepancies were attributed to the fact that the primary contribution to closure at near-threshold levels, where short crack effects mostly are observed, in the investigated Al 2124 alloy is due to roughness-induced closure. The relative importance of various types of crack closure was investigated by studying both underaged and overaged microstructures [12, 14].

Despite such shortcomings as mentioned above, the plasticity-induced crack closure concept has been utilized in the core programme of the current AGARD activity with very good results [4]. The model used, originally developed by Newman [15] and already applied to short cracks in Refs. [16, 17], is based on the Dugdale model but modified to leave plastically deformed material in the wake of the crack. Here, an extension of this model [18] to include the concept of weight functions in order to facilitate the analysis of any two-dimensional geometry is used to evaluate experimental data from both the core programme and the supplemental programme. The utilized model has been verified [18] for both plane stress and plane strain computations of crack closure in a CT-specimen subjected to constant amplitude loading at different stress ratios by comparing the results with those earlier obtained by elastic-plastic finite element modelling [19, 20]. Further on, the model has been used very successfully to predict the transient crack growth rate response of a titanium alloy following various overloads [21].

Numerical predictions presented subsequently have been performed with the same input parameters, regarding effective crack growth properties etc., for the Al 2024-T3 alloy as in Ref. [4]. This also means that plane strain conditions have been assumed for short crack growth under all loading conditions.

4. RESULTS

Below will results from both the core programme and the supplemental programme be given. As all the experimental data of the core programme have already been included in Ref. [4], a detailed account will not be repeated here. Instead, the performed numerical predictions will be presented and compared to the data in Ref. [4] and to the calculations included therein.

4.1 Core Programme

Identical computations as those performed in Ref. [4] were carried out to evaluate the computer code being used. Firstly, the increase in computed crack opening stresses upon crack extension is shown in Figure 3(a) for the four stress ratios being used in constant amplitude testing. The results are in rather good agreement to those presented in Figure 75 of Ref. [4]. For the two negative stress ratios minima in predicted crack growth rates occur at crack lengths indicated in Figure 3(a). Such minima have indeed been observed experimentally, e.g. [22], but are mostly attributed to interaction of the advancing crack with grain boundaries. It is interesting to note that the predicted development of closure at $R = 0$ is similar to plane strain elastic-plastic finite element calculations performed at $R = 0.1$ in Ref. [12]. Further on, it should be observed that virtually no closure effect occurs at $R = 0.5$, but that the effect is becoming more prevalent at negative stress ratios, in accordance with experimental observations, where also an effect or plastic stress level becomes important.

Figure 3(b) compares experimental and predicted surface crack shapes under constant amplitude loading at $R = -1$. It appears that the growth behaviour of both naturally initiated cracks and artificially introduced defects is accurately modelled.

Experimental and predicted crack growth rates for short cracks under all the various loading conditions are shown in Figures 4 through 9, for $R = -2, -1, 0, 0.5$, FALSTAFF and GAUSSIAN loading, respectively. Also shown in these figures are the long crack data for comparison. The GAUSSIAN load sequence used for these calculations is not identical to the sequence used for testing. That sequence has a block size of about one million cycles. Here, another GAUSSIAN sequence, see Figure 10, consisting of only 10 000 load cycles, but with the same irregularity factor ($I = N_0/N_1 = 0.99$ where N_0 is the no. of mean level crossings with positive slope and N_1 is the no. of peak loads) was devised for the computations. For $I = 0.99$, this difference from the test sequence should be negligible. All other input data to the calculations, e.g. initial crack size, plane strain constraint factor and effective stress intensity range versus crack growth rate relationship, were the same as in Ref. [4].

Comparing the predictions in Figures 4 to 9 with those in Ref. [4], it is readily seen that the two sets of calculations are in good general agreement. However, a closer comparison shows that the current numerical model always predicts slightly lower crack growth rates than the predictions in Ref. [4]. At a stress ratio $R = 0.5$, Figure 7, the effect of applied stress level on predicted results is rather small whereas particularly at negative stress ratios, Figures 4 and 5, but also in spectrum loading, Figures 8 and 9, this effect becomes very obvious. Altogether, the general agreement of measured and predicted short crack growth rates is clearly excellent albeit somewhat unexpected in view of the above discussion on many additional mechanisms that are known to influence short crack growth behaviour.

Finally, predicted fatigue lives to breakthrough, i.e. when a continuous crack was all the way across the notch root, are shown together with experimental data in Figures 11 to 13 for positive stress ratios, negative stress ratios and the spectrum loading conditions, respectively. Note that the TWIST results for Al 2024-T3, from the supplemental programme, also are included in Figure 13. A careful comparison of the current predictions to those in Ref. [4] reveals that the current numerical model predicts about 10% higher life and around 5-6% higher closure loads than Newman's original model as applied in Ref. [4]. The one exception to this general result is the GAUSSIAN loading case for which slightly shorter lives were predicted in the current paper than in Ref. [4]. This may, however, be attributed to the difference in the GAUSSIAN load sequences, as mentioned above.

4.2 Supplemental Programme

The experimental short crack data obtained on Al 2024-T3 under TWIST loading are shown in Figure 14 together with predicted results using exactly the same input parameters as in the core programme. As can be seen from Figure 14 the effect of the applied stress levels, $\sigma_{max} = 225$ and 275 MPa, on the growth rates is very small. Also shown in Figure 14 are long crack growth rates as obtained with the load shedding procedure of the TWIST sequence. The short crack effect is observed also for the TWIST sequence. At higher crack growth rates the short and long crack data overlap.

Short crack growth data for the Al-Li 2090-T8E41 alloy are summarized in Figures 15 to 17 for $R = 0.5$, FALSTAFF and TWIST loading, respectively. The first interesting observation from these Figures is that the growth rates are remarkably close to those presented for aluminium alloy 2024-T3 above. It should be noted though, that surface crack lengths were taken as the projected crack length normal to the loading direction, whereas the actual crack growth morphology is highly deflected for the $R = 0.5$ and FALSTAFF loading, see Figures 18 and 19, respectively. For some hitherto unknown reason the crack paths for TWIST loading is entirely different, see Figure 20.

Comparing the short crack growth rates for $R = 0.5$ to long crack growth data obtained on the same Al-Li alloy, and in the same orientation, L-T, by other workers [4, 5] it seems that the short crack effect is virtually absent at this high stress ratio, Figure 15. The comparison to Ref. [5], which is most relevant as they tested specimens cut from the same sheet, gives almost identical growth rates for short and long cracks at $R = 0.5$. This is also what was found for Al 2024-T3 at the same stress ratio in the core programme [4].

For the FALSTAFF results shown in Figure 16 the author has not yet access to any long crack data. He would expect significantly slower growth rates for long cracks though. A detailed comparison of the Al-Li data in Figure 16 to FALSTAFF data for Al 2024-T3 shows that the aluminium lithium alloy has a higher mean crack growth rate, although the data is overlapping.

For TWIST loading, the Al-Li data is within the scatterband for Al 2024. Long crack data for the TWIST sequence is included in Figure 17. Also here a short crack effect is obvious for low stress intensities, whereas the data converge at higher crack growth rates.

It is particularly interesting to compare the crack growth paths shown in the data charts in Figures 18-20. The results shown for $R = 0.5$ and FALSTAFF loading, Figures 18 and 19, agree excellently with published results valid for constant amplitude loading, e.g. [23]. The TWIST results in Figure 20, however, are of entirely different character. The crack path is very straight, exhibiting no typical aluminium-lithium features, and the data is repetitive in the sense that several performed tests yield the same smooth crack path.

The specific reason for this behaviour during TWIST loading is still unknown. It may perhaps be related to the high mean stress of the many gust loads occurring in the spectrum, which gives a very small ratio of reversed to monotonic plastic zone size at the crack tip.

Modelling of the Al-Li data is under way but not yet completed. Those results will be published in a separate report.

5. CONCLUSIONS

Based on numerical modelling and short crack growth experiments conducted on a 2024-T3 aluminium alloy and a 2090-T8E41 aluminium-lithium alloy, the following conclusions can be made:

- The analytical results coincide in general very well with observed experimental results.
- The performed calculations constitute an independent verification of the crack closure model being used in the AGARD core programme on short cracks.
- The current numerical model predicts about 10% higher life and around 5-6% higher closure loads than Newman's original model.
- Short crack data for the two studied alloys are overlapping for all load conditions.
- During constant amplitude loading short cracks grew below the long crack threshold stress intensity factors.
- During spectrum loading and for constant amplitude loading at negative stress ratios, short cracks grew faster than long cracks at the same stress intensity ranges.
- A stress level effect is very pronounced at negative stress ratios and also becomes apparent for some spectrum loading. This effect manifests itself in higher short crack growth rates at higher load levels for the same stress intensity range.
- The crack path in the aluminium-lithium alloy is highly deflected for $R = 0.5$ and FALSTAFF loading but straight for THIST loading.

6. REFERENCES

1. Miller, K.J. and de los Rios, E.R. (Eds), The Behaviour of Short Fatigue Cracks, Mechanical Engineering Publications, Institution of Mechanical Engineers, London, 1986.
2. Ritchie, R.O. and Lankford, J. (Eds), Small Fatigue Cracks, TMS-AIME, Warrendale, PA, 1986.
3. Behaviour of Short Cracks in Airframe Components, AGARD Conference Proceedings, AGARD-CP-328, 1983.
4. Short-Crack Growth Behaviour in an Aluminum Alloy - An AGARD Cooperative Test Programme, AGARD Report No. 722, December 1988.
5. Mazur, C and Rudd, J., Informal presentation at the AGARD SHP meeting in Luxembourg, spring 1988.
6. Venkateswara Rao, K.T., Yu, W. and Ritchie, R.O., Fatigue Crack Propagation in Aluminum-Lithium Alloy 2090: Part I. Long Crack Behaviour, Metall. Trans. A, Vol. 19A., 1988. pp. 549-561.
7. Bowen, A.W., Texture Analysis of 2090 Al-Li Alloy Sheet, R 178, The Royal Aerospace Establishment, July 1988. Also an annex in the current supplemental report.
8. Aicher, H., Branger, J., van Dijk, G.M., Ertelt, J., Hück, H., de Jonge, J., Lowak, H., Rhorberg, H., Schütz, D. and Schütz, W., Description of a Fighter Aircraft Loading Standard for Fatigue Evaluation, FALSTAFF, F+W (Switzerland), LBF (Germany), NLR (The Netherlands), and IABG (Germany), March 1976.
9. van Dijk, G.M. and de Jonge, J.B., Introduction to a Fighter Aircraft Loading Standard for Fatigue Evaluation FALSTAFF, NLR MP 75017U, May 1975.
10. Schütz, D., Erstellung eines standardisierten Kollektives für die Flugelwurzel eines Verkehrsflugzeuges, LBF-Technical Note No. TM 55/70, 1972.
11. de Jonge, J.B., Schütz, D., Lowak, H. and Schijve, J., A Standardized Load Sequence for Flight Simulation Tests on Transport Aircraft Wing Structures, LBF-Bericht FB-106, NLR-Report TR73, 1973.
12. Ritchie, R.O., Yu, W., Blom, A.F. and Holm, D.K., An Analysis of Crack Tip Shielding in Aluminum Alloy 2124: A Comparison of Large, Small, Through-Thickness and Surface Fatigue Cracks, Fatigue Fract. Engng Mater. Struct., Vol. 10, 1987, pp. 343-362.
13. Holm, D.K. and Blom, A.F., Short Cracks and Crack Closure in Al 2024-T3, Proceedings of the 14th Congress of the Int. Council of Aeronautical Sciences, Toulouse, France, 1984, pp. 783-790.
14. Ritchie, R.O., Yu, W., Holm, D.K. and Blom, A.F., Development of Fatigue Crack Closure with the Extension of Long and Short Cracks in Aluminum Alloy 2124: A Comparison of Experimental and Numerical Results, Mechanics of Fatigue Crack Closure, J.C. Newman, Jr. and W. Eiber, eds., American Society for Testing and Materials, ASTM STP 982, 1988.
15. Newman, J.C., Jr., A Crack-Closure Model for Predicting Fatigue Crack Growth Under Aircraft Spectrum Loading, Methods and Models for Predicting Fatigue Crack Growth Under Random Loading, J.B. Chang and C.M. Hudson, eds., American Society for Testing and Materials, ASTM STP 748, 1981, pp. 53-84.

16. Newman, J.C., Jr., A Nonlinear Fracture Mechanics Approach to the Growth of Small Cracks, in Ref. [3], 1983, pp. 6.1-6.26.
17. Newman, J.C., Jr., Swain, M.H. and Phillips, E.P., An Assessment of the Small-Crack Effect for 2024-T3 Aluminum Alloy, in Ref., [2], 1986, pp. 491-511.
18. Wang, G.S. and Blom, A.F., A modified Dugdale-Barenblatt Model for Fatigue Crack Growth Predictions Under General Load Conditions, FFA TN 1987-79, The Aeronautical Research Institute of Sweden, Bromma, 1987, Submitted for publication.
19. Blom, A.F., Near-Threshold Fatigue Crack Growth and Crack Closure in 17-4 PH Steel and 2024-T3 Aluminium Alloy, Fatigue Crack Growth Threshold Concepts, D.L. Davidson and S. Suresh, eds., TMS-AIME, Warrendale, PA, 1984, pp. 263-279.
20. Blom, A.F. and Holm, D.K., An Experimental and Numerical Study of Crack Closure, Engng Fract. Mech., Vol. 22, 1985, pp. 997-1011.
21. Ward-Close, C.M., Blom, A.F. and Ritchie, R.O., Mechanisms Associated with Transient Fatigue Crack Growth Under Variable-Amplitude Loading: An Experimental and Numerical Study, Engng Fract. Mech., in press.
22. Blom, A.F., Hedlund, A., Zhao, W., Fathulla, A., Weiss, B. and Stöckler, R., Short Fatigue Crack Growth Behaviour in Al 2024 and Al 7475, in Ref. [1], 1986, pp. 37-66.
23. Venkateswara Rao, K.T., Yu, W. and Ritchie, R.O., Fatigue Crack Propagation in Aluminum-Lithium Alloy 2090: Part II. Small Crack Behavior, Metall. Trans. A, Vol. 19A, 1988, pp. 563-569.

ACKNOWLEDGEMENTS

The financial support of the Defence Material Administration for this work is gratefully acknowledged. The author is indebted to H. Bjermert, A. Linder, B. Wallstenius, L. Nystedt, G.S. Wang, B. Palmberg and G. Ahlberg for help during the course of this work.

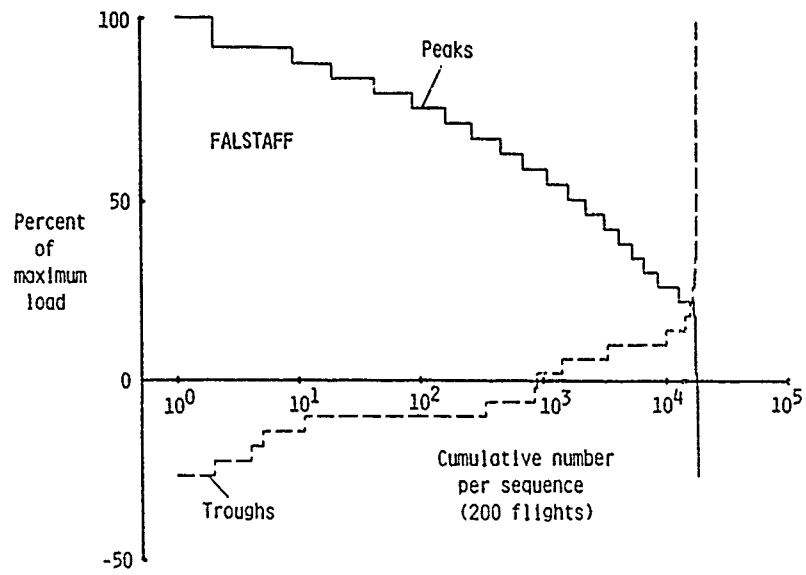


Figure 1(a). - Cumulative number of peaks and troughs in FALSTAFF sequence

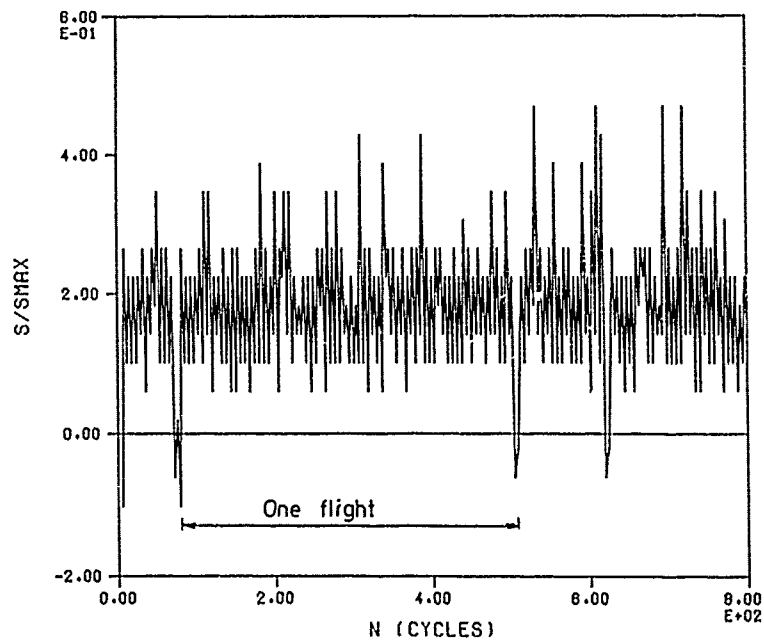


Figure 1(b). - Typical flights in FALSTAFF sequence

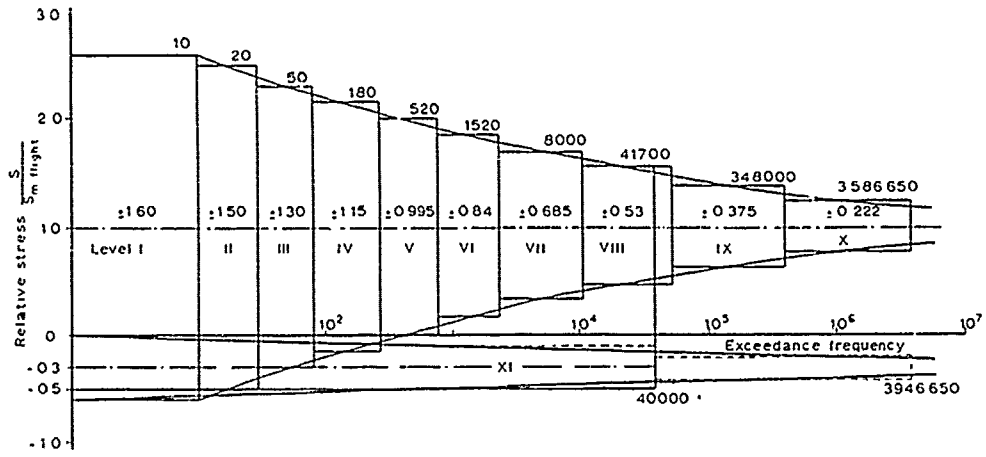


Figure 2(a). - THIST load spectrum for 40 000 flights

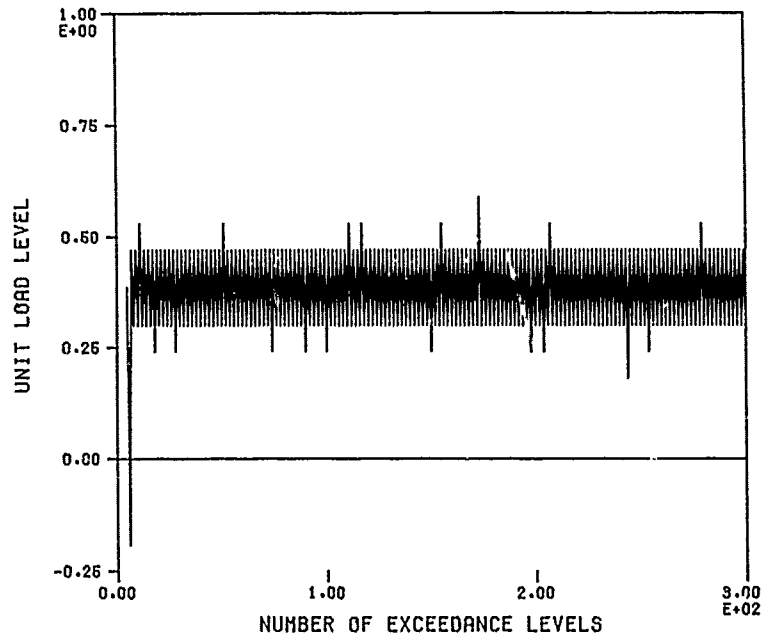


Figure 2(b). - THIST Flight Type H. First 150 cycles

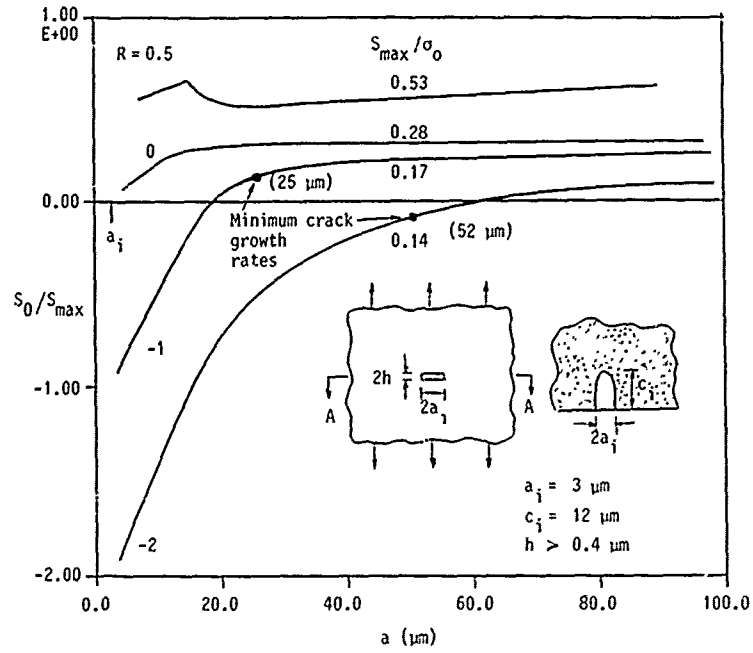


Figure 3(a). - Calculated crack opening stress levels at different stress ratios as function of crack length. Al 2024-T3 under plane strain conditions

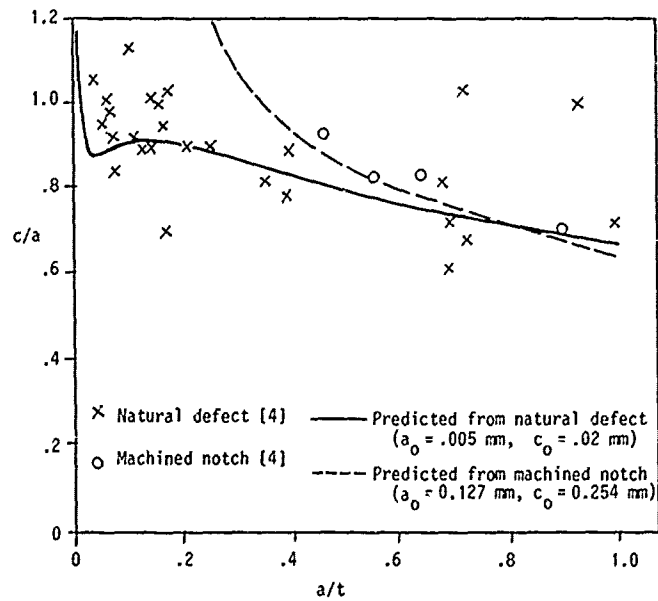


Figure 3(b). - Comparison of experimental and predicted surface crack shapes in Al 2024-T3 at R = -1

da/dN (m/cycle)

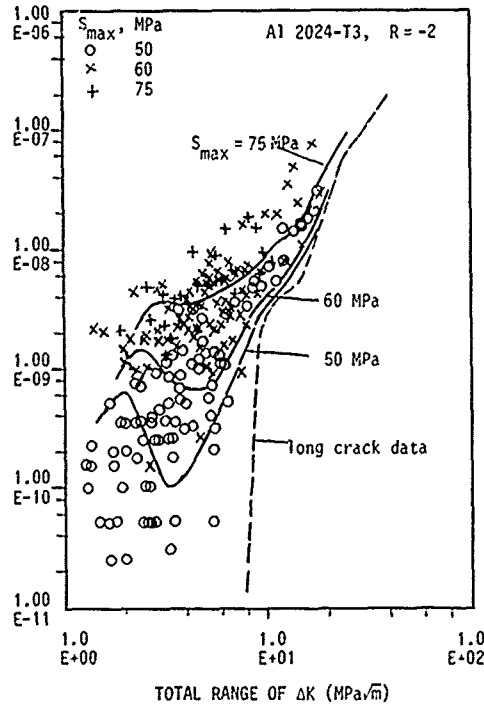


Figure 4. - Experimental and predicted crack growth rates for short cracks in Al 2024-T3 under R = -2 loading

da/dN (m/cycle)

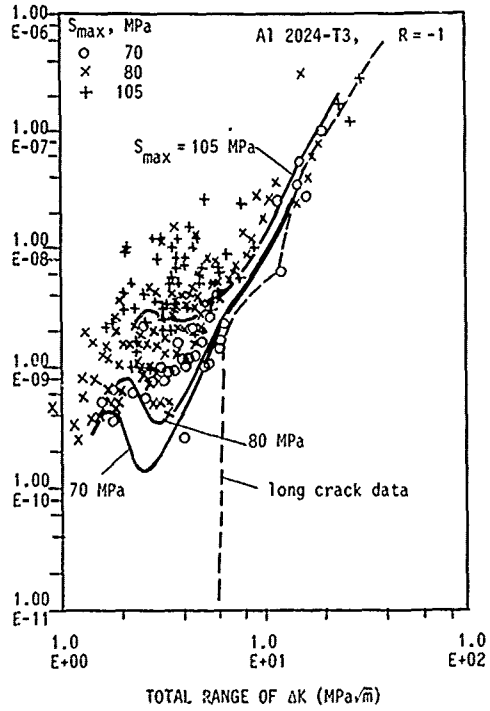


Figure 5. - Experimental and predicted crack growth rates for short cracks in Al 2024-T3 under R = -1 loading

da/dN (m/cycle)

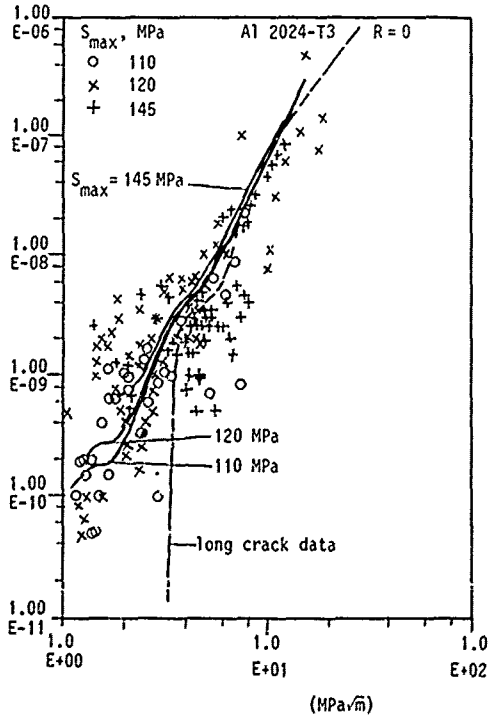


Figure 6. - Experimental and predicted crack growth rates for short cracks in Al 2024-T3 under R = 0 loading

da/dN (m/cycle)

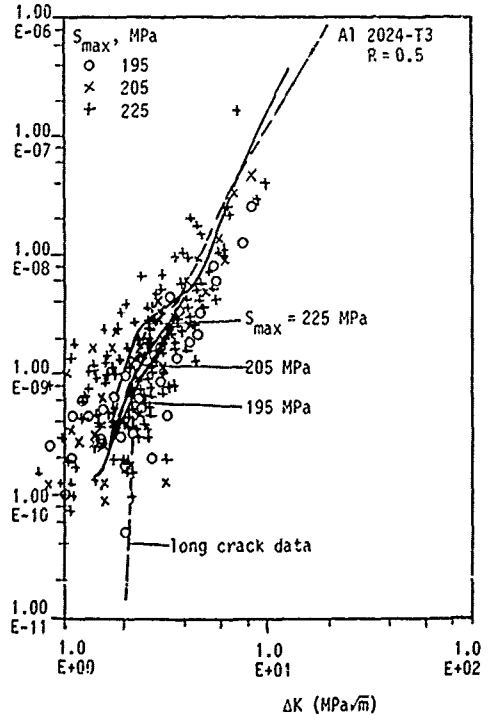


Figure 7. - Experimental and predicted crack growth rates for short cracks in Al 2024-T3 under R = 0.5 loading

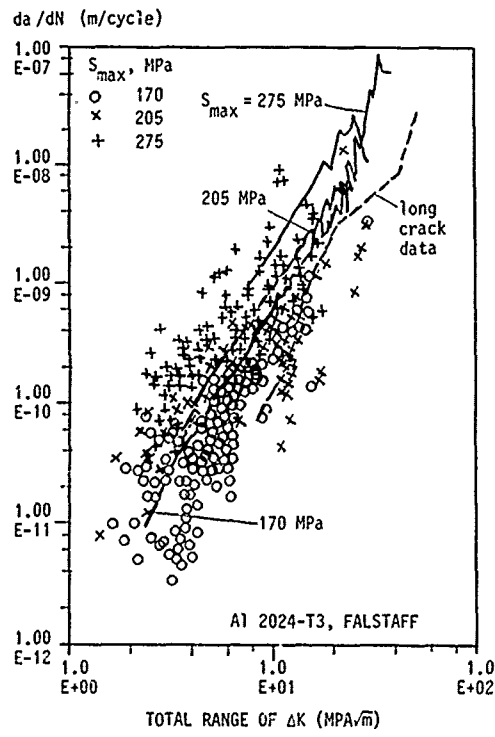


Figure 8. - Experimental and predicted crack growth rates for short cracks in Al 2024-T3 under FALSTAFF loading

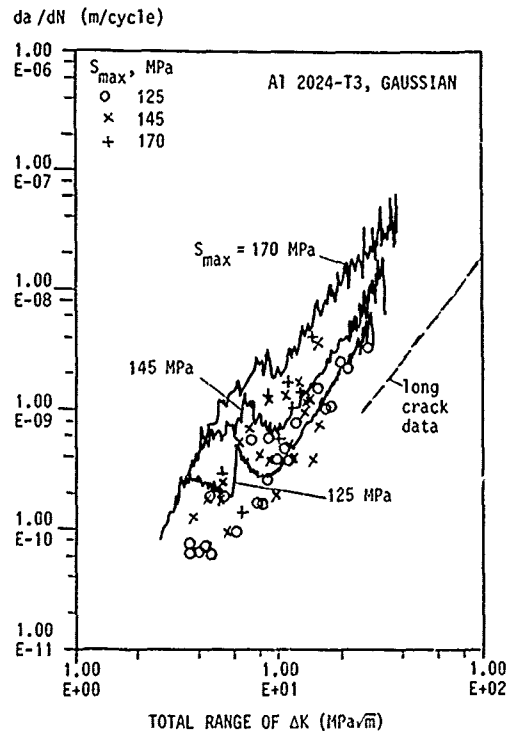


Figure 9. - Experimental and predicted crack growth rates for short cracks in Al 2024-T3 under GAUSSIAN loading

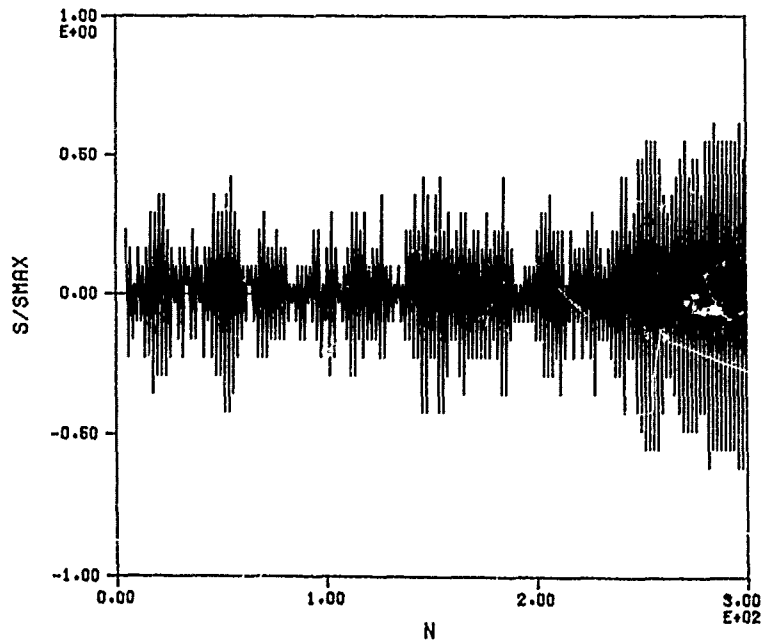


Figure 10. - Part of the GAUSSIAN sequence ($I = 0.99$) used for numerical predictions

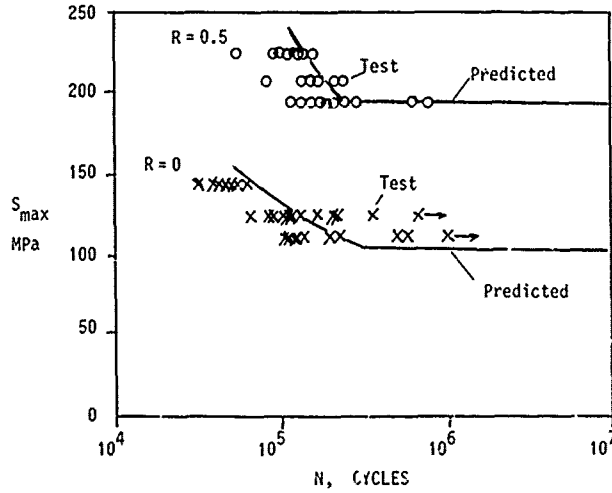


Figure 11. - Experimental and predicted fatigue life to breakthrough in Al 2024-T3 under constant-amplitude loading at positive stress ratios

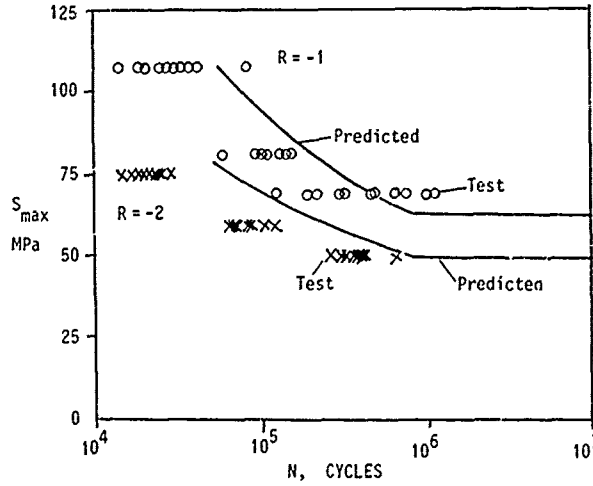


Figure 12. - Experimental and predicted fatigue life to breakthrough in Al 2024-T3 under constant-amplitude loading at negative stress ratios

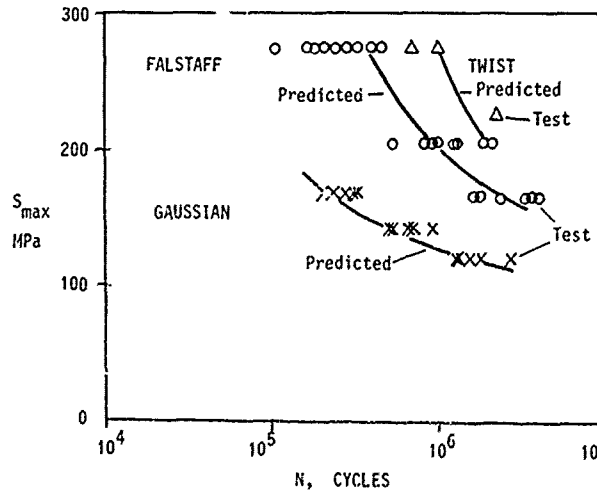


Figure 13. - Experimental and predicted fatigue life to breakthrough in Al 2024-T3 under FALSTAFF, GAUSSIAN and TWIST loading

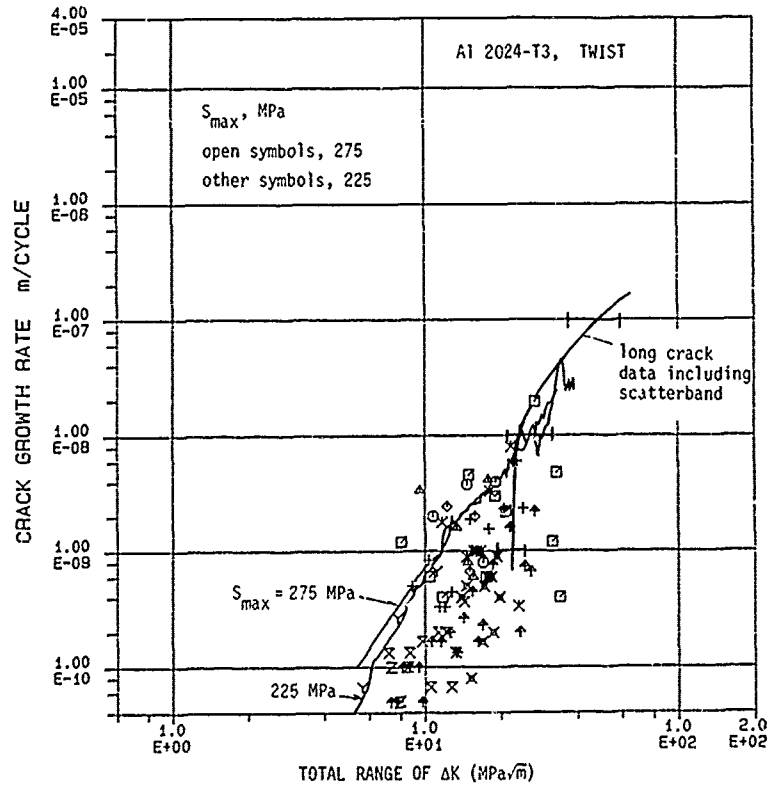


Figure 14. - Experimental and predicted crack growth rates for short cracks in Al 2024-T3 under TWIST loading

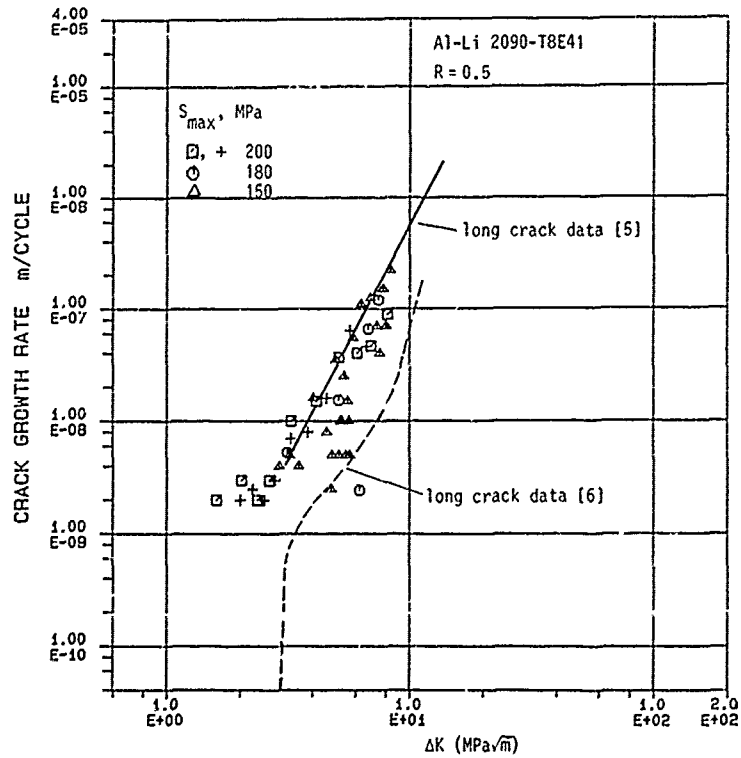


Figure 15. - Short and long crack growth data for Al-Li 2090-T8E41 at R = 0.5

Downloaded from ascelibrary.org by University of California, San Diego on 06/16/15. Copyright ASCE. For all rights reserved.

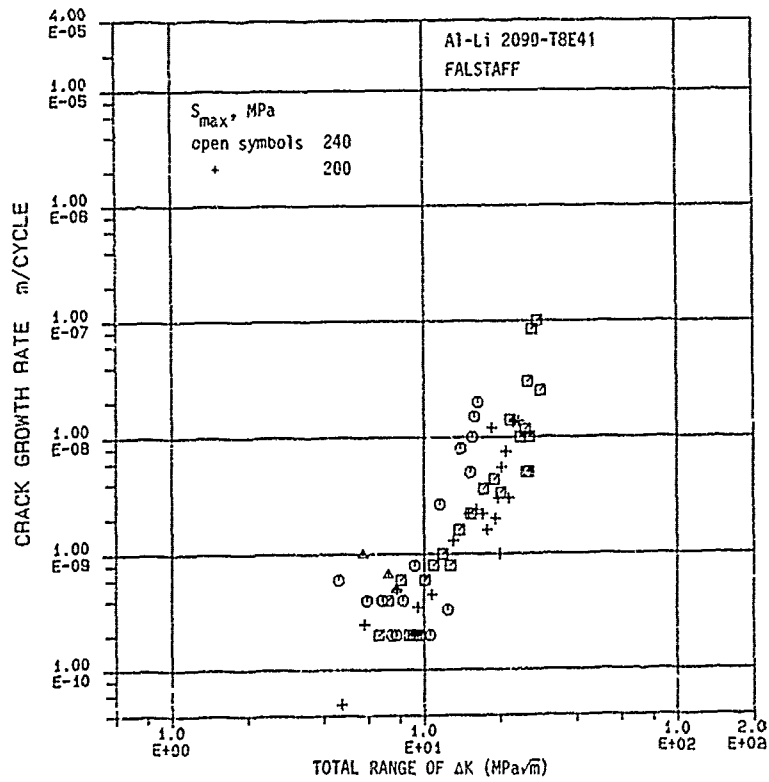


Figure 16. - Short crack growth data for Al-Li 2090 T-8E41 under FALSTAFF loading

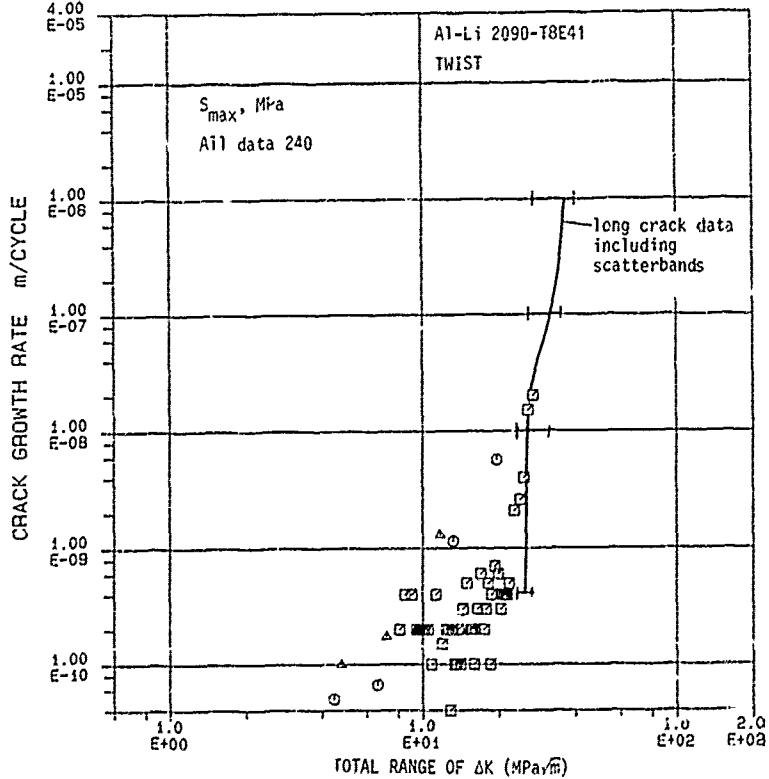


Figure 17. - Short and long crack growth data for Al-Li 2090-T8E41 under TWIST loading

THE GROWTH OF SHORT CRACKS IN 4340 STEEL AND ALUMINUM-LITHIUM 2090

M.H. Swain
Lockheed Engineering & Sciences Company
Hampton, VA 23666

R.A. Everett
U.S. Army, Aviation Research and Technology Activity
Army Aviation Systems Command
Hampton, VA 23665

J.C. Newman, Jr., and E.P. Phillips
NASA Langley Research Center
Hampton, VA 23665

ABSTRACT

This work was undertaken as part of an AGARD Supplemental Test Programme for investigating the short crack growth behavior in various airframe alloys. The objectives of the research were to investigate crack initiation characteristics and short crack growth behavior for Al-Li 2090 and 4340 steel and to evaluate the ability of a closure-based crack-growth model to predict fatigue crack growth rates and total fatigue lives for the steel. Single-edge-notched tension specimens of each alloy were used to obtain the short crack growth rate information via an acetate replica technique. In addition to constant amplitude loading, tests on the steel were conducted using the Felix/28 variable amplitude spectrum (a shortened form of a standard loading sequence for 'fixed' or semi-rigid helicopter rotors). The short crack growth rates were compared to those for long cracks grown under similar loading conditions. Metallurgical features associated with crack initiation are discussed.

For Al-Li 2090 under $R = -1$ loading, the short cracks grew well below the long crack threshold and grew at acute angles (approximately 35°) to the loading axis. For 4340 steel under constant amplitude loading at $R = 0.5$ and 0 and for the Felix/28 spectrum loading, short-crack growth rates agreed well with long-crack growth rates, even near the long-crack threshold. A slight short-crack effect, growth below the long-crack threshold, was observed at $R = -1$. Fatigue lives were found to depend on the size and type of initiation site, especially for the Felix/28 loading sequence.

A semi-empirical crack-growth model incorporating crack-closure effects was used to predict crack growth rates and total fatigue lives of notched 4340 steel specimens. An initial defect size and shape typical of those identified in this steel was assumed for the life predictions. For all loading conditions, reasonable agreement was found between measured and predicted values for both crack growth rates and fatigue lives. In general, the predicted lives were somewhat shorter than those measured experimentally and, therefore, were conservative. For $R = -1$ loading conditions, however, the model tended to predict lives which were slightly longer than experimental values.

INTRODUCTION

The current investigation of short-crack growth behavior in 4340 steel and Al-Li 2090 was undertaken as part of an AGARD Supplemental Programme on short-crack growth behavior. It follows an extensive cooperative testing and analytical project on 2024-T3 aluminum alloy sheet, the results of which have been published in AGARD Report Number 732 [1], and will hereinafter be referred to as the Core Programme.

In the present work it was of interest to investigate the crack initiation and short-crack growth characteristics for quenched and tempered 4340 steel, a high strength alloy which exhibits a small prior austenite grain size containing an even more finely divided microstructure of tempered martensite. Because the crack would traverse several martensite lathes when it was still quite small, it was expected [2,3] that a material with this type of microstructure would exhibit less pronounced short crack behavior than was observed in the Core Programme for 2024-T3. The objectives were to obtain crack growth data for short and long cracks over a range of loading conditions and to determine the capability of a crack-growth model, incorporating crack closure effects, to predict fatigue crack growth rates and total fatigue lives from small pre-existing material defects in each case.

The 4340 steel selected is commonly used in dynamically loaded helicopter rotor components. For this reason, it was appropriate to choose Felix/28, a standard spectra developed for 'fixed' or semi-rigid helicopter rotors, [4] for the variable amplitude load spectra employed in this study. The combination of experimental results from this spectrum with the range of constant amplitude loadings serves as a representative sampling of loading histories for this alloy.

The selection of 2026-T8E41 alloy for limited testing (at $R = -1$) allowed a comparison of the short crack growth behavior of the new light aluminum alloy with the vintage airframe alloy, 2024-T3. The addition of approximately two percent by weight of lithium produces an alloy with a six percent decrease in density and a ten percent increase in stiffness over conventional airframe aluminum alloys. The lithium, however, also increases the propensity for planar slip which, in combination with sheet texture developed during processing, has been shown to produce a highly angular fracture path for long, through cracks [5].

TESTS

The test program conducted on aluminum-lithium alloy 2090-T8E41 consisted of short-crack tests on single-edge-notched tension (SENT) specimens under constant amplitude loading at $R = -1$. A more extensive test program conducted on 4340 steel consisted of standard tensile tests, short-crack tests on SENT specimens and long-crack tests on center-cracked-tension (CCT) specimens. For the steel, both short- and long-crack tests were conducted under constant amplitude loading at $R = 0.5$, 0 and -1 and under variable amplitude loading using the Felix/28 spectrum.

The load profile for one flight from the load sequence is shown in Figure 1. The complete load sequence for Felix/28 contains 140 flights and 161,034 cycles. The ratio of minimum to maximum stress in the entire sequence is -0.28 .

This section describes the material properties, specimen preparation and procedures used to obtain short- and long-crack data. Methods used to calculate stress intensity factors and crack growth rates under the various test conditions are also presented.

Material and Specimens

Al-Li 2090.—The aluminum-lithium 2090-T8E41 material was furnished by Alcoa in a single sheet, 2.15 mm thick, with composition as specified in Table 1. The yield strength (0.2% offset) and ultimate tensile strength were given as 525 MPa and 580 MPa, respectively. SENT specimens, shown in Figure 2(a), were identical in configuration, machining practices and chemical polishing to the 2024-T3 specimens used for the Core Programme. For the Supplemental Short Crack Programme, several laboratories tested Al-Li 2090 specimens which were machined at Wright Research and Development Center (WRDC) and chemically polished at NASA Langley Research Center. For the 50-mm wide specimen, the notch stress concentration factor of 3.17 (based on gross section stress) is identical to that of the Core Programme specimens.

Figures 2(b) and 2(c) show the microstructure of the 2090 alloy for the crack growth (T-S) plane and notch root surface (L-S) plane, respectively. These metallographic specimens were immersed for 2.5 minutes, with no agitation, in an etchant solution of 60 ml H_2O , 3 ml HBF_4 and 3 ml HNO_3 . The pancake microstructure, typical of a rolled aluminum sheet, appears to contain strings of recrystallized grains approximately 5 μm in thickness. Two types of constituent particles are present in the microstructure. Larger particles, up to 5 μm , which were visible on the polished surface prior to etching were shown by energy dispersive x-ray analysis to be Al_7Cu_2Fe . The smaller particles which precipitated along the grain boundaries are the Θ phase (Al_2Cu).

4340 Steel.—The steel specimens were manufactured from a single AISI 4340 steel plate, 9.5 mm in thickness, supplied in the annealed condition. The chemical composition of the steel is given in Table 2. All specimens were machined with the loading axis parallel to the rolling direction (L) of the plate and were ground to a thickness of 5.1 mm. Specimens were heat treated to a hardness level of 45 on the Rockwell C scale by a one hour soak at 840°C, tempering in vacuum at 440°C for two hours followed by furnace cooling in nitrogen gas. The resultant tempered martensite microstructure in the L-S and T-S planes of the plate is shown in Figure 3. The prior austenite grain size was approximately 10 μm . Two types of inclusion particles, spherical calcium-aluminate particles and manganese-sulfide particles elongated in the rolling direction of the plate were identified by x-ray analysis and are indicated on the photomicrographs. These particles will be shown to serve as crack initiation sites in the SENT specimens. The measured tensile strength of the steel was 1505 MPa, the yield strength (0.2% offset) was 1413 MPa and the elastic modulus was 190 GPa. Results of the tensile tests are given in Table 3.

The CCT specimen used for the long-crack tests is shown in Figure 4(a). The slot was electro-discharged machined in the specimen after heat treatment. In order to measure crack growth on the long-crack specimens using an optical microscope, at least one surface of the specimen was mechanically polished using standard metallographic specimen preparation techniques down to a 1 μm diamond polish.

Figure 4(b) depicts the configuration of the SENT steel specimen used for the short-crack tests. The notch radius of 3.18 mm was achieved by final milling cuts of 0.25, 0.13 and 0.05 mm to minimize residual stresses. The stress concentration factor for this notch in the 25 mm wide gage section is 3.36, as calculated by the Boundary Force Method [6]. This is approximately 5% higher than K_T for the 50-mm wide SENT specimens used in the Core Programme.

Prior to testing, the notch area was electropolished for four minutes in a flowing solution of 70% ethanol, 10% glycerin and 20% perchloric acid maintained between 18–20°C. Electropolishing removed the thin oxide layer formed during heat treatment and the metal just beneath the oxide to a depth of about 0.1 mm.

Testing Procedures

Al-Li 2090—Short-Crack Tests.—Short-crack tests on Al-Li 2090 were conducted at $R = -1$ for maximum stress levels of 97 and 99 MPa. These levels were selected to produce fatigue lives in the 1×10^5 to 5×10^5 cycle range based on results from fatigue life tests which were conducted by Mazur and Rudd [7] on specimens prepared concurrently with those described herein. To prevent buckling of the thin sheet under compressive loading, Teflon lined anti-buckling guide plates were loosely fastened against the specimen. Crack length measurements along the bore of the notch were obtained with the replica technique using acetate film 0.04 mm in thickness. As described for the Core Programme, replicas were taken at 80% of maximum load (to insure that any cracks present would be open) periodically during the test. The replicas were subsequently coated with a thin layer of Pd-Au and examined directly in the scanning electron microscope (SEM) at a beam energy of 5 keV. Crack length (measured as a projected length perpendicular to the loading axis) and crack position along the bore of the notch were recorded (for the five largest cracks on each specimen) as a function of fatigue cycles. The nomenclature for crack length measurement is illustrated in Figure 5.

4340 Steel—Short-Crack Tests - A number of fatigue life tests were conducted, using SENT specimens, under each of the loading conditions to establish fatigue life curves. From these data, stress levels were selected to be used for the short-crack, crack-growth tests.

As indicated in the previous description of the Al-Li 2090 tests, replicas were taken periodically during the short-crack tests under each loading condition. Crack length measurements along the bore of the notch and crack position were obtained from observations of the replicas in an SEM. As in the Core Programme, the load was held at 80 percent of maximum while each replica was made during the constant amplitude tests. To obtain replicas in the Felix/28 test, the application of the sequence was stopped and held at 60 percent of the spectrum maximum (a level which occurs frequently in the sequence) and then continued from that point.

Several tests were stopped when there was still a surface crack along the notch and the specimen was pulled to failure under a tensile load. Examination of the fracture surface yielded information on the shape of the fatigue crack as a function of crack size. On all of the SENT specimen fracture surfaces, river markings could be followed back to the crack origin and the initiation-site defects identified.

4340 Steel—Long-Crack Tests - Long-crack tests (crack lengths greater than 5 mm) were conducted under each of the constant amplitude stress conditions, -1, 0 and 0.5, and under the Felix/28 spectrum. The specimens were gripped in either hydraulic or friction grips in a hydraulic load frame calibrated to 89 kN. The test machines were aligned using the criteria from the Core Programme and, additionally, each specimen was strain gaged and alignment was verified at installation. The cyclic frequency was 30 Hz for tests at $R = 0.5$ and 0, and 12 Hz for the $R = -1$ and Felix/28 tests. In tests involving compressive loading, guide plates containing a rectangular cutout for monitoring the crack were loosely fastened on either side of the specimen.

In all tests, cracks were initiated and grown about 2 mm at each end of the central slot before growth rate data were recorded. For $R = 0.5$ loading conditions the crack was initiated under $R = 0$ loading and then the minimum load was increased to obtain $R = 0.5$. For the other loading conditions, the same stress ratio (or Felix/28 spectrum) used to initiate the crack was used for the remainder of that test. Crack length measurements were made visually using a 60X microscope mounted on a micrometer slide. In the Felix/28 tests, crack length measurements were always made at the end of a complete pass through the load sequence (161,034 cycles). Crack growth rates were calculated from the crack length against cycles data using the secant (point-to-point) method employed in the Core Programme.

Growth rates above about 10^{-5} mm/cycle were generated in conventional increasing ΔK tests. Growth rates below about 10^{-5} mm/cycle were obtained in decreasing load amplitude tests in which a manually-controlled, discrete-step load shedding method was employed. After each 0.5 mm increment of crack growth, the maximum and minimum loads were decreased by 6 percent. This resulted in a rate of reduction of ΔK which was within the guidelines recommended in the recently revised ASTM Standard E-647-88-Standard Test Method for the Measurement of Fatigue Crack Growth Rates. After the "threshold" rate (10^{-7} mm/cycle) was achieved, several tests were continued as increasing ΔK tests to corroborate the decreasing- ΔK data.

ANALYSIS

Calculation of Stress-Intensity Factors

In the following, approximate stress-intensity factor equations for a surface crack or a corner crack emanating from a semi-circular edge notch are presented. These equations are used later to compare crack growth rates measured for short cracks with those measured for long cracks as a function of the stress-intensity factor range. The calculation of stress-intensity factor assumes that either a semi-elliptical surface crack is located at the center of the edge notch or a quarter elliptical corner crack is located at an edge, as shown in Figure 4. For a surface crack located at other locations along the bore of the notch, the calculation is adequate if the crack is small compared to thickness.

To calculate the stress-intensity factor at the point where the crack intersects the notch surface ($\phi = \pi/2$), the crack length (a) and the crack depth (c) must be known. This relationship can be determined from measurements made on specimens broken in tension with small fatigue cracks. For Al-Li 2090, the c/a relationship developed from crack shape measurements on 2024-T3 specimens in the Core Programme was used. The crack depth (c) for either a surface crack or a corner crack was calculated from the following equation

$$c/a = 0.9 - 0.25(a/t)^2 \quad (\text{Al-Li 2090}) \quad (1a)$$

For 4340 steel, a different relationship was the best visual fit to the crack-shape data generated from the short-crack specimens tested in this study. These data are presented in the Test Results section. The crack depth (c) for either a surface crack or a corner crack was calculated from the following equation

$$c/a = 1 - 0.25(a/t) \quad (4340 \text{ Steel}) \quad (1b)$$

The stress-intensity factor range equation for a surface crack located at the center of the edge notch subjected to remote uniform displacement is [8]

$$\Delta K = \Delta S \sqrt{(\pi a/Q)} F_{3n} \quad (2a)$$

for $0.2 < a/c < 2$ and $a/t < 1$. Equations for Q , the shape factor, and F_{sn} , the boundary-correction factor, are given in the Appendix.

For a corner crack, the stress-intensity factor is

$$\Delta K = \Delta S \sqrt{(\pi a/Q)} F_{cn} \quad (2b)$$

for $0.2 < a/c < 2$ and $a/t < 1$, where

$$F_{cn} = F_{sn}(1.13 - 0.09a/c) \quad \text{for } a/c \leq 1$$

$$F_{cn} = F_{sn}(1 + 0.04c/a) \quad \text{for } a/c > 1$$

The stress range (ΔS) is full range ($S_{\max} - S_{\min}$) for constant amplitude and spectrum loading. For example, $\Delta S = 2S_{\max}$ for $R = -1$ loading. For spectrum loading, the highest peak stress is S_{\max} and the lowest trough is S_{\min} .

Crack-Growth Model

A crack-growth model that accounts for crack-closure effects was used to predict growth rates and total fatigue lives for 4340 steel under both the constant amplitude and Felix/28 spectrum loading. This growth model was developed in reference 9 and was previously applied to short-crack growth analyses in references 1, 10 and 11.

The basic assumption in the growth model is that the growth rate for any loading cycle lies on a single, master ΔK_{eff} against rate curve, where the ΔK_{eff} is ΔK modified to account for crack-closure effects. The growth model incorporates a model of the crack-closure process that is used to calculate crack opening stresses (and thereby, ΔK_{eff}) as a function of loading history. The ΔK_{eff} was then used to enter the master ΔK_{eff} -rate curve to obtain a predicted crack-growth rate.

The crack growth model was developed for a central through crack in a finite-width specimen subjected to uniform applied stress. This model was later extended to through cracks emanating from a circular hole in a finite-width specimen also subjected to uniform applied stress [11]. The growth model is based on the Dugdale plastic-zone model [12], but modified to leave plastically deformed material in the wake of the crack. The primary advantage in using the Dugdale model is that the plastic-zone size and crack-surface displacements are obtained by superposition of two elastic problems—a crack in a plate subjected to: (1) a remote uniform stress and (2) a uniform stress applied over a segment of the crack surface. In the current work, it was assumed that the opening stresses calculated for a through crack of length "c" were the same as those for a surface crack of depth "c".

TEST RESULTS AND DISCUSSIONS

Al-Li 2090

Short-Crack Tests - A total of six tests were run at $R = -1$, three at each of two stress levels. Figure 6 shows a plot of maximum stress against number of cycles until a crack was first observed on a replica and against number of cycles until failure for each specimen. One test was stopped prior to failure. Cracks were first observed when they were between 6 and 73 μm in length. The cracks which were large when first detected were corner cracks and, as such, were more difficult to find on the replicas early in life. Of the eleven cracks catalogued in this study, three initiated as corner cracks or very close to the sheet surface. All others initiated as surface cracks along the root of the notch. Crack propagation, within this limited data set, was found to consume from 26 to 92 percent of the total life. At the lower stress level, two specimens with corner cracks were detected late in life at 73 and 76 μm , giving relatively short propagation lives (one of these tests was terminated prior to failure with a 500 μm crack). At the upper stress level, the specimen with the propagation life which was much shorter than the other two specimens contained multiple surface cracks which were positioned such that they linked together and the specimen experienced rapid crack growth to failure. The average crack propagation life for the remaining three specimens was 80 percent.

In this alloy, cracks were found to propagate at acute angles to the loading axis. The following description of crack growth behavior is illustrated by the SEM photos of replicas from three specimens in Figures 7 and 8. (Crack initiation sites are labeled with an "I".) Cracks which initiated along the bore of the notch often, but not always, initiated at inclusion particle sites which were visible on the replicas of the notch surface, as in Figure 7(a). The cracks in some cases grew in a horizontal direction for a short distance (5-50 μm) and then turned to a direction approximately 35 degrees to the loading axis. Other cracks grew at this acute angle from the point of initiation. Figure 7(b) shows the crack from Figure 7(a) after an additional 24,000 cycles (upper crack). It has continued to grow, essentially in a planar fashion, to the surface on the right and to intersect another crack at the specimen midthickness. Sometimes the cracks would bifurcate along directions of ± 35 degrees to the loading axis, as in Figure 7(b) (lower crack at location 'B'). At this point, one of three behaviors would result: (1) the crack would continue in the new orientation (Fig. 8(a) at location 'B') or (2) the crack would exhibit a jog in the new orientation and then revert back to the original orientation. A "V"-shaped crack might also be formed by the intersection of two cracks propagating on planes at + and -35 degrees to the loading axis (Fig. 7(b) at center and Fig. 8(b) at inverted "V"). Figure 8(a) illustrates a case where three cracks which were propagating in a nearly coplanar situation linked to form a single crack. Fractures of the specimens discussed in Figure 8 are shown in Figure 9. In general, the presence of the pancake

grain boundaries did not seem to offer any resistance to crack propagation. This would be consistent with a sheet which is textured such that preferred slip planes and slip directions are aligned from one grain to the next. Although the sheet is likely to be textured, as Al-Li alloys are often found to be [5], the exact nature of the texture is uncertain. In the texture analysis of this alloy performed by Bowen [13], the Royal Aeronautical Establishment, at various locations through the thickness, it was determined that the sheet was strongly textured. He reported a deformation texture which indicated that the sheet was unrecrystallized. Examination of the microstructure optically in this work indicated evidence of recrystallization within the pancake grains, as mentioned previously. In the paper by Carvalho and deFreitas in this document [14], they site data obtained using the back reflection Laue x-ray method which indicates a recrystallized texture structure. It would seem that the sheet is perhaps partially recrystallized and, as such, exhibits characteristics of both a deformation and a recrystallized texture.

The crack growth rate against ΔK plot for these short crack tests is shown in Figure 10. As stated previously, the crack lengths for this analysis have been measured parallel to the short transverse direction of the sheet. The long crack data lines are this author's visual fit to the data from tests conducted by Mazur and Rudd [7]. For the short crack data, over the range of stress tested, there appears to be no stress level effect. The short cracks grow at stress intensity factor levels below the long crack threshold (approximately $4.5 \text{ MPa}\sqrt{\text{m}}$) and grow at somewhat higher rates than long cracks above threshold. This relative short crack—long crack behavior is similar to that observed in the Core Programme for 2024-T3 under $R = -1$ loading at the lower stress levels. It should be noted, however, that ΔK_{th} for 2024-T3 is somewhat higher ($6 \text{ MPa}\sqrt{\text{m}}$). There also is significantly more scatter in the long crack data for 2090-T8E41 at $R = -1$ than was found for 2024-T3, resulting in considerable overlap of long and short crack 2090 data for $\Delta K > 4.5 \text{ MPa}\sqrt{\text{m}}$. No attempt has been made to account for Mode II or Mode III contributions to the calculated stress intensity factors or crack growth rates caused by the slanted crack growth. However, using a Mode I analysis, the calculated crack growth rates for long and short cracks approach one another for large ΔK . In addition, the long cracks reported in reference 7 were well-behaved and grew essentially normal to the loading axis from initiation down to threshold, the same orientation that has been assumed in this short-crack analysis.

4340 Steel

Long-crack Tests.—Crack growth rate against ΔK plots for the three constant amplitude test conditions and for the Felix/28 load sequence are presented in Figures 11 through 14. On each data set, a visual best fit line has been drawn through the data. Scatter band lines have been drawn at 1.15 and 1/1.15 times the values for ΔK of the best fit line. The majority of the data points fall within the scatter band lines.

For each type of loading, data obtained under decreasing load conditions agreed with that from increasing load conditions. No threshold value was obtained from the single decreasing load test run under Felix/28 spectrum loading. For each constant amplitude R ratio, at least three tests were conducted. The long-crack threshold for $R = 0.5$ occurred at a value of $\Delta K = 3.36 \text{ MPa}\sqrt{\text{m}}$, for $R = 0$ the threshold occurred at a value of $\Delta K = 5.00 \text{ MPa}\sqrt{\text{m}}$ while the threshold for $R = -1$ loading occurred at a value of $\Delta K = 12.4 \text{ MPa}\sqrt{\text{m}}$.

Fatigue Life Tests.—A series of fatigue life curves were established from tests to failure on the SENT specimens run under both the $R = 0.5, 0$ and -1 constant amplitude loading conditions and the Felix/28 variable amplitude spectrum. The results from the constant amplitude tests are shown in Figure 15. These series of tests were conducted near the fatigue limit condition which may account for the considerable amount of scatter. The horizontal dashed lines indicate the stress levels which were selected for the short-crack tests. High and low stress levels for each stress ratio were chosen to give fatigue lives of approximately 50,000 and 200,000 cycles, respectively, and to avoid the fatigue limit. Only one level was selected for the $R = 0.5$ loading condition due to the limited load capacity of the test machine. The local notch-root stress at the maximum and minimum gross stress levels for each constant amplitude test condition, divided by yield stress, is given in Table 4. Note that for $R = 0.5$, the notch root stress is greater than the yield stress.

The results of the fatigue life tests under the Felix/28 load sequence are shown in Figure 16. The stress levels chosen for the short-crack replica tests are indicated by dashed lines and the local notch root stresses are given in Table 4. For both stress levels selected there was a large amount of scatter in the fatigue life results. Inspection of the fracture surface in the SEM showed that in each case a crack had initiated at an inclusion particle defect. Those specimens which had the shorter lives had cracks which initiated at spherical calcium aluminate particle defects, whereas those with the longer lives had cracks which initiated at manganese sulfide stringer inclusion particle defects. An example of each type of initiation site is shown in Figure 17. In Figure 17(a) the calcium aluminate particle is present just below the notch root surface. In some cases, the particle is on the surface and is removed by final machining or polishing, leaving a hemispherically-shaped void or pit on the notch root surface to serve as the crack initiation point. An example of this situation will be shown later in this section.

Examination of the initiation sites for over 30 fatigue cracks from SENT specimens yielded information on the distribution of crack initiation site dimensions. The spherical particle defects range in size from 10 to $40 \mu\text{m}$ in diameter. The stringer particles are typically 5 to $20 \mu\text{m}$ in the 2a direction and range up to $60 \mu\text{m}$ in the c direction. These data are shown in a graph in Figure 18. The median values of the defect dimensions measured were $2a_c = 16 \mu\text{m}$ and $c_c = 13 \mu\text{m}$. In Figure 19, the c and 2a values for each initiation site have been paired in an aspect ratio, c/a . The predominant ratio size is $1 < c/a < 2$, which is the range for a hemisphere to a sphere. The aspect ratio for the median defect is 1.62. Clearly the stress concentration at a large spherical defect would be greater and would cause matrix cracking to occur earlier in life and at larger initial crack sizes than would be the case for the other defects. However, only a limited volume of the 4340 steel material is being sampled at the notch root. Therefore, a large spherical particle is not always present in this area and initiation must be left to occur at a smaller spherical particle or stringer, thereby causing a large variation in observed fatigue lives. In an investigation of the growth of short cracks in 4340 steel heat treated to somewhat lower strengths ($\sigma_u = 1260$ and 1000 MPa), Lankford [2] observed crack initiation under $R = 0.1$ loading only at spherical inclusions. That result is consistent with the

current work. The specimens used in reference 2 were unnotched and thus had a larger volume of highly stressed material that could contain defects leading to crack initiation.

Fatigue cracks tended to initiate as surface cracks along the bore of the notch rather than as corner cracks. The distribution of initiation sites as a function of position along the bore of the notch is shown in Figure 20. The largest number of cracks initiated near the mid-thickness of the notch root and another favored location was at about one-sixth of the total thickness from the specimen surface. No corner crack initiation was observed in this group of specimens.

Short-Crack Tests.— The inclusion particle defect which caused fatigue crack initiation could generally be seen on the replica, except in the case of a spherical particle defect which was buried just beneath the surface. Once initiated, the crack grew essentially perpendicular to the loading axis. Figure 21(a) shows a series of SEM micrographs of a crack growing from a spherical inclusion particle defect site until it has grown more than halfway across the notch root thickness. At this point in the fatigue test, the specimen was loaded to failure in order to reveal the fatigue crack shape, see Figure 21(b). An enlarged detail of the initiation area shows half of a hemispherically shaped pit and a faceted fracture surface typical of the 4340 alloy.

A total of six short crack tests were terminated before the crack had grown to intersect either surface of the plate. These specimens were pulled in tension to failure and fatigue crack shapes measured. Figure 22 shows the crack shape data, c/a , plotted against crack size, a/t , for these specimens. A linear fit was made visually to the points as shown by the solid line on the graph. This crack shape equation, given by equation (1b), was used in the ΔK calculations for the short-crack data from 4340 steel. The dashed line is the equation used for aluminum alloys, 2024-T3 and 2090-T8E41, and is shown here for reference.

Crack growth rate results from the replica measurements of short cracks are shown in Figures 23 through 26. For $R = 0.5$, the results are for two tests run at a single stress level (see Fig. 23). The solid line indicates the values for the corresponding long-crack data. The short-crack data fall at slightly slower crack-growth rates when compared to the range of the long-crack data. As indicated in Table 4, the material at the notch root yields in tension at this applied stress amplitude. A similar result was found for the 2024-T3 Core Programme tests at $R = 0.5$ with notch-root yielding. For the aluminum alloy, however, the short cracks grew to a greater extent below threshold.

The results for $R = 0$ at two stress levels are plotted in Figure 24. The replica data show no stress level effect over this range in maximum stress. Again, the solid line is from the long-crack results for this stress ratio. The short-crack data agreed well with the long crack data for growth rates less than 5×10^{-8} m/cycle. Short cracks grew slower than long cracks at the rates greater than 5×10^{-8} m/cycle. At this stress ratio, there appears to be no short-crack effect near threshold. A comparison of long- and short-crack growth behavior for $R = -1$ is shown in Figure 25. Below a stress intensity range of approximately $15 \text{ MPa}\sqrt{\text{m}}$, the band of the short-crack data begins to deviate from the long-crack data and to lie at somewhat higher crack growth rates. The short cracks also grew well below the long-crack threshold.

Hence, for the three constant amplitude stress ratios tested, the case which had a compressive component to the loading, $R = -1$, was the only one to show a short-crack effect. This result agrees with the trend from the 2024-T3 tests in the Core Programme. In that study, more pronounced short-crack effects were observed as the stress ratio became more negative. The short-crack effect noted for the 2024-T3 aluminum, however, was substantially greater than that found for the 4340 steel in the current tests.

The short-crack results for the Felix/28 load sequence are shown in Figure 26. Over the range of long-crack data available, the short cracks grew at somewhat slower rates. If long-cracks results are extrapolated to lower ΔK levels, there is no evidence of a short-crack effect.

ANALYTICAL RESULTS AND DISCUSSIONS FOR 4340 STEEL

ΔK_{eff} Against Crack-Growth-Rate Relationship

Application of the closure-based crack growth model requires a ΔK_{eff} against crack growth rate relationship as input. To establish this relationship, the long crack data generated in the current study under constant amplitude loading conditions on CCT specimens were used. The data are shown in Figure 27(a). In addition, data for long cracks grown in single-side-cracked-hole (SSCH) specimens tested at stress ratios of 0.5, 0.1, and -1 by Wanhill at the National Aerospace Laboratory (NLR) were included. These specimens were cut from the same plate as the specimens in the current study and were given the same heat treatment at NASA prior to shipping to NLR. The SSCH specimen and testing procedures used are described in Reference 15. The NLR data is presented in Figure 27(b).

The effective stress intensity factor is given by

$$\Delta K_{eff} = \frac{S_{max} - S_0}{S_{max} - S_{min}} \Delta K$$

where S_0 was calculated from the equations given in Reference 16. For these calculations, a constraint factor (α) of 2.5, reflecting plane strain conditions, was used over the entire range of crack growth rates. Figure 27(c) shows the combined plot of all the available long crack growth rate data plotted on a ΔK_{eff} basis. The solid line segments were generated using a visual fit to the data and the end points of these segments are listed in Table 5. The ΔK_{eff} threshold value of $3.75 \text{ MPa}\sqrt{\text{m}}$ falls within the range of 'effective' thresholds for crack growth rate data from the three stress ratios. The median crack initiation defect size ($2a_i = 16 \mu\text{m}$, $c_i = 13 \mu\text{m}$; see Fig. 18) measured on the fracture surfaces of the fatigue life test specimens was used as the initial flaw size in all crack growth and total fatigue life calculations.

Crack-Growth Rate Predictions

Using the crack growth model, along with the experimentally derived ΔK_{eff} relationship and initial flaw size, crack growth rates for all loading conditions can be calculated. These model predictions of crack-growth rates were made for each of the constant amplitude loadings and for the Felix/28 spectrum at an applied stress level used for the experimental work. The predicted curves are shown in Figures 28(a) through 28(d) superimposed over the respective set of short-crack data and long-crack data curve from the current work. For $R = 0.5$ loading above ΔK levels of about $4 \text{ MPa}\sqrt{\text{m}}$, the predicted crack growth rates agreed well with those for long cracks and, therefore, are slightly higher than the short-crack data. This is a consequence of the absence of closure effects at high stress ratios, i.e., the crack is always open. The starting ΔK value (shown as solid symbol) for the predicted curve is a function of the selected stress level and the assumed initial defect size. For $R = 0$, the predicted curve is initially on the high side of observed crack growth rates and then blends with the experimental data at about $15 \text{ MPa}\sqrt{\text{m}}$. The model predicted higher crack growth rates for short cracks at this stress ratio. In Figure 28(c), the predicted curve for $R = -1$ follows the short crack growth behavior occurring below and just above the long crack threshold quite well. This stress ratio has the greatest closure effects and the predicted curve displays the classic short-crack behavior. The crack growth rates are initially high due to the low value of crack-opening stress, $S_o \approx S_{min}$, and, hence, high values of ΔK_{eff} . As the crack grows, S_o increases rapidly causing ΔK_{eff} to decrease (while ΔK increases) and, consequently, causes the crack-growth rate to drop. If the applied stress level was lower or the initial defect size was smaller, a condition could arise where the cracks would initially grow but arrest as the crack opening stress approached an equilibrium value and ΔK_{eff} became less than $\Delta K_{eff(th)} = 3.75 \text{ MPa}\sqrt{\text{m}}$. Arrest of short cracks was observed experimentally in a few cases for cracks initiating at defects considerably smaller than the median size. For the Felix/28 spectrum, the crack growth model predicted higher crack growth rates over the whole range of ΔK .

Total Fatigue Life Predictions

Predictions of total fatigue life were made using the crack-growth model by calculating the number of cycles necessary to grow a crack from the assumed initial defect size, located at the center of the notch root, to failure ($K_C = 170 \text{ MPa}\sqrt{\text{m}}$ [17]). Fatigue life predictions for $R = 0.5, 0$ and -1 are shown in Figure 29 superimposed on experimental data from fatigue life tests. Agreement between fatigue limit for model predictions and the experimental data is good for $R = 0.5$ and $R = -1$. The fatigue limit for $R = 0$ is somewhat low. This reflects the fact that the $R = 0$ long crack data near threshold fell to the low ΔK_{eff} side ($3.2 \text{ MPa}\sqrt{\text{m}}$) of the $\Delta K_{eff(th)}$ value selected ($3.75 \text{ MPa}\sqrt{\text{m}}$). At stress levels above the fatigue limit, the life predictions at all stress ratios are in fair agreement with experimental data. For stress ratios of $R = 0.5$ and $R = 0$, predictions were somewhat on the conservative side of the experimental data, coinciding with the prediction of slightly higher crack-growth rates shown in the previous set of plots. The life calculations at $R = -1$ are somewhat long. Inspection of the predicted crack growth rate curve at this stress ratio shows the predicted rates to be on the lower edge of the experimental data for high values of ΔK .

For the Felix/28 load sequence, the comparison between model predictions and experimental fatigue lives, are shown in Figure 30. The predicted results fell somewhat short of the experimental data for those specimens which contained spherical defects as crack initiation sites. As expected, the predicted lives fell far short for those specimens with no large inclusion particles at the notch root, where cracks were left to initiate from stringer inclusions or where no cracks of minimum size necessary for continued propagation were formed. It is desirable to have the good agreement occur for the spherical inclusion particle data. For an engineering component which contains a number of fastener holes or other areas of stress concentration, the likelihood of a critical sized inclusion particle being located at one of these sites is large. In previous variable amplitude testing, the model had also performed well in predicting fatigue life for 2024-T3 SENT specimens tested under the Falstaff, inverted Falstaff and Gaussian load spectra [1,10]. Use of a predictive model such as this might eliminate or significantly reduce the amount of testing which needs to be done under spectrum loading by producing reliable predictions of crack growth behavior under any desired load sequence using only constant amplitude crack growth test data. This capability should be of considerable interest to industry.

CONCLUSIONS

The following conclusions have been reached from the fatigue crack growth study of Al-Li 2090-T8E41 and of 4340 steel (quenched and tempered to 45Rc):

A. For Al-Li 2090-T8E41 alloy subjected to $R = -1$ loading

1. Cracks often initiated at inclusion particle ($\text{Al}_7\text{Cu}_2\text{Fe}$) sites which were visible on the specimen notch surface
2. For the single-edge-notched specimens, cracks grew at acute angles to the load axis, approximately 35 degrees, across the major portion of the notch root. The crack propagation direction was, in general, not altered when the crack traversed a longitudinal grain boundary on the specimen surface.
3. For crack growth measured normal to the load axis, short cracks grew below the long crack threshold ($4.5 \text{ MPa}\sqrt{\text{m}}$) and at somewhat higher rates than long cracks above threshold. The Mode I analysis was successful in correlating the long and short crack data, in that crack growth rates agreed for larger ΔK .

B. For 4340 alloy steel, quenched and tempered to 45Rc

1. Fatigue cracks initiated at either calcium aluminate ($10\mu\text{m} < 2a < 40\mu\text{m}$) or manganese-sulfide ($5\mu\text{m} < 2a < 20\mu\text{m}$) inclusion particle sites. Fatigue life, especially under the Felix/28 load spectrum, was greater for specimens with cracks initiating at the manganese-sulfide stringer sites.
2. Crack growth from inclusion particles was essentially perpendicular to the loading axis.
3. For $R = 0.5$ and 0 constant amplitude and Felix/28 spectrum loading, no short-crack growth was found to occur below the long-crack threshold. For $R = 0.5$, short cracks grew at slightly slower rates than those exhibited for long cracks at the same stress-intensity factor range. For $R = 0$ and for the Felix/28 spectrum good agreement was found between long and short crack growth rates.
4. For $R = -1$ loading a short-crack effect was observed, in that, short cracks grew below the long-crack threshold.
5. The closure-based crack-growth model employing a master ΔK_{eff} -rate relationship derived from constant amplitude long-crack data was capable of predicting short-crack crack-growth rates for both constant amplitude and Felix/28 spectrum loading conditions.
6. Model predictions for fatigue life were in reasonable agreement with experiments. Of particular note is the fact that the model was able to accurately predict total fatigue life for specimens subjected to the Felix/28 load sequence solely from input from constant amplitude crack-growth tests. Use of this type of model in design might significantly reduce the amount of spectrum-specific experimental data required.

REFERENCES

1. Newman, J. C., Jr.; and Edwards, P. R.: Short Crack Growth Behavior in an Aluminum Alloy—An AGARD Cooperative Test Programme, AGARD Report No. 732, 1988.
2. Lankford, J. Initiation and Early Growth of Fatigue Cracks in High Strength Steel, Engineering Fracture Mechanics, Vol. 9, No. 3, 1977, pp 617-624.
3. Brown, C. W., and King, J. E.: The Relevance of Microstructural Influences in the Short Crack Regime to Overall Fatigue Resistance, Small Fatigue Cracks, R. O. Ritchie and J. Lankford, eds., The Metallurgical Society, 1986, pp. 73-95
4. Edwards, P. R.; and Darts, J.: Standardised Fatigue Loading Sequences for Helicopter Rotors (Helix and Felix) Part 2: Final Definition of Helix and Felix, RAE Technical Report 84085, 1984.
5. Yoder, G. R.; Pao, M. A.; Imam, M. A.; and Cooley, L. A.: On Corrosion-Fatigue Crack Growth Behavior of Aluminum-Lithium Alloy 2090 in Salt Water, 1st International SAMPE Metals Conference, Vol. 1, 1987, pp. 25-36.
6. Tan, P. W.; Raju, I. S.; and Newman, J. C., Jr.: Stress Intensity Factor Calculations Using the Boundary Force Method, NASA TM 89158, 1987.
7. Mazur, C. J.; and Rudd, J. L.: Determination of the Short Crack Effect in 2090-T8E41 Aluminum-Lithium Alloy, AGARD Report No. 767. (This publication)
8. Swain, M. H.; and Newman, J. C., Jr.: On the Use of Marker Loads and Replicas for Measuring Crack Growth Rates for Small Cracks, Fatigue Crack Topography, AGARD Conference Proceedings No. 376, 1984, pp. 12.1-12.17
9. Newman, J. C., Jr.: A Crack Closure Model for Predicting Fatigue Crack Growth Under Aircraft Spectrum Loading, Methods and Models for Predicting Fatigue Crack Growth Under Random Loading, J. B. Chang and C. M. Hudson, eds., ASTM STP 748, 1981, pp. 53-84.
10. Newman, J. C., Jr.; Swain, M. H.; and Phillips, E. P.: An Assessment of the Small-Crack Effect for 2024-T3 Aluminum Alloy, Small Fatigue Cracks, R. O. Ritchie and J. Lankford, eds., The Metallurgical Society, 1986, pp. 427-452.
11. Newman, J. C., Jr.: A Nonlinear Fracture Mechanics Approach to the Growth of Small Cracks, Behavior of Short Cracks in Airframe Components, AGARD Conference Proceedings No. 328, 1982, pp. 6.1-6.26.
12. Dugdale, D. S.: Yielding of Steel Sheets Containing Slits, Journal of Mechanics, Physics, and Solids, Vol. 8, No. 2, 1960, pp. 100-104.
13. Bowen, A. W.: Texture Analysis of 2090-T8E41 Aluminum-Lithium Sheet, AGARD Report No. 767. (This publication.)
14. Carvalho, H.; and deFreitas, M.: Short Crack Behavior in Al-Li Alloy 2090, AGARD Report No. 767. (This publication.)
15. Wanhill, R. J. H.: Low Stress Intensity Fatigue Crack Growth in 2024-T3 and T351, Engineering Fracture Mechanics, Vol. 30, 1988, pp. 233-260.

16. Newman, J. C., Jr. A Crack Opening Stress Equation for Fatigue Crack Growth, International Journal of Fracture, Vol. 24, 1984, R131-R134.
17. Damage Tolerant Design Handbook, J. Gallagher, ed., Metals and Ceramics Information Center, 1983, pp 6 29-8 9.

Table 1. Composition of Al-Li 2090-T8E41

| ELEMENT | PERCENT | ELEMENT | PERCENT |
|---------|---------|---------|---------------------------------|
| Al | BASE | Cu | 2.4-3.0 |
| Li | 1.9-2.6 | Mg | 0.25 |
| Zr | 0.10 | Fe | 0.12 |
| Mn | 0.05 | Cr | 0.05 |
| Ti | 0.15 | Others | 0.05 max each
0.15 max total |

Table 2 Composition of AISI 4340 Steel

| ELEMENT | PERCENT | ELEMENT | PERCENT |
|---------|---------|---------|---------|
| Fe | BASE | Ni | 1.75 |
| C | 0.39 | Mo | 0.25 |
| Mn | 0.69 | Cu | 0.11 |
| P | 0.008 | Al | 0.007 |
| S | 0.002 | Ca | <0.001 |
| Si | 0.27 | Mg | <0.002 |
| Cr | 0.79 | | |

Table 3 Mechanical Properties of 4340 Steel from Tensile Tests

| Yield Strength
(0.2% offset)
σ_{ys}
MPa | Ultimate Tensile
σ_u
MPa | Elastic Modulus
E
GPa |
|---------------------------------------------------------|---------------------------------------|-----------------------------|
| 1418 | 1512 | 194.4 |
| 1420 | 1498 | 189.6 |
| 1407 | 1507 | 193.7 |
| 1425 | 1513 | 179.3 |
| 1402 | 1496 | 192.4 |
| 1413* | 1505* | 189.6* |

*average of five tests

Table 4. Gross Stress and Local Notch-Root Stress for 4340 Steel

| Loading | Maximum
Gross Stress
S_{max} (MPa) | $\frac{K_T S_{max}}{\sigma_{ys}}$ | $\frac{K_T S_{min}}{\sigma_{ys}}$ |
|------------------------------------|--------------------------------------------|-----------------------------------|-----------------------------------|
| Constant
Amplitude
$R = 0.5$ | 585 | 1.42 | 0.71 |
| Constant
Amplitude
$R = 0$ | 385
360 | 0.93
0.87 | 0.00
0.00 |
| Constant
Amplitude
$R = -1$ | 270
240 | 0.65
0.58 | -0.65
-0.58 |
| Variable
Amplitude
Felix/28 | 415
380 | 1.00
0.92 | -0.28
-0.26 |

Table 5. Effective Stress-Intensity Factor Range
Against Crack-Growth Rate Relationship

| ΔK_{eff}
MPa \sqrt{m} | dc/dN
m/cycle |
|------------------------------------|------------------|
| 3.75 | 3.0E-10 |
| 5.30 | 2.0E-09 |
| 7.30 | 7.0E-09 |
| 15.0 | 4.5E-08 |
| 50.0 | 5.5E-07 |
| 120.0 | 3.0E-05 |

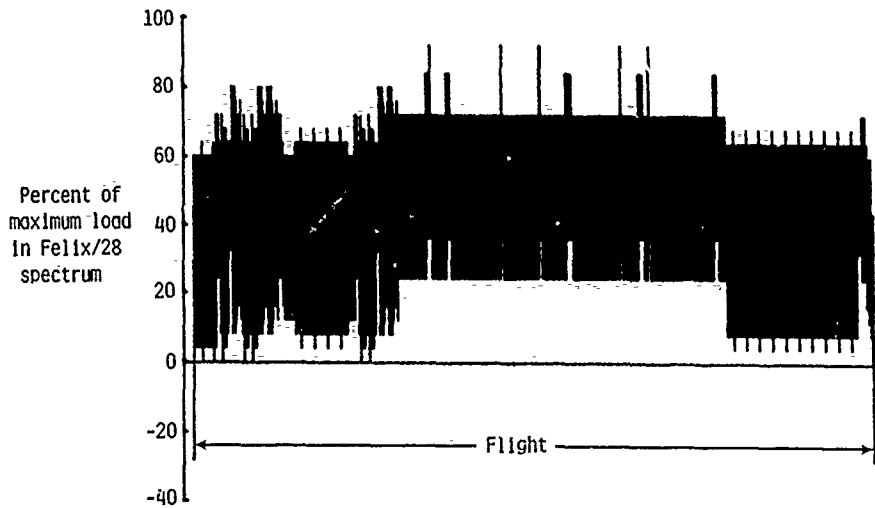


Figure 1.- Load time history for one flight of Felix/28 sequence.

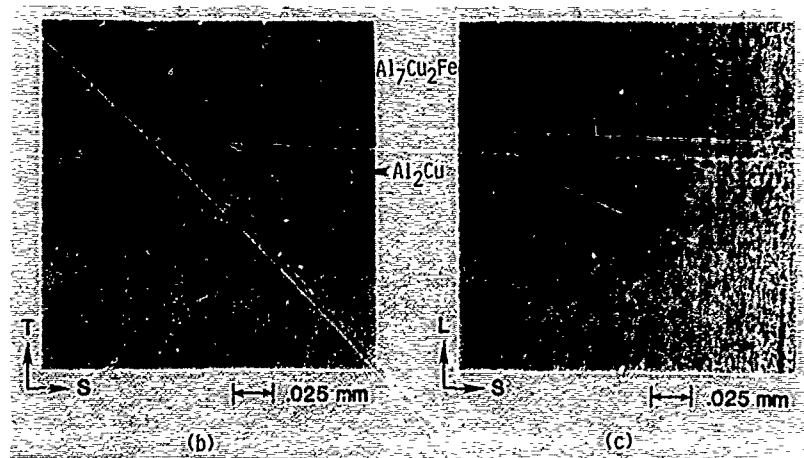
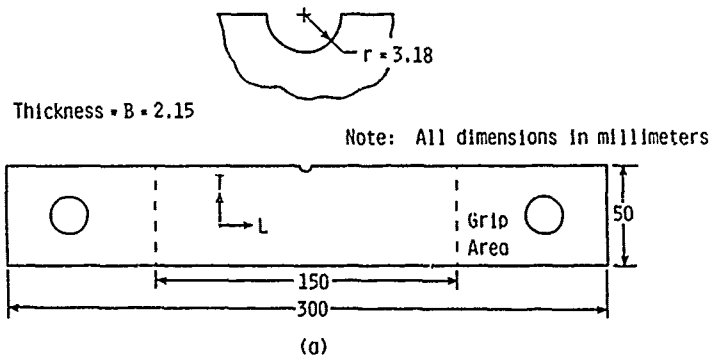


Figure 2.- (a) Core Programme SENT specimen. (b) Al-Li 2090-T8E41 microstructure in nominal crack growth plane and (c) notch root surface plane.

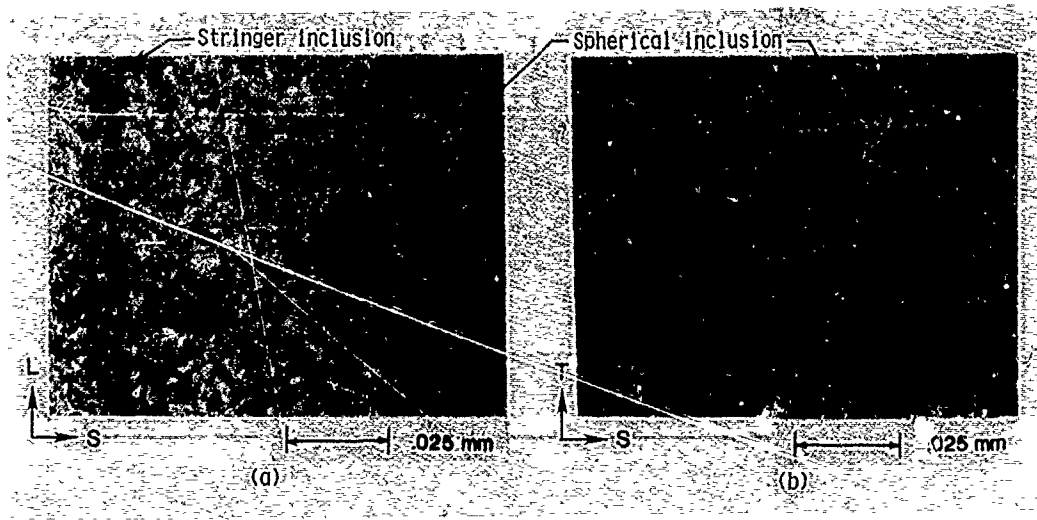


Figure 3.- Microstructure of 4340 steel in the (a) notch root surface plane and (b) nominal crack growth plane.

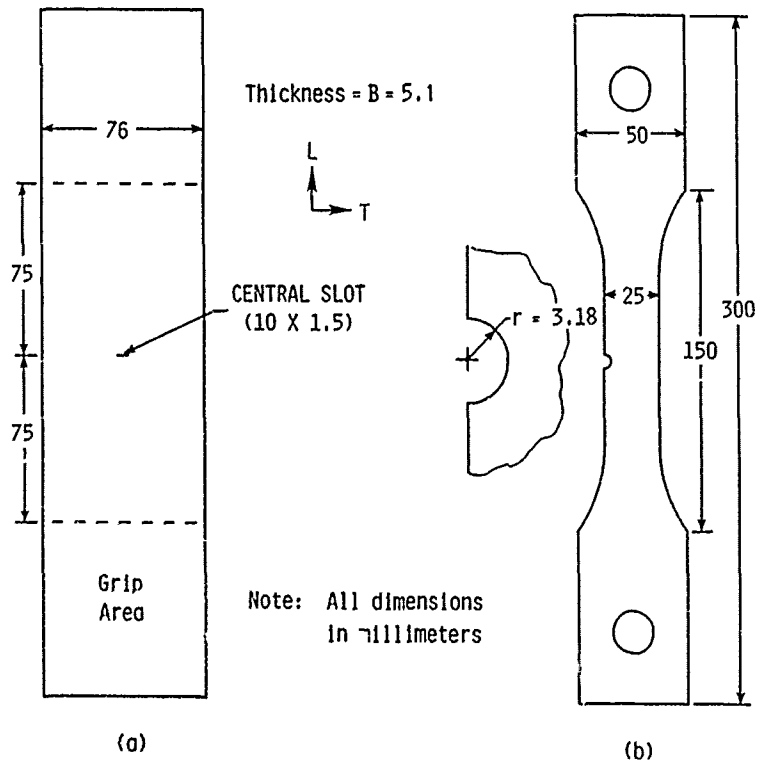


Figure 4.- Configuration of (a) long crack specimen and (b) short crack specimen for 4340 steel.

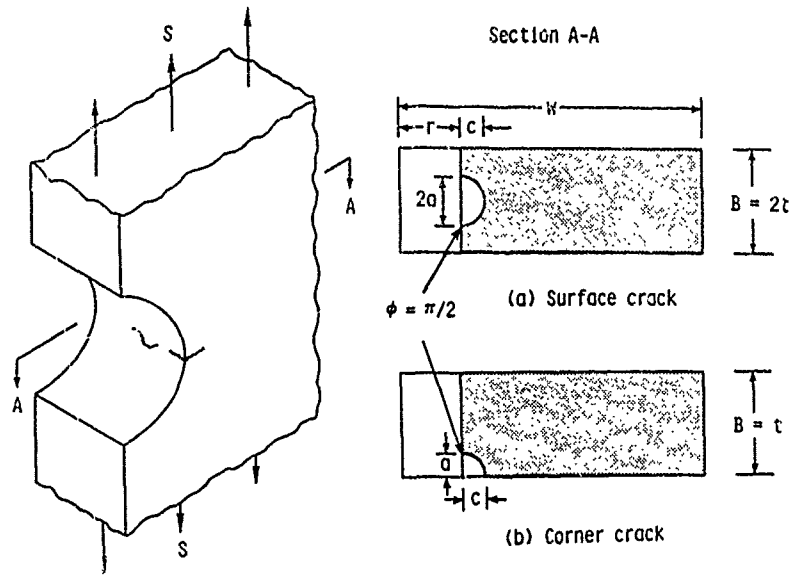


Figure 5.- Nomenclature for crack measurement.

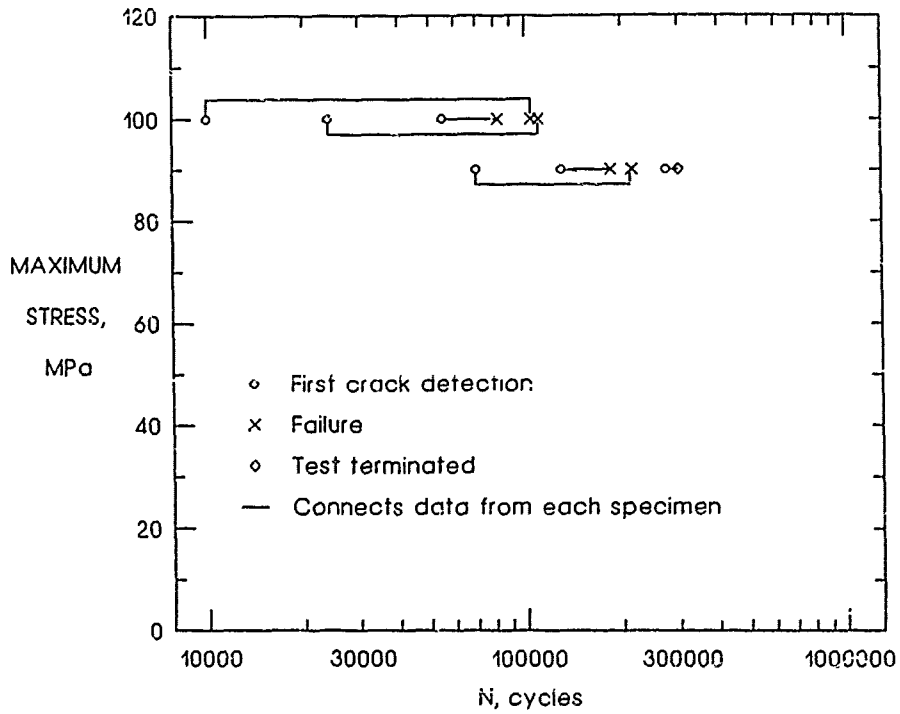


Figure 6.- Cycles to first crack detection and cycles to failure for Al-Li 2090-T8E41 alloy under R = -1 loading.

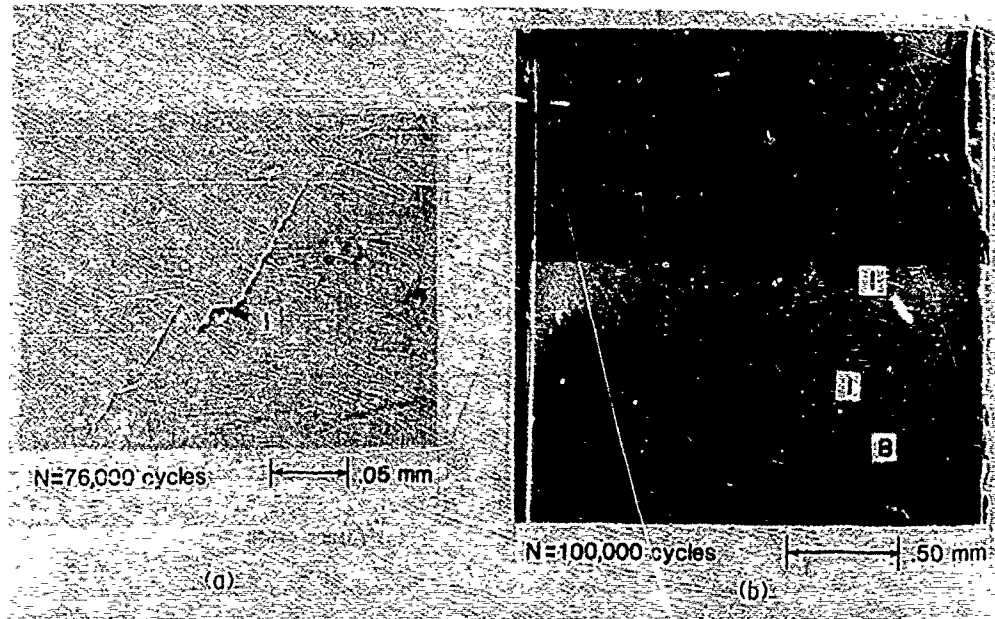


Figure 7.- Replicas of notch surface of a single Al-Li 2090 specimen at different times during test. (a) Initiation (I) at inclusion particle site and conversion to crack growth at acute angles. (b) Growth of two intersecting cracks and crack bifurcation (B).

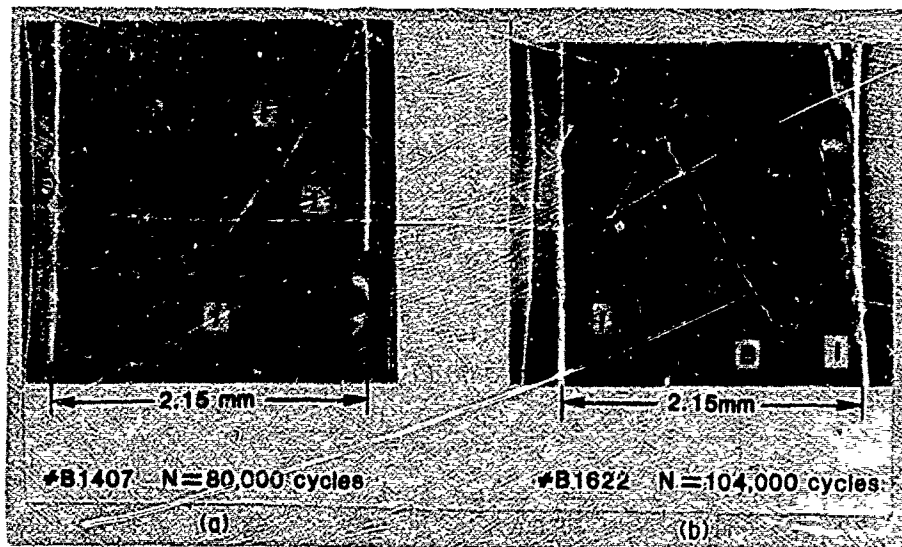


Figure 8.- Replicas of Al-Li 2090 specimens with (a) overall slant fracture and (b) crack bifurcation (B) leading to "V"-shape crack and secondary crack initiation at edge of notch.

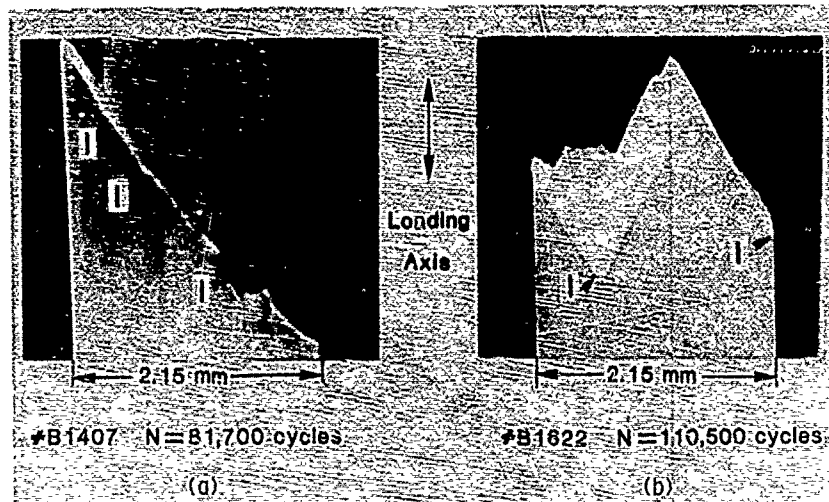


Figure 9.- Fracture surface profile of Al-Li 2090 specimens shown in Figure 8. Arrows indicate crack initiation sites.

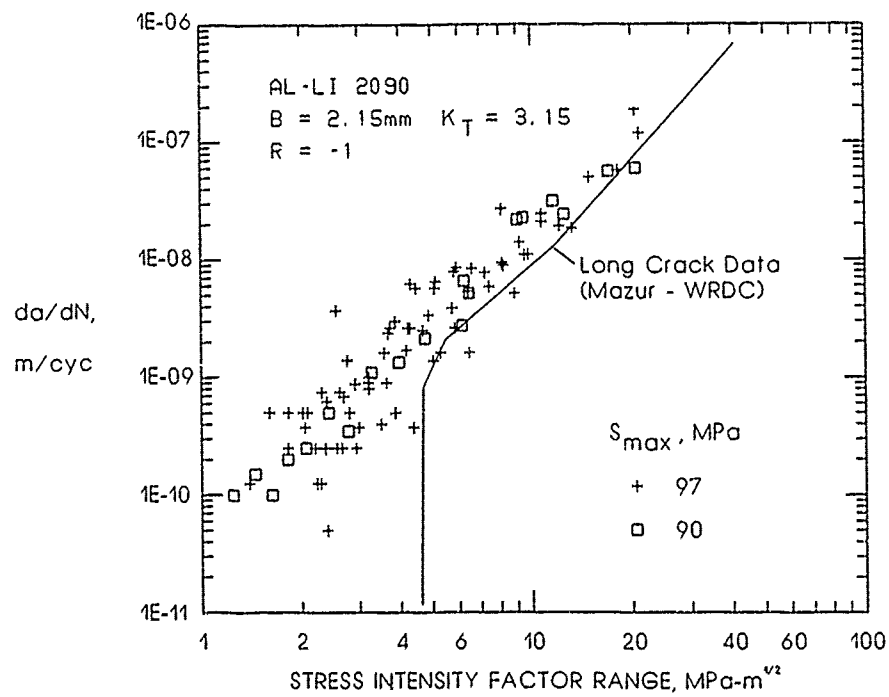


Figure 10.- Short crack growth rate data from Al-Li 2090-T8E41 R = -1 tests.

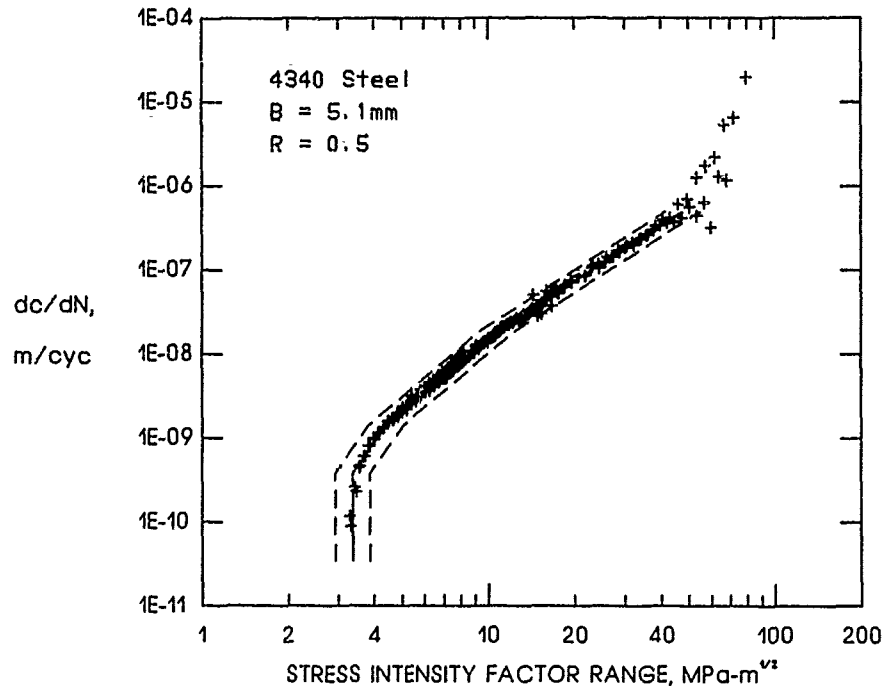


Figure 11.- Long crack growth rate data from 4340 steel R = 0.5 tests.

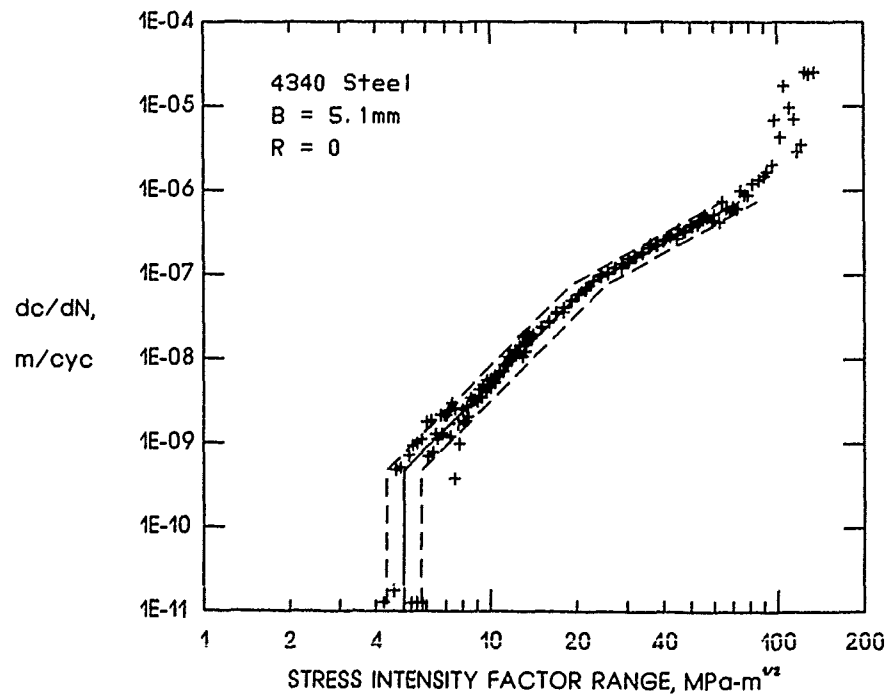


Figure 12.- Long crack growth rate data from 4340 steel R = 0 tests.

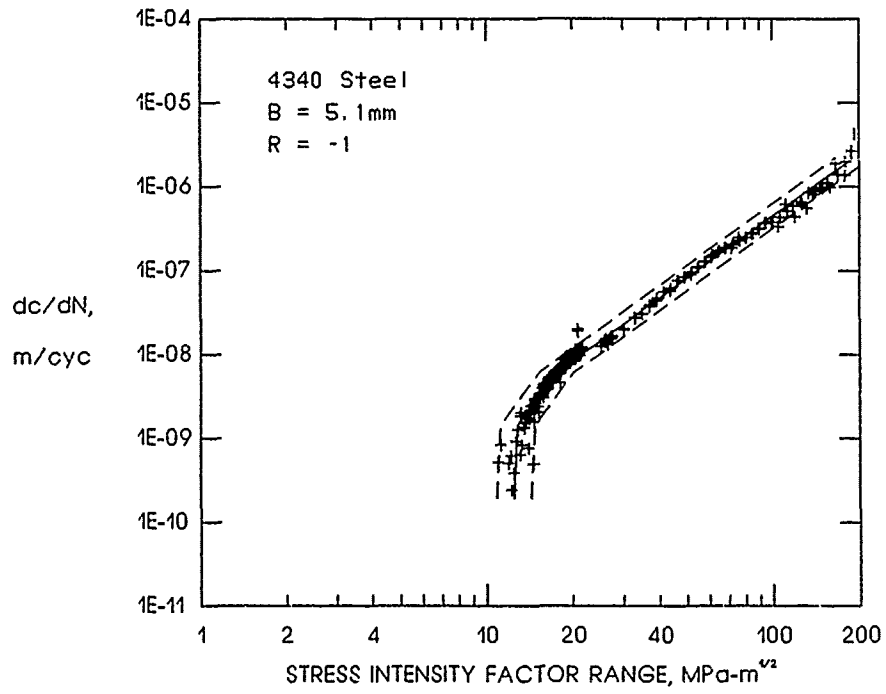


Figure 13.- Long crack growth rate data from 4340 steel R = -1 tests.

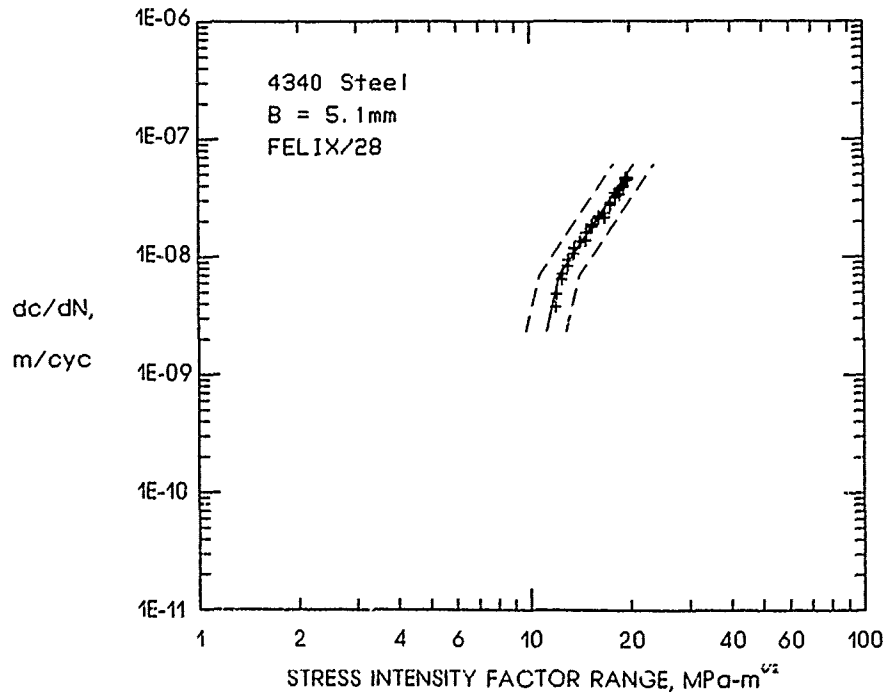


Figure 14.- Long crack growth rate data from 4340 steel Felix/28 spectrum tests.

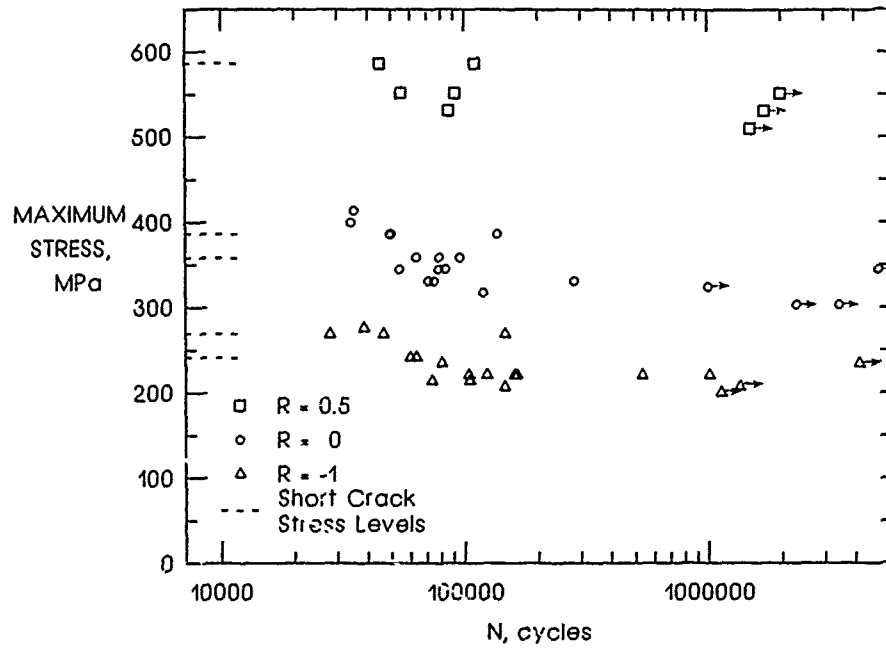


Figure 15.- Fatigue life of 4340 steel under constant amplitude loading.

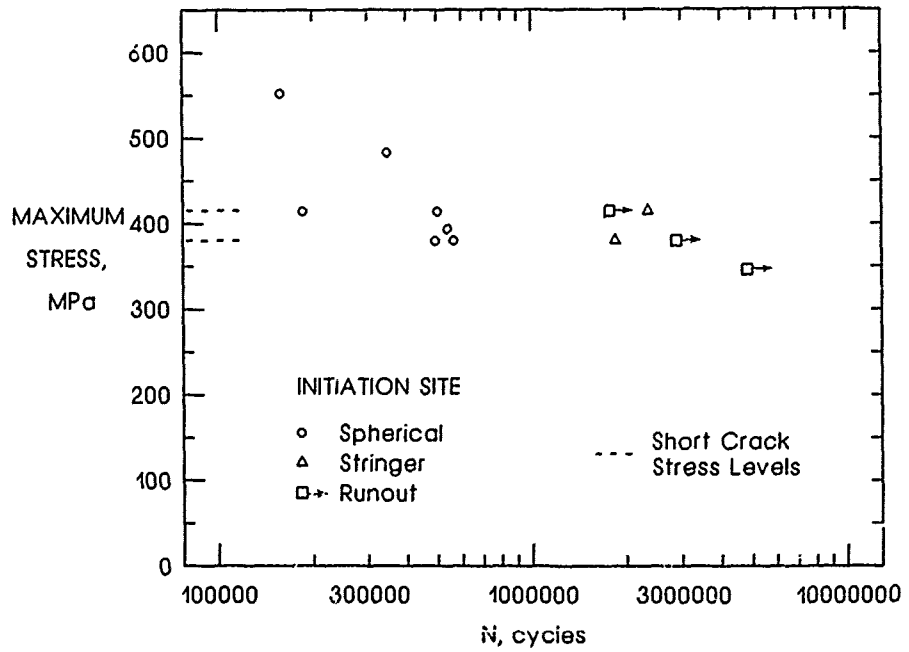


Figure 16.- Fatigue life of 4340 steel under Felix/28 spectrum loading.

Downloaded from ascelibrary.org by University of California, San Diego on 06/16/15. Copyright ASCE. For all rights reserved.

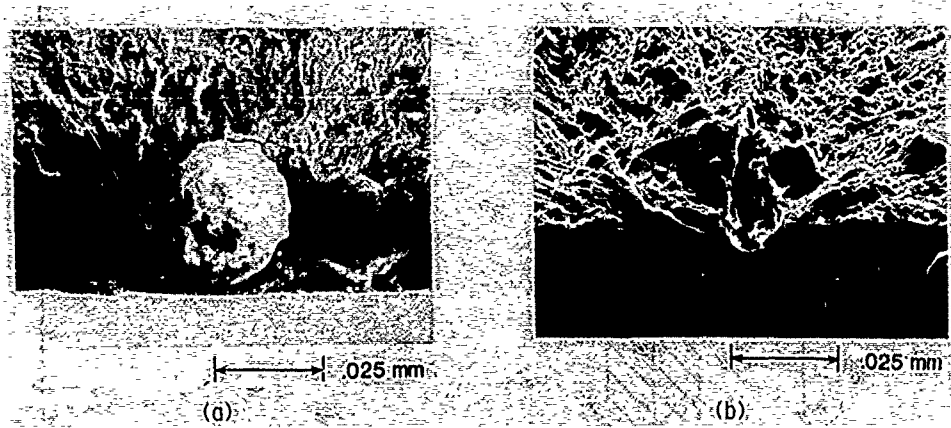


Figure 17.- Fatigue crack initiation sites in 4340 steel. (a) Spherical inclusion particle and (b) stringer inclusion particle site.

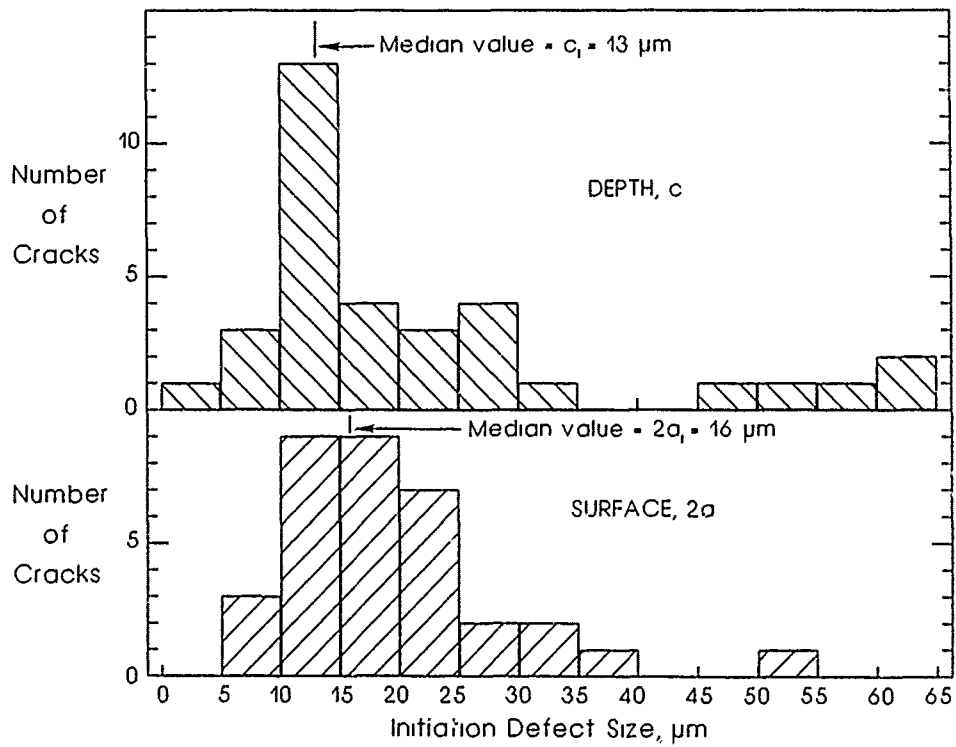


Figure 18.- Size distribution of crack initiation defect site in 4340 steel.

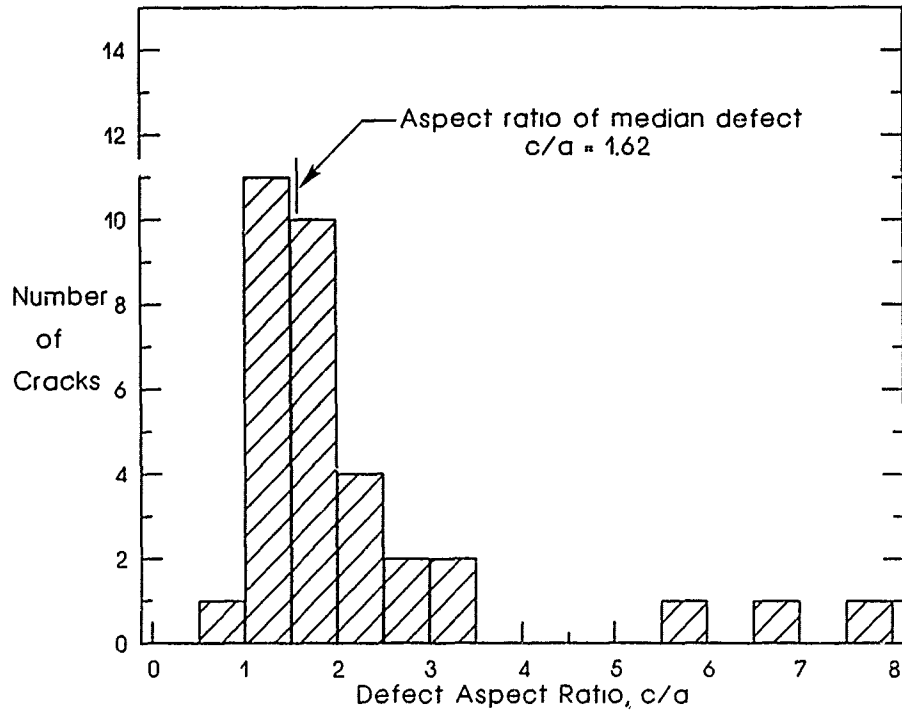


Figure 19.- Aspect ratio of crack initiation sites in 4340 steel.

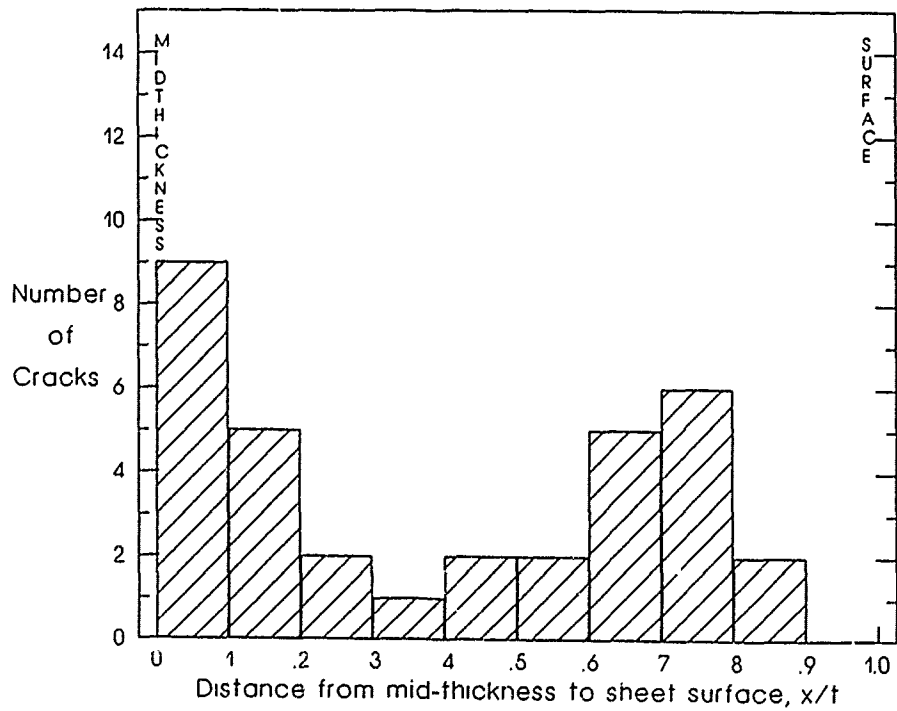


Figure 20.- Distribution of crack initiation sites across the notch root in 4340 steel.

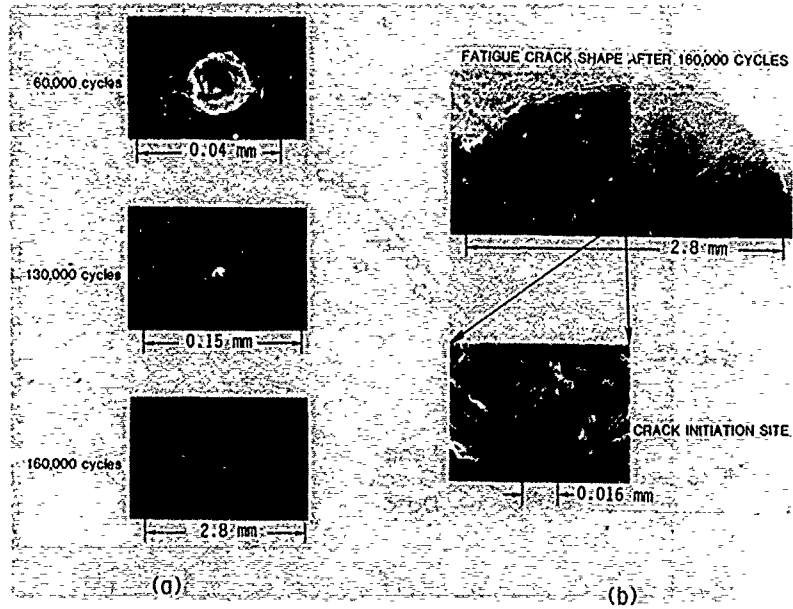


Figure 21.- Crack growth characteristics of 4340 steel. (a) Replicas of notch surface. (b) Fracture surface showing shape of fatigue crack.

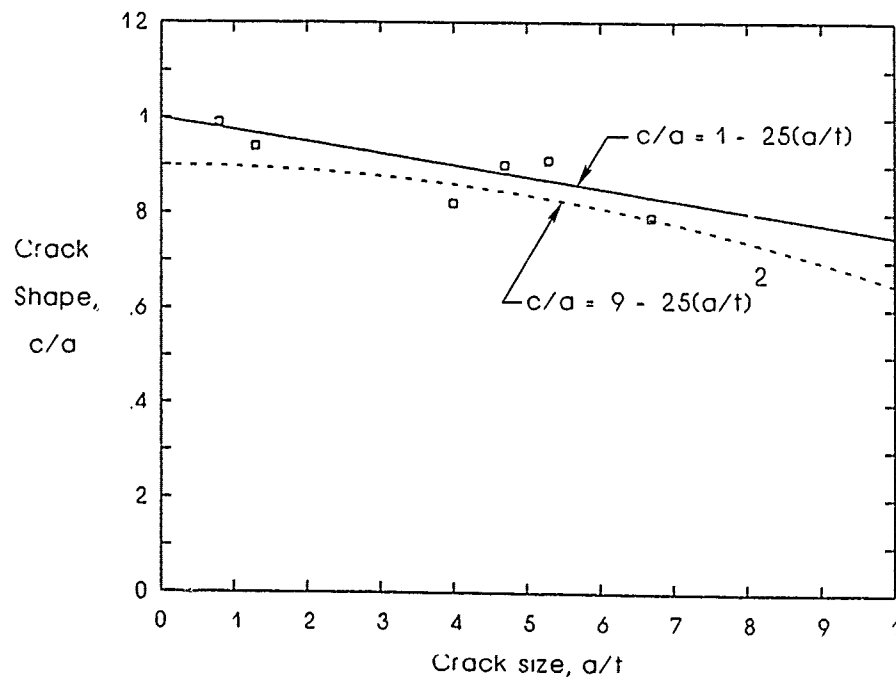


Figure 22.- Experimental fatigue crack shape measurements.

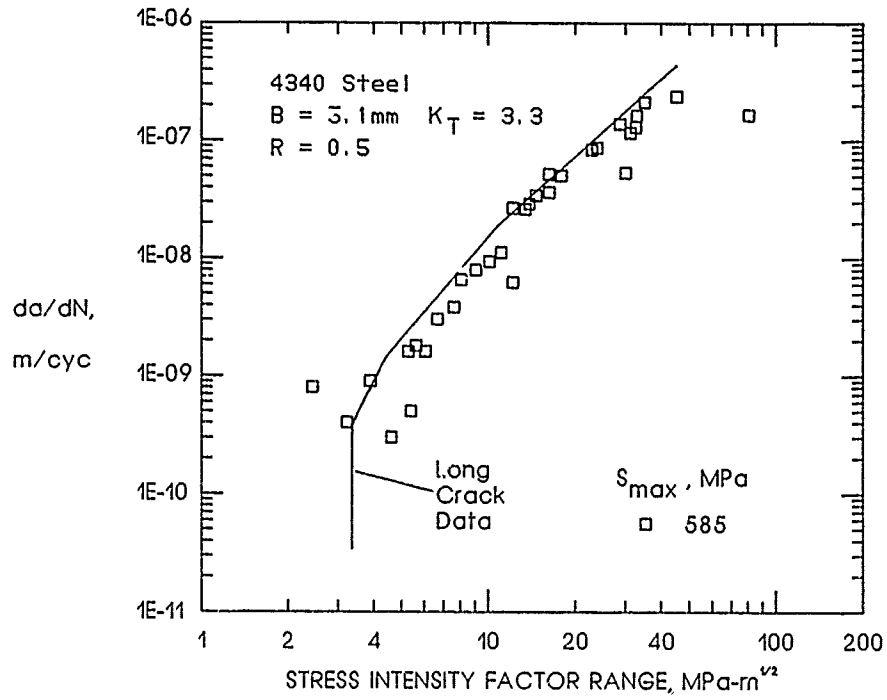


Figure 23.- Short crack growth rate data from 4340 steel R = 0.5 tests.

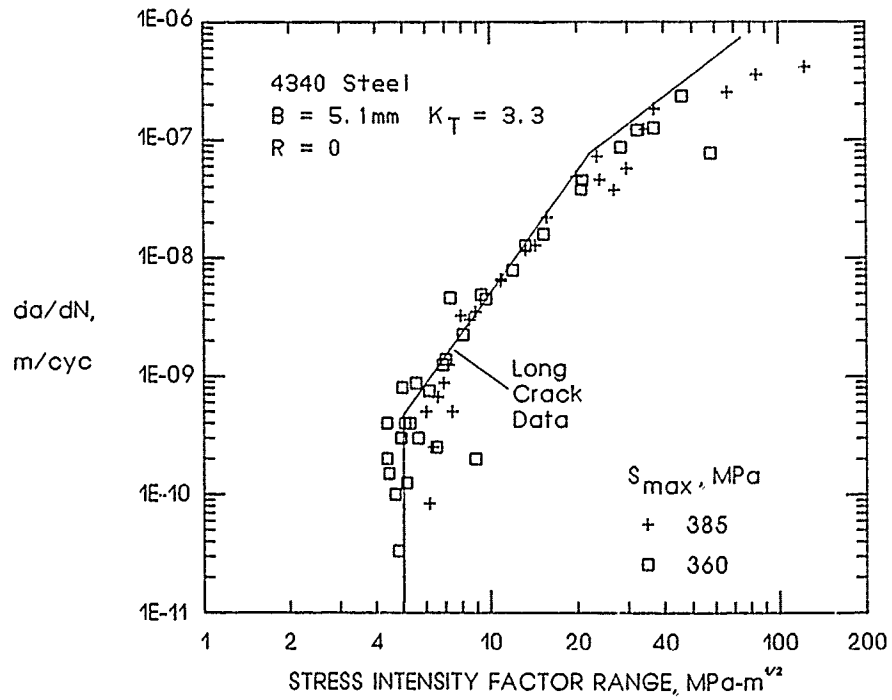


Figure 24.- Short crack growth rate data from 4340 steel R = 0 tests.

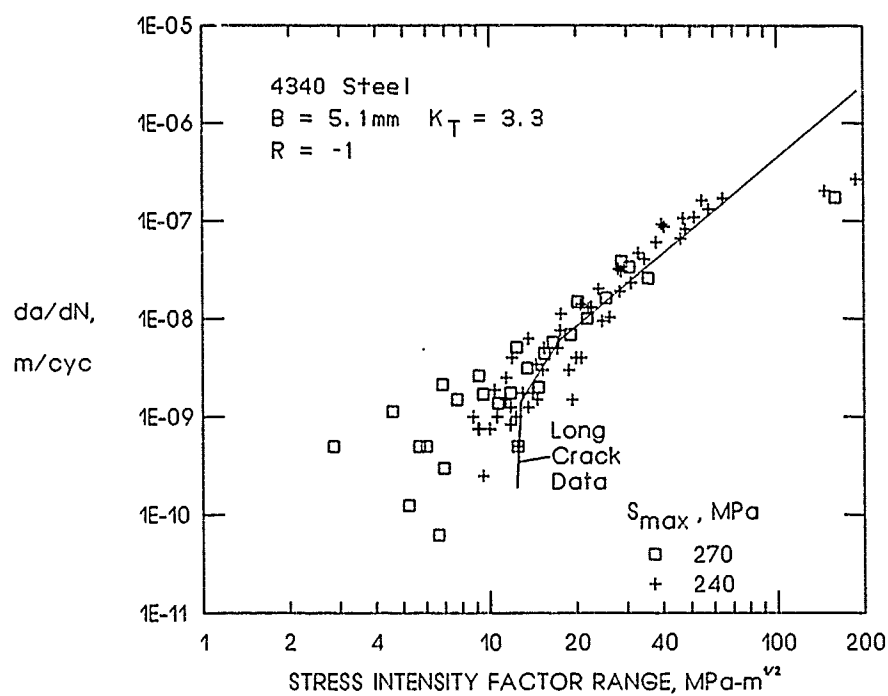
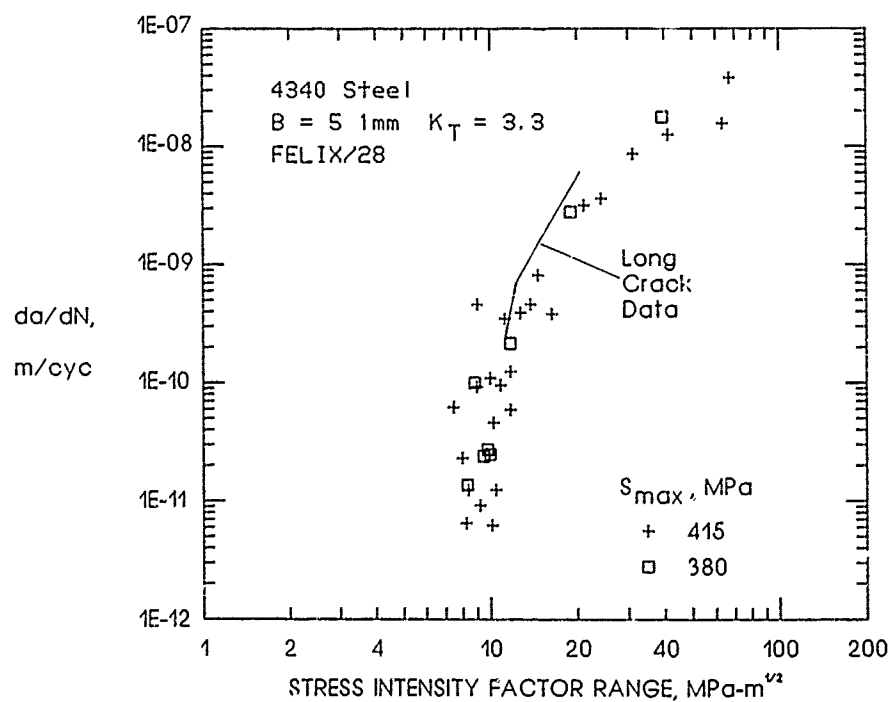
Figure 25.- Short crack growth rate data from 4340 steel $R = -1$ tests.

Figure 26.- Short crack growth rate data from 4340 steel Felix/28 spectrum tests.

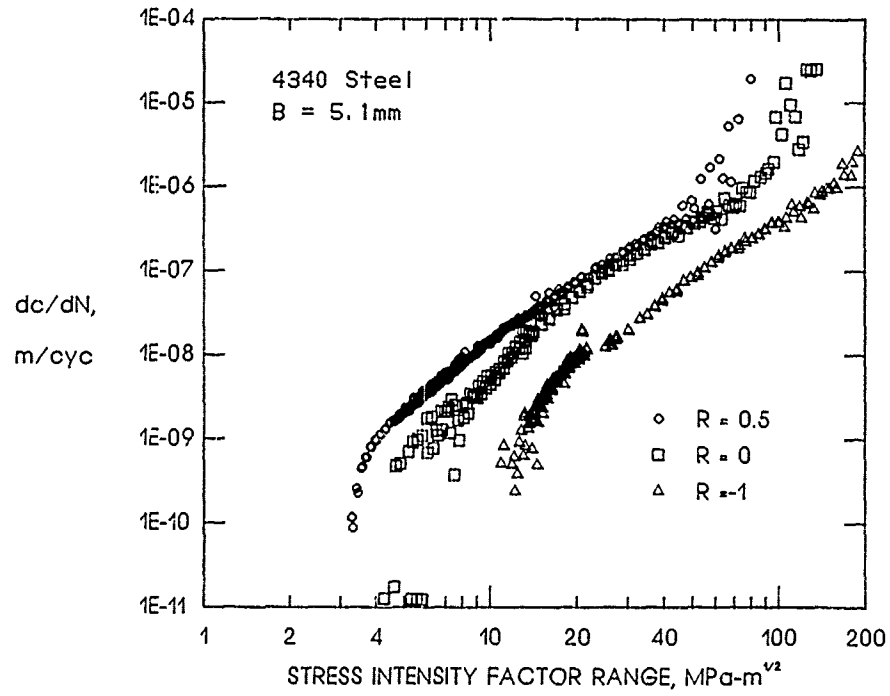


Figure 27(a).- Long-crack growth-rate data for 4340 steel center-crack specimens under R = -1, 0 and 0.5 conditions.

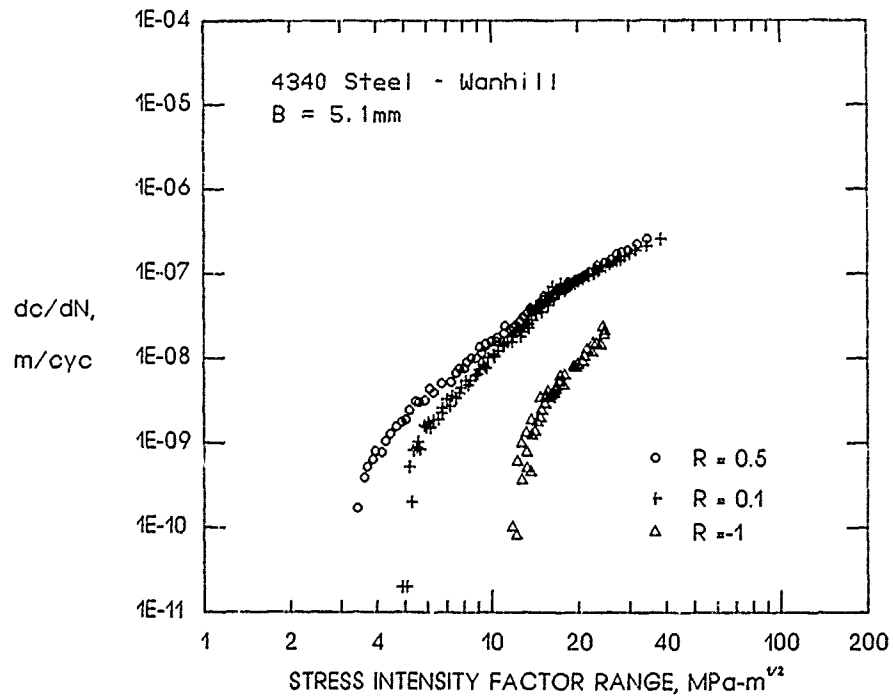


Figure 27(b).- Long-crack growth-rate data for 4340 steel SSCH specimens tested at NLR under R = -1, 0.1 and 0.5.

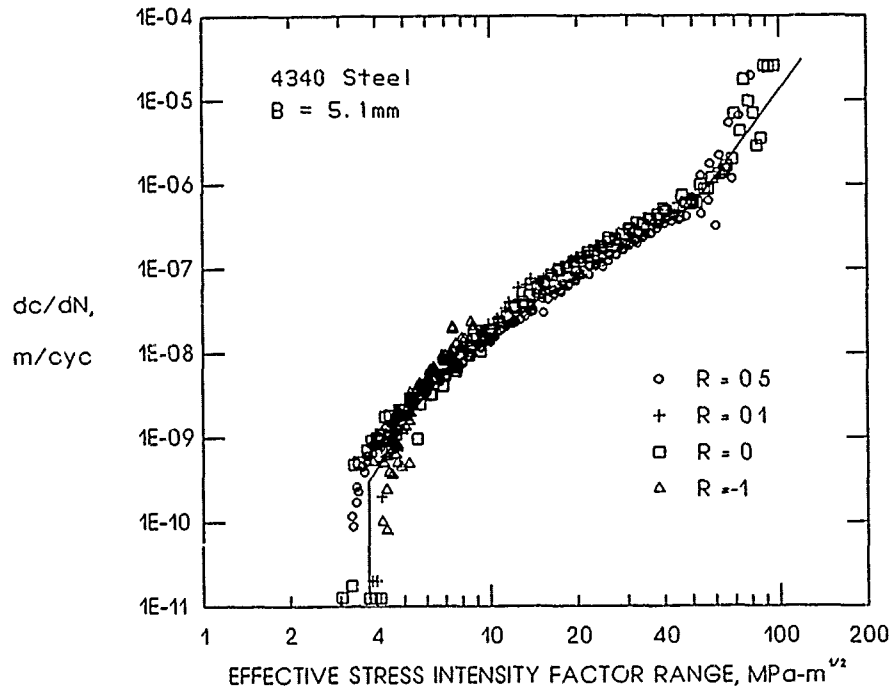


Figure 27(c).- Effective stress-intensity factor range against crack-growth rate relationship for 4340 steel.

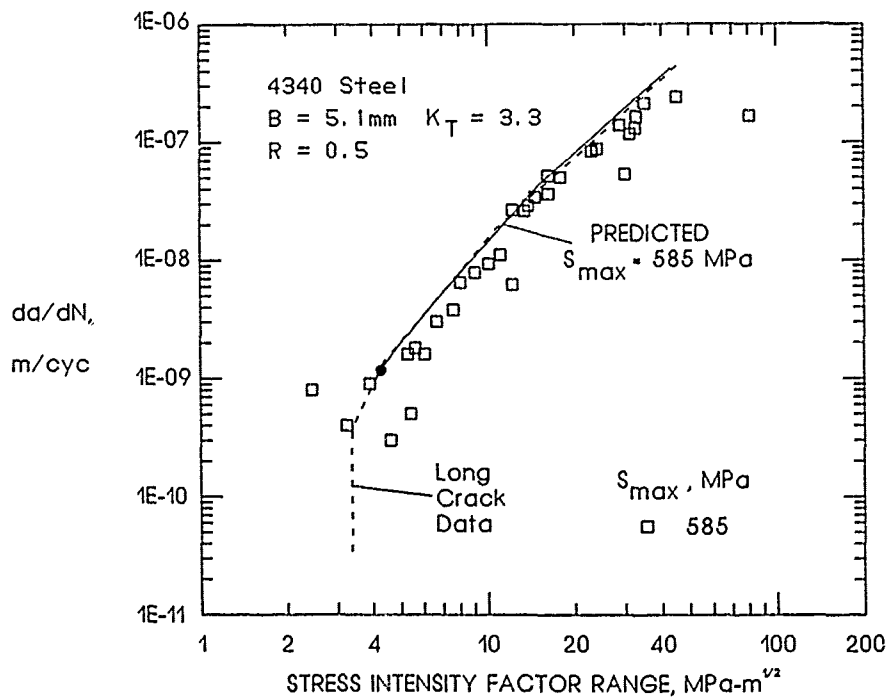


Figure 28(a).- Experimental and predicted crack-growth rates for 4340 steel for R = 0.5 loading.

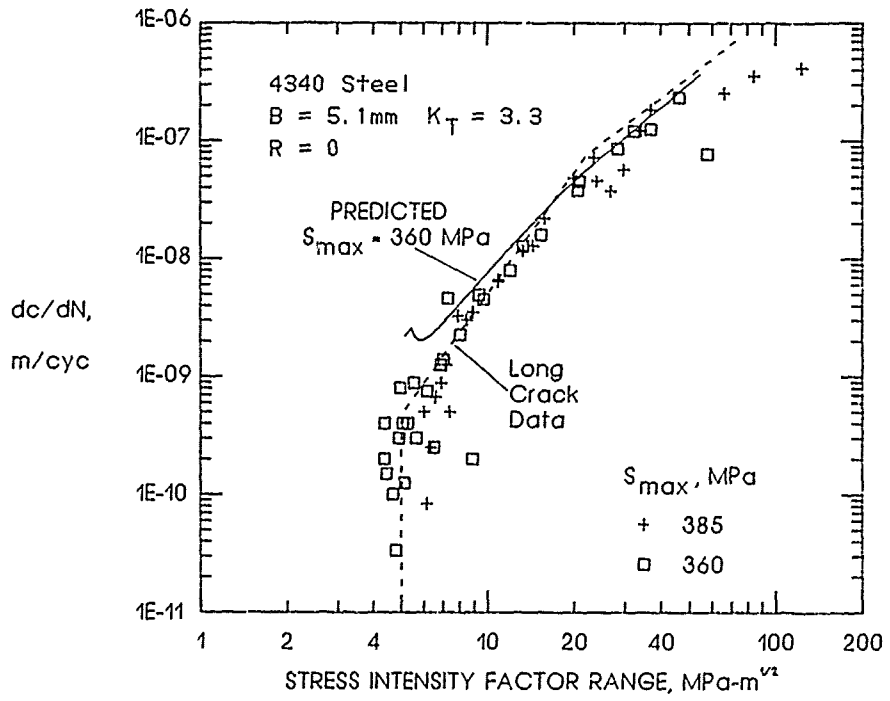


Figure 28(b).- Experimental and predicted crack-growth rates for 4340 steel for $R = 0$ loading.

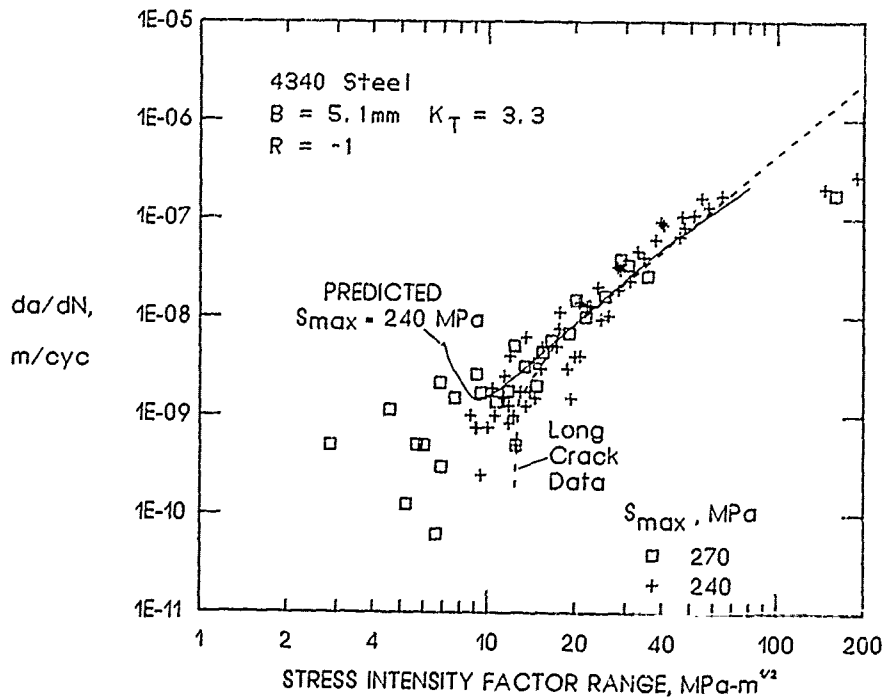


Figure 28(c).- Experimental and predicted crack-growth rates for 4340 steel for $R = -1$ loading.

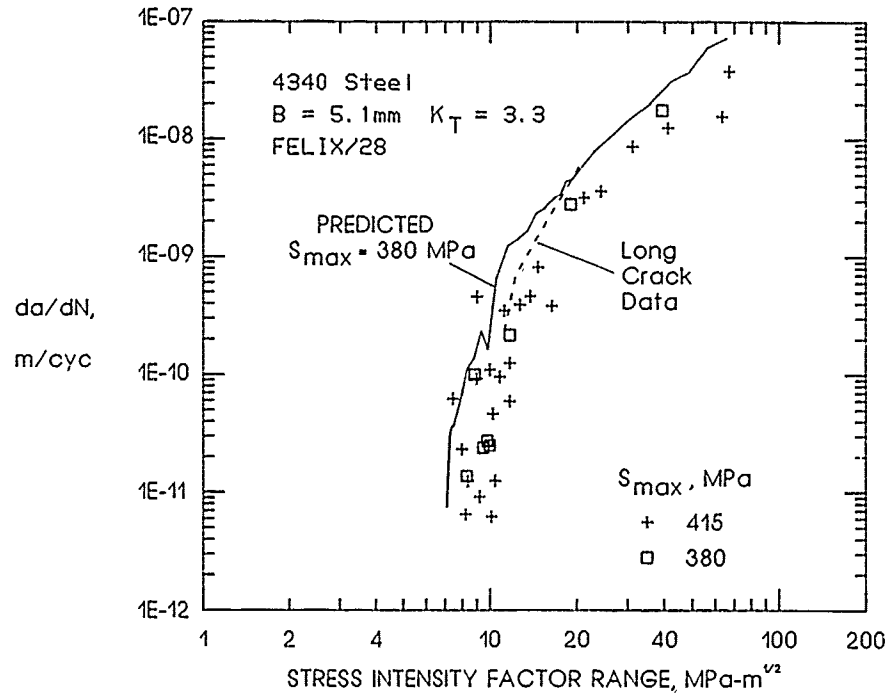


Figure 28(d).- Experimental and predicted crack-growth rates for 4340 steel for Felix/28 loading.

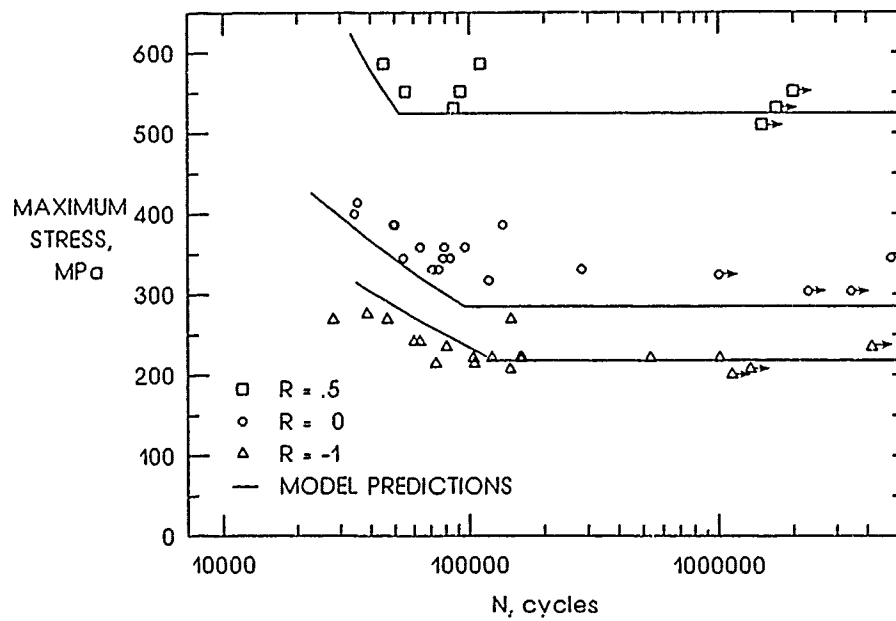


Figure 29.- Experimental and predicted total fatigue life for 4340 steel for constant amplitude loading.

NATIONAL BUREAU OF STANDARDS - GAITHERSBURG, MARYLAND

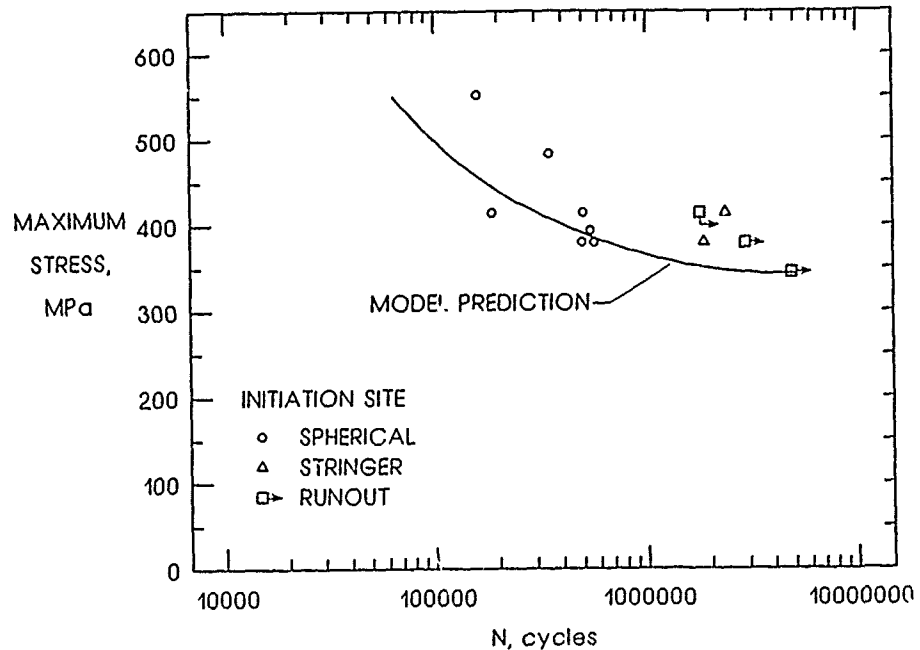


Figure 30.- Experimental and predicted total fatigue life for 4340 steel for Felix/28 loading.

APPENDIX

Approximate Stress-Intensity Factors for a Surface Crack and Through Crack at a Semi-Circular Notch¹

An approximate stress-intensity factor equation for a semi-elliptical surface crack located at the center of a semi-circular edge notch (Fig. 4) subjected to remote uniform displacement is

$$K = S\sqrt{(\pi a/t)Q}F_{sn} \left(\frac{a}{r}, \frac{r}{t}, \frac{r}{w}, \frac{c}{w}, \phi \right) \quad (3)$$

for $0.2 < a/c < 2$, $a/t < 1$, $0.5 < r/t < 3$, $(c+r)/w < 0.5$, and $-\pi/2 \leq \phi \leq \pi/2$. (Note that here t is defined as one half of the full sheet thickness for a surface crack and as full sheet thickness for a corner crack.) The shape factor, Q , is given by

$$Q = 1 + 1.464 \left(\frac{a}{c} \right)^{1.65} \quad \text{for} \quad \frac{a}{c} \leq 1 \quad (4a)$$

$$Q = 1 + 1.464 \left(\frac{c}{a} \right)^{1.65} \quad \text{for} \quad \frac{a}{c} > 1 \quad (4b)$$

and

$$F_{sn} = \left\{ M_1 + M_2 \left(\frac{a}{t} \right)^2 + M_3 \left(\frac{a}{t} \right)^4 \right\} g_1 g_2 g_3 g_4 f_\phi f_w \quad (5)$$

¹ The equations in this appendix, with three exceptions, are identical to those in the Core Programme Report, AGARD Report No. 732 [1]. The form of Eq. (13), for g_4 , has been altered to allow the stress concentration factor, K_T , to appear as a separate variable. This was necessary because the two short crack specimens have slightly different values for K_T . The finite width equations, (14a) and (14b), reflect a change from an assumption of remote uniform stress to an assumption of remote uniform displacement. Also, separate equations are necessary for the steel and Al-Li as the specimens have different aspect ratios, h/w , where h is the half-height and w is the width of the specimen test section. The final change was made to the function γ , the variable in the finite width equation, to include the dependence on normalized crack size, a/t . This factor, $(a/t)^{1/2}$, was inadvertently omitted from the original document. For the specimen used in the AGARD Cooperative Test Programme, the effect of leaving out this term causes less than a two percent difference in the calculation of the stress intensity factors and, therefore, does not significantly affect results from the Core Programme.

For $a/c \leq 1$.

$$M_1 = 1 \quad (6)$$

$$M_2 = \frac{0.05}{0.11 + \left(\frac{a}{c}\right)^{3/2}} \quad (7)$$

$$M_3 = \frac{0.29}{0.23 + \left(\frac{a}{c}\right)^{3/2}} \quad (8)$$

$$g_1 = 1 - \frac{\left(\frac{a}{t}\right)^4 (2.6 - 2\frac{a}{t})^{1/2}}{1 + 4\frac{a}{c}} |\cos \phi| \quad (9)$$

$$g_2 = \frac{1 + 0.358\lambda + 1.425\lambda^2 - 1.578\lambda^3 + 2.156\lambda^4}{1 + 0.08\lambda^2} \quad (10)$$

$$\lambda = \frac{1}{1 + \frac{a}{t} \cos(0.9\phi)} \quad (11)$$

$$g_3 = 1 + 0.1(1 - \cos \phi)^2 \left(1 - \frac{a}{t}\right)^{10} \quad (12)$$

$$g_4 = K_T \left\{ 0.36 - 0.032 / \left(1 + \frac{c}{r}\right)^{1/2} \right\} \quad (13)$$

The finite-width correction, f_w , was

$$f_w = 1 + 2.7\gamma^2 - 3.5\gamma^4 + 3.8\gamma^6 \quad \text{for } h/w = 2(\text{Al-Li specimen}) \quad (14a)$$

$$f_w = 1 + 3.93\gamma^2 - 5.59\gamma^4 + 5.93\gamma^6 \quad \text{for } h/w = 3(\text{Steel specimen}) \quad (14b)$$

where

$$\gamma = \frac{c+r}{w} \left(\frac{a}{t}\right)^{1/2} \quad (15)$$

The function f_ϕ is given by

$$f_\phi = \left[\left(\frac{a}{c}\right)^2 \cos^2 \phi + \sin^2 \phi \right]^{1/4} \quad (16)$$

For $a/c > 1$.

$$M_1 = \left(\frac{c}{a}\right)^{1/2} \quad (17)$$

The functions M_2 , M_3 , g_1 , g_2 , γ , g_3 , g_4 , and f_w are given by Eqs. (7) through (14), respectively, and f_ϕ is given by

$$f_\phi = \left[\left(\frac{c}{a}\right)^2 \sin^2 \phi + \cos^2 \phi \right]^{1/4} \quad (18)$$

When the surface-crack half-length, a , reaches one-half sheet thickness, t , the crack is assumed to be a through crack of length, c . The stress-intensity factors for a through crack emanating from a semi-circular notch subjected to remote uniform displacement are then used. An equation fit to these results is

$$K = S\sqrt{(\pi c)} F_n \left(\frac{c}{w}, \frac{r}{w}\right) \quad (19)$$

for $(c+r)/w < 0.8$. The boundary correction factor, F_n , is

$$F_n = f_1 g_4 f_w \quad (20)$$

where g_4 and f_w are given by Eqs. (13) and (14), respectively. The function f_1 is given by

$$f_1 = 1 + 0.358\lambda + 1.425\lambda^2 - 1.578\lambda^3 + 2.156\lambda^4 \quad (21)$$

where

$$\lambda = \frac{1}{1 + \frac{c}{r}}$$

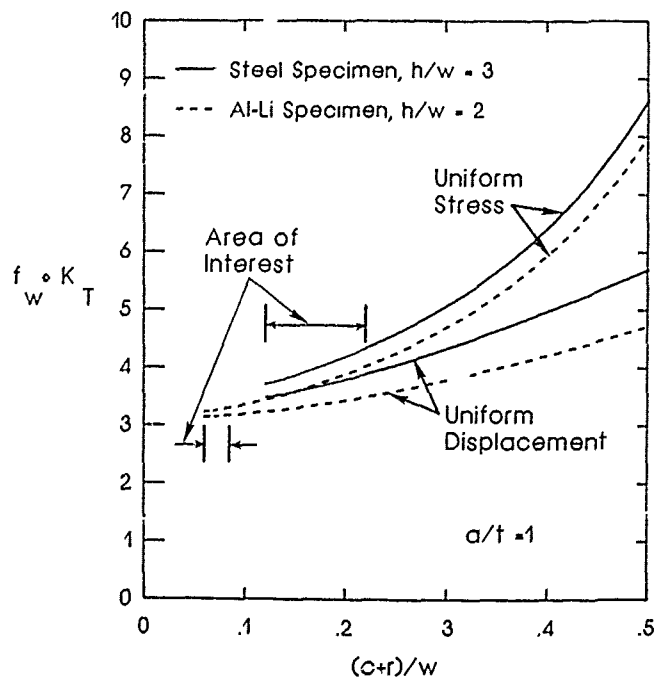
The difference in specimen configuration between the steel and Al-Li specimens affects the stress intensity factor calculations through two parameters, K_T and f_w . Figure A1 shows the variation of the product, $f_w K_T$, with crack size factor, $(c+r)/w$, for the case of remote uniform displacement and for remote uniform stress. The solid curves show these relationships for the steel specimen, with $h/w = 3$; and the dashed curves represent the Al-Li specimen configuration, with $h/w = 2$. The stress concentration factor applicable for each specimen under each condition as calculated by the Boundary Force Method [6] is listed in the following table.

| Specimen Material | Uniform Stress K_T | Uniform Displacement K_T |
|-------------------|----------------------|----------------------------|
| Steel | 3.42 | 3.30 |
| Al-Li | 3.17 | 3.15 |

For each specimen the range of crack size over which short crack data is obtained is indicated in the figure. Note that the difference between the two curves and, hence, the difference between the uniform stress and uniform displacement formulations in the area of interest for the Al-Li specimen varies from approximately 3 to 4 percent. For the thicker and narrower steel specimens, however, the variation in $f_w K_T$ between uniform stress and displacement formulations is on the order of 7 to 12 percent. Because of the significant difference in the results for the steel specimens and the fact that the remote uniform displacement more accurately describes the experimental test conditions, it was decided to use a uniform displacement formulation for this work.

Figure A1.-

Comparison of finite width correction factor for uniform stress and uniform displacement for two specimen configurations.



SHORT AND LONG FATIGUE CRACK GROWTH IN 2024-T3 UNDER FOKKER 100 SPECTRUM LOADING

R.J.H. Wanhill and L. Schra

National Aerospace Laboratory NLR, P.O. Box 90502, 1006 BM Amsterdam, The Netherlands

SUMMARY

The behaviours of short and long fatigue cracks in the widely used damage tolerant aluminium alloy 2024-T3 were compared using flight simulation loading representative for the Fokker 100 wing/fuselage structure. The results showed that the apparently anomalous behaviour of short cracks is not significant for durability analysis of the current wing/fuselage structure. Also the data provide a reference for evaluating new, candidate materials for durable wing/fuselage structures in transport aircraft.

NOMENCLATURE

| | |
|-----------------------------------------------------------------------------------------------------|-----------------------------------------------------------------|
| a, c | crack dimensions |
| BP3HT | Bonded Patch Three Hole crack Tension (specimen) |
| C | specimen geometry factor |
| CCT | Centre Crack Tension (specimen) |
| da/dn | constant amplitude fatigue crack growth rate |
| da/dn _f , dc/dn _f | flight simulation fatigue crack growth rate |
| $\Delta K/\Delta \epsilon$ | stress intensity factor - crack length gradient |
| $\Delta \epsilon$ | cyclic strain range |
| EPFM | Elastic - Plastic Fracture Mechanics |
| K | stress intensity factor |
| K _{mf} | characteristic stress intensity factor based on S _{mf} |
| K _t | elastic stress concentration factor |
| ΔK | stress intensity factor range |
| l ₁ , l ₂ , l ₃ , l ₄ , l ₅ , l ₆ | short cracks |
| L, T, S | longitudinal, long transverse and short transverse directions |
| LEFM | Linear Elastic Fracture Mechanics |
| n _f | number of flights |
| r | notch radius (SENT specimen) |
| R | stress ratio (= S _{min} /S _{max}) |
| S | stress |
| S _{max} , S _{min} | maximum and minimum stresses |
| S _{mf} | mean stress in flight |
| SENT | Single Edge Notch Tension (specimen) |
| σ_y | yield stress (0.2 % offset) |
| t | specimen thickness |
| TH3 | Three Hole crack Tension (specimen) |
| UTS | Ultimate Tensile Strength |
| W | specimen width |
| 2024-T3 | damage tolerant naturally aged Al-Cu-Mg alloy |

NOTE

In this contribution the short crack nomenclature is the reverse of that in the AGAW core programme and the other supplemental programme contributions. Thus the notch surface crack length is 2c (surface crack) or c (corner crack) and the crack depth or side surface dimension is a. The reasons for choosing this nomenclature are:

- (1) It is used more or less consistently in aircraft damage tolerance requirements (MIL-A-83444) and in aerospace fracture control guidelines (ESA PSS-03-1203).
- (2) It is consistent when dealing with the transition from short to long crack growth.

1. INTRODUCTION

Modern transport aircraft are designed for economic service lives ~ 50,000 - 100,000 flights. This means that permissible fatigue stress levels in the airframe are low and that a large part of the fatigue life is spent in initiating and growing small cracks. A schematic illustration is given in figure 1: long fatigue lives are achieved only when the cyclic stress and strain levels are low and initial flaws are absent or very small.

The engineering significance of small fatigue cracks depends on three main factors [2]:

- (1) Design principles and fatigue design categories.
- (2) Applicability of non-destructive inspection (NDI).
- (3) Service load characteristics.

The airframes of transport aircraft are designed according to damage tolerance principles [3]. Safe and economic service lives must be established on the basis of fatigue crack growth from pre-existing flaws. Small cracks are therefore potentially relevant, depending on the other two factors. The most important of these is non-destructive inspection. Pre- and in-service NDI are required for demonstrating safe crack growth lives, but not for the estimation of economic crack growth lives (durability).

With respect to safety, figure 1 indicates that microstructurally short cracks are not relevant to the determination of fatigue crack growth lives from inspectable flaw sizes. This is shown in more detail in figure 2: all inspectable flaw sizes are beyond 0.5 mm, which is about the limit of the so-called short crack regime for most materials [4].

On the other hand, durability analyses are concerned with the widespread initiation and growth of very small cracks [5-7]. Assumed and estimated initial flaw sizes are well within the short crack regime, and a better understanding of the apparent, anomalous behaviour of short fatigue cracks is therefore essential.

The primary objective of the present work is to examine the significance of short fatigue crack growth for durability analysis of the Fokker 100 wing/fuselage structure. The Fokker 100 aircraft is designed to have an economic repair life of 90,000 flights and a guaranteed crack-free life for the primary structure of 45,000 flights [3].

2. MATERIALS

The materials were 2024-T3 and 2024-T3 Alclad aluminium alloy sheet. Average longitudinal tensile properties and microstructural characteristics are given in table 1. The main difference in properties was the higher UTS for the NASA material. Constant amplitude fatigue crack growth data for long cracks and a wide range of R are presented in figure 3 and compared in figure 4. As can be seen from figure 4, the crack growth rate dependences on ΔK and R were very similar.

3. FATIGUE TEST SPECTRUM

The Reduced Basic (RB) spectrum for the Fokker 100 wing root area was used in this investigation. The RB spectrum differs from the basic (B) spectrum only in replacing taxi load cycles by a maximum downward load during each ground phase (landing + takeoff). This approximation has no effect on fatigue crack growth [12].

For testing purposes the RB spectrum for the wing root area is approximated by the stepped gust and taxi load levels shown in figure 5. The stresses have been expressed non-dimensionally by dividing them by the stresses pertaining to undisturbed cruising flight. Thus the load scale is expressed as S/S_{mf} , where S is stress and S_{mf} is the mean stress in flight. There are eight gust load levels and three taxi load levels.

The test load sequence consists of blocks of 5000 different flights. There are eight different flight types (A-H) ranging from storm (A) to calm (H) conditions. Table 2 gives the frequency of occurrence of each flight and each load level within each type of flight. The load sequence was derived by defining the sequence of application of the different flights, the sequence of gust loads within each flight and the appropriate taxi load for each flight. Important properties of the defined load sequence are:

- (1) The complete sequence of 5000 flights is subdivided into four sub-blocks of 1250 flights, namely one "A" sub-block and three "B" sub-blocks. The positions of the severest flights in these sub-blocks are listed in table 3. These positions are random except that clustering of severe flights has been avoided. Also the arrangement of A and B type flights provides characteristic markers on fatigue fracture surfaces and enables fractographic tracing of crack growth back to flaw depths less than 0.2 mm [13].
- (2) Load sequences have been generated individually for each flight within a sub-block. This means that flights of the same type will generally have a different load sequence. Also, the different taxi load levels have been distributed randomly over each sub-block. Hence there is no relation between flight type severity and taxi load level.
- (3) The loads within each flight are applied as a random sequence of half cycles in such a way that a positive gust half-cycle is followed by a negative gust half-cycle of arbitrary magnitude. Naumann defined such a sequence as "random half-cycle, restrained" [14].

- (4) The highest load level (in flight type A) corresponds to a cumulative frequency of 1 per 5000 flights, i.e. 18 occurrences during the economic repair life of 90,000 flights. This peak load level is considered to be reasonable for obtaining sufficiently conservative fatigue crack growth results [12].

Examples of the RB test load sequence (flight types A, F, G and H) for the wing root area are given in figure 6. These illustrate a minor refinement. During the approach (flaps-out) phase the mean load is reduced by about 2 %. This is an approximate way of simulating mean load changes during the different flight phases [8].

4. FATIGUE TEST SPECIMENS

There were three types of fatigue specimens. Their configurations are shown in figure 7. The Single Edge Notch Tension (SENT) specimens were identical to those used in the AGARD core programme [15] and were used for studying short crack growth under Fokker 100 spectrum loading. Centre Crack Tension (CCT) specimens were used for K-increasing tests with the Fokker 100 spectrum. The starter notches were Electric Discharge Machined (EDM) slots 2 mm long on either side of 3 mm diameter central holes. Stress intensity factors were calculated using appropriate stresses and crack lengths in the Feddersen secant formula [16].

The third specimen type was the Bonded Patch Three Hole crack Tension (BPTHT) specimen. This configuration was derived from the THT specimen, without bonded patches, developed for monotonic fracture testing by Newman [17]. The bonded patches were found to be necessary for fatigue testing in order to resist crack initiation at the other side of the starter notch hole. A cold setting adhesive, Agomet F310, was first used. This was replaced by a 125 °C curing adhesive, AF163, which gave a better bond but no improvement in resistance to crack initiation at the other side of the starter notch hole.

There were two reasons for using the BPTHT specimen configuration:

- (1) K decreases naturally with increasing crack length, thereby enabling spectrum fatigue long crack growth tests down to low stress intensities without imposed load shedding.
- (2) Unlike concentrated force pin-loaded specimens [18] the BPTHT specimen is suitable for load histories containing compressive loads.

Stress intensity factors for a range of THT geometries were supplied by J.C. Newman, Jr. (NASA Langley Research Centre). These solutions were used to derive the BPTHT specimen. Figure 8 compares stress intensity factors for the BPTHT specimen and a THT specimen with the same geometry. The BPTHT specimen has another advantage besides resisting crack initiation at the other side of the starter notch hole: the negative dK/da is shallower.

5. EXPERIMENTAL PROCEDURES

The SENT and CCT specimens were tested in a 200 kN AMSLER electrohydraulic machine. The BPTHT specimens were tested in a 2°0 kN MTS electrohydraulic machine. For specimens made from the thinner gauge NASA material (see table .) it was necessary to use antibuckling guides to suppress buckling during compressive loads. The procedures for SENT specimen testing and short crack growth measurements were according to guidelines and requirements for the AGARD core programme [15]. In other words, the SENT specimens were most carefully aligned and crack growth was monitored using the plastic replica method [19].

The AMSLER machine was controlled by an NLR-developed device called MIDAS (Magnetic tape Input Digital-to-Analogue Signal) and the Fokker 100 RB spectrum load sequence was stored on magnetic tape and read by an incremental recorder. The MTS machine was controlled by a PDP 11 computer and the load sequence was stored on a hard disc. All tests were begun at flight number 1. The tests were run at 12 - 20 Hz in laboratory air with relative humidity of 40 - 60 % at 295 K.

The standard S_{mf} level of the Fokker 100 wing root area is 65 MPa [12]. As with many new aircraft, it may be anticipated that future developments will lead to significant load increases [8]. To allow for this eventuality and to provide conservative results a baseline S_{mf} of 81.25 MPa (i.e. 125 % of the standard level) was used in the present investigation. Some BPTHT tests were done at lower S_{mf} levels in order to reach lower stress intensities.

6. DATA ANALYSIS PROCEDURES

6.1 Short Crack Stress Intensity Factors

As described in the AGARD core programme [15] the calculation of stress intensity factors for short cracks assumes that either a semi-elliptical surface crack is located at the centre of the edge notch or a quarter-elliptical corner crack is located at an edge. A key assumption in the calculation is that the aspect ratios (a/c) of these cracks are approximated by:

$$\boxed{\text{surface crack}} \quad a/c = 0.9 - 0.25 (2c/t)^2 \quad (1)$$

$$\boxed{\text{corner crack}} \quad a/c = 0.9 - 0.25 (c/t)^2 \quad (2)$$

where a and c are the ellipse semi-axes perpendicular and parallel to the notch surface respectively. The notch surface crack lengths $2c$ were derived from projection of the actual crack lengths onto a line perpendicular to the stress axis and parallel to the notch surface.

Use of Fokker 100 spectrum loading enables checking the applicability of equations (1) and (2) because the load sequence results in characteristic markers on the fracture surfaces. An example is given in figure 9, which shows that crack front markers can be traced back to flaw depths less than 25 μm .

The fracture surfaces of specimens tested under the Fokker 100 RB spectrum loading were examined by scanning electron microscopy (SEM). All cracks initiated as semi-elliptical surface cracks. The a/c dependence on crack size and specimen thickness is plotted in figure 10 together with the approximation equation (1) and constant amplitude data from Swain and Newman [20]. Equation (1) fits the data well for surface crack lengths $2c > 100 \mu\text{m}$. For smaller cracks a better fit is obtained with the dashed line bounded by a/c values of 0.4 and 0.9.

In view of this result, short crack stress intensity factors were calculated using equation (1) or the dashed line in figure 10, depending on the appropriate crack size regime.

6.2 Short-to-Long Crack Stress Intensity Factors

Short cracks in SENT specimens were allowed to become through cracks. This enabled comparison of SENT and CCT specimen long crack growth data. Stress intensity factors for through cracks in the SENT specimens were estimated as follows:

- (1) For $0.3 \text{ mm} < a < 1.5 \text{ mm}$ use was made of a transitional curve between

$$K = 2.95S \sqrt{\pi a} \quad (3)$$

$$K = CS \sqrt{\pi(a+r)} \quad (4)$$

$$\text{and } C = 1.12 - 0.231 \{(a+r)/W\} + 10.55 \{(a+r)/W\}^2 - 21.72 \{(a+r)/W\}^3 + 30.39 \{(a+r)/W\}^4.$$

- (2) For $a > 1.5 \text{ mm}$ equation (4) was used.

Equation (3) is derived from the Smith and Miller approximation for short cracks at notches [21] and equation (4) is the Brown and Srawley approximation for a single edge cracked plate [22].

6.3 Non-interaction Criteria for Crack Coalescence and "Shadowing"

Multiple cracking at the notch roots of SENT specimens results in crack interactions (coalescence and "shadowing") that affect crack growth rates. Straightforward criteria for rejecting crack growth data when interactions occur were proposed by J. Foth (formerly with the Industrieanlagen-Betriebsgesellschaft, Federal Republic of Germany) and are illustrated in figure 11. There are three basic criteria for non-interaction:

- (1) Crack growth data for colinear cracks (l_1 and l_2 in figure 11a) are rejected when the distance $d_{1,2}$ between adjacent crack tips is less than the length of the larger crack, l_1 . In this case crack interaction is expected to accelerate crack growth.
- (2) Crack growth data for cracks one above the other (l_1 and l_3 in figure 11a) are rejected when the distance $h_{1,3}$ between them is less than the length of the larger crack, l_1 . Here it is expected that the larger crack "shadows" the smaller one, i.e. the stresses in the vicinity of the shorter crack are reduced and its growth rate decreases.
- (3) Crack growth data for coalesced cracks, figure 11b, are rejected until the combined crack length l is twice the total length at coalescence, $l_1 + l_2$. This criterion allows for the development of a stable, representative crack front for the combined crack.

These three non-interaction criteria have been used in the AGARD core programme [15] and were also applied to the crack growth data from the present work.

6.4 Calculation of Crack Growth Rates

Crack growth rates for both long and short cracks were calculated by the point-to-point method, i.e.

$$\frac{da}{dn_f} = \frac{a_{i+1} - a_i}{n_{i+1} - n_i} \quad (5)$$

or

$$\frac{dc}{dn_f} = 0.5 \left[\frac{(2c)_{j+1} - (2c)_j}{n_{i+1} - n_i} \right] \quad (6)$$

The corresponding crack lengths and stress intensity factors were determined using the means of the crack growth increments.

7. RESULTS

7.1 Short Crack Growth

The short crack growth data will be presented in the following ways:

- notch surface crack lengths, $2c$, versus number of flights, n_f
- valid notch surface crack growth rates, dc/dn_f , versus $2c$
- valid in-depth crack growth rates, da/dn_f , versus K_{mf} .

In the latter instance figure 10 was used to convert $2c$ versus n_f data into a versus n_f values, which were then used to derive da/dn_f . The a values were also used to calculate the means of the in-depth crack growth increments and hence K_{mf} , which is the in-depth stress intensity factor corresponding to S_{mf} , the mean stress in flight.

Several cracks initiated at the notch roots of each specimen and some of the cracks coalesced. Figures 12 and 13 show the crack length versus number of flights data for the five or six main cracks in each specimen. The growth of individual cracks was extremely slow: only a few tenths of a millimetre in more than one hundred thousand simulated flights.

Crack growth rates versus crack lengths are plotted in figures 14 and 15. Large variations in crack growth rates and temporary slowing of crack growth appear to be characteristic. These features may well reflect the resistance to crack growth afforded by grain boundaries [23-27], but this could not be ascertained from the plastic replicas. However, it was possible to determine the crack initiation mechanism. All cracks initiated at the interfaces between inclusions and the alloy matrix. This is consistent with the results of the AGARD core programme [15] and earlier investigations of high-cycle fatigue in 2024 alloy [28-30].

In-depth crack growth rates versus the characteristic stress intensity factor K_{mf} are shown in figure 16. A best fit linear relationship between $\log da/dn_f$ and $\log K_{mf}$ is indicated together with 95 % confidence limits for the data. It is evident that despite considerable variations in crack growth rates at similar K_{mf} values there is a trend of increasing crack growth rates with increasing K_{mf} .

7.2 Long Crack Growth Under K-Increasing Conditions

The long crack growth behaviour of the NASA and Fokker 100 materials is compared in figure 17. Crack growth rates were significantly different up to $K_{mf} \sim 20 \text{ MPa}\sqrt{\text{m}}$. In particular, the NASA material exhibited an initially decreasing crack growth rate. This behaviour is characteristic of ductile, thin sheet materials tested under gust spectrum loading [31], whereby peak loads in severe flights cause significant crack growth retardation. The difference in crack growth behaviour between the two materials can be explained by differing constraint (stress state) during peak loads as a consequence of different sheet thicknesses.

Figure 18 compares the long crack growth behaviour of SENT and CCT specimens of the NASA material. Again there are differences in crack growth rates up to $K_{mf} \sim 20 \text{ MPa}\sqrt{\text{m}}$. In this case it is thought that differing constraint occurs during peak loads at similar K_{mf} values because of the different specimen geometries. Also there may be differing start-up effects during which crack closure levels gradually stabilise [15].

7.3 Long Crack Growth Under K-Decreasing Conditions

The long crack growth behaviour of BPTH specimens of the NASA material is shown in figure 19. The crack growth rate data were poorly correlated by K_{mf} . Crack growth rates below 2×10^{-8} m/flight were not obtained owing to secondary crack initiation at the other side of the starter notch hole.

7.4 Comparisons of Short and Long Crack Growth Behaviour for the NASA material

Figure 20 combines the short and long crack growth rate data plotted against K_{mf} . The data envelopes give an indication - despite the considerable spread in the data - that short cracks propagate at higher crack growth rates than would be expected from extrapolation of the long crack data. The differences between long crack growth rate data for different specimen types may be due to differing constraint during peak loads, differences in start-up effects, and differing dK/da .

8. DISCUSSION

8.1 Practical Significance of Short Cracks

The practical significance of short fatigue cracks in aerospace aluminium alloys involves two main - and interrelated - aspects:

- (1) The potential importance of short crack behaviour for durability analysis of widespread cracking at fastener holes in airframes [2].

- (2) In the development of new airframe materials (e.g. aluminium - lithium alloys) the short crack behaviour should be compared with that of established materials which have proven capable of being built into durable structures.

The results of this investigation are relevant primarily to assessing the importance of short fatigue crack growth for durability analysis of the Fokker 100 wing/fuselage structure. However, because the material tested is the widely used damage tolerant alloy 2024-T3, the data also provide a reference for evaluation of new materials.

Comprehensive durability analysis requires a probabilistic approach to characterizing initial flaw sizes and predicting crack growth at fastener holes in airframes [5,6,32-35]. The scope of the present work allows only simple crack growth predictions, which are nevertheless useful for assessing the significance of short cracks in the Fokker 100 wing/fuselage structure. The approach is as follows:

- | | |
|----------------------------------------|----------------------------------------------------------------------------------------------------------------------------------------------------------------------------------------------------------------------------------------------------------------------------------------------------------------------------------------------------------------------------------------------------------------------------------------------------------------------------------------------------------------------------------------------------------------------------------------------------------------------------------------------------------------------------------------------------------------------------------------------------------------------------------------------------------------------------------------------------------------------------------------------------------------------------------------------------------------------------------------------------------------------------------------------------------------------------------------------------------------------------------------------------------------------------------------------------------------------------------------------------------------------------------------------------------------------------------|
| USE SHORT
CRACK GROWTH
RATE DATA | <ul style="list-style-type: none"> • assume initial corner flaws with side surface dimension $a = 0.127$ mm at each fastener hole: this is a reasonably conservative assumption in lieu of actual data on as-manufactured airframe quality [3] • derive a versus K_{mf} for a quarter-elliptical corner crack at the notch in a SENT specimen with thickness $t = 4$ mm (representative for the Fokker 100 wing/fuselage skin) using the appropriate stress intensity factor equation [1b] and S_{mf} levels of 65 MPa and 81.25 MPa: the SENT specimen configuration is suitable because the notch K_t is representative for fastener holes in airframes [15] • transform the best fit and 95 % confidence upper limit relationships between da/dn_f and K_{mf} in figure 16 into curves of dn_f/da versus a for quarter-elliptical corner cracks at the notches in SENT specimens with S_{mf} levels of 65 MPa and 81.25 MPa • numerically integrate the curves of dn_f/da versus a to obtain a versus n_f plots up to $c = 4$ mm (side surface dimension $a = 2.6$ mm, see equation (2)) |
| USE LONG
CRACK GROWTH
RATE DATA | <ul style="list-style-type: none"> • at $c = 4$ mm assume instantaneous transition from a quarter-elliptical corner crack to a through crack of length $a = 2.6$ mm • derive a versus K_{mf} for a through crack using $K_{mf} = 1.12S_{mf}\sqrt{\pi(a+t)}$, i.e. neglecting finite width effects in equation (4), and S_{mf} levels of 65 MPa and 81.25 MPa • transform the upper bound relationship between da/dn_f and K_{mf} for through cracks in SENT specimens (see figure 18) into curves of dn_f/da versus a at S_{mf} levels of 65 MPa and 81.25 MPa • numerically integrate the curves of dn_f/da versus a to give a versus n_f plots • sum the results of the short and long crack a versus n_f plots to obtain estimates of crack dimensions after 45,000 flights (guaranteed crack-free life) and 90,000 flights (economic repair life): compare these dimensions with in-service NDI limits. |

Figure 21 shows the estimated crack sizes as functions of n_f , the best fit and upper limit da/dn_f versus K_{mf} relationships, and S_{mf} . At 45,000 flights the estimated crack sizes are below 6.35 mm, which is the minimum detectable by in-service inspection (last column of figure 2). This result is consistent with the design goal of a guaranteed crack-free life of 45,000 flights.

At 90,000 flights the situation is more complicated. With the current design S_{mf} level of 65 MPa the maximum estimated crack size is 7.7 mm. Taking into account the presence of fasteners in actual structures, this crack size is below the minimum detectable by in-service inspection. Thus in view of the consistently conservative assumptions used in the estimate, we conclude that short fatigue crack behaviour is not significant for durability analysis of the current wing/fuselage structure of the Fokker 100. In other words, widespread detectable cracking at fastener holes would not be expected to occur within the design economic repair life of 90,000 flights unless the initial flaw sizes were larger - which is unlikely - and probably beyond the short crack regime.

On the other hand, figure 21 also shows that with an S_{mf} level of 81.25 MPa the maximum estimated crack size at 90,000 flights is 84 mm. This is well beyond the minimum detectable by in-service inspection, and such a crack would be repaired before 90,000 flights were reached. The differences within and between the upper and lower diagrams in figure 21 are dramatic and illustrate the important influence of design stress level and choice of short crack growth rate relationships. It seems fair to state that if future developments lead to design stress level increases of 10 % or more, the significance of short fatigue crack behaviour for durability analysis of the Fokker 100 wing/fuselage structure should be examined by a comprehensive probabilistic approach, as mentioned earlier. Important aspects of this problem are the generation of representative short crack growth data and the use of short crack growth models to provide additional analytical capabilities.

8.2 Models of Short Crack Growth

Short crack growth models are in two categories: the microstructural barrier model developed by Miller and co-workers [36-40] and the analytical crack closure model used by Newman [15,41,42]. The applicability of these models to aluminium alloys will be discussed briefly and in a general way.

The microstructural barrier model describes short crack growth by two simple equations whose regions of applicability are defined by a critical crack length at which the slowing down of early crack growth changes to acceleration. This model has been successful for carbon steels [36-40] but the behaviour of aluminium alloys is more complicated. Specifically, there may be several temporary slowings of crack growth at different crack lengths. This can be seen in figures 14 and 15, and also more conclusively in [23-27]. Much of the attractive simplicity of the microstructural barrier model would be lost if one attempted to apply it to aluminium alloys.

The analytical crack closure model is capable of predicting crack growth rate variations caused by peak loads but not by microstructural barriers. Nevertheless, the model predicts the general trends of short crack growth under both constant amplitude and spectrum loading [15,41,42]. This should be sufficient provided upper limits can be defined to give consistently conservative predictions, e.g. by using a probabilistic approach.

8.3 Characteristic-K Correlations of Long Crack Growth Rates and their Significance for Crack Growth Prediction

As discussed recently [43] successful correlations of flight simulation fatigue crack growth rates by characteristic stress intensity factors can be useful for interpolative predictions of crack growth. However, such correlations are empirical and by themselves provide little insight into crack growth behaviour.

Ironically, unsuccessful correlations are more instructive. The long crack growth results from the present work indicate that characteristic-K correlations fail when the constraint during peak loads is different. This means that temporary changes in constraint during peak loads should be taken into account by more sophisticated prediction methods, for example the models of Newman [44], De Koning [45] and Baudin and Robert [46].

Characteristic-K correlations will also fail as a consequence of start-up effects that depend on specimen geometry, and may fail owing to differing dK/da . This means that careful consideration must be given to the choice of specimen geometry in relation to crack growth in an actual structure, and that test results must be screened to eliminate suspect or spurious data. Analytical strip-yield models based on crack closure [44,47] can be helpful in this respect.

9. CONCLUSIONS

From the results of the present investigation the most important conclusions are:

- (1) The apparently anomalous behaviour of short fatigue cracks is not significant for durability analysis of the current wing/fuselage structure of the Fokker 100 aircraft.
- (2) If future developments result in design stress increases of 10 % or more, the significance of short fatigue crack behaviour for durability analysis of the Fokker 100 wing/fuselage structure should be examined by a comprehensive probabilistic approach.
- (3) The data provide a reference for evaluating new materials (e.g. aluminium-lithium alloys) as candidates for durable wing/fuselage structures in transport aircraft.

There are several additional conclusions:

- (4) Under flight simulation loading short cracks initiated in the damage tolerant 2024-T3 alloy at the interfaces between inclusions and the alloy matrix. This is consistent with previous results for low stress/high-cycle fatigue.
- (5) Individual short cracks grew very slowly: only a few tenths of a millimetre in more than one hundred thousand simulated flights. Large variations in crack growth rates and temporary slowing of crack growth at different crack lengths appear to be characteristic. This behaviour complicates the use of models to predict short crack growth.
- (6) Short cracks propagated at higher crack growth rates than would be expected from extrapolation of long crack data.
- (7) Characteristic-K correlation of long crack growth rates for different specimen types failed, especially at lower stress intensities. The lack of correlation is attributed to differing constraint during peak loads, start-up effects and differing dK/da . The effect of differing constraint during peak loads should be taken into account by long crack growth models. Also, analytical strip-yield models can be helpful in determining which data must be eliminated because of start-up effects.
- (8) The Bonded Patch Three Hole crack Tension (BPTHT) specimen is at present unsatisfactory for spectrum fatigue long crack growth tests, owing to secondary crack initiation at the other side of the starter notch hole. It is recommended to evaluate specimens with higher modulus patches, e.g. titanium alloy or steel patches.

- (9) The Fokker 100 Reduced Basic (RB) spectrum load sequence for the wing root area results in crack front markers that can be traced back to flaw depths less than 10 μm in favourable circumstances. This is useful for determination of small crack geometries and also post-test measurement of crack growth rates.

10. ACKNOWLEDGEMENTS

This investigation was sponsored by the Netherlands Agency for Aerospace Programs (NIVR). The technical assistance of A.M. Otter, A. Bogert and P.R. Hessels is much appreciated.

11. REFERENCES

1. H. Nowack, R. Marissen, K.H. Trautmann and J. Foth, "Significance of the short crack problem as a function of fatigue life range", *Fatigue of Engineering Materials and Structures*, Mechanical Engineering Publications Ltd., pp. 511-524 (1986): London.
2. R.J.H. Wanhill, "Short cracks in aerospace structures", *The Behaviour of Short Fatigue Cracks*, Mechanical Engineering Publications Ltd., pp. 27-36 (1986): London.
3. T. Swift, "Verification of methods for damage tolerance evaluation of aircraft structures to FAA requirements", *Proceedings of the Twelfth ICAF Symposium, Centre d'Essais Aéronautique de Toulouse*, pp. 1.1/1 - 1.1/87 (1983): Toulouse.
4. R.F.W. Anstee, "An assessment of the importance of small crack growth to aircraft design", *Behaviour of Short Cracks in Airframe Components*, AGARD Conference Proceedings No. 328, pp. 3-1 - 3-9 (1983): Neuilly-sur-Seine.
5. J.L. Rudd, J.N. Yang, S.D. Manning and W.R. Garver, "Durability design requirements and analysis for metallic airframes", *Design of Fatigue and Fracture Resistant Structures*, ASTM STP 761, American Society for Testing and Materials, pp. 133-151 (1982): Philadelphia.
6. J.L. Rudd, J.N. Yang, S.D. Manning and B.G.W. Yee, "Probabilistic fracture mechanics analysis methods for structural durability", *Behaviour of Short Cracks in Airframe Components*, AGARD Conference Proceedings No. 328, pp. 10-1 - 10-23 (1983): Neuilly-sur-Seine.
7. D.Y. Wang, "A study of small crack growth under transport spectrum loading", *Behaviour of Short Cracks in Airframe Components*, AGARD Conference Proceedings No. 328, pp. 14-1 - 14-15 (1983): Neuilly-sur-Seine.
8. A.A. Jongebreur, E.P. Louwaard and R.V. van der Velden, "Damage tolerance test program of the Fokker 100", *Proceedings of the Thirteenth ICAF Symposium*, Engineering Materials Advisory Services Ltd., pp. 317-349 (1985): Warley, U.K.
9. R.J.H. Wanhill, "Low stress intensity fatigue crack growth in 2024-T3 and T351", *Engineering Fracture Mechanics*, Vol. 30, pp. 233-260 (1988).
10. E.P. Phillips, Personal Communication from NASA Langley Research Centre.
11. L. Schra, "Constant amplitude fatigue crack growth data for the Fokker 100 lower wing skin material", NLR Memorandum SM-85-020 U, National Aerospace Laboratory NLR, Amsterdam, June 1985.
12. H.H. van der Linden and J.B. de Jonge, "Justification of the test load programme for the damage tolerance test on the Fokker 100 wing/fuselage (TA-15): issue 2", NLR Technical Report TR 86074, National Aerospace Laboratory NLR, Amsterdam, July 1987.
13. H.H. van der Linden and H.N. Huisman, "Investigation of the fracture surface of the Fokker 100 panel final failure", NLR Technical Report TR 87065, National Aerospace Laboratory NLR, Amsterdam, April 1987.
14. E.C. Naumann, "Evaluation of the influence of load randomization and of ground-to-air cycles on fatigue life", NASA Technical Note TN D-1584, October 1964.
15. J.C. Newman, Jr. and P.R. Edwards, "Short - crack growth behaviour in an aluminium alloy - an AGARD cooperative test programme", AGARD Report No. 732 (1988): Neuilly-sur-Seine.
16. C.E. Feddersen, Discussion in: *Plane Strain Crack Toughness Testing of High Strength Metallic Materials*, ASTM STP 410, American Society for Testing and Materials, pp. 77-79 (1966): Philadelphia.
17. J.C. Newman, Jr., "An evaluation of fracture analysis methods", *Elastic-Plastic Fracture Mechanics Technology*, ASTM STP 896, American Society for Testing and Materials, pp. 5-26 (1985): Philadelphia.
18. I.E. Figge and J.C. Newman, Jr., "Fatigue crack propagation in structures with simulated rivet forces", *Fatigue Crack Propagation*, ASTM STP 415, American Society for Testing and Materials, pp. 71-93 (1967): Philadelphia.
19. C.W. Brown and G.C. Smith, "A two stage plastic replication technique for monitoring fatigue crack initiation and early fatigue crack growth", *Advances in Crack Length Measurement*, Engineering Materials Advisory Services Ltd., pp. 41-51 (1982): Warley, U.K.

20. M.H. Swain and J.C. Newman, Jr., "On the use of marker loads and replicas for measuring growth rates for small cracks", *Fatigue Crack Topography*, AGARD Conference Proceedings No. 376, pp. 12.1-12.17 (1984): Neuilly-sur-Seine.
21. R.A. Smith and K.J. Miller, "Prediction of fatigue regimes in notched components", *International Journal of Mechanical Science*, Vol. 20, pp. 201-206 (1978).
22. W.F. Brown, Jr. and J.E. Srawley, *Plane Strain Crack Toughness Testing of High Strength Metallic Materials*, ASTM STP 410, American Society for Testing and Materials, p. 12 (1966): Philadelphia.
23. J. Lankford, "The growth of small fatigue cracks in 7075-T6 aluminium", *Fatigue of Engineering Materials and Structures*, Vol. 5, pp. 233-248 (1982).
24. J. Lankford, "The effect of environment on the growth of small fatigue cracks", *Fatigue of Engineering Materials and Structures*, Vol. 6, pp. 15-31 (1983).
25. A.F. Blom, A. Hedlund, W. Zhao, A. Fathulia, B. Weiss and R. Stickler, "Short fatigue crack growth behaviour in Al 2024 and Al 7475", *The Behaviour of Short Fatigue Cracks*, Mechanical Engineering Publications Ltd., pp.37-66 (1986): London.
26. R.K. Bolingbroke and J.E. King, "A comparison of long and short fatigue crack growth in a high strength aluminium alloy", *The Behaviour of Short Fatigue Cracks*, Mechanical Engineering Publications Ltd., pp. 101-114 (1986): London.
27. K. Tanaka, Y. Akiniwa and E. Matsui, "Propagation of small fatigue cracks in 2024-T3 aluminium alloy", *Fatigue 87*, Engineering Materials Advisory Services Ltd., pp. 361-370 (1987): Warley, U.K.
28. J.E. Grosskreutz and G.G. Shaw, "Critical mechanisms in the development of fatigue cracks in 2024-T4 aluminium", *Fracture 1969*, Chapman and Hall Ltd., pp. 620-629 (1969): London.
29. C.Y. Kung and M.E. Fine, "Fatigue crack initiation and microcrack growth in 2024-T4 and 2124-T4 aluminium alloys", *Metallurgical Transactions A*, Vol. 10A, pp. 603-610 (1979).
30. D. Sigler, M.C. Montpetit and W.L. Haworth, "Metallography of fatigue crack initiation in an overaged high-strength aluminium alloy", *Metallurgical Transactions A*, Vol. 14A, pp. 931-938 (1983).
31. R.J.H. Wanhill, "The effect of sheet thickness on flight simulation fatigue crack propagation in 2024-T3, 7475-T761 and mill annealed Ti-6Al-4V", *Journal of the Society of Environmental Engineers*, Vol. 17, pp. 27-32 (1978).
32. B. Palmberg, A.F. Blom and S. Eggwertz, "Probabilistic damage tolerance analysis of aircraft structures", *Probabilistic Fracture Mechanics and Reliability*, Martinus Nijhoff Publishers, pp. 47 - 130 (1986): The Hague.
33. A.F. Blom, "Relevance of short fatigue crack growth data for durability and damage tolerance analyses of aircraft", *Small Fatigue Cracks*, The Metallurgical Society, Inc., pp. 623-638 (1986): Warrendale, Pennsylvania.
34. A.F. Blom and B. Palmberg, "Fatigue crack growth: statistical considerations", *Fatigue 87*, Engineering Materials Advisory Services Ltd., pp. 1365-1399 (1987): Warley, U.K.
35. S.D. Manning, J.N. Yang and J.L. Rudd, "Durability of aircraft structures", *Probabilistic Fracture Mechanics and Reliability*, Martinus Nijhoff Publishers, pp. 213-267 (1986): The Hague.
36. E.R. de los Rios, H.J. Mohamed and K.J. Miller, "A micro-mechanics analysis for short fatigue crack growth", *Fatigue of Engineering Materials and Structures*, Vol. 8, pp. 49-63 (1985).
37. K.J. Miller, H.J. Mohamed and E.R. de los Rios, "Fatigue damage accumulation above and below the fatigue limit", *The Behaviour of Short Fatigue Cracks*, Mechanical Engineering Publications Ltd., pp. 491-511 (1986): London.
38. K.J. Miller, H.J. Mohamed, M.W. Brown and E.R. de los Rios, "Barriers to short fatigue crack propagation at low stress amplitudes in a banded ferrite-pearlite structure", *Small Fatigue Cracks*, The Metallurgical Society, Inc., pp. 639-656 (1986): Warrendale, Pennsylvania.
39. M.W. Brown, "Interfaces between short, long and non-propagating cracks", *The Behaviour of Short Fatigue Cracks*, Mechanical Engineering Publications Ltd., pp. 423-439 (1986): London.
40. P.D. Hobson, M.W. Brown and E.R. de los Rios, "Two phases of short crack growth in a medium carbon steel", *The Behaviour of Short Fatigue Cracks*, Mechanical Engineering Publications Ltd., pp. 441-459 (1986): London.
41. J.C. Newman, Jr., "A non-linear fracture mechanics approach to the growth of small cracks", *Behaviour of Short Cracks in Airframe Components*, AGARD Conference Proceedings No. 328, pp. 6-1 - 6-26 (1983): Neuilly-sur-Seine.
42. J.C. Newman, Jr., M.H. Swain and E.P. Phillips, "An assessment of the small-crack effect for 2024-T3 aluminium alloy", *Small Fatigue Cracks*, The Metallurgical Society, Inc., pp. 427-452 (1986): Warrendale, Pennsylvania.
43. R.J.H. Wanhill and J. Schijve, "Current status of flight simulation fatigue crack growth concepts", *Fatigue Crack Growth Under Variable Amplitude Loading*, Elsevier Applied Science Publishers Ltd., to be published.

44. J.C. Newman, Jr., "A crack-closure model for predicting fatigue crack growth under aircraft spectrum loading", Methods and Models for Predicting Fatigue Crack Growth Under Random Loading", ASTM STP 748, American Society for Testing and Materials, pp. 53-84 (1981): Philadelphia.
45. A.U. de Koning, "A simple crack closure model for prediction of fatigue crack growth rates under variable-amplitude loading", Fracture Mechanics: Thirteenth Conference, ASTM STP 743, American Society for Testing and Materials, pp. 63-85 (1981): Philadelphia.
46. G. Baudin and M. Robert, "Crack growth life-time prediction under aeronautical type loading", Life Assessment of Dynamically Loaded Materials and Structures, Proceedings of the Fifth European Conference on Fracture, National Engineering and Industrial Technology Laboratory, pp. 779-792 (1984): Lisbon.
47. A.U. de Koning and G. Liefding, "Analysis of crack opening behaviour by application of a discretized strip yield model", Mechanics of Fatigue Crack Closure, ASTM STP 982, American Society for Testing and Materials, pp. 437-458 (1988): Philadelphia.

TABLE 1
Average longitudinal tensile properties and microstructural characteristics
of the materials [9]

| MATERIAL | 2024-T3 | 2024-T3 Alclad |
|---------------------------------------------------------------|-------------------------------------------------|-------------------------------------------------|
| SOURCE | NASA Langley Research Centre | Fokker 100 Programme |
| SHEET THICKNESS (mm) | 2.3 | 3.8 |
| σ_y (MPa) | 359 | 352 |
| UTS (MPa) | 497 | 456 |
| ELONGATION (%) | 21 | 19 |
| MEAN PLANAR DISTANCE
BETWEEN DISPERSOIDS (μm) | L 0.65 \pm 0.12
T,S 0.43 \pm 0.07 | L 0.90 \pm 0.12
T,S 0.57 \pm 0.07 |
| GRAIN DIMENSIONS (μm) | L 108 \pm 45
T 59 \pm 23
S 29 \pm 7 | L 153 \pm 70
T 61 \pm 18
S 20 \pm 3 |

TABLE 2
Definition of flight types and the number of gust cycles
within each flight for the Fokker 100 spectrum [8]

| FLIGHT
NUMBER | NUMBER OF FLIGHTS
IN ONE BLOCK
OF 5000 FLIGHTS | NUMBER OF GUST LOADS (FULL CYCLES) AT THE
8 AMPLITUDE LEVELS | | | | | | | | TOTAL NUMBER
OF CYCLES
PER FLIGHT |
|----------------------------------------------------------|------------------------------------------------------|-----------------------------------------------------------------|-----|----|----|-----|------|--------|--------|-----------------------------------------|
| | | VIII | VII | VI | V | IV | III | II | I | |
| A | 1 | 1 | 1 | 2 | 4 | 9 | 17 | 28 | 62 | 124 |
| B | 3 | | 1 | 0 | 4 | 6 | 12 | 24 | 62 | 109 |
| C | 8 | | | 1 | 1 | 4 | 8 | 19 | 50 | 83 |
| D | 28 | | | | 1 | 1 | 8 | 15 | 44 | 69 |
| E | 148 | | | | | 1 | 2 | 10 | 29 | 42 |
| F | 676 | | | | | | 1 | 5 | 23 | 29 |
| G | 1588 | | | | | | | 2 | 12 | 14 |
| H | 2548 | | | | | | | | 13 | 13 |
| TOTAL NUMBER OF CYCLES PER
BLOCK OF 5000 FLIGHTS | | 1 | 4 | 10 | 52 | 235 | 1313 | 8708 | 73,900 | |
| CUMULATIVE NUMBER OF CYCLES
PER BLOCK OF 5000 FLIGHTS | | 1 | 5 | 15 | 67 | 302 | 1615 | 10,323 | 84,223 | |
| AVERAGE NUMBER OF GUST CYCLES PER FLIGHT = 16.8 | | | | | | | | | | |

TABLE 3
Positions of severest flights in the Fokker 100 spectrum test load sequence [12]

| FLIGHT
TYPE | FLIGHT NUMBER IN SUB-BLOCK | |
|----------------|-----------------------------|-----------------------------|
| | "A" SUB-BLOCK | "B" SUB-BLOCK |
| A | 699 | |
| B | | 699 |
| C | 369,1013 | 369,1013 |
| D | 140,321,551,769,780,823,929 | 140,321,551,769,780,823,929 |

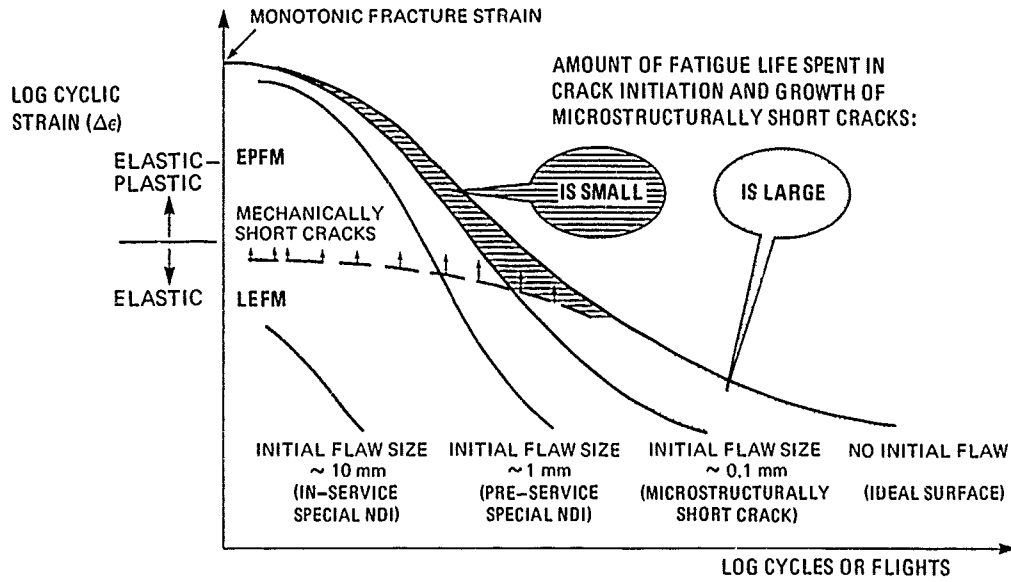


Fig. 1 Schematic relation between fatigue lives, stress-strain levels and initial flaw sizes. After [1]

| TYPES OF FLAW | | ASPECT RATIO (a/c) | FLAW SIZE a (mm) TO BE ASSUMED IMMEDIATELY AFTER INSPECTION | | | | | |
|------------------------------|----------|--------------------|-------------------------------------------------------------|------------------|--------------------------------------|-------------|----------------------------------------------------------|-------------------------------------|
| DESCRIPTION | GEOMETRY | | NEW STRUCTURES WITH PRE-SERVICE INSPECTION CAPABILITIES | | | | IN-SERVICE INSPECTION OF USAF AIRFRAMES WITH SPECIAL NDI | |
| | | | USAF AIRFRAMES WITH HIGH STANDARD NDI | | SPACE SHUTTLE ORBITER EXCEPT ENGINES | | | |
| | | | FAIL-SAFE | SLOW FLAW GROWTH | HIGH STANDARD NDI | SPECIAL NDI | STS PAYLOADS WITH HIGH STANDARD NDI | |
| SURFACE FLAW | | 1.0
0.2 | 1.27 | 3.18 | 1.9 | 0.635 | 1.9
0.65 | 6.35 |
| CORNER FLAW | | 1.0
0.2 | | | | | 1.9
0.65 | |
| THROUGH CRACK | | | 2.54 | 6.35 | | | 1.9 | 12.7 |
| EMBEDDED FLAW | | | | | 2.54 | 1.19 | | |
| THROUGH EDGE CRACK | | | | | | 1.9 | | |
| CORNER FLAW AT A HOLE | | 1.0
0.2 | 0.51 | 1.27 | 1.27 | 1.19 | 2.5 | 6.35 mm BEYOND FASTENER HEAD OR NUT |
| SURFACE FLAW IN BORE OF HOLE | | 1.0
0.2 | | | | | 2.5
1.25 | |
| THROUGH CRACK AT A HOLE | | | 0.51 | 1.27 | 1.27 | | 2.5 | 6.35 mm BEYOND FASTENER HEAD OR NUT |

Fig. 2 Current well-defined NDI limits for initial flaw sizes in aerospace structures [2]

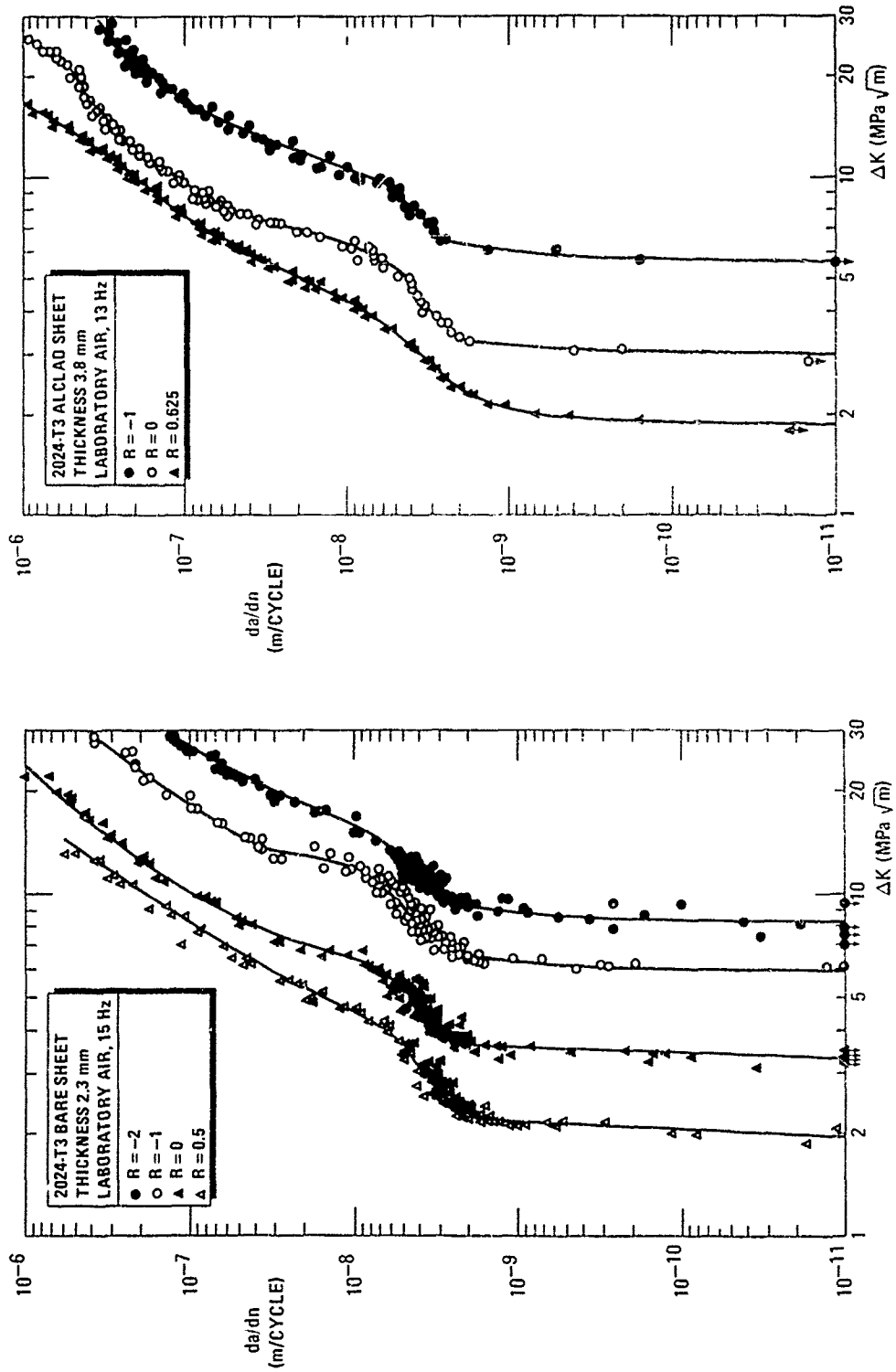


Fig. 3 Constant amplitude long fatigue crack growth rates for the sheet materials [10,11]

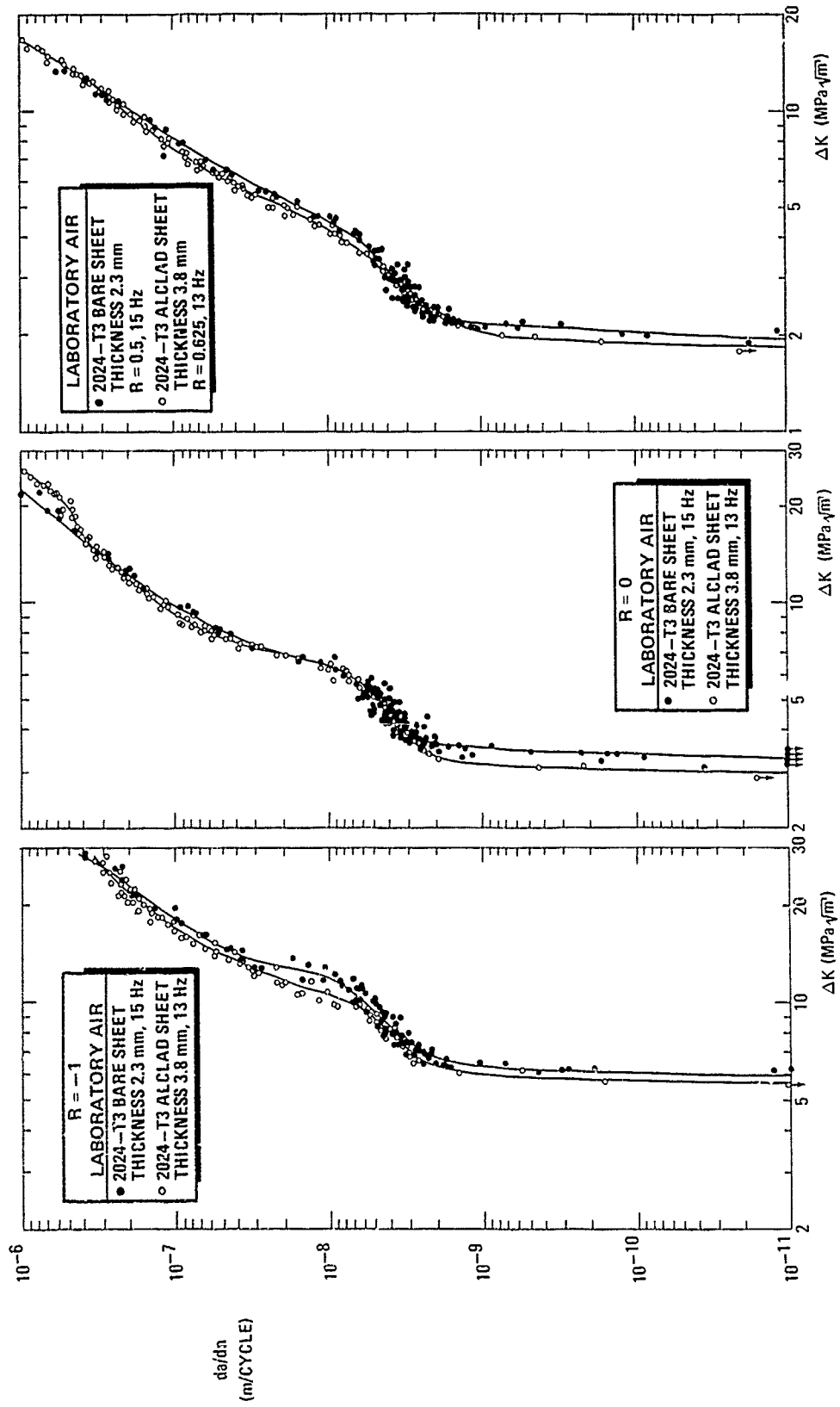


Fig. 4 Comparisons of constant amplitude long fatigue crack growth rates for similar R values

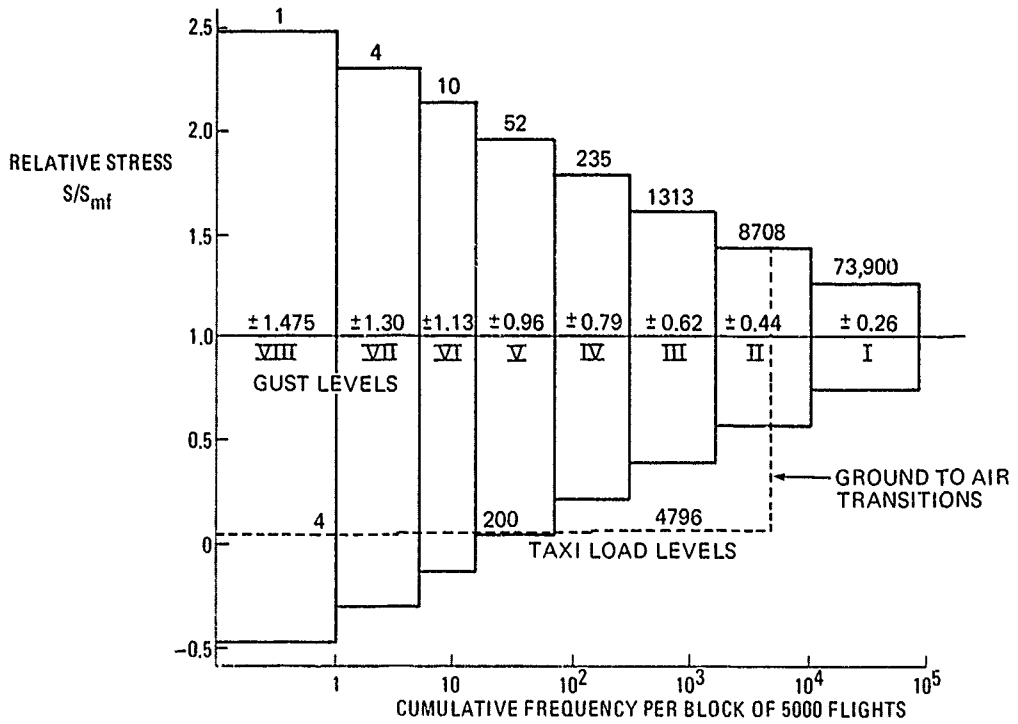


Fig. 5 Stepped approximation to the Fokker 100 Reduced Basic spectrum for the wing root area

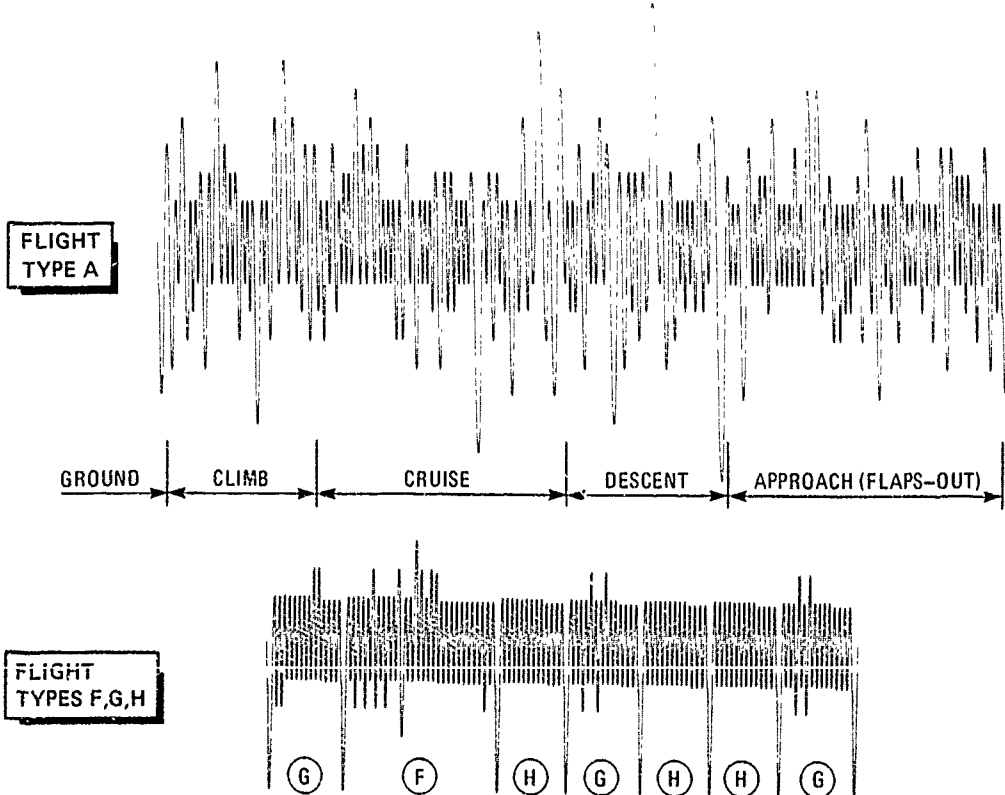
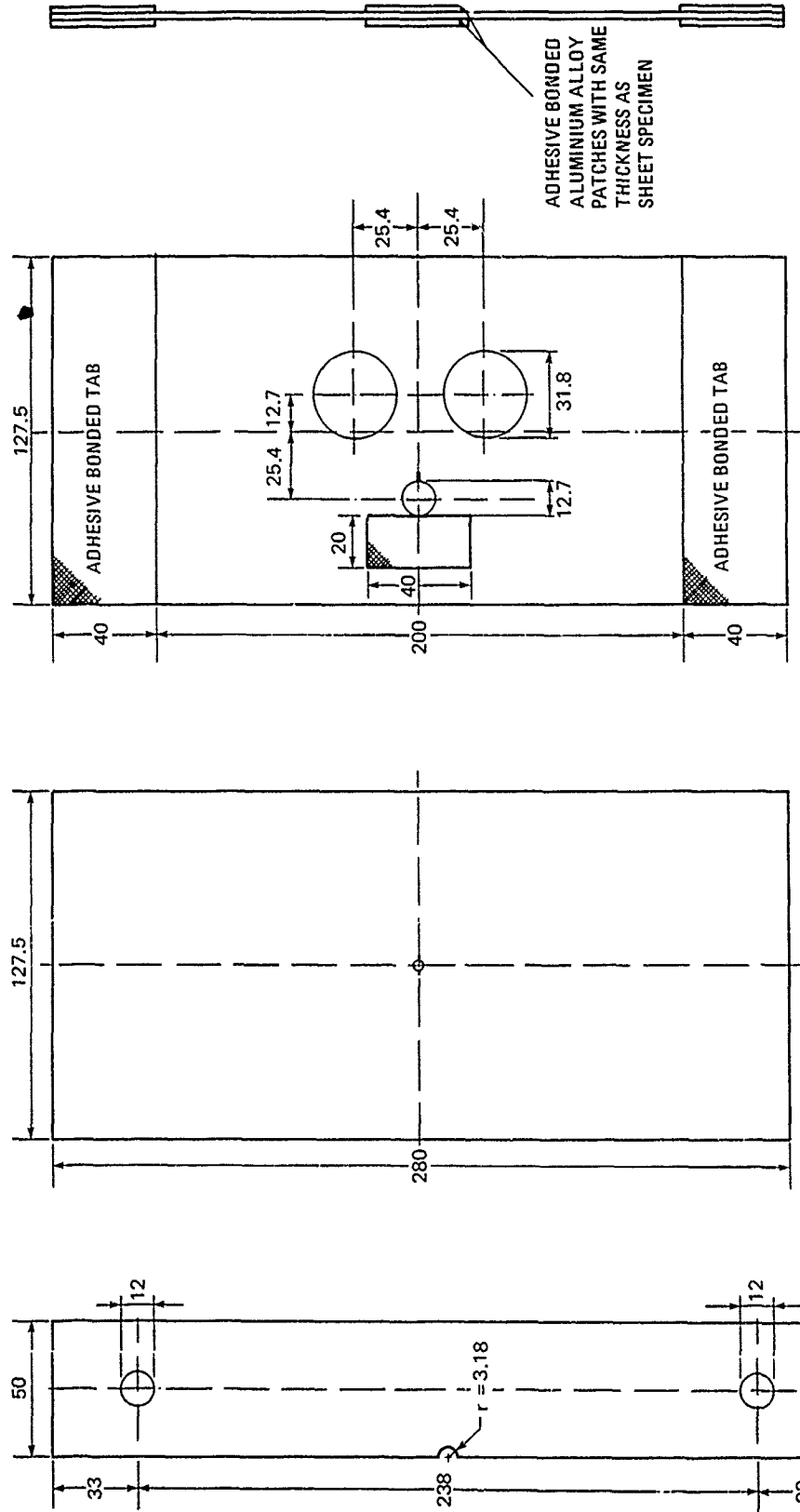


Fig. 6 Examples of flights from the Fokker 100 Reduced Basic test load sequence



BPTHIT

CCT

SENT: $K_t = 3.17$

Fig. 7 Fatigue specimen configurations used in the present investigation. see text for details. All dimensions in millimetres.

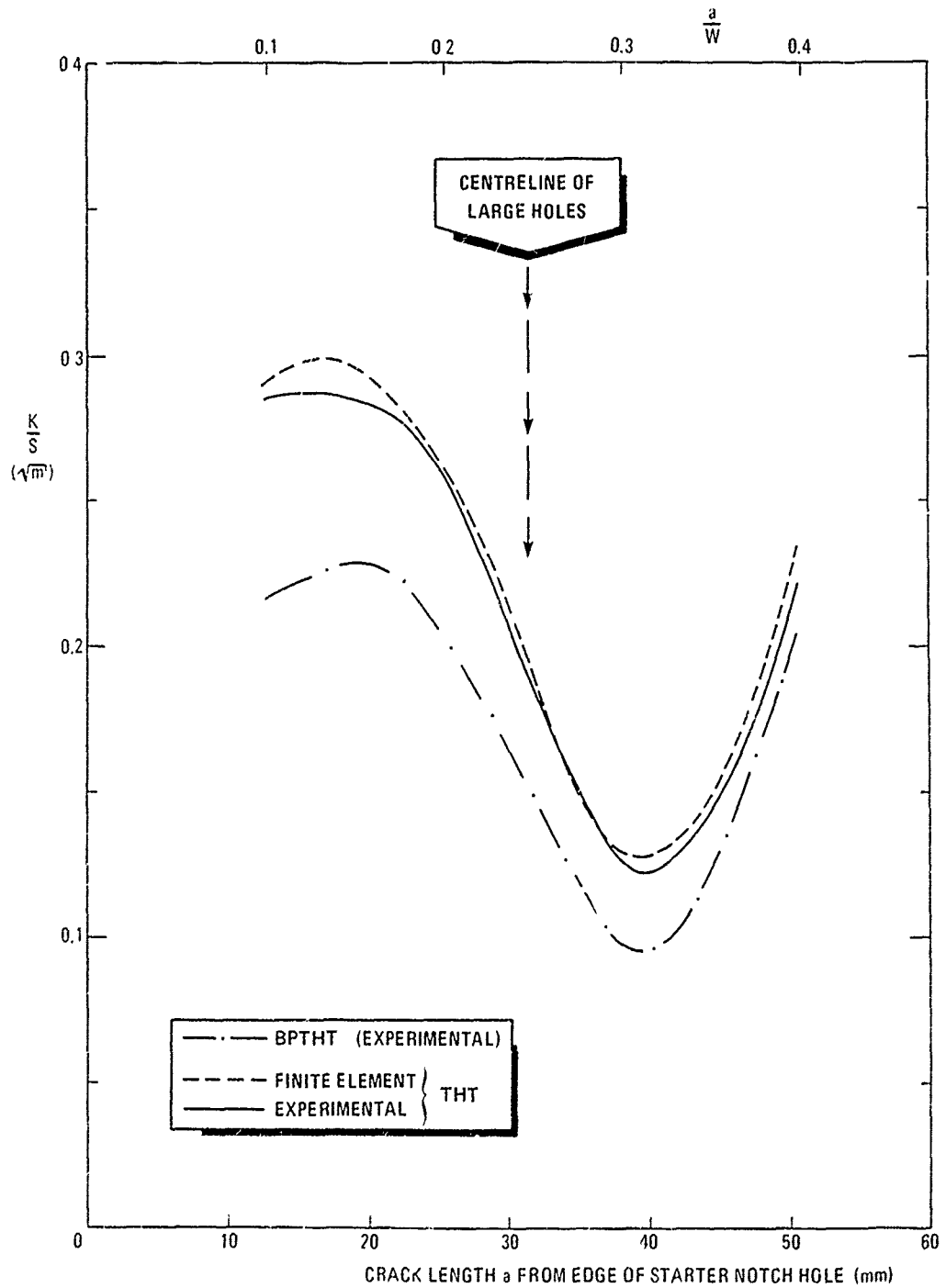


Fig. 8 Stress intensity factors for the BPTH specimen and a THT specimen with the same geometry

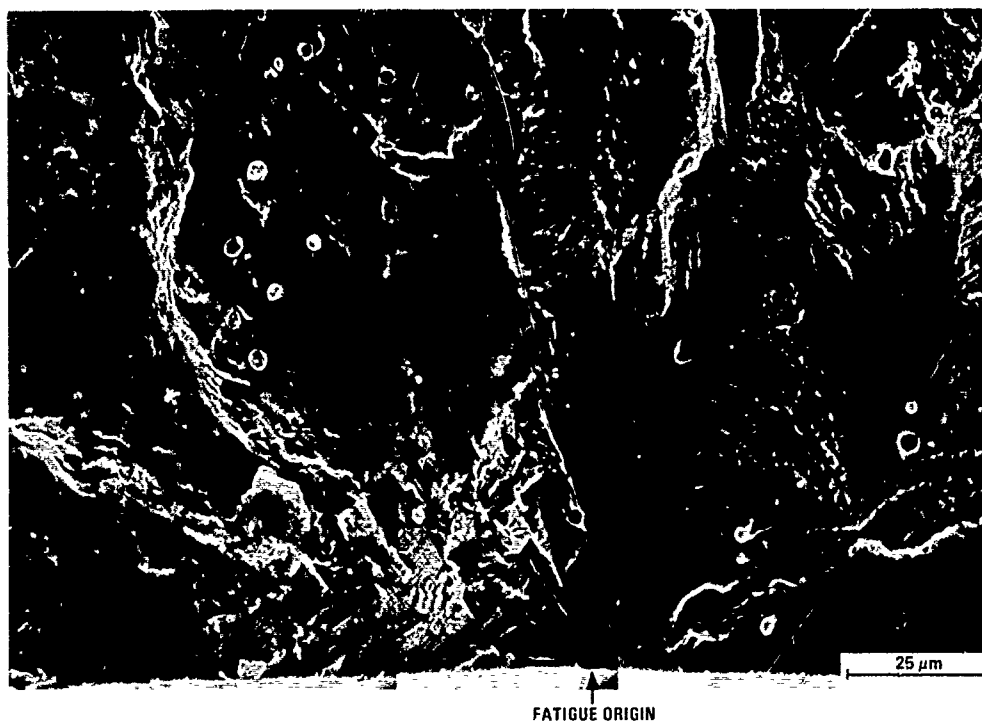


Fig. 9 Photomontage of fatigue crack initiation in a specimen tested with the Fokker 100 RB spectrum

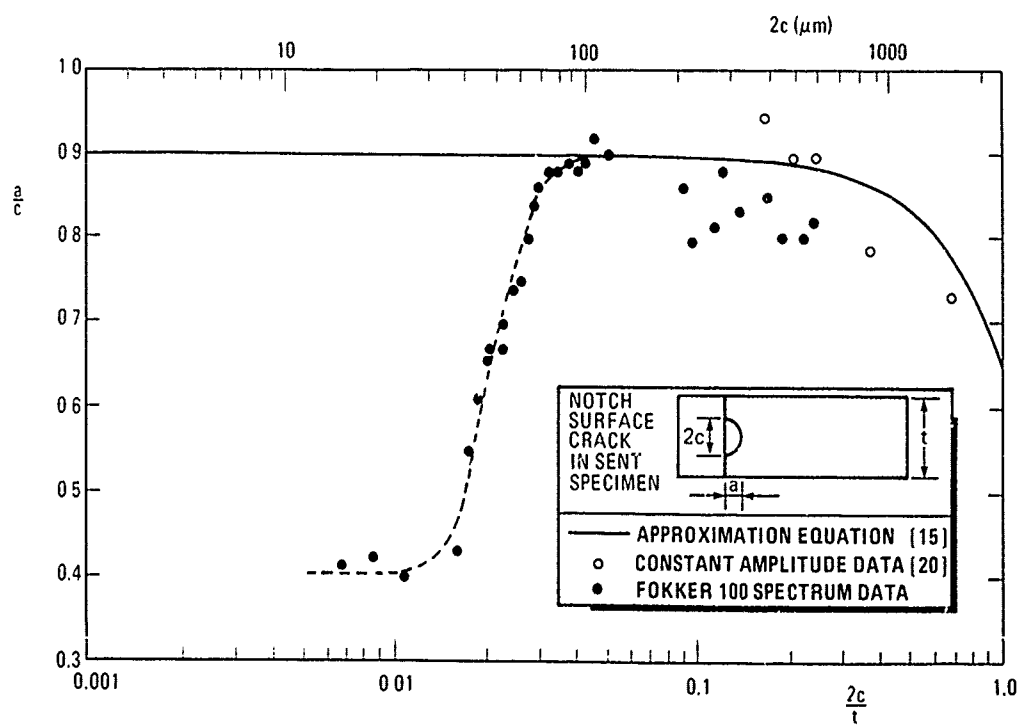
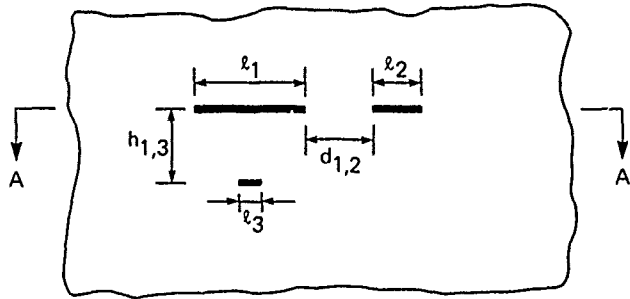
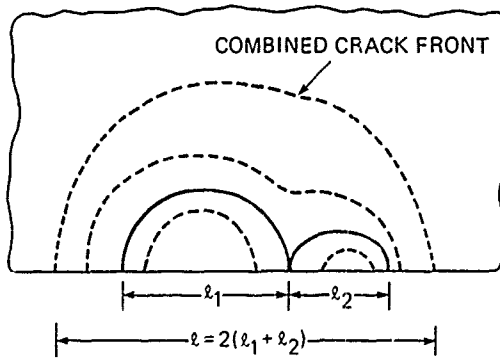


Fig. 10 Results of fractographic determination of natural crack shapes in SENT specimens

a MULTIPLE CRACKING AT NOTCH ROOT



b INTERACTING SURFACE CRACKS FOR $d_{1,2} = 0$ (SECTION A-A)



c DEFINITION OF VALID AND INVALID CRACK GROWTH DATA

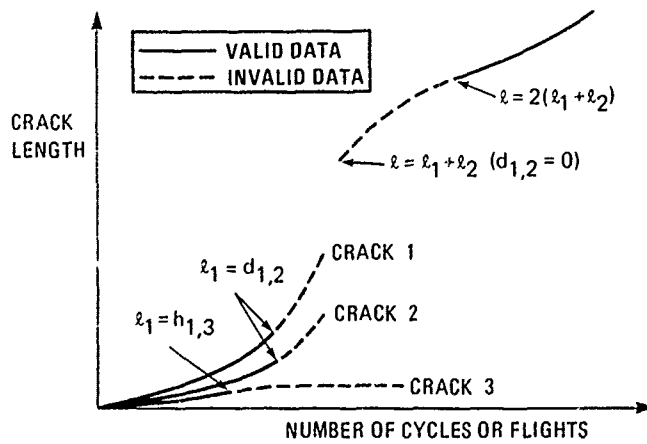


Fig. 11 The Foth non-interaction criteria for crack coalescence and "shadowing" (see text)

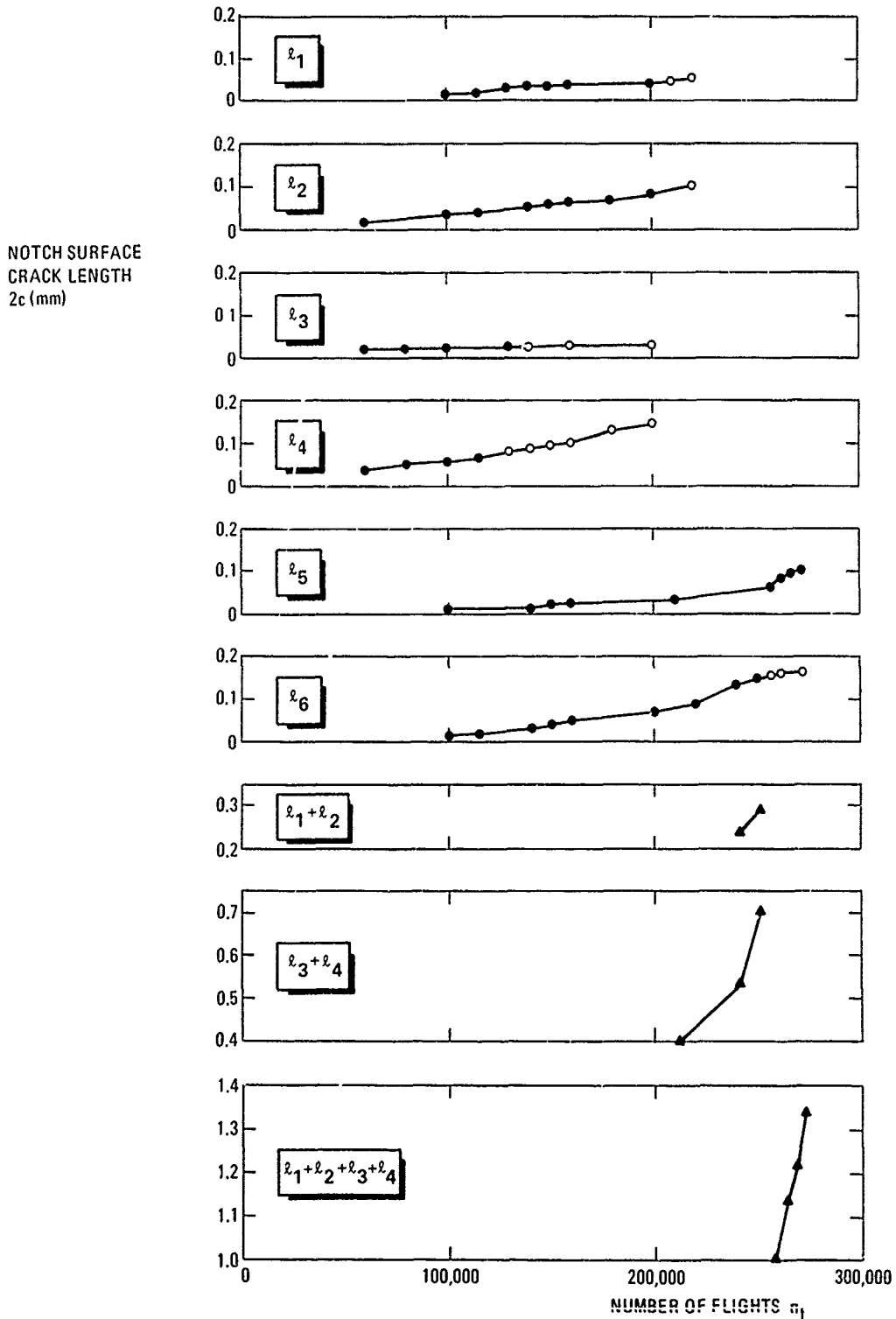


Fig. 12 Short crack lengths versus number of simulated flights for the Fokker 100 Reduced Basic spectrum load sequence with $S_{mf} = 81.25$ MPa. SENT specimen A67-14: ● non-interaction; ○ possible interaction; ▲ non-representative crack front after coalescence

NATIONAL BUREAU OF STANDARDS - Gaithersburg, MD 20899-1092

NOTCH SURFACE
CRACK LENGTH
 $2c$ (mm)

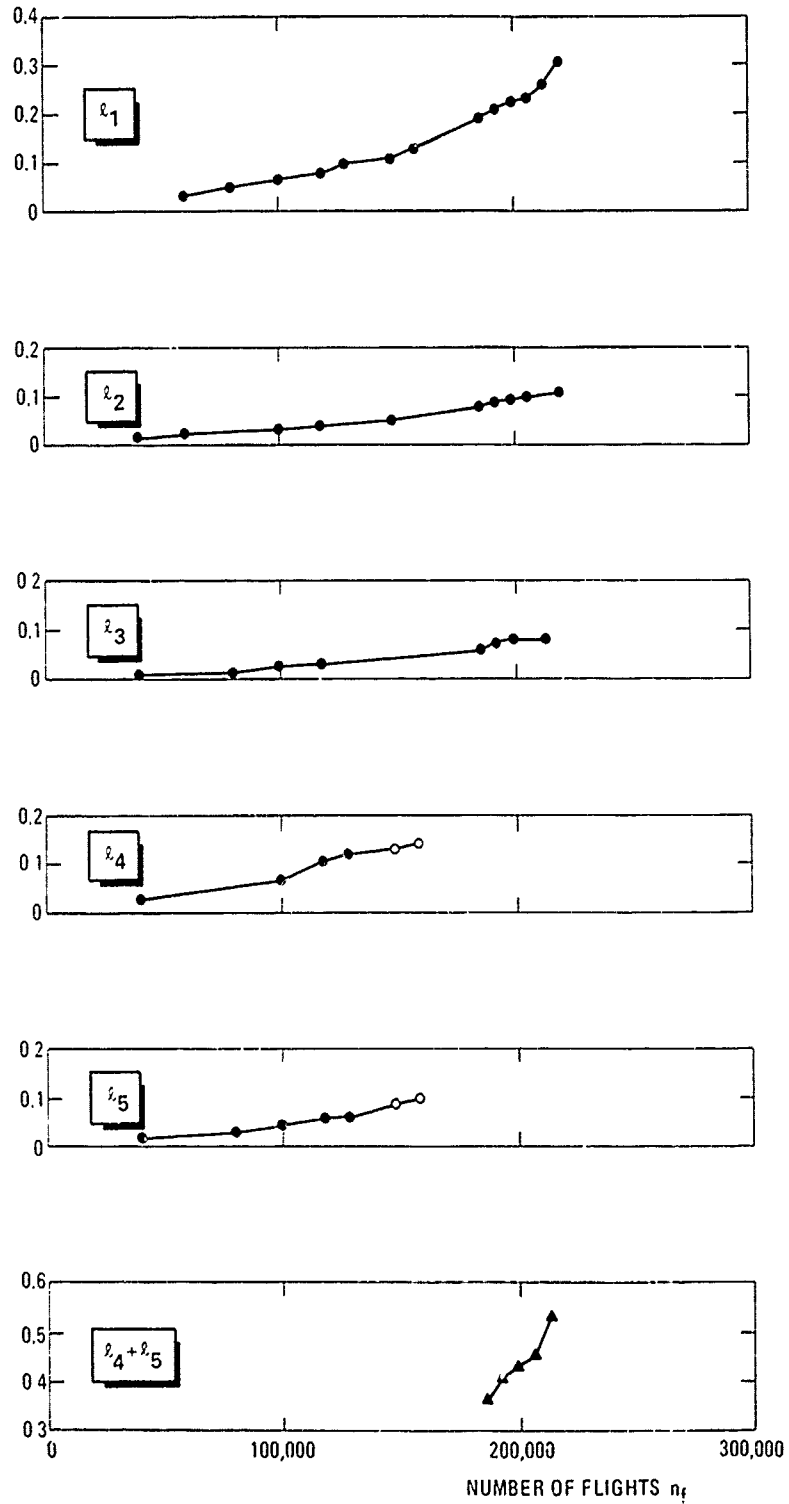


Fig. 13 Short crack lengths versus number of simulated flights for the Fokker 100 Reduced Basic spectrum load sequence with $S_{mf} = 81.25$ MPa. SENT specimen A68-11: ● non-interaction; ○ possible interaction; ▲ non-representative crack front after coalescence

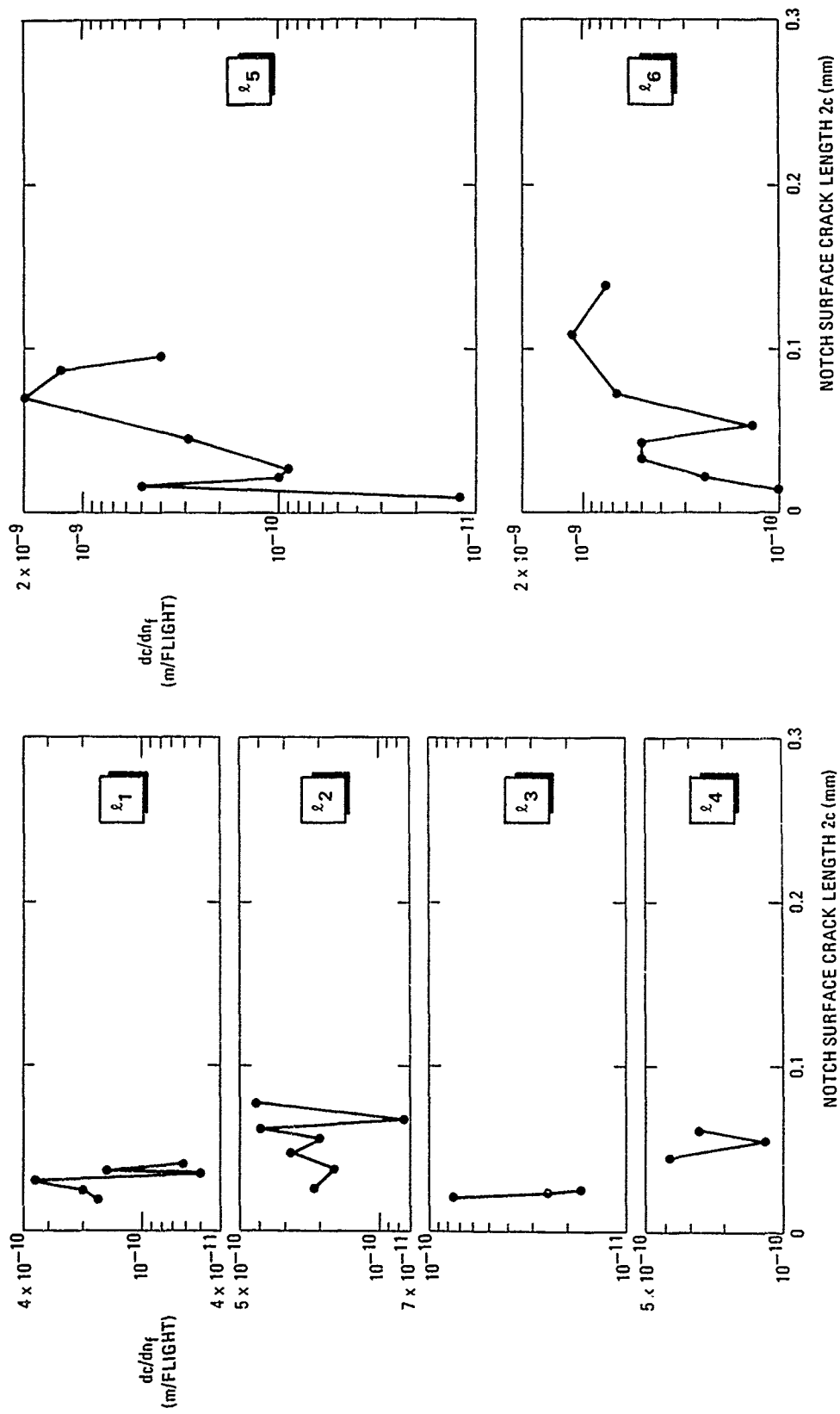


Fig. 14 Valid short crack growth rates versus crack lengths for SENT specimen A67-14 tested with the Fokker 100 Reduced Basic spectrum load sequence: $S_{mf} = 81.25$ MPa

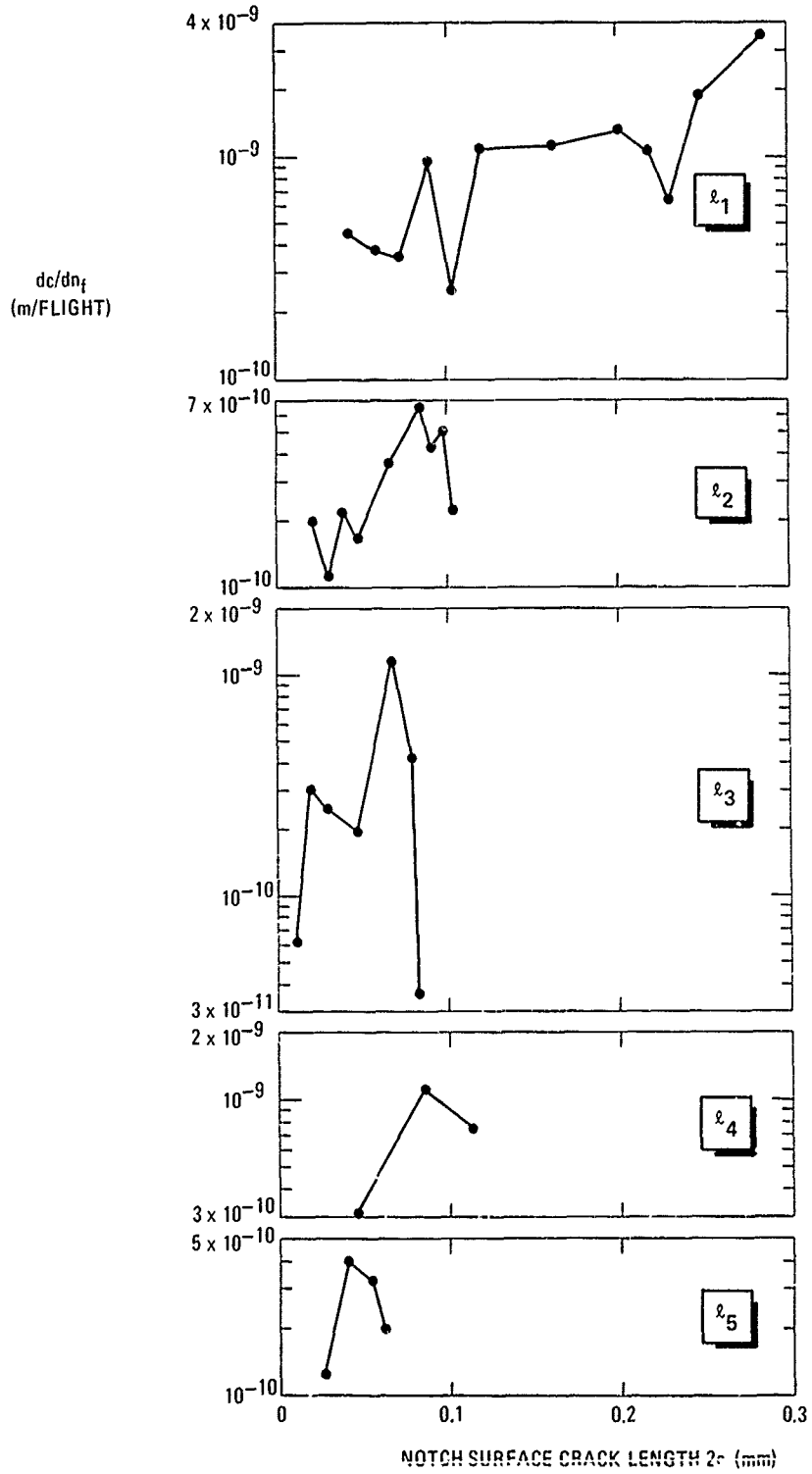


Fig. 15 Valid short crack growth rates versus crack lengths for SENT specimen A68-11 tested with the Fokker 100 Reduced Basic spectrum load sequence: $S_{mf} = 81.25$ MPa

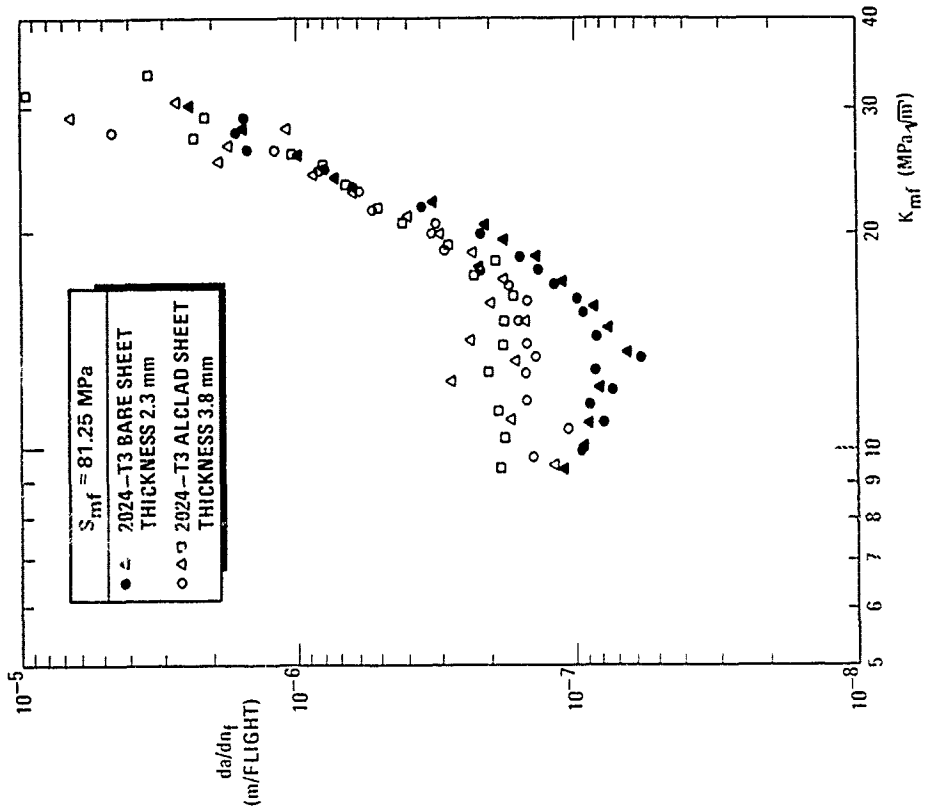


Fig. 17 Comparison of long fatigue crack growth rates for CCT specimens of NASA and Fokker 100 materials tested with the Fokker 100 Reduced Basic spectrum load sequence

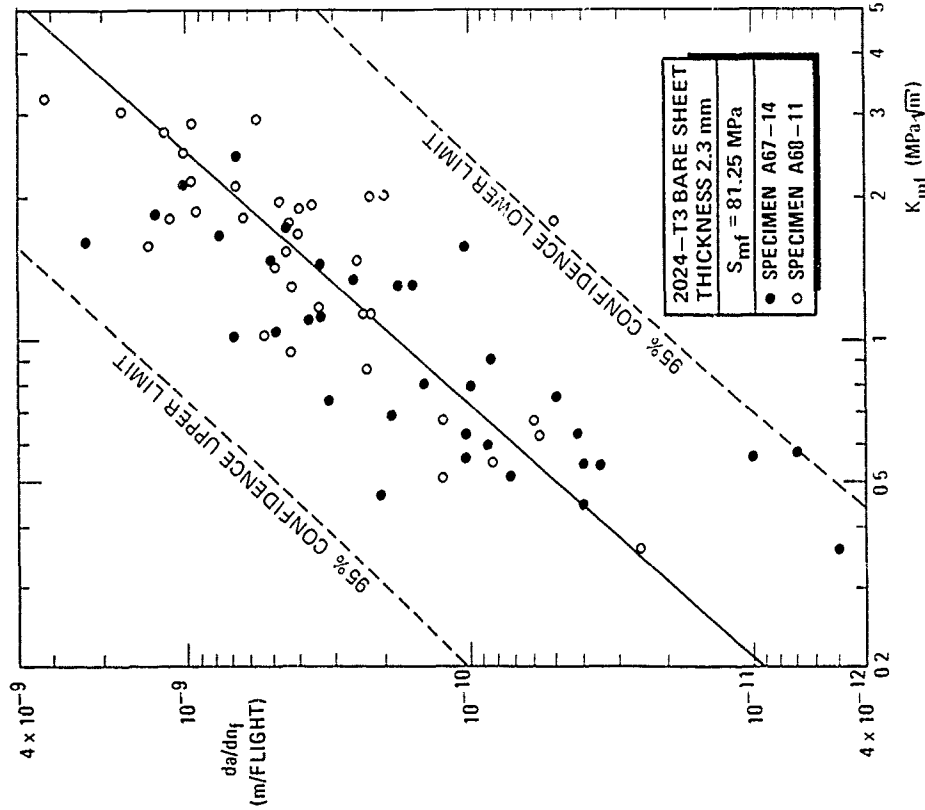


Fig. 18 Valid short crack growth rates versus K_{mf} for SENT specimens A67-14 and A68-11 tested with the Fokker 100 Reduced Basic spectrum load sequence

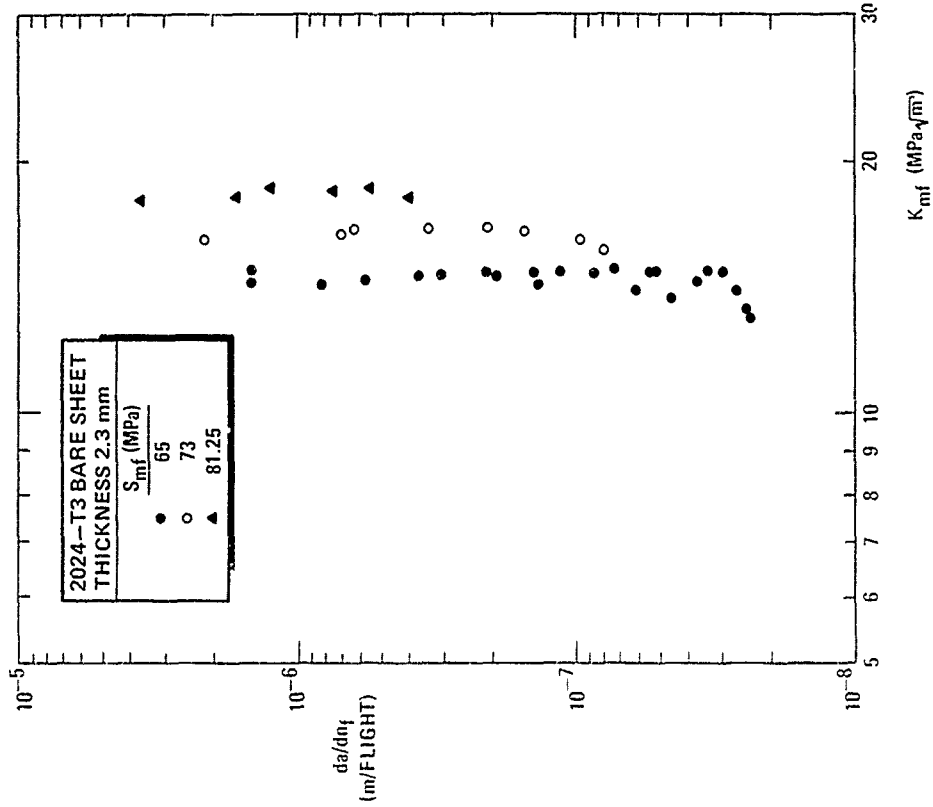


Fig. 19 Long fatigue crack growth rates for B7HT specimens of NASA material tested with the Fokker 100 Reduced Basic spectrum load sequence

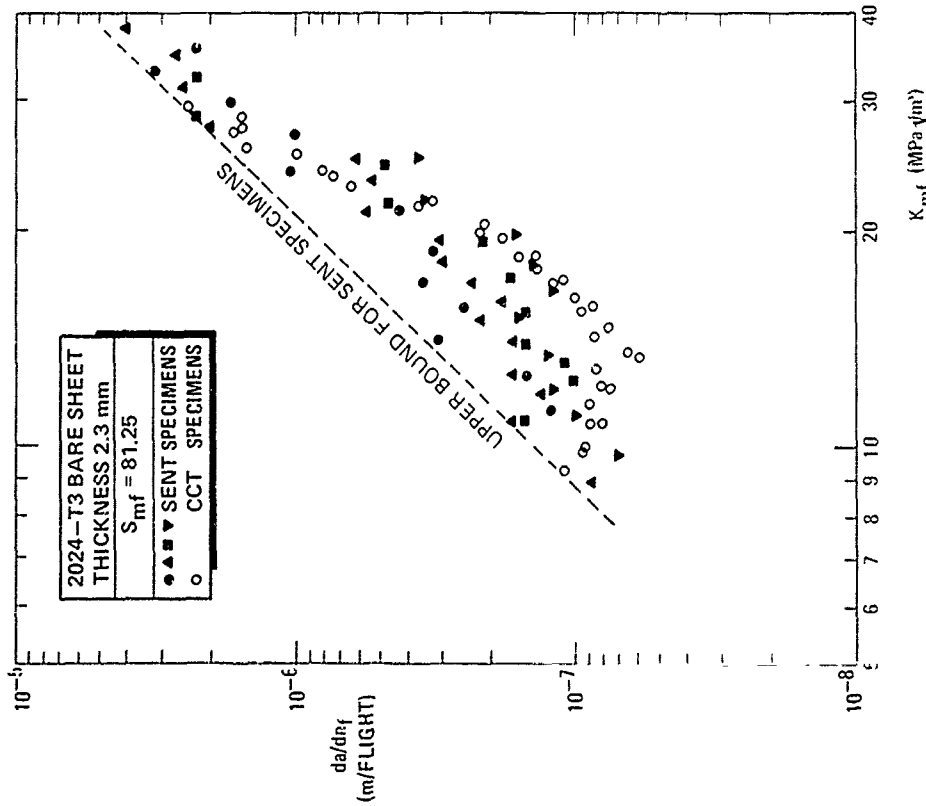


Fig. 18 Comparison of long fatigue crack growth rates for SENT and CCT specimens of NASA material tested with the Fokker 100 Reduced Basic spectrum load sequence

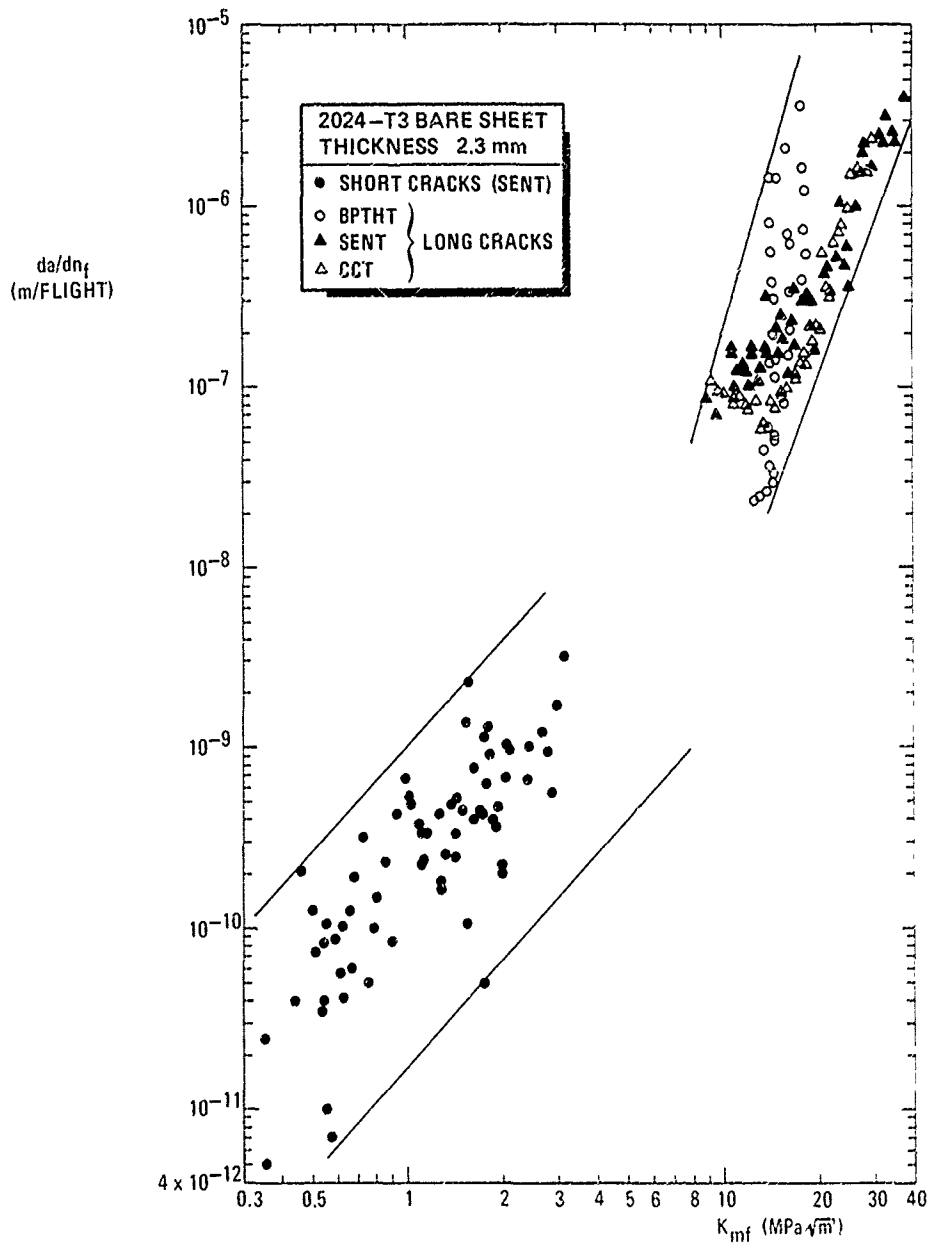


Fig. 20 Comparison of short and long fatigue crack growth rates for the NASA material tested with the Fokker 100 Reduced Basic spectrum load sequence

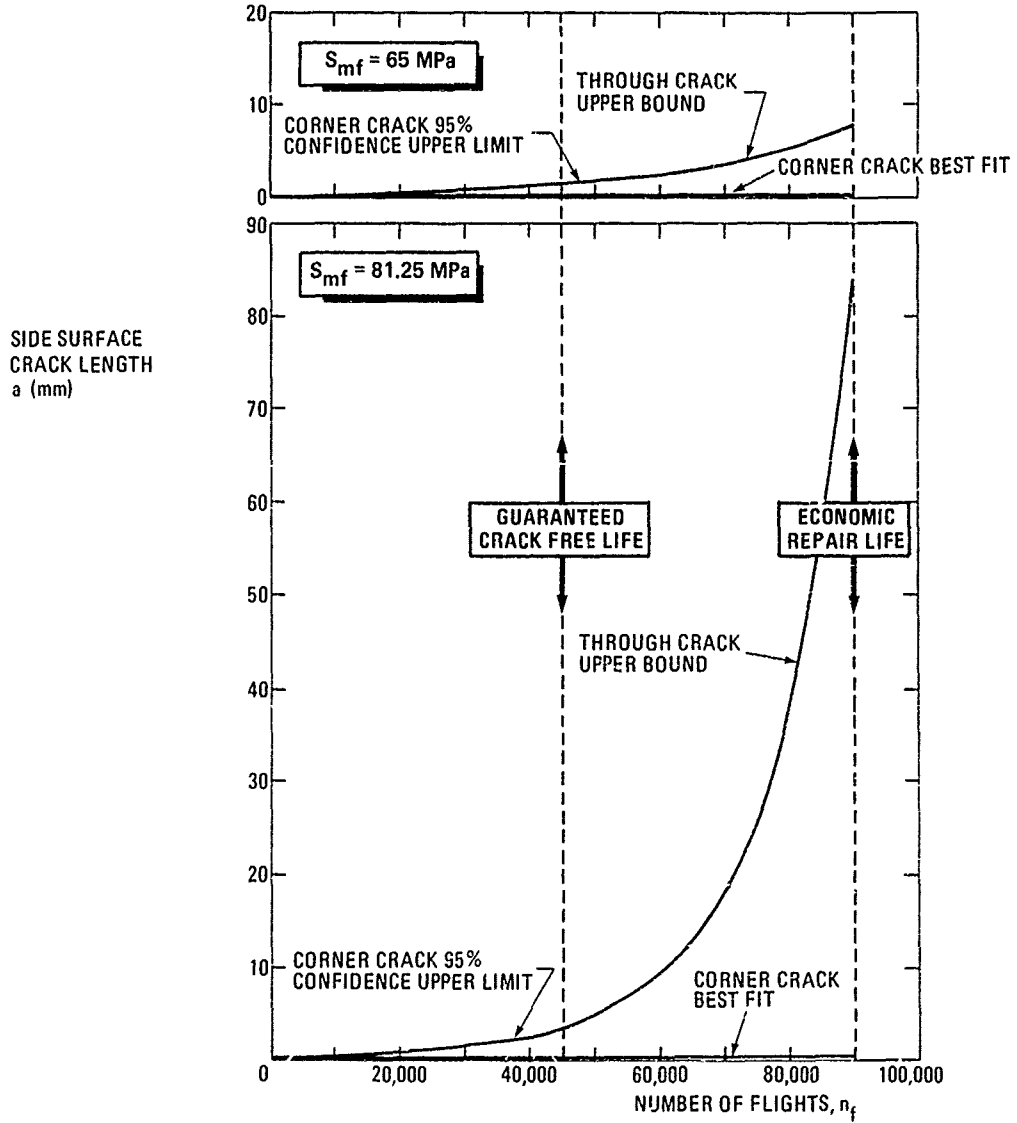


Fig. 21 Estimated fatigue crack growth from an initial corner flaw (side surface dimension $a = 0.127 \text{ mm}$) at a fastener hole in 4 mm thick 2024-T3 subjected to the Fokker 100 Reduced Basic spectrum load sequence

GROWTH OF SHORT FATIGUE CRACKS IN 7075-T6 ALUMINUM ALLOY

Cevdet KAYNAK and Alpay ANKARA
Metallurgical Engineering Department
Middle East Technical University
06531 Ankara, Turkey

SUMMARY

In this study, as part of the Supplemental Programme of the AGARD Collaborative Effort on Short Cracks, the growth of short fatigue cracks was monitored using a plastic replica method for cracks propagating on the specimen notch from the initial length of 40-50 μm up to the specimen thickness of 2.3 mm. Single-edge-notched tension (SENT) Al 7075-T6 specimens were tested under R-ratios of 0.5, 0, -1 and at two different stress levels of each R-ratio.

The general conclusion is that the growth rates of short cracks seem to be faster than the growth rates of long cracks for an R-ratio of -1. No significant differences were observed for $R = 0$, and the short cracks actually grew more slowly at $R = 0.5$.

INTRODUCTION

Fatigue crack propagation in engineering materials has been the subject of considerable research. Most of these researches were especially on the behaviour of "long" fatigue cracks. However, the growth characteristics of "short" cracks in metals and alloys were less investigated, even though they have undoubted importance from an engineering point of view.

Fatigue cracks can be defined as "short" or "small" (i) when their length is small compared to relevant microstructural dimensions (a continuum mechanics limitation), (ii) when their length is small compared to the scale of local plasticity (a linear elastic fracture mechanics (LEFM) limitation), or (iii) when they are simply physically small (eg $< 0.5 - 1 \text{ mm}$) [1].

Following the initial work of Pearson [2] and the general overview of Suresh and Ritchie [1], some attention has been focussed on the growth of short fatigue cracks. Experiments have been done to study the differences observed between short and long crack behaviour on several materials such as aluminum alloys [3-6], steels [7,8], titanium alloys [9,10], aluminum-lithium alloys [11,12], copper alloys [13,14], and nickel-based superalloys [15].

Numerous investigators [3-6] have observed that the growth characteristics of short fatigue cracks in plates and at notches differ from those of long cracks in the same material under the same loading conditions.

Usually short cracks are observed to initiate and grow at stress intensities below the long crack threshold stress intensity factor values. Some of the short cracks grow with decreasing rates until arrest, while others propagate quite rapidly and merge with long crack data (Figure 1).

Since crack growth from "short" pre-existing flaws in many engineering structures is an important part of their fatigue life, the growth behaviour of short fatigue cracks has great importance for understanding the total fatigue process of the component.

The purpose of this study was to generate short crack growth data on 7075-T6 aluminum alloy. The growth of short cracks in edge-notched sheet specimens of Al 7075-T6 in laboratory air and at room temperature under loading conditions of three different R-ratios, 0.5, 0, -1 and at two different stress levels of each, were measured using a replication technique.

MATERIAL, SPECIMEN AND EXPERIMENTAL PROCEDURE

The short crack specimen used in this study was the single-edge-notched tension (SENT) fatigue specimen. The notch was semi-circular with a radius of 3.18 mm (Figure 2).

The material was 7075-T6 aluminum alloy sheet with a thickness of 2.3 mm. This material was taken from a special stock of aluminum alloy sheets retained in NASA Langley Research Center for fatigue testing. The fatigue crack growth properties of this material are discussed in References 16 and 17.

An MTS servo-controlled hydraulic testing machine with hydraulic grips was used for constant amplitude fatigue testing. Aluminum shims were used between the specimen and the grip jaws to prevent any damage to the specimen by the grips.

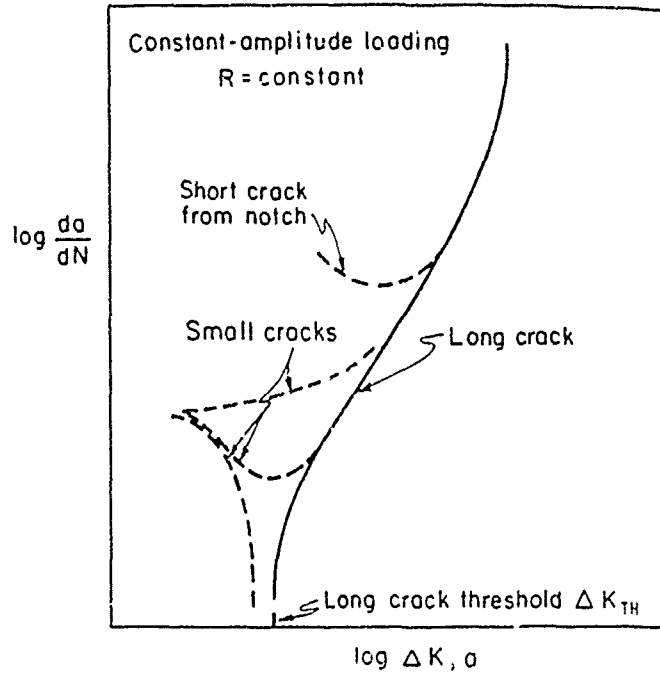


Figure 1. Schematic fatigue crack growth rate data for short and long cracks

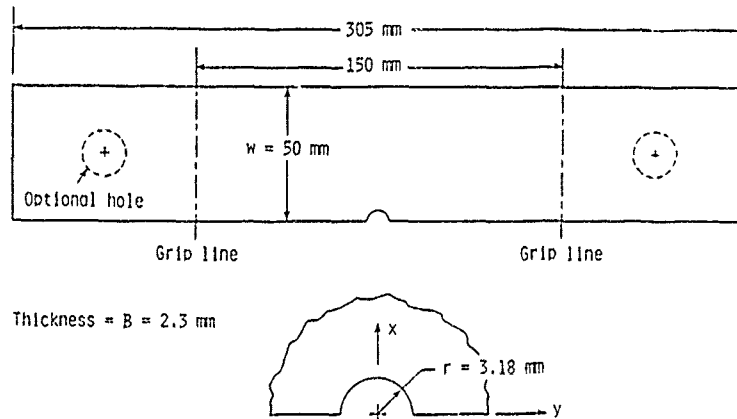


Figure 2. Single-edge-notched tension fatigue specimen

Under compressive loading ($R = -1$), anti-buckling guide plates lined with teflon sheets were used (Figure 3) to eliminate buckling of samples.

In the testing programme, constant amplitude sinusoidal loading was used with a frequency of 15 Hz at all stress ratios. At each R-ratio, two stress levels (S_{max}) were applied, providing a total of six different loading conditions:

$S_{max} = 220 \text{ MPa}$ and 195 MPa for $R = 0.5$
 $S_{max} = 140 \text{ MPa}$ and 120 MPa for $R = 0$
 $S_{max} = 95 \text{ MPa}$ and 80 MPa for $R = -1$.

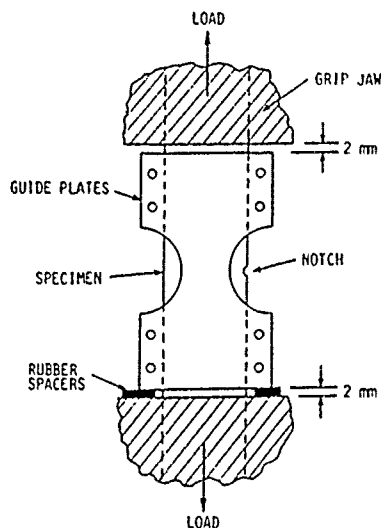


Figure 3. Schematic of anti-buckling guide plates

For each test condition there were two objectives. The first was to obtain surface crack length against cycles data, and the second was to obtain short crack depth information.

For the first objective one specimen was tested to obtain surface crack length against cycles data, using the plastic replica method, until one continuous crack was all the way across the notch root. The specimen was then pulled to failure.

For the second objective one specimen was tested until the total surface crack length along the bore of the notch was between 1 and 2 mm. The specimen was then statically pulled to failure. Microscopic examination of the fracture surface revealed the surface crack shape and size.

To take replicas, tests were interrupted at certain cyclic intervals. The cycle interval was selected so that about 15 replicas were taken during one test. While taking replicas the specimen was loaded to about 80% of maximum load so that any cracks present would be open. The replicas were then examined under a stereo optical microscope to measure the length and determine the location of the crack(s).

DATA ANALYSIS

Figure 4 shows the area over which crack(s) were monitored and recorded by plastic replicas.

After measuring the crack length along the bore of the notch, its value and location were recorded on the Data Chart as a function of cycles. The Data Chart includes the specimen number, loading type, peak stress, and a grid upon which the information obtained from a replica was recorded. Each record of crack length, location and cycles was taken at specified cycle intervals.

At the lower stress levels usually a single crack initiated and dominated for most of the fatigue life. However, at the higher stress levels several cracks developed along the bore of the notch.

To calculate the stress intensity factor, the crack length (a) and the crack depth (c) must be known. Since replica method only gives information on the crack length, the crack depth (c) was calculated from the equation:

$$\frac{c}{a} = 0.9 - 0.25 \left(\frac{a}{t}\right)^2$$

where t is the specimen thickness. This equation is in good agreement with experimental measurements and analytical calculations made on surface cracks growing from an edge notch in Reference 18.

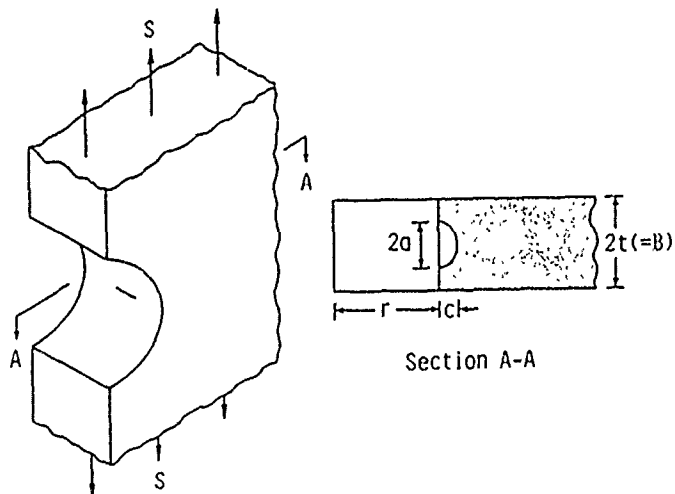


Figure 4. Surface crack at center of semi-circular notch

The stress intensity factor range equation used was [18]:

$$\Delta K = \Delta S \sqrt{\pi a / Q} F$$

where ΔS is the stress range ($S_{\max} - S_{\min}$), Q is the shape factor and F is the boundary-correction factor.

The calculation of crack growth rate was a simple point-to-point calculation, i.e.:

$$\frac{da}{dN} = \frac{\Delta a}{\Delta N} = \frac{a_2 - a_1}{N_2 - N_1}$$

The cycle interval, $N_2 - N_1$, is the interval between replicas.

The corresponding stress intensity factor range (ΔK) is calculated at an average crack length (a) given by:

$$a = \frac{a_2 + a_1}{2}$$

RESULTS AND DISCUSSION

Fractographic examination of the broken specimens showed that crack initiation in general occurred at inclusion particle clusters. These cracks appear to have initiated from defects caused by the separation of the alloy matrix material from an inclusion cluster.

The initiation sites were generally within the middle one-half of the specimen notch thickness and the cracks tended to grow as semi-elliptical surface cracks. Only in two specimens did cracks initiate near the corner of the specimen notch and propagate as quarter-elliptical corner cracks.

In order to compare the growth behaviour of short cracks with those of long cracks, crack growth rate (da/dN) versus stress intensity factor range (ΔK) curves for six different loading conditions were drawn (Figures 5-10). Crack growth rates and stress intensity factors used in these curves were calculated as defined in Reference 18.

The solid lines drawn in these graphs are for Long Crack Growth Data of the same material and under the same loading conditions used in this Cooperative Programme. These data were determined by Phillips [19] from NASA Langley Research Center.

To compare the short and long crack growth rate data the rate da/dN is assumed to be equivalent to dc/dN for the same ΔK value. The short cracks are growing in the a -direction while the long cracks are growing in the c -direction.

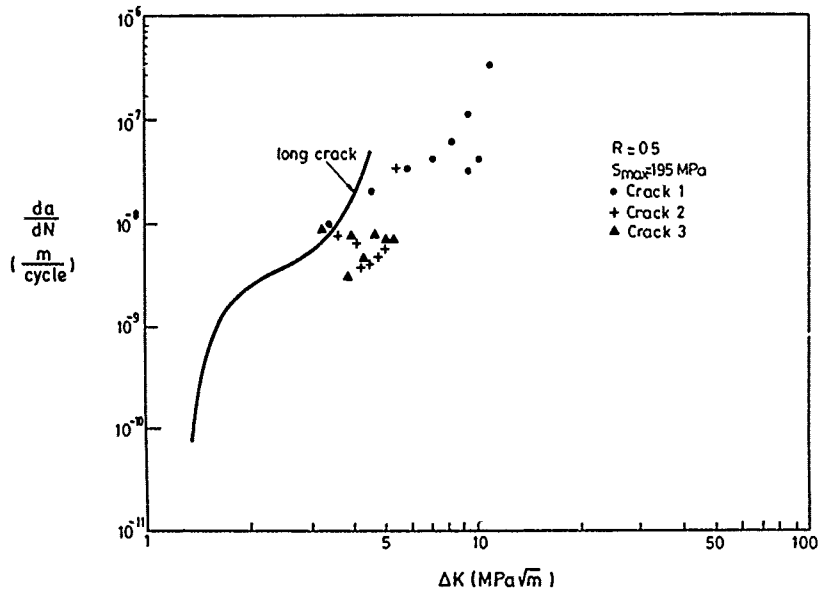


Figure 5. Crack Growth Rate versus Stress Intensity Factor Range curve for $R = 0.5$ $S_{max} = 195$ MPa

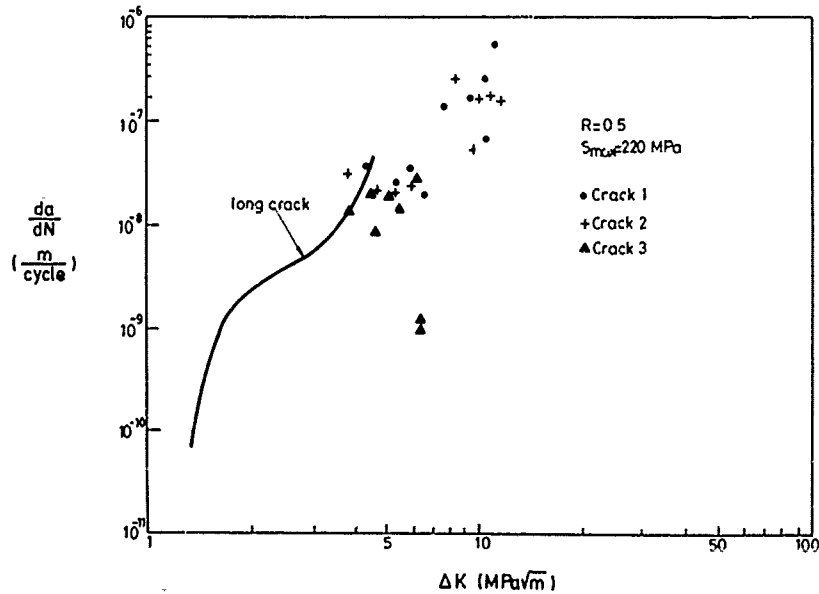


Figure 6. Crack Growth Rate versus Stress Intensity Factor Range curve for $R = 0.5$ $S_{max} = 220$ MPa

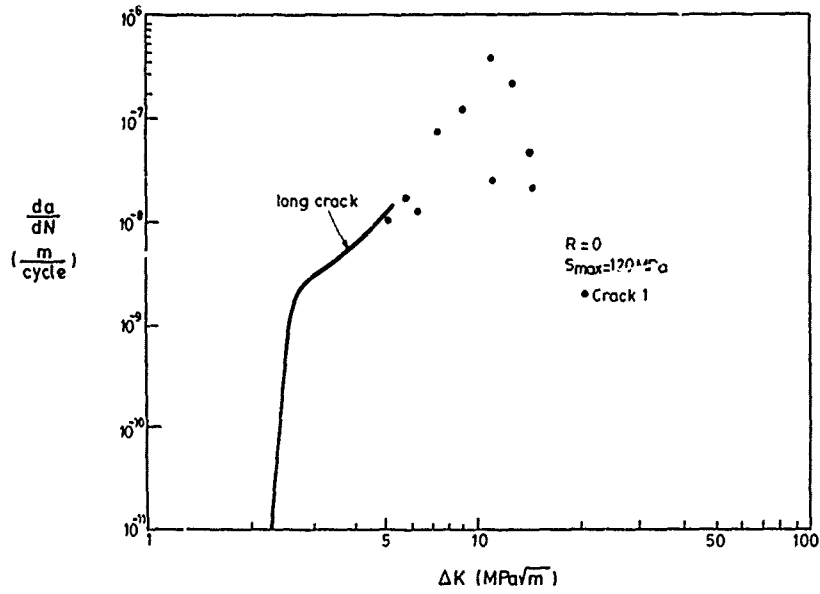


Figure 7. Crack Growth Rate versus Stress Intensity Factor Range curve for $R = 0$ $S_{max} = 120 \text{ MPa}$

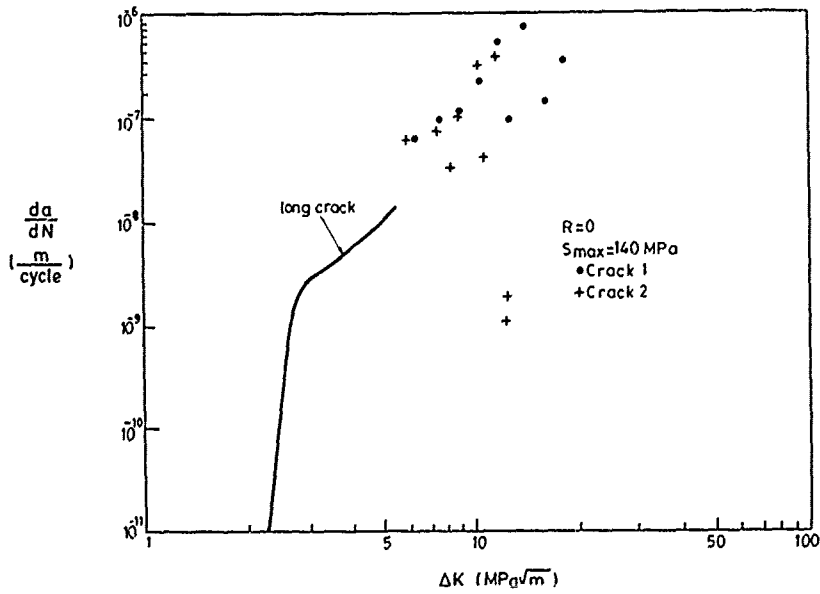


Figure 8. Crack Growth Rate versus Stress Intensity Factor Range curve for $R = 0$ $S_{max} = 140 \text{ MPa}$

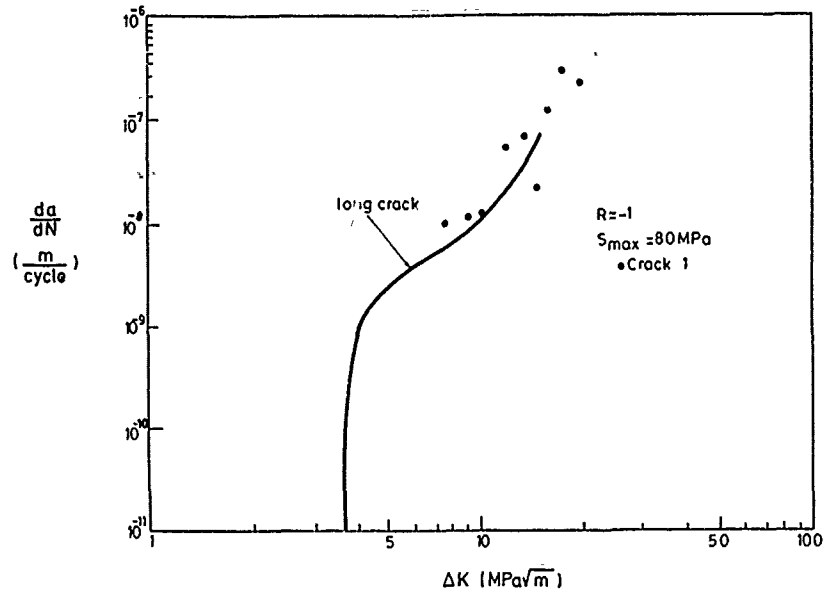


Figure 9. Crack Growth Rate versus Stress Intensity Factor Range curve for $R = -1$ $S_{max} = 80 MPa$

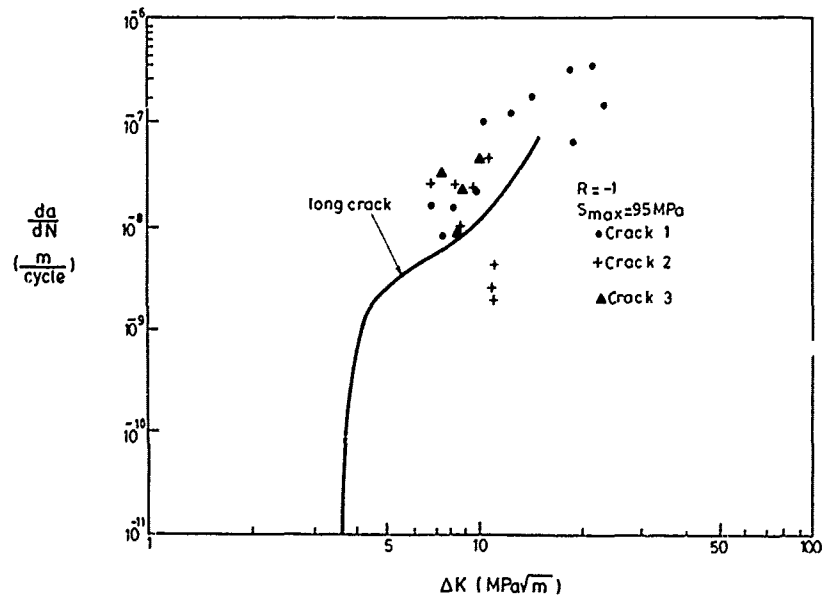


Figure 10. Crack Growth Rate versus Stress Intensity Factor Range curve for $R = -1$ $S_{max} = 95 MPa$

The results for $R = 0.5$ loadings are shown in Figures 5 and 6. No stress level (S_{max}) effect on the growth rate was observed for this loading. At both of the stress levels short cracks grew at substantially slower rates than those measured for long cracks for ΔK values greater than the long crack threshold. Only a few data were above the solid line of the long crack growth data.

The $R = 0$ results, shown in Figures 7 and 8, indicated an influence of stress level both on the number of cracks initiated and their growth rate. Increasing the S_{max} increases both the number of cracks and their growth rate. If the long crack data are extrapolated, the growth rates of short cracks at lower stress level (Figure 7) are similar to those of long cracks, while at the higher stress level (Figure 8) short cracks seem to grow faster than the long cracks.

Under $R = -1$ loading, short and long cracks have similar growth behaviour at the low stress level (Figure 9), but at the high stress level (Figure 10) almost all short crack data are above the solid line, showing the faster crack growth rate of short cracks as compared to long cracks. Also a higher stress level increased the number of short cracks initiated.

REFERENCES

1. Suresh, S. and Ritchie, R.O., Int. Met. Rev., 29(6), 1984, 445-476.
2. Pearson, S., Eng. Fract. Mech., 7, 1975, 235-247.
3. Lee, J.J. and Sharpe, W.N. Jr., Small Fatigue Cracks, eds. R.O. Ritchie and J. Lankford, TMS AIME, Warrendale, 1986, 323-339.
4. Newman, J.C., Swain, M.H. and Phillips, E.P., Small Fatigue Cracks, eds. R.O. Ritchie and J. Lankford, TMS AIME, Warrendale, 1986, 427-452.
5. Lankford, J., Fat. Eng. Mat. Str., 5(3), 1982, 233-248.
6. Morris, W.L., James, M.R. and Buck, O., Met. Trans.A, 12A, 1981, 57-64.
7. Daeubler, M.A. and Thompson, A.W., Small Fatigue Cracks, eds. R.O. Ritchie and J. Lankford, TMS AIME, Warrendale, 1986, 157-165.
8. Klesnil, M., Polak, J. and Liskutin, P., Script. Met., 18, 1984, 1231-1234.
9. Bolingbroke, R.K. and King, J.E., Small Fatigue Cracks, eds. R.O. Ritchie and J. Lankford, TMS AIME, Warrendale, 1986, 129-144.
10. Gerdes, C., Gysler, A. and Lütjering, G., Fatigue Crack Growth Threshold Concepts, eds. D.L. Davidson and S. Suresh, TMS AIME, Warrendale, 1984, 465-478.
11. James, M.R., Script. Met., 21, 1987, 738-788.
12. Venkateswara Rao, K.T. and Yu, W., Script. Met., 20, 1986, 1459-1464.
13. Ma, B.T. and Laird, C., Small Fatigue Cracks, eds. R.O. Ritchie and J. Lankford, TMS AIME, Warrendale, 1986, 9-28.
14. Neumann, P. and Tonnessen, A., Small Fatigue Cracks, eds. R.O. Ritchie and J. Lankford, TMS AIME, Warrendale, 1986, 41-49.
15. Newman, P. and Beevers, C.J., Small Fatigue Cracks, eds. R.O. Ritchie and J. Lankford, TMS AIME, Warrendale, 1986, 97-116.
16. Rice, R.C., Davies, K.B., Jaske, C.E. and Feddersen, C.E., NASA CR-2586, 1975.
17. Hudson, C.M., NASA TND-5390, 1969.
18. Newman, J.C., Swain, M.H., AGARD CP-376, AGARD, France, 1984, 12.1-12.7.
19. Phillips, E.P., NASA Langley Research Center, private communication.

SHORT CRACK OBSERVATIONS IN Ti-6Al-4V UNDER CONSTANT AMPLITUDE LOADING

by

A. Lanciotti and R. Galatolo
 Department of Aerospace Engineering
 University of Pisa
 Diotisalvi 2
 56100 Pisa
 Italy

SUMMARY

This paper describes the Italian contribution to the AGARD supplementary test programme on the growth of short fatigue cracks.

Constant amplitude loading fatigue tests (zero-to-tension and fully reversed loading) were carried out on annealed Ti-6Al-4V titanium alloy, to establish the behaviour of short and long cracks in this material.

The results indicate that short cracks grow faster than long cracks at the same stress intensity factor range and they can also grow below the long crack threshold stress intensity factor range.

1. INTRODUCTION

Several investigators observed that the growth of short fatigue cracks differs from that of long cracks in the same material. On the basis of Linear Elastic Fracture Mechanics, short cracks - cracks ranging in length from 10 μm to 1 mm - grow faster than would be predicted from long-crack data at the same stress intensity factor range, ΔK , and they can also grow below the long crack threshold ΔK values.

AGARD promoted international cooperation on the growth of "short" fatigue cracks to define the significance of the "short crack effect" and to compare test results produced by different laboratories. Cooperation started in 1984 and is now completed /1/. The "core programme" was carried out on single-edge notched tensile specimens made of 2024-T3 aluminum alloy sheet material; specimens were machined by the United States Air Force Wright Aeronautical Laboratory. Tests were conducted under several constant amplitude and spectrum loading conditions at three stress levels each. Twelve laboratories, included the Department of Aerospace Engineering at the University of Pisa, conducted fatigue tests. Growth of short cracks at the notch surface was recorded by plastic replicas; this method is very simple to apply but is very time consuming.

The results of the participants are in good agreement with one another and they show several characteristics of short crack behaviour. All results are described in /1/.

The cooperation was continued and each participant performed a supplementary programme on short cracks; in this programme the choice of the material, the machining of the specimens and the type of fatigue loads were selected by the participants, depending on their specific interests.

This report describes the Italian contribution to the supplementary programme on short-crack growth behaviour. The work involves Ti-6Al-4V titanium alloy in annealed condition under constant amplitude loading at $R=S_{\text{min}}/S_{\text{max}}=0$ and $R=-1$.

2. EXPERIMENTAL PROCEDURE

The experimental procedure for the supplementary programme is similar to that specified for the core programme /1/, so only specific details will be given below.

2.1 Material

Annealed Ti-6Al-4V sheet 1.5 mm. thick was the material selected for the research; it was supplied by Aeritalia GVC. The results of static tests carried out on this material show an ultimate tensile stress of 970 MPa, a yield stress of 920 MPa and elongation of 8.5%.

Optical microscope observations show that the grain size in the rolling direction is about 8 μm and the typical dimension in crack growth direction, $2a$, along the notch root is about 5 μm .

2.2 Specimens

All short-crack growth tests were carried out using the same single-edge notch specimen previously used in the core programme. Specimens (305 mm. long, 50 mm. wide) were cut so that the loading direction was parallel to the rolling direction of the material.

Notches were very carefully milled. Several problems were encountered in the mechanical polishing of the notches; particularly, scratches were produced by using diamond paste. Good results were obtained by very small grain emery paper (4000) and alumina (0.25 μm). A drilling machine was used to polish the specimens by a felt bonded on a metallic wire. Now and then specimens were tilted in order to round the sharpened edges. This operation proved to be efficient; only in certain specimens did the crack begin in a corner. The mechanical polishing proved to be quite complex and time consuming, about 30 minutes for each specimen; moreover, unless these operations are very carefully done, residual stresses may be present.

Conventional central crack specimens, 200 mm. wide, L-T orientation, were used for long-crack growth tests.

2.3 Test equipment

Tests were carried out by means of a servocontrolled electro-hydraulic machine of the capacity of 200 KN.

Grip alignment was checked by a strain gauged dummy specimen, as described in /1/, Annex C.

2.4 Loading conditions

Constant amplitude loading tests, $R=0$ and $R=-1$, were carried out; the test frequency was between 6 and 12 Hz. Antibuckling guides were used for the negative R value.

2.5 Short crack measurements

Cracks were observed by means of a 400x travelling optical microscope and plastic replicas.

Low-quality replicas were obtained by using the same replica material used in the core programme; in particular small cracks observed by the microscope were not present in replicas. The problem was solved by using a replica - kit produced by Struers; these replicas also have a pre-bonded adhesive surface so that their manipulation and catalogation are very easy.

Measurements were recorded on data charts, as shown in Figures 12 and 14 of /1/. Crack growth rates and stress intensity factors were evaluated according to Section 3.5 and Annex F in /1/. The non-interaction criteria between multiple cracks, Section 4.2 in /1/, were applied to the data.

A system for electronic image treatment was analyzed as a possible alternative technique to the plastic replica method; it consists of a digital television camera connected with the microscope. Images are stored in a Personal Computer and can be analyzed. The results were encouraging but to obtain a good resolution high magnifications were necessary and so several images were required to cover the thickness of the specimen. Due to this complication the automation of the tests is very difficult, and the system was temporarily given up.

3. RESULTS

3.1 Fatigue results

Several specimens were fatigue tested to complete failure, to establish S-N curves, while crack propagation was monitored only in a small group of specimens.

Fretting failure under grips happened in some specimens tested at low stress level, in spite of the high stress concentration factor for this type of specimen. The problem was solved by inserting an adhesive aluminum strip between the grips and the specimen.

Results are graphically shown in Figure 1 and are characterized by a high scatter. The S-N curve is well established for $R=-1$, while the drawing of the S-N curve for $R=0$ is very uncertain, due to several anomalous results.

The following stress levels were selected for short crack monitoring:

| R | S_{max_1} (MPa) | S_{max_2} (MPa) | S_{max_3} (MPa) |
|----|--------------------------|--------------------------|--------------------------|
| 0 | 380 | 390 | 405 |
| -1 | 210 | 225 | 245 |

Stress levels are quite close together but this choice was made necessary by the scatter in fatigue results.

Figures 2 and 3 show the fatigue results of tests in which short-crack monitoring was performed. Different symbols refer to crack initiation (crack length greater than 0.01 mm) and final failure. Results indicate that cracks initiate early under higher

stress levels and crack propagation covers 60±70% of fatigue life.

3.2 Long crack results

Centre cracked specimens, 200 mm. wide, were used to obtain long-crack data by the load shedding technique. Load shedding was performed by manually decreasing the load by 10 % after a crack growth of 0.5 mm. Tests were stopped when the near threshold condition was reached; then the load was increased to obtain crack growth data under ΔK increasing condition. The results are shown in Figure 4.

A 6% load shedding test, $R=0$, was carried out to analyze the effect of this parameter on crack growth. The results, Figure 5, are wholly comparable, confirming that the threshold values are $\Delta K=10$ and $6.1 \text{ MPa}\sqrt{\text{m}}$ for $R=1$ and $R=0$, respectively.

The absence of significant differences between the 6% and 10% load-shedding procedures can probably be explained as a consequence of the high-yield stress of this material, so that the plastic zone is small.

3.2 Short-crack results

Plastic replicas were observed through a 400x optical microscope; typical crack length at crack initiation was 0.01 mm. and only in some cases were shorter cracks sighted.

Results relative to each stress level and R value are shown in Figures 6 to 11, in the form of da/dN versus ΔK diagrams. In all diagrams ΔK is the total range of the stress intensity factor.

Scatter in the results is high, but it is of the same order as that of the aluminum alloy in the core programme. All data relative to the same R value are shown in Figures 12 and 13, together with log-log best-fit lines. A log-log best-fit line does not seem adequate to represent the data, so other best-fit curves were tried. An exponential best-fit curve seems to be the most adequate, as shown in Figures 14 and 15. In this form of presentation, the results are virtually independent of maximum stress levels. Generally, crack growth at the same ΔK is a little higher under higher maximum stress levels. The results are also independent of R values at low values of ΔK , as can be observed, Figure 16, by superimposing Figures 14 and 15.

3.3 Comparison between long and short cracks

The comparison between long-crack data and short crack best-fit curves relevant to all of the results at the same R value is shown in Figure 17 for $R = -1$ and in Figure 18 for $R = 0$.

The short-crack effect is evident for $R=-1$ at low values of ΔK while long and short cracks behave in the same way when ΔK is greater than about $20 \text{ MPa}\sqrt{\text{m}}$.

The situation is more complex at $R=0$. Short and long cracks do not show comparable behaviour at high values of ΔK . The explanation is in the fact that residual compressive stresses are present in short crack tests. Indeed, the maximum stress at the notch root in the short crack tests at $R=0$ is greater than the yield stress of the material, so compressive residual stresses are present. The consequence is that the effective value of R in these tests is less than zero and so a correct comparison is not possible. In any case the long-crack curve for the effective R value is on the right of $R=0$ curve, so a short crack effect seems present in this case too.

Residual stresses at the notch root in $R=0$ tests can also explain the similar short-crack behaviour of $R=0$ and $R=-1$ tests at low values of ΔK .

4. CONCLUSIONS

The material selected, annealed Ti-6Al-4V, showed some negative characteristics for this type of research; particularly, high scatter in fatigue results caused trouble in the selection of stress levels for short-crack tests. The small size of the grains does not allow us to study certain aspects of short-crack behaviour as the smaller cracks observed were about as large as two grains. Some problems were also encountered in specimen preparation and in the observation of short cracks by means of plastic replicas.

Comparison between short and long cracks shows a clear "short crack effect" at $R=-1$ while residual compressive stresses, due to notch yielding, were inevitably present in short-crack tests at $R=0$, so the results are not fully comparable with the relevant long-crack data, but a short crack effect seems present in this case too.

5. REFERENCES

1. Newman, J.C., Jr and Edwards, P.R.: " Short Crack Growth Behaviour in an Aluminum Alloy. An AGARD Cooperative Test Programme", AGARD Report n.732, 1988.

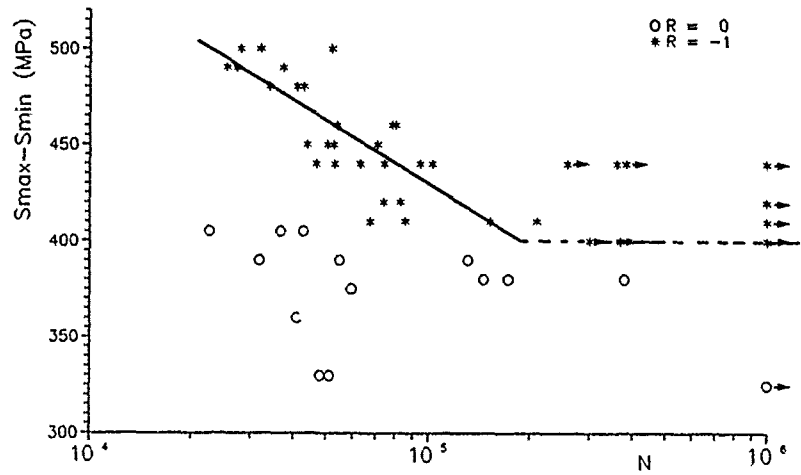


Fig. 1 - Fatigue results of T1-6Al-4V single edge notched specimen

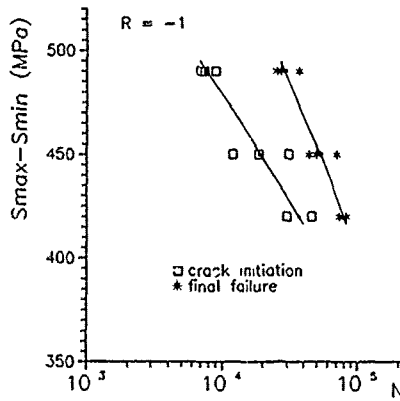


Fig. 2 - Fatigue life from crack initiation to final failure, R=-1.

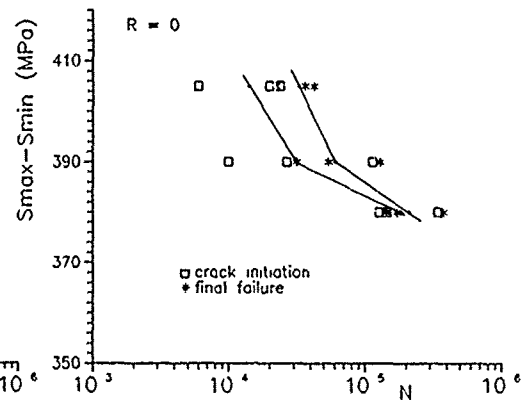


Fig. 3 - Fatigue life from crack initiation to final failure, R=0.

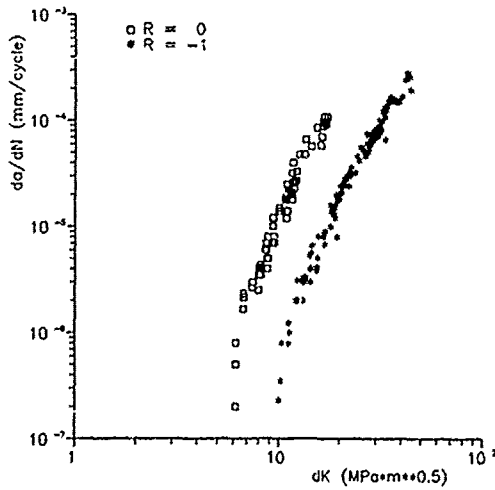


Fig. 4 - Long crack growth rate.

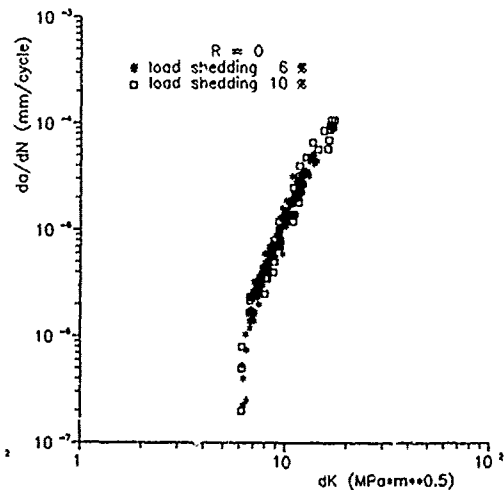


Fig. 5 - Comparison between long crack results obtained by a load shedding of 10% and of 6%.

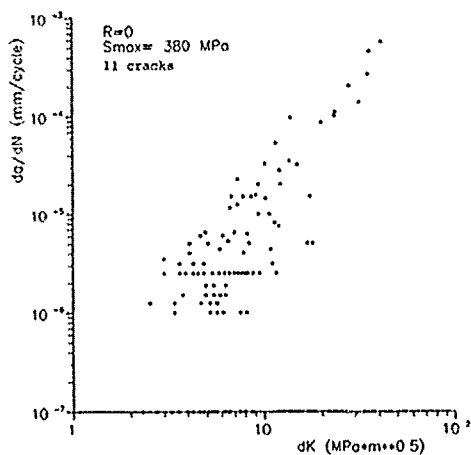


Fig. 6 - Short crack growth rate.
 $R=0$, $S_{max}=380$ MPa.

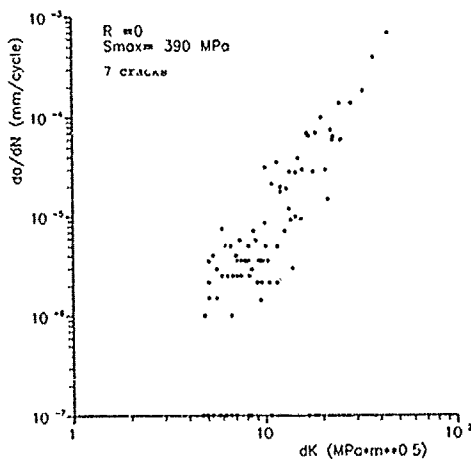


Fig. 7 - Short crack growth rate.
 $R=0$, $S_{max}=390$ MPa.

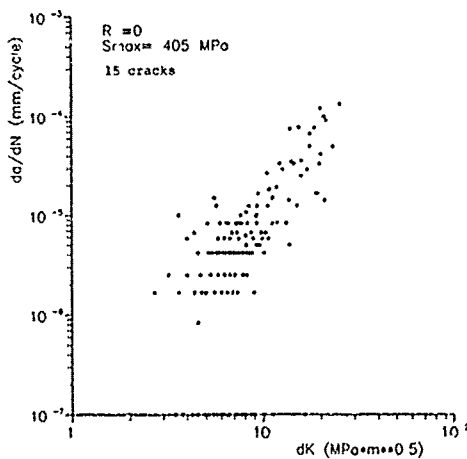


Fig. 8 - Short crack growth rate.
 $R=0$, $S_{max}=405$ MPa.

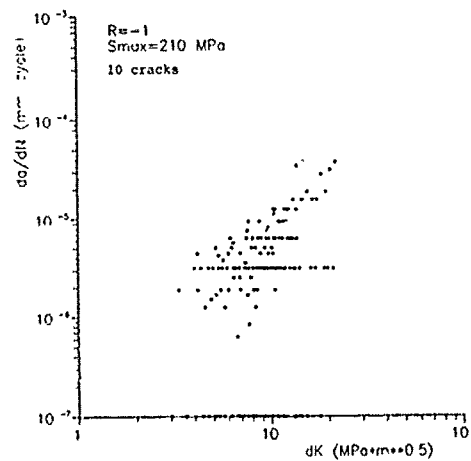


Fig. 9 - Short crack growth rate.
 $R=-1$, $S_{max}=210$ MPa.

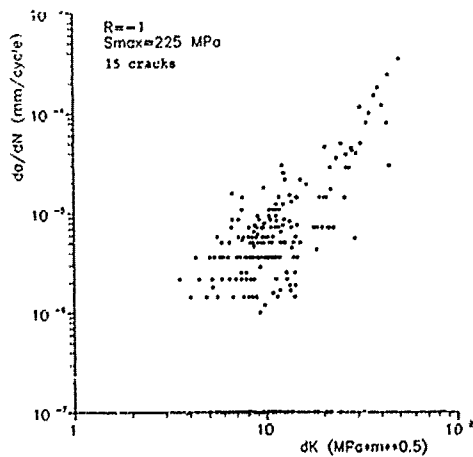


Fig. 10 - Short crack growth rate.
 $R=-1$, $S_{max}=225$ MPa.

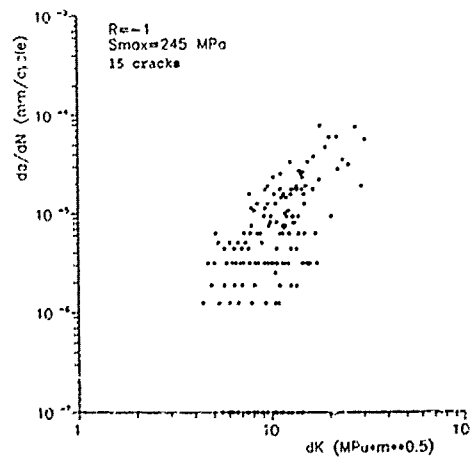


Fig. 11 - Short crack growth rate.
 $R=-1$, $S_{max}=245$ MPa.

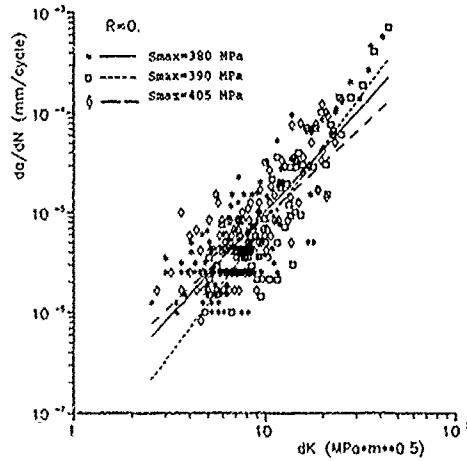


Fig. 12 - Short crack growth rate and log-log best-fit curves. R=0.

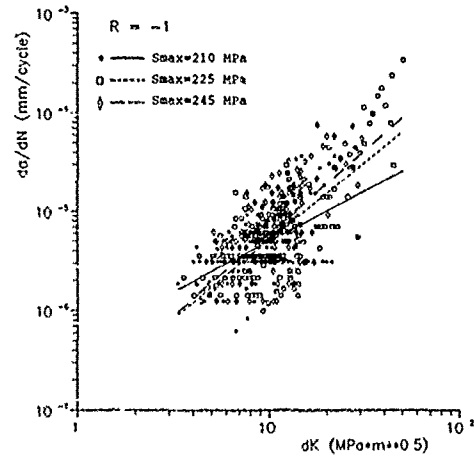


Fig. 13 - Short crack growth rate and log-log best-fit curves. R=-1.

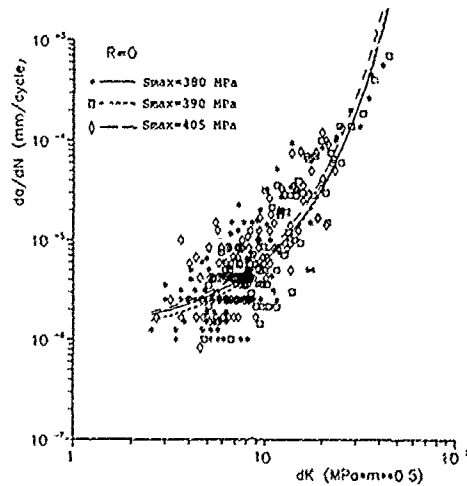


Fig. 14 - Short crack growth rate and exp. best-fit curves. R=0.

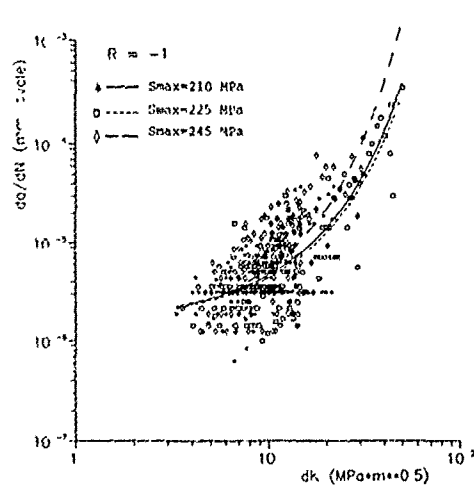


Fig. 15 - Short crack growth rate and exp. best-fit curves. R=-1.

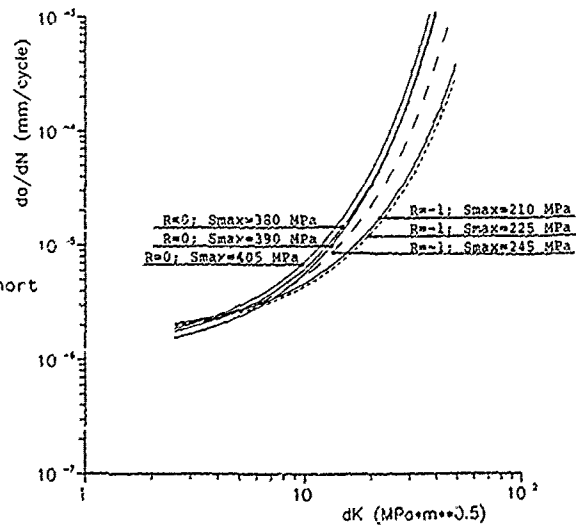


Fig. 16 - Comparison between short crack growth rates.

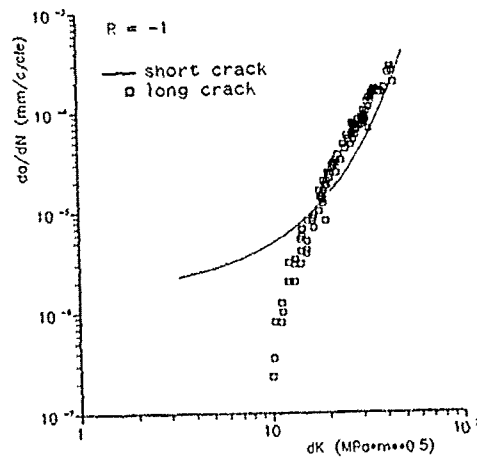


Fig. 17 - Comparison between long and short cracks. $R = -1$.

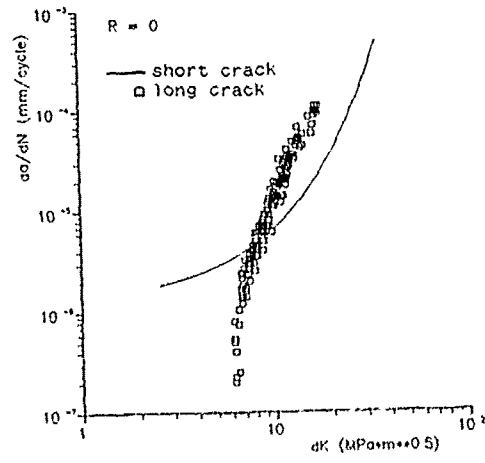


Fig. 16 - Comparison between long and short cracks. $R = 0$.

ANNEX
TEXTURE ANALYSIS OF 2090-T8E41 ALUMINUM-LITHIUM ALLOY SHEET

A. W. Bowen
Materials and Structures Department
Royal Aerospace Establishment
Farnborough, England

This annex describes the texture analysis that was made on the 2090-T8E41 aluminum-lithium alloy sheet used in the AGARD Supplemental Test Programme. The information obtained in this analysis was supplied to all participants who tested the aluminum-lithium alloy.

EXPERIMENTAL

Four samples of 2.15 mm-thick 2090 aluminum-lithium sheet were studied in the as-received condition. Incomplete (max 85° tilt) 111, 200, 220 and 311 pole figures were measured on an automated Siemens texture goniometer, using $Cu K\alpha$ radiation, in the Materials and Structures Department of the Royal Aerospace Establishment. The data were then processed to produce white orientation distribution functions (ODF) by the series expansion method using the Bunge notation [1]. The as-received surface was initially examined, after which material was progressively removed by polishing, with periodic texture analysis, until the mid-thickness was reached.

One sample, B1706, was examined in detail, with the remaining samples being measured only at $3/4 t$ and $1/2 t$ (where t = sheet thickness).

RESULTS

The (111) pole figures for sample B1706 are shown in Figures 1(a) to 1(e) for the surface ($t = 2.15$ mm), and at $t = 2.0$, 1.6 ($3/4 t$), 1.45, and 1.09 ($1/2 t$) mm. Note that in this figure, and in Figure 2, the contours are at intervals of 1, 5, 10, 15 etc. times the intensity of that of a randomly-oriented specimen. The most informative section through the ODF (at $\phi_2 = 45^\circ$, where ϕ_1 , ϕ_2 , and Φ are the Euler angles [1]) for these conditions are shown in Figures 2(a) to 2(e). These figures indicate that the sheet has a very strongly developed texture that changes its type from the surface to the mid-plane. These textures are deformation textures and indicate that the sheet is in the unrecrystallised form. Orientation A ($\{112\}[111]$, often called the copper-type texture) decreases in intensity from surface to mid-thickness, whereas orientation B ($\{110\}[112]$, often called the brass-type texture) increases in intensity (see Figures 2(a) for the locations of orientations A and B, and similarly in Figures 2(b) to 2(e)). These data are plotted, as the orientation density along the fibre texture from A, through the S orientation ($\{123\} \langle 634 \rangle$), to orientation B in Figure 3, showing decreases in the intensities of orientations A and S and an increase in that of orientation B. No evidence of any recrystallisation is indicated in these figures, which would be located at C (for the cube texture $\{001\} \langle 100 \rangle$) and at G (for the Goss texture $\{110\} \langle 100 \rangle$). The results are very similar to those reported recently for 2090 [2] and 8090 sheet [3], and confirm that texture cannot be ignored when evaluating mechanical property anisotropy in Al-Li based alloys. This is further complicated by the marked gradients in texture that exist between surface and mid-thickness.

Analysis of the other three samples are shown in Figures 4 and 5 for the $3/4 t$ condition, and in Figures 6 and 7 for the $1/2 t$ condition. Comparison of Figures 1(c) with 1(e), and 2(c) with 2(e), show that the texture is consistent in type although variable in intensity. This is also shown by the texture sharpness index listed in Table 1.

TABLE 1
Texture Sharpness Index (J) [1] for 2.15 mm-thick 2090 Sheet

| Sample | $t = 2.15$ | 2.0 | 1.6 | 1.45 | 1 |
|--------|------------|-----|-----|------|------|
| B1706 | 7.8 | 7.1 | 7.3 | 8.9 | 9.5 |
| B1623 | - | - | 5.6 | - | 12.7 |
| B1425 | - | - | 7.2 | - | 10.6 |
| B1403 | - | - | 7.5 | - | 12.7 |

REFERENCES

1. Bunge, H. J.: Texture Methods in Materials Science, Butterworths, Ltd., London, 1982.
2. Vasudevan, A. K.; Fricke, W. G., Jr.; Przystupa, M. A. and Panchanadeswaran, S.: Synergistic Effects of Crystalline Texture and Precipitation on Yield Strength Anisotropy in Al-Li-Cu-Zr Alloy, Presented at the 8th International Conference on Textures of Materials, 1987.
3. Bowen, A. W.: Texture Characterisation of Al-Li Alloy Sheet, RAE TM Mat/St 1099, 1987. (Also presented at the 8th International Conference on Textures of Materials, 1987.)

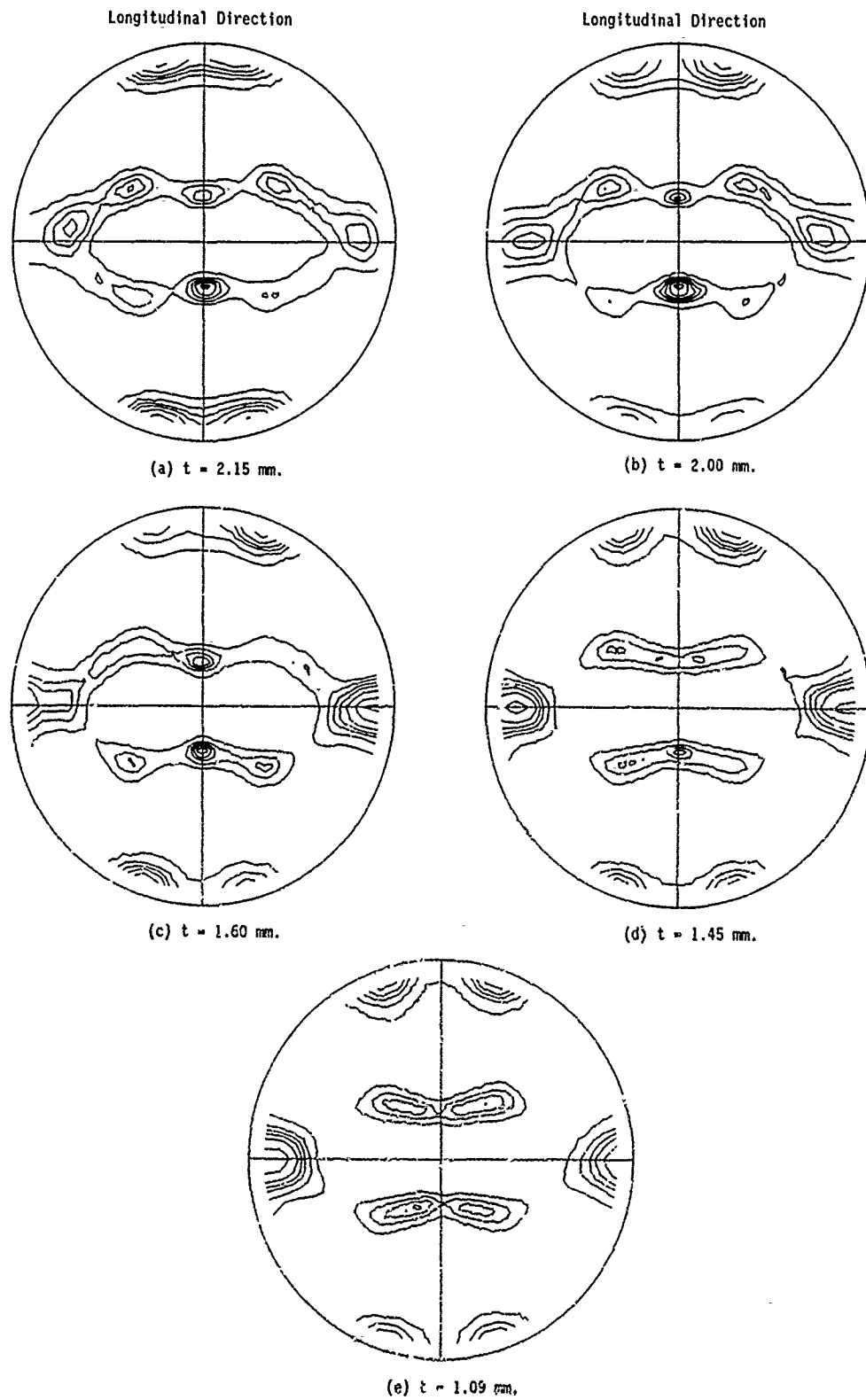


Figure 1.- (111) Pole figures for sample B1706 as a function of thickness, t .

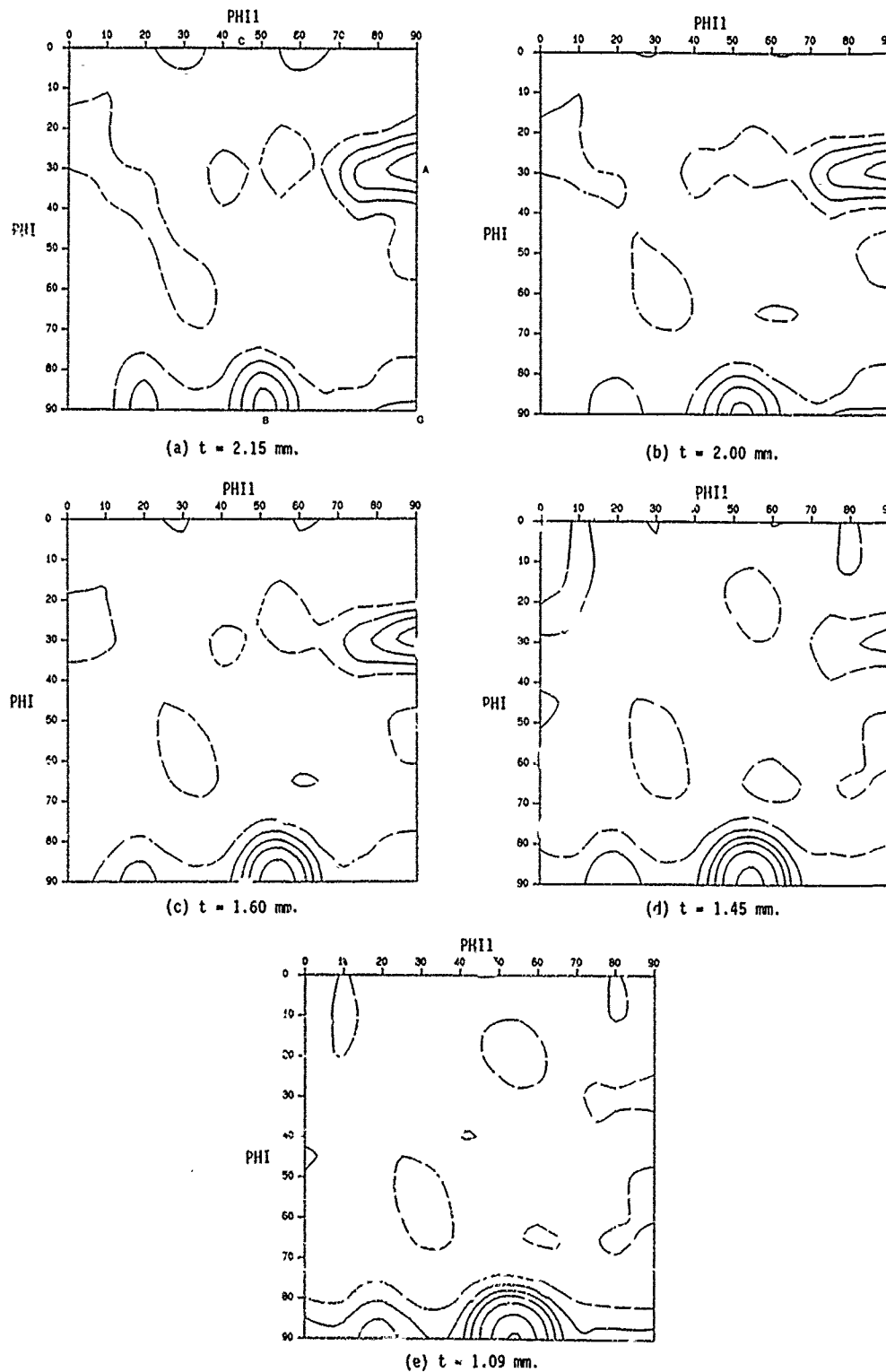


Figure 2.- $\text{Phi}2 = 45^\circ$ sections through the ODF for sample B1706 as a function of thickness, t . (A, B, C and G are the positions of the orientations referred to in the text.)

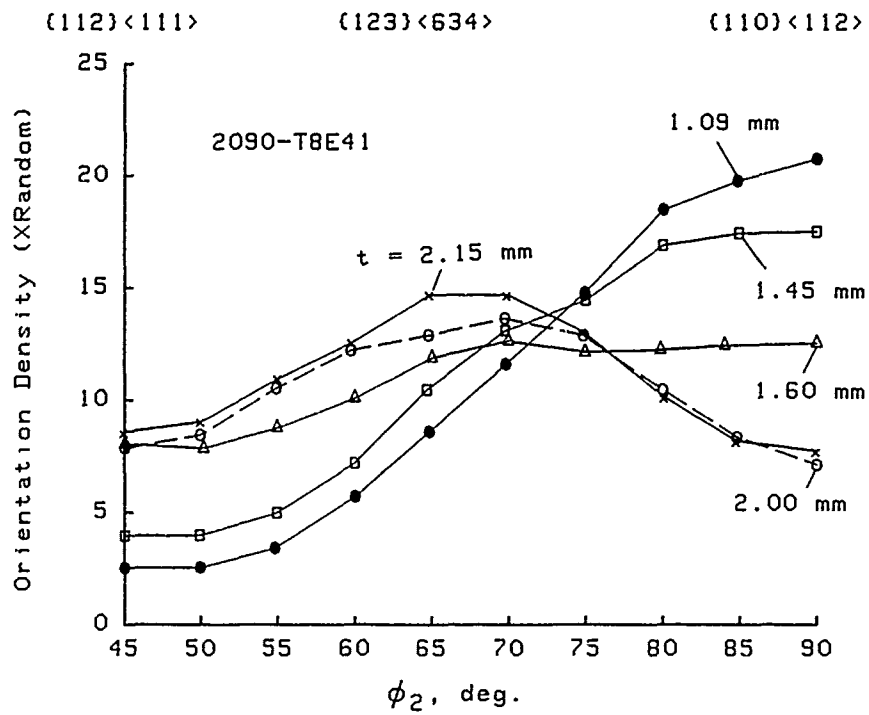


Figure 3.- Orientation density along copper-brass fibre texture as a function of thickness, t .

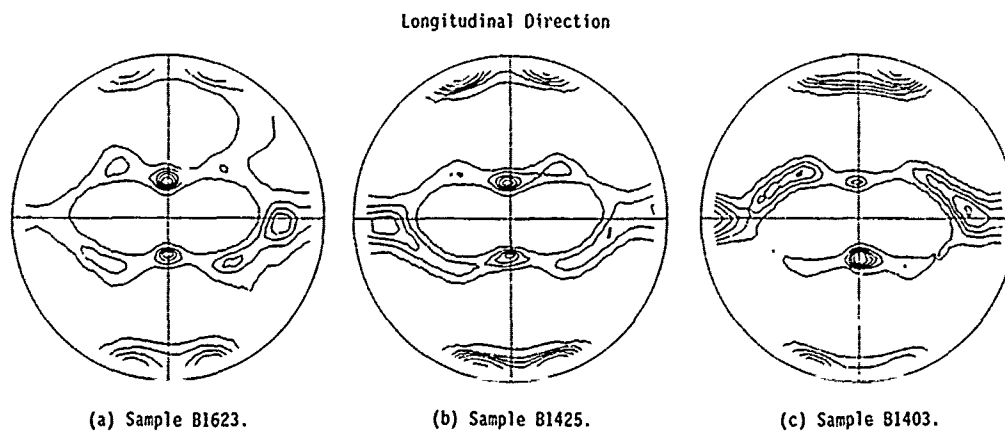


Figure 4.- (111) Pole figures for various samples at $3/4 t$.

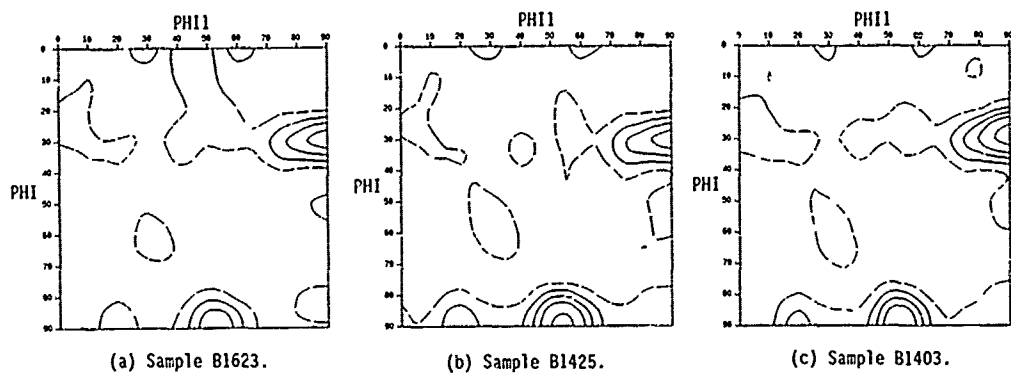


Figure 5.- $\Phi_2 = 45^\circ$ sections through the ODF for various samples at $3/4 t$.

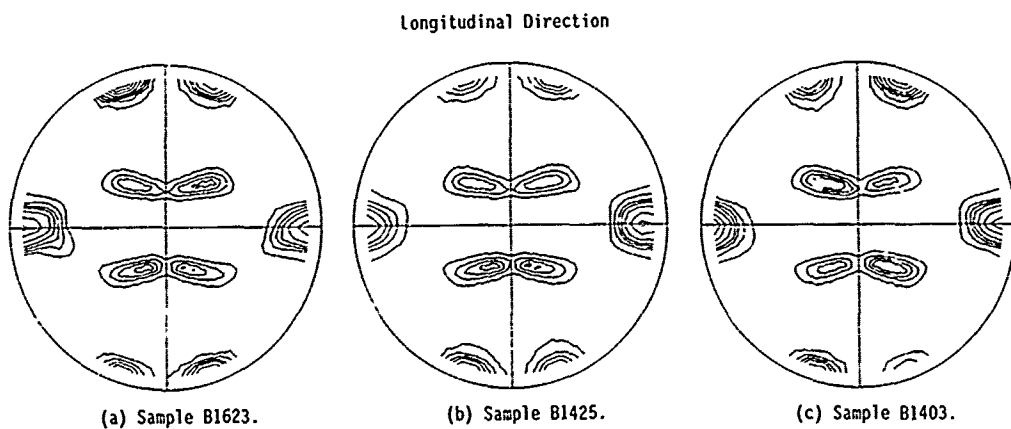


Figure 6.- (111) Pole figures for various samples at $1/2 t$.

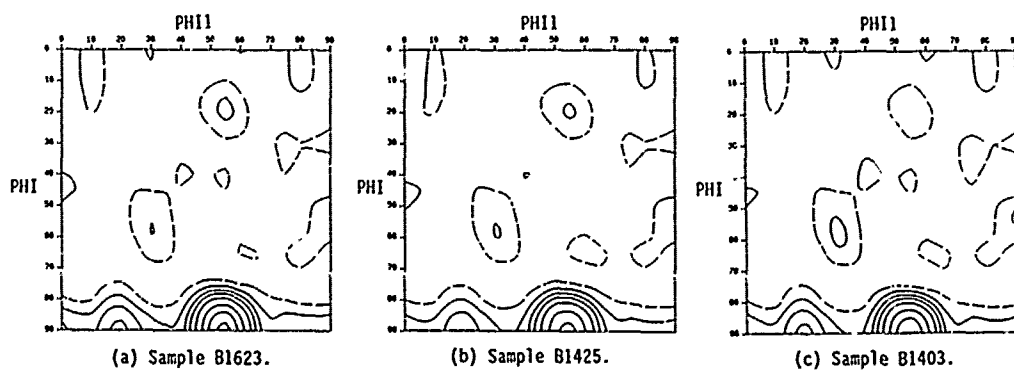


Figure 7.- $\Phi_2 = 45^\circ$ sections through the ODF for various samples at $1/2 t$.

| REPORT DOCUMENTATION PAGE | | | |
|-------------------------------|--------------------------------------------------------------------------------------------------------------------------------------------------------------------------------------------------------------------------------------------------------------------------------------------------------------------------------------------------------------------------------------------------------------------------------------------------------------------------------------------------------------------------------------------------------------------------------------------------------------------------------------------------------------------------------------------------------------------------------------------------------------------------------------------------------------------------------------------------------------------------------------------------------------------------------------------------------------------------------------------------------------------------------------------------------------------------------------------------------------------------------------------------------------------------------------------|----------------------|----------------------------------------|
| 1. Recipient's Reference | 2. Originator's Reference | 3. Further Reference | 4. Security Classification of Document |
| | AGARD-R-767 | ISBN 92-835-0577-8 | UNCLASSIFIED |
| 5. Originator | Advisory Group for Aerospace Research and Development
North Atlantic Treaty Organization
7 rue Ancelle, 92200 Neuilly sur Seine, France | | |
| 6. Title | SHORT-CRACK GROWTH BEHAVIOUR IN VARIOUS AIRCRAFT MATERIALS | | |
| 7. Presented at | | | |
| 8. Author(s)/Editor(s) | Compiled by: P.R.Edwards and J.C.Newman, Jr | | 9. Date |
| | | | August 1990 |
| 10. Author's/Editor's Address | See Flyleaf. | | 11. Pages |
| | | | 200 |
| 12. Distribution Statement | This document is distributed in accordance with AGARD policies and regulations, which are outlined on the Outside Back Covers of all AGARD publications. | | |
| 13. Keywords/Descriptors | <p>Crack propagation
Mathematical models,
Data processing,
Fatigue life,
Fatigue tests,</p> <p>Aluminum/
Aluminum alloys,
Titanium alloys,
Steels, (SS)</p> | | |
| 14. Abstract | <p>AGARD Report R-732 reviews the results of the first phase of an AGARD Cooperative Test Programme on the behaviour and growth of "short" fatigue cracks. That report describes; the establishment of a common test method, means of data collection/analysis and crack growth modelling in an aircraft alloy AA 2024-T3. The second and concluding phase of this Programme allowed participants to test various materials and loading conditions. The results of this second phase are described in this report.</p> <p>All materials exhibited a "short-crack" effect to some extent. The effect was much less evident in 4340 steel than in the other materials. For the aluminium, aluminium-lithium and titanium alloys, short cracks grew at stress-intensity factor ranges lower, in some cases much lower, than the thresholds obtained from long crack tests. Several laboratories used the same crack growth model to analyze the growth of short cracks. Reasonable agreement was found between measured and predicted short-crack growth rates and fatigue lives. <i>Key words.</i></p> <p>This publication was sponsored by the Structures and Materials Panel of AGARD.</p> | | |

| | |
|-------------------------------------------------------------------------------------------------------------------------------------------------------------------------------------------------------------------------------------------------------------------------------------------------------------------------------------------------------------------------------------------------------------------------------------------------------------------------------------------------------------------------------------------------------------------------------------------------------------------------------------------------------------------------------------------------------------------------------------------------------------|-------------------------------------------------------------------------------------------------------------------------------------------------------------------------------------------------------------------------------------------------------------------------------------------------------------------------------------------------------------------------------------------------------------------------------------------------------------------------------------------------------------------------------------------------------------------------------------------------------------------------------------------------------------------------------------------------------------------------------------------------------------|
| <p>conditions. The results of this second phase are described in this report.</p> <p>All materials exhibited a "short-crack" effect to some extent. The effect was much less evident in 4340 steel than in the other materials. For the aluminum, aluminum-lithium and titanium alloys, short cracks grew at stress-intensity factor ranges lower, in some cases much lower, than the thresholds obtained from long crack tests. Several laboratories used the same crack growth model to analyze the growth of short cracks. Reasonable agreement was found between measured and predicted short-crack growth rates and fatigue lives.</p> <p>This publication was sponsored by the Structures and Materials Panel of AGARD.</p> <p>ISBN 92-835-0577-8</p> | <p>conditions. The results of this second phase are described in this report.</p> <p>All materials exhibited a "short-crack" effect to some extent. The effect was much less evident in 4340 steel than in the other materials. For the aluminum, aluminum-lithium and titanium alloys, short cracks grew at stress-intensity factor ranges lower, in some cases much lower, than the thresholds obtained from long crack tests. Several laboratories used the same crack growth model to analyze the growth of short cracks. Reasonable agreement was found between measured and predicted short-crack growth rates and fatigue lives.</p> <p>This publication was sponsored by the Structures and Materials Panel of AGARD.</p> <p>ISBN 92-835-0577-8</p> |
| <p>conditions. The results of this second phase are described in this report.</p> <p>All materials exhibited a "short-crack" effect to some extent. The effect was much less evident in 4340 steel than in the other materials. For the aluminum, aluminum-lithium and titanium alloys, short cracks grew at stress-intensity factor ranges lower, in some cases much lower, than the thresholds obtained from long crack tests. Several laboratories used the same crack growth model to analyze the growth of short cracks. Reasonable agreement was found between measured and predicted short-crack growth rates and fatigue lives.</p> <p>This publication was sponsored by the Structures and Materials Panel of AGARD.</p> <p>ISBN 92-835-0577-8</p> | <p>conditions. The results of this second phase are described in this report.</p> <p>All materials exhibited a "short-crack" effect to some extent. The effect was much less evident in 4340 steel than in the other materials. For the aluminum, aluminum-lithium and titanium alloys, short cracks grew at stress-intensity factor ranges lower, in some cases much lower, than the thresholds obtained from long crack tests. Several laboratories used the same crack growth model to analyze the growth of short cracks. Reasonable agreement was found between measured and predicted short-crack growth rates and fatigue lives.</p> <p>This publication was sponsored by the Structures and Materials Panel of AGARD.</p> <p>ISBN 92-835-0577-8</p> |